



**COCHLEAR PROPERTIES AND  
MICROMACHINED HAIR-LIKE  
SHEAR SENSORS**

by  
Shuangqin Liu

A dissertation submitted in partial fulfillment  
of the requirements for the degree of  
Doctor of Philosophy  
In Mechanical Engineering

**TUFTS UNIVERSITY**

February 2012

**ADVISER: Robert White, Ph.D**

©

SHUANGQIN LIU

2012

---

All Rights Reserved

## ABSTRACT

Orthotropic material properties of the gerbil basilar membrane are determined using a geometrically nonlinear finite element composite orthotropic plate model. This model extracts material properties based on point stiffness and space constant reported from two sets of experimental data. Two boundary conditions are investigated. The material properties are quantified at different locations along the length of basilar membrane for both boundary conditions. The orthotropy of gerbil basilar membrane varies along the length of the gerbil basilar membrane from a maximum of 65 close to the base to a minimum of 10 in the upper middle turn.

A sixteen fold scaled-up guinea pig cochlea model is designed and fabricated. The physical model geometry and fluid properties were chosen in a way to satisfy *scaling law* which is derived from dimensionless analysis with *Buckingham Pi theorem* to ensure the motion of the enlarged cochlear model resembles that of the guinea pig cochlea. The frequency responses of the cochlear basilar membrane were recorded and compared with a mathematical model based on WKB method. The test results show the experiment characteristic frequencies are about 100-300Hz different from those computed using WKB and the magnitudes of the ratio of cochlear membrane to drive velocity are about

15-25dB lower than those calculated from WKB method. The phases for WKB and experimental results are very close.

A novel hair-like sensor using capacitive sensing scheme for direct shear measurement is designed, fabricated and tested. The capacitive sensor base is fabricated using PolyMUMPs™ foundry process and hair posts sitting on the sensor base are post fabricated at Tufts cleanroom facility. The sensors were successfully fabricated, released and packaged. The sensors are tested in a flow cell with laminar air flow at different flow rates using both LCR meter and a commercial differential capacitance measurement sensor MS3110. The test results are compared with benchmark sensors which have no hair posts. LCR meter tests showed a bulged sensor membrane under flow due to flow pressure. Differential capacitance measurements using MS3110, which eliminate pressure effect on sensor, showed higher sensitivities for the hair sensors than sensors without hairs. The measured single hair sensor sensitivity is  $0.74 \times 10^{-17} \text{ Farad} / \text{Pa}$  , about half of the predicted sensitivity  $1.437 \times 10^{-17} \text{ Farad} / \text{Pa}$  . The RMS resolution of the sensors in a 1Hz band for 32 sensors in parallel is 5.1Pa and the RMS resolution is 0.33Pa with 120 seconds of averaging.

## **ACKNOWLEDGEMENTS**

There are so many people that I am indebted to. Without whom, it would have been impossible for me to finish my Ph.D work and this dissertation.

I always consider myself blessed to have Professor White as my adviser. I am amazed at his intelligence and knowledge, and impressed by his patience. He always patiently explains things in the great detail in order to help me understand the big picture. I am thankful for his teaching and guidance that have equipped me with the knowledge and character to become an independent researcher. Not only is he a great mentor, but also a good friend who cares for my personal life. Thank you for your understanding and support when I face difficult personal issues.

I want to thank my committee members, Professor Jason Rife, Professor Barry Trimmer, Professor David Mountain and Dr. Judith Gallman for taking time to read my thesis and give me insightful feedback.

Thanks to NASA and Spirit AeroSystems for supporting the hair-like shear stress sensor project financially, especially to Judy Gallman and Mark Moeller for their help along the way.

Thanks to my coworkers Josh, Minchul, Zhengxin, Rameen and John for their help and friendship, especially for Josh's help on sensor packaging.

Without my family, this day would have never come. I want to thank my husband Yue. His love and support are demonstrated through his concrete actions through six years of my Ph.D study. Thank you for taking care of my life, lightening my burden so that I can focus on my study and research. Though six years is not a short time, without you my time as a student might have been doubled.

To my parents, my parents-in-law and my siblings, though they cannot physically be with me in the States, their love and care are always there with me.

To Joseph and Lydia Han, two of the most important people in my life.

Thank you for your unconditional love and your lives that inspire me.

To the International Student Ministry (ISM) for being my extended family. Thank you all who have been here to love me and support me.

# CONTENTS

ABSTRACT .....	III
ACKNOWLEDGEMENTS .....	V
LIST OF FIGURES .....	XI
LIST OF TABLES .....	XVI
<b>1 INTRODUCTION</b> .....	<b>1</b>
<b>2 DETERMINATION OF GERBIL COCHLEA BASILAR MEMBRANE</b>	
<b>PROPERTIES</b> .....	<b>4</b>
2.1 PHYSIOLOGY OF EAR AND MECHANISM OF HEARING .....	4
2.1.1 <i>Structure of Cochlea</i> .....	6
2.1.2 <i>Structure of Basilar Membrane</i> .....	9
2.2 BACKGROUNDS AND OBJECTIVES .....	10
2.3 OVERVIEW OF MATHEMATIC MODELS .....	17
2.4 BEAM MODEL .....	22
2.5 PLATE MODEL .....	25
2.5.1 <i>Composite Material Model</i> .....	25
2.5.2 <i>Analytic Linear Plate Model</i> .....	28
2.5.3 <i>Nonlinear Finite Element Model</i> .....	33
2.6 RESULTS AND DISCUSSIONS .....	35
2.6.1 <i>Linearity vs. Nonlinearity</i> .....	35
2.6.2 <i>Comparison with Hemicochlea Experiment</i> .....	41
2.6.3 <i>Probe Area</i> .....	44
2.6.4 <i>Stiffness Linearity</i> .....	45
2.6.5 <i>Basilar Membrane Dimensions</i> .....	46

2.7 CONCLUSION .....	48
<b>3 SCALED HYDROMECHANICAL GUINEA PIG COCHLEA MODEL.....</b>	<b>53</b>
3.1 BACKGROUND .....	54
3.2 PHYSICAL MODEL .....	57
3.3 MATHEMATIC MODEL USING WKB METHOD.....	62
3.4 SCALING LAW .....	65
3.5 SCALING PARAMETERS OF THE COCHLEAR MODEL.....	68
3.6 EXPERIMENTS .....	69
3.7 RESULT AND DISCUSSION.....	71
3.7.1 <i>Experiment Repeatability of the Cochlear Model</i> .....	71
3.7.2 <i>Viscosity Influence on the Cochlear Model</i> .....	72
3.7.3 <i>Comparison of WKB with Experimental Results</i> .....	73
3.8 CONCLUSION .....	79
<b>4 INTRODUCTION TO SHEAR SENSORS .....</b>	<b>81</b>
4.1 MOTIVATION .....	82
4.2 OBJECTIVE.....	85
4.3 EXISTING TECHNOLOGIES OF FLOW MEASUREMENT SENSORS .....	88
4.3.1 <i>Conventional Techniques for flow measurements</i> .....	88
4.3.2 <i>MEMS Sensors for flow measurements</i> .....	93
4.3.2.1 Direct Shear Stress Measurements .....	95
Capacitive Shear Stress Sensors .....	96
Piezoresistive Shear Stress Sensors .....	101
Optical Shear Stress Sensors.....	104
4.3.2.2 Indirect Shear Stress Measurements.....	115
Thermal Shear Stress Sensors.....	115
Micro-Pillar Shear Stress Sensors.....	121
<b>5 MODELING AND DESIGN.....</b>	<b>126</b>
5.1 PLATE MODELING.....	129

5.1.1	<i>Analytical Kirchoff Plate Model</i> .....	129
5.1.2	<i>FEA Mindlin Plate Model</i> .....	133
5.2	HAIR POST LOCATION AND DIAMETER OPTIMIZATION .....	135
5.3	SENSOR AND ARRAY LAYOUT .....	139
5.4	DESIGN OF FLOW CELL.....	144
5.5	PREDICTED SENSITIVITY.....	147
5.5.1	<i>Fluid Mechanics Analyses of Hair Post</i> .....	148
5.5.2	<i>Structure Mechanics Analyses of Mindlin Plate</i> .....	154
5.6	ELECTRONICS DESIGN .....	158
<b>6</b>	<b>FABRICATION, PACKAGING AND TESTING</b> .....	<b>168</b>
6.1	SHEAR SENSOR FABRICATION .....	168
6.1.1	<i>PolyMUMPs™ Foundry Process Fabrication</i> .....	168
6.1.2	<i>Hair Posts Fabrication</i> .....	173
6.1.3	<i>Sensor Releasing</i> .....	178
6.2	SENSOR PACKAGING .....	181
6.3	DYNAMIC CHARACTERIZATION .....	187
6.3.1	<i>Capacitance and Resistance Measurement</i> .....	187
6.3.2	<i>Frequency Response</i> .....	190
6.4	LAMINAR FLOW CELL TESTING .....	197
6.4.1	<i>Wall Shear Stress in the Flow Cell</i> .....	197
6.4.2	<i>LCR Capacitance Testing</i> .....	199
6.4.3	<i>Integrated System Testing</i> .....	206
6.4.3.1	Experiment Setup .....	206
6.4.3.2	Sensor Sensitivity Testing .....	207
6.5	DISCUSSION .....	210
6.5.1	<i>Noise</i> .....	210
6.5.2	<i>Drift</i> .....	212
6.5.3	<i>Repeatability</i> .....	214
6.5.4	<i>Comparison of current work with previous work</i> .....	214

6.6 CONCLUSION .....	216
<b>7 CONCLUSIONS AND FUTURE WORK .....</b>	<b>218</b>
7.1 CONCLUSIONS .....	218
7.2 FUTURE WORK FOR COCHLEAR MODELS AND HAIR-LIKE SHEAR SENSORS .....	220
<b>APPENDIX A: MATLAB® SCRIPTS .....</b>	<b>242</b>
A1 WKB CALCULATION FOR COCHLEAR DUCT RESPONSE .....	226
A2 OPTIMIZATION OF HAIR POSTS LOCATIONS .....	233
<b>APPENDIX B: LABVIEW® BLOCK DIAGRAM .....</b>	<b>242</b>
<b>APPENDIX C: CAD DRAWING .....</b>	<b>243</b>
C1 HAIR SENSOR MASKS LAYOUT .....	243
C2 ALUMINUM FLOW CELL CAD DRAWING .....	247
<b>APPENDIX D: SENSOR FABRICATION RUNSHEET .....</b>	<b>248</b>
<b>BIBLIOGRAPHY .....</b>	<b>251</b>

# LIST OF FIGURES

FIGURE 2.1 SCHEMATIC VIEW OF HUMAN EAR.....	5
FIGURE 2.2 CROSS SECTIONAL VIEW OF A COCHLEAR STRUCTURE .....	7
FIGURE 2.3 SCHEMATIC OF ORGAN OF CORTI [12] .....	8
FIGURE 2.4 SCHEMATIC OF BASILAR MEMBRANE AND TRAVELING WAVE.....	10
FIGURE 2.5 SCHEMATIC OF BM STIFFNESS MEASUREMENT PROCEDURE FROM NAIDU AND MOUNTAIN ([7, 8]) :	
(A) A CIRCULAR PROBE IS PUSHED INTO THE COCHLEAR PARTITION, AND THE FORCE VS. DEFLECTION CURVE	
IS MEASURED; (B) A TOP-DOWN VIEW OF BM: THE CONTOURS SHOW THE SHAPE OF THE LATERAL	
(X-DIRECTION) DEFLECTIONS (C) DEFLECTION SPACE CONSTANT IS DESCRIBED AS THE DISTANCE $x_2 - x_1$	
ALONG X DIRECTION WHERE THE DEFLECTION DECREASES EXPONENTIALLY FROM ITS MAXIMUM VALUE TO	
37% OF MAXIMUM VALUE. IN THIS DRAWING, BM IS THE BASILAR MEMBRANE, LAM IS THE SPIRAL	
LAMINA, AND LIG IS THE SPIRAL LIGAMENT. DRAWING TAKEN FROM [41] .....	19
FIGURE 2.6 SCHEMATIC OF A BEAM MODEL UNDER LOAD WITH .....	22
FIGURE 2.7 COMPOSITE MATERIAL WITH FIBERS AND MATRIX.....	26
FIGURE 2.8 COMPARISON OF VERTICAL DISPLACEMENT COMPUTED WITH DIFFERENT FIBER .....	28
FIGURE 2.9 SCHEMATIC OF PLATE BOUNDARY CONDITIONS AND LOAD AREA .....	30
FIGURE 2.10 DEFLECTION PROFILE USING LINEAR MODEL .....	33
FIGURE 2.11 A MESHED SYMMETRIC PLATE MODEL (AT A POSITION OF 1.14 MM FROM THE BASE) IN ABAQUS.	
62158 ELEMENTS ARE USED FOR THIS MODEL, AND THE MODEL IS TRUNCATED TO PRODUCE A SQUARE	
MODEL .....	34
FIGURE 2.12 COMPARISON OF ANALYTICAL SOLUTION WITH ABAQUS SOLUTION FOR SS BOUNDARY CONDITIONS	
AT A POSITION 3.99 MM FROM THE BASE OF THE BM .....	36
FIGURE 2.13 CONTOUR PLOT SHOWS PLATE DEFLECTION AT 1.14 MM FROM BASE. THIS IS FOR AN APPLIED LOAD	
OF 4 mN DISTRIBUTED UNIFORMLY OVER THE 5 MM RADIUS CONTACT REGION. ....	37
FIGURE 2.14 COMPARISON OF OUT-OF-PLANE DEFLECTION AND IN-PLANE DEFLECTION FOR SS BOUNDARY	
CONDITIONS AT A POSITION 3.99 mm FROM THE BASE OF THE BM. OUT-OF-PLANE DEFLECTION USES LEFT	

VERTICAL AXIS AND IN-PLANE DEFLECTION USES RIGHT VERTICAL AXIS. NOTE THAT THE SPACE CONSTANT FOR THE OUT-OF-PLANE DEFLECTION AND IN-PLANE DEFLECTION ARE DIFFERENT .....	38
FIGURE 2.15 MATERIAL PROPERTY VARIATIONS ALONG THE LONGITUDINAL DIRECTION .....	39
FIGURE 2.16 COMPARISON OF STIFFNESS PROFILE IN HEMICOCICLEA EXPERIMENT .....	42
FIGURE 2.17 COMPARISON OF CONTACT AREA EFFECT FOR ABAQUS SOLUTION.....	44
FIGURE 2.18 PLATE MODEL LINEARITY IN THE CONSTANT STIFFNESS RANGE AT 3.99 MM FROM BASE .....	46
FIGURE 3.1 COCHLEAR DUCT AND ITS BASE .....	58
FIGURE 3.2 COCHLEAR MEMBRANE AND ITS SUPERSTRUCTURE DIMENSIONS.....	59
FIGURE 3.3 COCHLEAR MODEL AND SHAKER SET UP.....	60
FIGURE 3.4 SETUP FOR COCHLEAR MODEL EXPERIMENT.....	70
FIGURE 3.5 REPEATABILITY OF THE COCHLEA MODEL.....	72
FIGURE 3.6 VISCOSITY INFLUENCE ON THE COCHLEAR MODEL.....	73
FIGURE 3.7 COMPARISON OF WKB AND EXPERIMENTAL RESULTS.....	74
FIGURE 3.8 COMPARISON OF WKB AND EXPERIMENTAL RESULTS.....	77
FIGURE 3.9 COMPARISON OF RESULTS FOR SIMPLY SUPPORTED AND CLAMPED BOUNDARIES.....	78
FIGURE 4.1 CLASSIFICATION OF WALL SHEAR STRESS MEASUREMENTS [71] .....	89
FIGURE 4.2 SCHEMATIC VIEW OF A TYPICAL FLOATING ELEMENT SENSOR .....	95
FIGURE 4.3 SCHEMATIC CROSS-SECTION VIEW OF DIFFERENTIAL CAPACITIVE .....	96
FIGURE 4.4 SCHEMATIC REPRESENTATION OF SECOND GENERATION .....	99
FIGURE 4.5 SCHEMATIC TOP VIEW OF CAPACITIVE FLOATING ELEMENT. ....	101
FIGURE 4.6 PIEZORESISTIVE SHEAR STRESS SENSOR BY [83]. (A) SCHEMATIC VIEW OF.....	102
FIGURE 4.7 OPTICAL SHEAR STRESS BY [86] (A) SCHEMATIC TOP-VIEW OF FLOATING ELEMENT .....	106
FIGURE 4.8 OPTICAL SHEAR STRESS BY [88] (A) SCHEMATIC TOP-VIEW .....	108
FIGURE 4.9 OPTICAL MOIRESHEAR STRESS SENSOR AND SENSING SCHEME [89] .....	110
FIGURE 4.10 PHOTOGRAPHS OF THE FIBER CONFIGURATION AT THE SENSOR PLUG .....	111
FIGURE 4.11 A SHEAR SENSOR USING WGM OPTICAL SENSING TECHNOLOGY [90] .....	113
FIGURE 4.12 SCHEMATIC VIEW OF A THERMAL SHEAR-STRESS SENSOR .....	117
FIGURE 4.13 PHOTOGRAPH OF FLEXIBLE SKIN SHEAR STRESS SENSOR ARRAY.....	119
FIGURE 4.14 PHOTOGRAPH OF FLEXIBLE SKIN SHEAR STRESS SENSOR ARRAY.....	123

FIGURE 4.15 PHOTOS OF HAIR-LIKE FORCE SENSOR ARRAY [104].....	124
FIGURE 5.1 SCHEMATIC OF HAIR-LIKE SENSOR.....	127
FIGURE 5.2 CONCEPT OF BIDIRECTIONAL FLOW SENSOR.....	128
FIGURE 5.3 SCHEMATIC OF A CLAMPED CIRCULAR PLATE SUBJECT TO POINT FORCE $P$ AT $A$ .....	131
FIGURE 5.4 COMPARISON OF PLATE DEFLECTION .....	135
FIGURE 5.5 INVESTIGATION OF HAIR POST LOCATIONS .....	137
FIGURE 5.6 OPTIMIZATION OF HAIR POST LOCATIONS AND THE EFFECT OF POST DIAMETER .....	138
FIGURE 5.7 SINGLE HAIR-LIKE SENSOR LAYOUT (A) TOP VIEW (B) SIDE VIEW .....	140
FIGURE 5.8 HAIR-LIKE SENSOR ARRAY LAYOUT.....	142
FIGURE 5.9 LAMINAR FLOW IN A FLOW CHAMBER .....	144
FIGURE 5.10 FLOW CELL COMPONENTS .....	146
FIGURE 5.11 ASSEMBLED FLOW CELL .....	147
FIGURE 5.12 FEA MODEL OF FLUID DOMAIN .....	149
FIGURE 5.13 FEA MESH FOR THE FLUID MECHANICS MODEL.....	151
FIGURE 5.14 VELOCITY DISTRIBUTION IN THE FLUID DOMAIN FOR 42717 ELEMENTS MODEL .....	152
FIGURE 5.15 VELOCITY DISTRIBUTION IN THE FLUID DOMAIN FOR 32689 ELEMENTS MODEL .....	153
FIGURE 5.16 SHEAR STRESS DISTRIBUTION ON THE HAIR POST FOR 42717 ELEMENTS MODEL .....	153
FIGURE 5.17 THE MESH OF 2D MINDLIN PLATE MODEL WITH 27696 ELEMENTS.....	155
FIGURE 5.18 TOP PLATE DEFLECTION (A) 2D VIEW (3) 3D VIEW.....	156
FIGURE 5.19 MS3110 CAPACITIVE READOUT SENSOR AND PIN-OUT DIAGRAM [37].....	158
FIGURE 5.20 MS3110 FUNCTIONAL BLOCK DIAGRAM AND CONNECTION WITH HAIR-LIKE SENSOR [109] ....	160
FIGURE 5.21 EEPROM PERMANENT WRITE MODE TIMING DIAGRAM [109].....	162
FIGURE 5.22 LABVIEW <sup>®</sup> PROGRAM INTERFACE .....	163
FIGURE 5.23 PROGRAMMING BOARD PROTOTYPE.....	164
FIGURE 5.24 ELECTRICAL BOARD FOR HAIR-LIKE SENSOR TESTING .....	166
FIGURE 6.1 OVERVIEW OF POLYMUMPS <sup>™</sup> PROCESS [110].....	169
FIGURE 6.2 CHIPS LAYOUT ON SILICON WAFER .....	175
FIGURE 6.3 SEM OF HAIR-LIKE SHEAR SENSOR.....	175
FIGURE 6.4 MICROSCOPE IMAGE OF HAIR-LIKE SENSOR CHIP.....	175

FIGURE 6.5 HAIR-LIKE SHEAR SENSOR FABRICATION FLOW CHART .....	176
FIGURE 6.6 SEM OF HAIR-LIKE SHEAR SENSORS APPLIED WITH UV-FILTER.....	177
FIGURE 6.7 SENSOR MEMBRANE DEFLECTIONS UNDER DIFFERENT LOADS AFTER RELEASING .....	178
FIGURE 6.8 MICROSCOPE IMAGES OF SINGLE SENSOR WITHOUT HAIR .....	180
FIGURE 6.9 CERAMIC PIN GRID PACKAGE (CPGA) FOR HAIR-LIKE SENSOR .....	181
FIGURE 6.10 PACKAGE TOP AND BOTTOM VIEW .....	182
FIGURE 6.11 PHOTOS SHOW THE PACKAGING PROCESS .....	184
FIGURE 6.12 SENSOR TESTING BREAKOUT BOARD .....	186
FIGURE 6.13 ZIF SOCKET PIN CONNECTION WITH BREAKOUT BOARD LAYOUT .....	187
FIGURE 6.14 SENSOR MEMBRANE VIBRATION UNDER A STEP INPUT CAPTURED ON OSCILLOSCOPE .....	191
FIGURE 6.15 FREQUENCY RESPONSE OF A SINGLE SENSOR GROUP .....	192
FIGURE 6.16 FREQUENCY RESPONSE OF DIFFERENT SENSOR GROUPS .....	196
FIGURE 6.17 COMPARISON OF SHEAR STRESS COMPUTED .....	198
FIGURE 6.18 BREAKOUT BOARD FOR LCR CAPACITANCE TEST.....	200
FIGURE 6.19 DEFORMATION SHAPE OF THE SENSOR WHEN SUBJECT TO FLOW .....	201
FIGURE 6.20 TOP ELECTRODES CAPACITANCE CHANGE.....	202
FIGURE 6.21 BOTTOM ELECTRODES CAPACITANCE CHANGE .....	202
FIGURE 6.22 TOP ELECTRODES CAPACITANCE CHANGE.....	203
FIGURE 6.23 BOTTOM ELECTRODES CAPACITANCE CHANGE .....	203
FIGURE 6.24 HYPOTHESIS OF SHEAR SENSOR DEFORMATION UNDER FLOW .....	205
FIGURE 6.25 EXPERIMENT SETUP FOR HAIR SENSOR FLOW CELL TEST USING ELECTRONIC BOARD .....	207
FIGURE 6.26 MEASURED MS3110 SENSITIVITY WHEN $CF=0.019\mu F$ .....	208
FIGURE 6.27 DIFFERENTIAL CAPACITANCE CHANGE FOR SENSORS .....	209
FIGURE 6.28 DIFFERENTIAL CAPACITANCE CHANGE FOR SENSORS .....	210
FIGURE 6.29 SENSOR NOISE AT DIFFERENT FLOW RATES.....	211
FIGURE 6.30 SENSOR DRIFT MEASUREMENT AT 10CFH .....	213
FIGURE 7.1 NEW DESIGN LAYOUT .....	223
FIGURE 7.2 ALUMINUM FLOW CELL.....	225
FIGURE B.1 LABVIEW <sup>®</sup> BLOCK DIAGRAM FOR TEMPORARY PROGRAMMING OF MS3110 CHIP .....	242

FIGURE C.1 HAIR-LIKE SHEAR SENSORS MASKS ..... 244

FIGURE C.2 INDIVIDUAL SENSOR DIFFERENT LAYER LAYOUT ..... 246

FIGURE C.3 CAD DRAWING OF ALUMINUM FLOW CELL (DIMENSION IN INCH) ..... 247

# LIST OF TABLES

TABLE 2.1 SUMMARY OF STUDIES IN COCHLEAR PARTITION PROPERTIES .....	12
TABLE 2.2 INITIAL ESTIMATE OF RADIAL ELASTIC MODULUS AS DETERMINED .....	24
TABLE 2.3 VOLUME FRACTIONS AT DIFFERENT LOCATIONS TAKEN FROM SCHWEITZER [28].....	26
TABLE 2.4 MATERIAL PROPERTIES COMPUTED USING THE ANALYTICAL LINEAR MODEL TO MATCH EXPERIMENTAL POINT STIFFNESS AND SPACE CONSTANT REPORTED BY NAIDU AND MOUNTAIN [7, 8]. THESE RESULTS ARE BASED ON THE ASSUMPTION OF NAIDU AND MOUNTAIN, THAT THE OBSERVED TRANSVERSE DISPLACEMENTS ARE LINEARLY PROPORTIONAL TO THE OUT-OF-PLANE DISPLACEMENTS, AN ASSUMPTION WE QUESTION IN THE NEXT SECTION .....	35
TABLE 2.5 RESULTS FOR MATERIAL PROPERTIES TO MATCH STIFFNESS AND <i>LATERAL</i> SPACE CONSTANT. THESE ARE COMPUTED USING THE GEOMETRICALLY NONLINEAR ORTHOTROPIC PLATE FEA MODEL .....	40
TABLE 2.6 MATERIAL PROPERTIES OBTAINED TO MATCH HEMICOCHLEA STIFFNESS EXPERIMENT [9] .....	43
TABLE 2.7 COMPOSITE PLATE FLEXURAL RIGIDITY COMPUTED USING PLATE MATERIAL PROPERTIES .....	47
TABLE 3.1 SCALED PHYSICAL COCHLEAR MODELS IN THE LITERATURE [12] .....	55
TABLE 3.2 PARAMETERS OF COCHLEAR MODEL .....	61
TABLE 3.2 PARAMETERS OF COCHLEAR MODEL—CONTINUED.....	62
TABLE 3.3 PARAMETERS CALCULATED FROM SCALING LAW.....	69
TABLE 4.1 SUMMARY OF DIRECT SHEAR STRESS MEASUREMENT MEMS SENSORS .....	114
TABLE 4.2 SUMMARY OF INDIRECT SHEAR STRESS AND FORCE MEASUREMENT MEMS SENSORS.....	125
TABLE 5.1 GEOMETRY AND STRUCTURE PARAMETERS OF SENSOR AND ARRAY .....	143
TABLE 5.2 FLUID MECHANICS FEA MODEL BOUNDARIES .....	150
TABLE 5.3 PARAMETERS USED IN FLUID MECHANICS FEA MODEL .....	150
TABLE 5.4 PROPERTIES USED IN MINDLIN PLATE MODEL .....	155
TABLE 6.1 POLYMUMPS™ PROCESS LAYERS, MATERIAL PROPERTIES AND REQUIREMENTS .....	170
TABLE 6.2 SENSOR PACKAGING PROCESS.....	185
TABLE 6.3 MEASURED CAPACITANCE AND RESISTANCE OF THE SENSORS .....	189

TABLE 6.4 LIST OF SHEAR STRESS COMPUTED FROM FLOW RATE AND FROM PRESSURE GRADIENT .....	198
TABLE 6.5 COMPARISON OF SENSITIVITY FOR SENSORS WITH HAIRS AND WITHOUT HAIRS USING LCR .....	204
TABLE 7.1 NEW DESIGN PROCESS PARAMETERS .....	223

# Chapter 1

## INTRODUCTION

This dissertation consists of two parts. The first part focuses on cochlear mechanics studies. It includes the determination of gerbil basilar membrane (BM) properties using finite element method and design and testing of a scaled physical hydromechanical cochlear model. The cochlea is the auditory portion of the inner ear. A vast amount of research has been done in order to understand the mechanics of the cochlea (e. g. [1-6]). The cochlear BM properties are among the most important parameters in the mathematical and physical cochlear models used to study cochlear mechanics. The quantified material properties determine the form and amplitude of the cochlea partition vibrations and are especially important for building accurate mechanical models to study traveling fluid-structure waves in the cochlea.

In this dissertation, a finite element model is developed to quantify gerbil BM properties based on point stiffness and space constant reported from both fresh cochlea experiments [7, 8] and hemicochlea experiments [9].

The first contribution of the thesis is the quantification of gerbil BM orthotropic stiffness. The gerbil material properties derived from the mathematic and FEA models in this dissertation are the highest accuracy reported among quantified orthotropic cochlea partition properties in cochlea studies. The quantified properties determined at different locations along the BM provide essential information for more accurate studies of cochlea mechanics including an improved understanding of the motion of cochlear structures and the pattern of the travelling wave. Sufficient understanding of the complex behavior of cochlea can contribute to improve prosthetic devices designs and clinical diagnoses. Due to the small size of the cochlea, scaled-up models have sometimes been used to study animal cochlear mechanics. The scaled cochlear models are designed and operated based on dimensional analysis to fulfill scaling law in order to resemble real cochlear movements. The second contribution of this thesis is the design, construction, and characterization of a scaled hydromechanical guinea pig cochlear model. The model's responses to drive signals are recorded and compared with those of a mathematical model. The hydromechanical model could be used as a platform for future studies that incorporate the BM material properties determined in the first part of thesis, and the hair-like sensors described in the later part of the thesis.

The second part of the dissertation focuses on the design, fabrication and

testing of hair-like capacitive sensors for flow measurements. The sensors were inspired by the hair cell structure in the cochlea, but were specifically designed for the air flow measurements in a wind tunnel. The hair-like shear stress sensors were tested and calibrated in a laminar flow cell. The sensors demonstrated perfect linearity up to  $17Pa$  for the current test setup. The hair-like shear sensor is the third major contribution of the thesis: it is the first kind of capacitive shear sensor based on a hair post structure that can be used for direct flow measurements with a large dynamic range and can measure large shear stresses. This new design provides a different means and perspective for the measurements of unsteady shear stress in flow.

The thesis is organized as follows. Chapter 2 describes the background on cochlear mechanics and motivation for finding the quantified cochlear material properties. The modeling and simulations used for extracting the gerbil basilar membrane properties are explained. Chapter 3 describes a physical cochlea model built using scaling laws tested and compared with a mathematical model. Chapter 4 introduces the background on existing shear stress sensors and the motivation behind the development of hair-like sensors. The modeling and designs of hair sensors are detailed in chapter 5. Chapter 6 discusses the fabrication, packaging and testing results of the sensors. Finally, concluding remarks and suggestions for future work are stated in Chapter 7.

# Chapter 2

## **DETERMINATION OF GERBIL COCHLEA BASILAR MEMBRANE PROPERTIES**

This chapter starts with introducing background on ear physiology and hearing mechanism. The importance of quantified cochlear material properties is addressed and the previous works on this topic are discussed. Following sections describe various models that are created in order to determine the material properties of BM of gerbil cochlea. The computation results will be discussed and conclusions are made at the end of the chapter.

### **2.1 Physiology of Ear and Mechanism of Hearing**

In mammals, the ear consists of three parts: outer ear, middle ear and inner ear. The anatomy of the human ear is shown schematically in Figure 2.1.

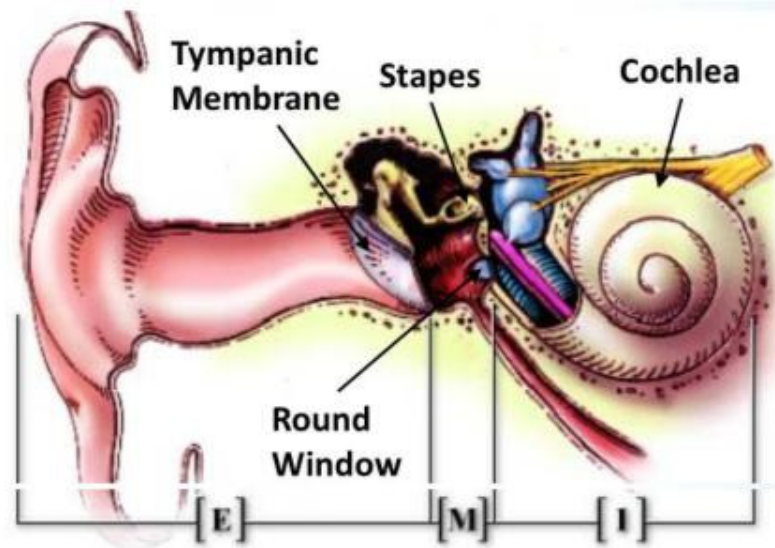


Figure 2.1 Schematic view of human ear

Image used with permission by Rémy Pujol

< image/anim by S. Blatrix, from the EDU website "Journey into the World of Hearing"  
<http://www.cochlea.org> by Rémy Pujol et al., NeurOreille, Montpellier >

Sound waves are collected by the outer ear and are funneled through the ear canal to the tympanic membrane (eardrum) and cause the tympanic membrane to vibrate. The tympanic membrane is connected to three middle ear bones, called ossicles. The ossicles transmit and amplify the vibrations of sound waves to the oval window of the inner ear. The middle ear bones act as an impedance network matching between the outer ear which is filled with air, and the cochlea in the inner ear which is filled with liquid. These vibrations induce pressure differences in the cochlea ducts and cause the movement of the basilar membrane (BM), which, in turn, causes the hair cells sitting on top of the BM in the cochlea to bend. The hair cells change the movement into electrical pluses. These electrical

impulses are transmitted to the hearing (auditory) nerve and up to the brain, where they are interpreted as sound.

### **2.1.1 Structure of Cochlea**

The role of the cochlea is to transduce complex mechanical sound waves into electrical neural activity in the auditory nerve. The human cochlea is capable of discriminate frequencies 0.2% apart over a wide range of frequencies of 20Hz-20KHz [10]. The detailed structure of cochlea can be found in [11].

The mammalian cochlea is a tapered spiral shaped structure divided into three fluid-filled ducts: scala media, scala vestibuli and scala tympani. The anatomy of cochlea is shown in Figure 2.2. The scala vestibuli and scala tympani are filled with perilymph, a liquid whose ionic composition resembles that of extracellular fluids. Two thin membranes form the boundary between the middle ear and the fluids of the cochlea. The oval window (OW) is the membrane that seals one end of scala vestibuli and is attached to the stapes middle ear bone. The round window (RW) is the other membrane-covered opening below the oval window and seals the scala tympani. The round window communicates with the air filled middle ear space. These two ducts are connected at the upper end of the cochlea by a small opening near the apex of the cochlea called the

helicotrema. Scala media is filled with endolymph, a fluid with a high potassium concentration, sustaining a large positive electrical potential in the duct. Scala media contains the organ of Corti (OC), a microstructure where the inner and outer hair cells transduce mechanical vibrations to electrical signals. The OC sits on the BM, which separates scala media from scala tympani, and scala vestibuli and scala media are separated by Reissner's membrane. A schematic of organ of Corti is shown in Figure 2.3.

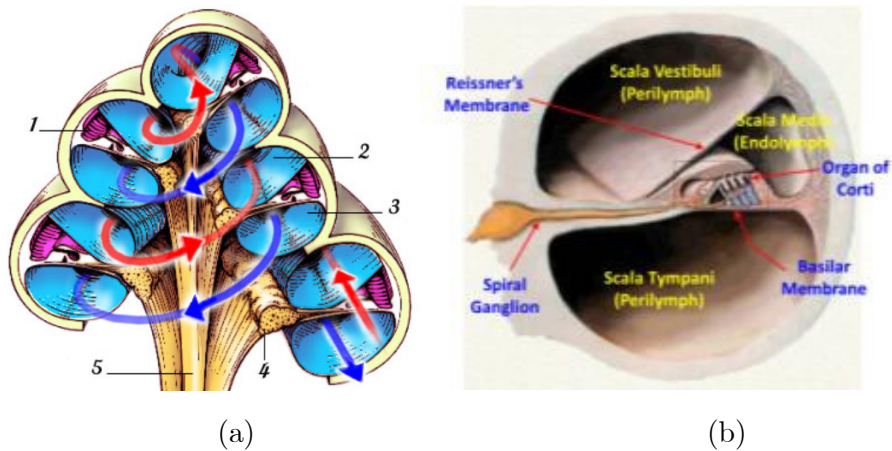


**Figure 2.2 Cross sectional view of a cochlear structure**

**(a) view of a spiral cochlea containing: 1. Scala media 2. Scala vestibuli  
3. Scala tympani 4. Spiral ganglion 5. Auditory nerve fibers**

**Image used with permission by Rémy Pujol < <http://www.cochlea.org>>**

**(b) view of one section of cochlea with most important structures**

**Image used with permission by Fabio Mammano**

**< <http://147.162.36.50/cochlea/cochleapages/anatomy/index.htm>>**

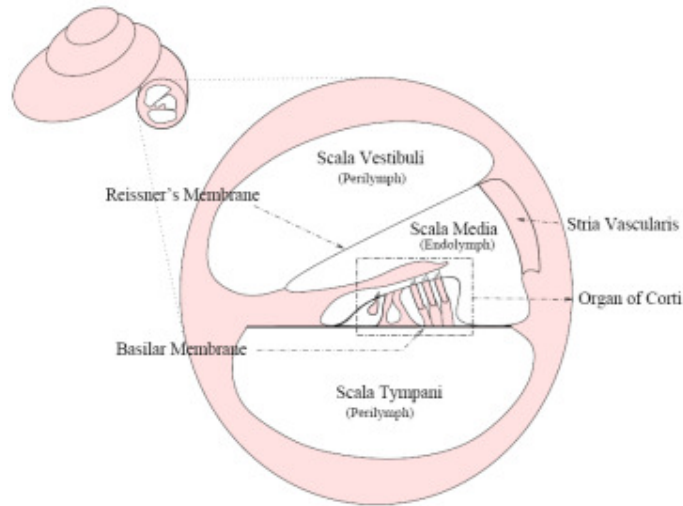


**Figure 2.3 Schematic of organ of Corti [12]**

**Image used with permission by Robert White**

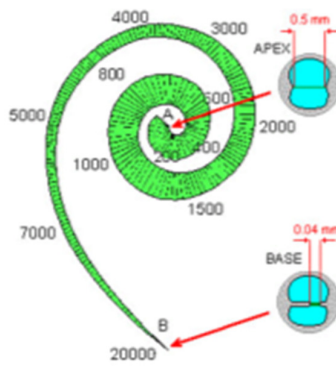
Acoustic energy is injected through vibrations of the middle ear bone, the stapes, which is connected to the oval window (OW). The vibrations create pressure differences between scala tympani and the other scalae. The pressure differences displace the BM in a transverse direction. The oscillations of the BM generate shearing forces that tilt the stereocilia (hair bundle) protruding from the outer hair cells. The tilting of the stereocilia opens the cationic channels located in their tips, allowing ions passing through and thus changing the membrane potential in the outer hair cells (OHC) [13]. The variations of the membrane potential of OHC change the length of OHC [14] and the shortening or lengthening of OHC amplify the movement of BM [15]. This function is called cochlear amplification. The mechanism is still not fully understood [16].

### **2.1.2 Structure of Basilar Membrane**

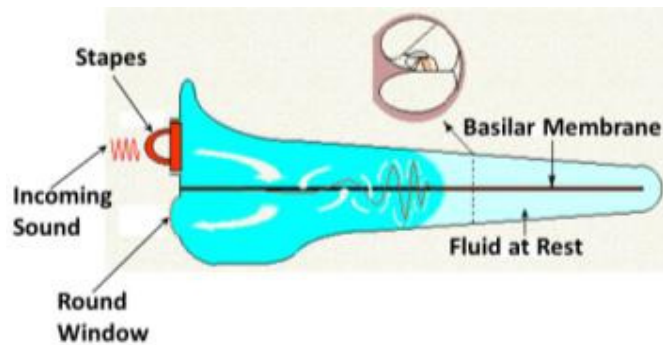
The basilar membrane is internally formed by thin elastic fibers across the cochlear duct. The fibers are short and closely packed in the basal region, and become longer and sparse proceeding towards the apex of the cochlea [17, 18]. Due to the geometry and mass change, the stiffness of the basilar membrane decreases from the base to apex. In addition, the basilar membrane is stiffer in the transverse direction than longitudinal direction due to embedded collagen fibers in the transverse direction [17, 18].

The BM is first displaced near the base the cochlea and the displacement moves down the membrane toward the helicotrema in response to incoming sound. The pattern of the motion of the basilar membrane has been described as a traveling wave [5]. As it travels, the wave grows in amplitude, reaching a maximum and dying out. Because of BM's varying acoustic impedance, the location of the maximum BM displacement is a function of the stimulus frequency, with high frequency waves being localized to the base of the cochlea and low frequency waves to the apex of the cochlea. Thus each cochlea location has a characteristic frequency (CF), to which it responds with maximum displacement. The hair cells connected to each part of the membrane thus preferentially send neural information about the presence of those frequencies to the brain [19].

Figure 2.4 shows a human BM and traveling wave.



(a)



(b)

Figure 2.4 Schematic of basilar membrane and traveling wave

(a) A human BM with varying geometry and responding frequency map (Unit in Hz)

(b) Sound generates traveling wave in cochlea

Image used with permission by Fabio Mammano

< <http://147.162.36.50/cochlea/cochleapages/theory/index.htm> >

## 2.2 Backgrounds and Objectives

The accuracy of mechanical models of traveling fluid-structure waves in the cochlea depend on accurate structural models for the cochlear partition. The cochlear partition has variously been modeled as a locally reacting impedance [20-22] a one dimensional beam[23, 24], a two dimensional orthotropic plate [25], or a two dimensional orthotropic

pretensioned plate [26]. The parameters required for each of these models can be determined from a knowledge of the geometry and the pointwise effective material properties of the cochlear partition. Geometry can be determined from physiological studies [27, 28]. Pointwise effective material properties must be determined indirectly by observing the response of the structure *in vivo* to carefully conducted experiments. A summary of the cochlear partition properties investigated by different research groups is listed in Table 2.1.

Table 2.1 Summary of studies in cochlear partition properties

Author	Properties Measured	Species	Description
Allair [29] 1974	Stiffness	human Isotropic	Use composite beam model calculated static and dynamic (due to the strain rate change) cochlear partition stiffness. Young's Modulus at 3.0cm from the base was $4 \times 10^6 \text{ dyn/cm}^2$ .
Voldrich [18] 1978	General Mechanical Properties	Guinea Pig	By probing BM, a narrow, radially oriented strip was deflected, indicating anisotropic material properties for fresh decapitated cochlea. Same experiments on 24 hours post-mortem cochlea showed circular deformation on BM, indicating material properties were homogenous for not fresh cochlea.
Ehret [30] 1978	Stiffness	Mouse	Stiffness was computed as a function of width and thickness in radial direction of the BM and as a function of BM length.
Gummer [31] 1981	Stiffness	Guinea Pig	BM stiffness was measured in the 0.8-2.3mm region within 1hour post mortem. For small BM displacement about 2-3um, the stiffness measured varied from 0.2 to 1.1 N/m for different animals. The flexural rigidity in the radial direction was estimated as $6.2 \pm 0.6 \times 10^{-10} \text{ N} \cdot \text{m}$ .
Miller [32] 1985	Compliance	Guinea Pig	Compliance of the BM in the excised guinea pig cochlea is measured across the width of the BM through static point-load measurements. The experimental results were in agreement with those in [31] with stiffness varied from 0.4 to 2.0 N/m. It computed $E = 1.8 \times 10^9 \text{ Pa}$ for BM filaments. Its arched beam model indicated no longitudinal coupling of stiffness in the pectinate zone and strong coupling in the arcuate zone due to the arches of Corti.

Table 2.1 Summary of studies in cochlear partition properties-continued

Author	Properties Measured	Species	Description
Olson [33] 1991	Stiffness	Gerbil	Stiffness was dynamically measured at the base of the gerbil cochlea. The first plateau stiffness ranged between 0.2 and 1.2 N/m up to 12um BM displacement; the second plateau from 1.4-2.0 N/m. No stiffness differences observed between pre-mortem and 1 hour post-mortem cochlea samples.
Ishii [34] 1995	Mechanical Properties	Human	Measured 6-7 hours post mortem human cochlea properties. Tensile stress, elongation, strain and Young's modulus were reported at three locations corresponding to basal, middle and apical turns of BM. The measured Young's moduli were $[0.97 \ 0.60 \ 0.64] \times 10^4 \text{ mN/mm}^2$ for basal, middle and apical turn respectively.
Naidu [7] 1998	Stiffness	Gerbil	Stiffness was measured at different longitudinal locations and data was fit to a logarithm function along the BM length. Experimental results indicated the changing stiffness of the partition is determined by multiple stiffness gradients exhibited by OC and BM cellular components.
Naidu [8] 2001	In-plane Displacement	Gerbil	In-plane displacements of particular points of interest induced by vertical probaton were analyzed. The results showed BM exhibited longitudinal coupling and the coupling was greater at the apex than at the base. Study also demonstrated that the cells of the OC increase the overall coupling exhibited by BM.

**Table 2.1 Summary of studies in cochlear partition properties-continued**

<b>Author</b>	<b>Properties Measured</b>	<b>Species</b>	<b>Description</b>
Emadi [9] 2004	Stiffness	Gerbil	Stiffness was measured multiple positions across the width of BM for several longitudinal locations in hemicochleas. Results indicate qualitative changes of stiffness-deflection curves as a function of radial position. Study showed relatively little longitudinal coupling within the pectinate zone of BM compared with result in [8]. Longitudinal stiffness gradients were also reported.
Fleischer [35] 2010	Compliance	Guinea Pig	A 3D uncoiled FEA was used to investigate the effects of geometry, boundary conditions and elastic material properties on the compliance profiles of BM. The results showed the longitudinal stiffness gradient primarily depends on variation of the effective thickness of BM; the gradients in longitudinal and radial coupling mainly depend on the width change of the BM; coiling had most significant influence on the apical turn of the BM; Boundary conditions affect the coiling; and exponential decrease of the radial component of Young's modulus from base to apex causes widening of the compliance profile.

This Chapter focuses on the determination of effective pointwise material properties using point load experiments published by Naidu and Mountain [7, 8] and Emadi , Richter, and Dallos [9]. It is well known that the cochlear partition is orthotropic, based on physiology [17, 24],

qualitative observations of static partition deflection [18], and quantitative dynamic measurements [36]. However, most prior quantitative static experimental work gave only point stiffness measurements [7, 24, 31, 33], from which it is not possible to determine orthotropic properties. Life-sized cochlear models have been developed [37-40]. However, the quantified material properties were not available for the basilar membrane, which greatly affect the response of the cochlea to vibratory stimulation and mapping of the characteristic frequencies. A particular aim of this work is to quantify the orthotropic properties of the cochlear partition.

In 2001, quantitative measurements of the *shape* of the deflected region during point load experiments were made by Naidu and Mountain [8]. These experiments allow quantitative determination of the level of orthotropy. In [8], the BM was deflected from 1  $\mu\text{m}$  to 15  $\mu\text{m}$  in a 1  $\mu\text{m}$  increment. In addition to the point stiffness, the shape of the *lateral* deflection region was measured quantitatively for each case. The normalized shape of the lateral deflection profile exhibited exponential decay away from the center; the exponent characterizing this decay was expressed as a “space constant”. Two sets of space constants were reported in their paper. One was with the Organ of Corti (OC) present and the other is with the OC removed. The space constant used in this thesis was the one with the OC present.

In Emadi *et al* [9], the point stiffness of the cochlear partition in a hemicochlea preparation was measured as a function of distance from the cut edge. The variation of stiffness as a function of distance from the cut edge is related to longitudinal coupling in the cochlear partition, albeit in a different way than the lateral deflection results of Naidu and Mountain. We used these two sets of experimental results to extract the two effective elastic moduli, the effective shear modulus, and the effective Poisson's ratio for the cochlear partition. In order to accomplish this, we employed a geometrically nonlinear composite orthotropic plate model. The *lateral deflections* were the quantities measured by Naidu and Mountain. Despite the small deflections, a nonlinear geometric model must be used in order to determine *lateral deflections*, which are not present in a linear plate model.

Two boundary conditions for the model were investigated. The first is all four edges of the plate simply supported (SS). The second is one edge clamped and others simply supported (CS). We also investigated the effect of probe contact area on the point measurements by pushing probes of radius from 2  $\mu\text{m}$  to 12.5  $\mu\text{m}$  on the BM to see how the shape of the deflected region changes.

The physiology of the cochlea basilar membrane is far more complicated than the model we used. Also the stiffness measurements can easily be affected by factors including the OC [7], and the tectorial membrane [9].

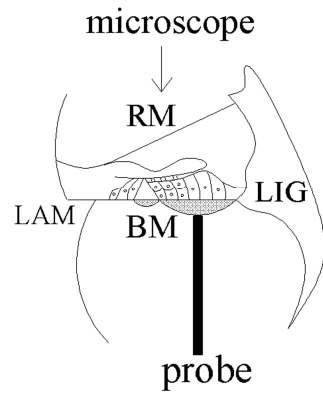
The stiffness is not uniform in arcuate zone or pectinate zone [7]. If all the complexities are embedded in the model, there would be too many free parameters to be determined. Using existing data, we will not be able to determine so many free parameters. By simplifying the model and reducing the number of free parameters, we can use available experimented data to compute the material properties, which are essential for the further study of cochlea mechanics.

In a 2007 paper, Naidu and Mountain [26] look at the effects of radial pretension on a cochlear partition model. Pretension, radial variation and the tectorial membrane are not included in our current model, as they are not needed to explain the observed longitudinally varying space constants and point stiffness.

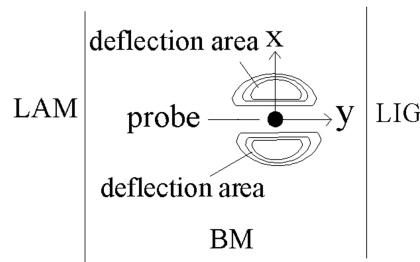
## **2.3 Overview of Mathematic Models**

As mentioned previously, point stiffness and the shape of deflected region were quantitative measured by Naidu and Mountain [7, 8]. Emadi *et al* measured the point stiffness of the cochlear partition in a hemicochlea [9]. Space constants were defined differently in these two works. Our goal is to use these two sets of experimental results to extract BM material properties including two effective elastic moduli, the effective shear modulus, and the effective Poisson's ratio for the cochlear partition.

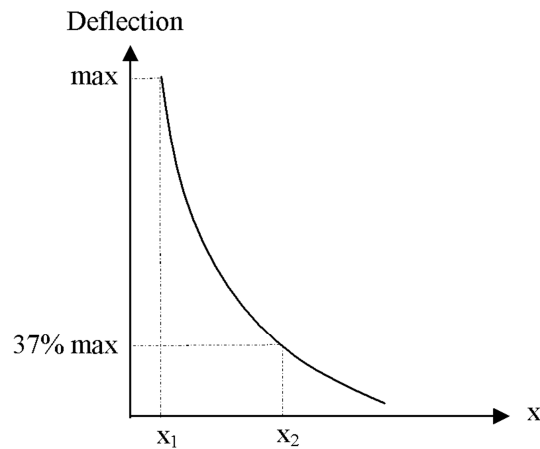
The structural model used to determine the material properties is best understood by considering the experiments it is used to analyze, shown schematically in Figure 2.5. These experimental works [7, 8], provide two pieces of information: (1) point stiffness, which is measured by pushing a probe into the partition and reporting the deflection vs. restoring force, and (2) the space constant, which is the distance from the location of the probe that the *lateral* deflection of a mark on the cochlear partition reduces to 37% of its maximum level.



(a)



(b)



(c)

**Figure 2.5 Schematic of BM stiffness measurement procedure from Naidu and Mountain ([7, 8]) : (a) A circular probe is pushed into the cochlear partition, and the force vs. deflection curve is measured; (b) a top-down view of BM: the contours show the shape of the lateral (x-direction) deflections (c) deflection space constant is described as the distance  $x_2 - x_1$  along x direction where the deflection decreases exponentially from its maximum value to 37% of maximum value. In this drawing, BM is the basilar membrane, LAM is the spiral lamina, and LIG is the spiral ligament. Drawing taken from [41]**

The space constant was determined by observing *lateral* deflections of the cochlear partition using microscopy [8]. It was assumed in [7, 8] that the out-of-plane deflections were proportional to these observed lateral deflections. Subsequently, [7, 8] used a linear plate model to analyze the space constant to compute orthotropy. However, a linear plate model has no lateral deflections. A geometrically nonlinear plate model does experience observable lateral deflections. The major motivation for the use of a geometrically nonlinear plate model in this work is to explore the validity of the assumed proportionality between out of plane and lateral deflections, and potential effects on predictions of the small-deflection material properties.

The orthotropic composite plate model used here requires four independent material properties: elastic moduli in both longitudinal and transverse directions ( $E_x, E_y$ ), shear modulus ( $G_{xy}$ ), and Poisson's ratio ( $\nu_{xy}$ ). These properties must be determined to match the point stiffness and space constants that have been reported. Since there are four quantities to determine, but only two available measurements, some additional assumptions must be made based on composite plate theory. These are explained in detail below.

The overall procedure is as follows. First, an Euler-Bernoulli beam model with a single material property,  $E_y$ , is used to match point stiffness data [7, 9]. This gives an initial estimate of the transverse plate modulus,  $E_y$ .

An orthotropy ratio,  $E_y/E_x$ , is then arbitrarily chosen.  $E_y/E_x$  is always in the range 1-1000. With  $E_y/E_x$  chosen, it is possible to compute  $G_{xy}$  and  $\nu_{xy}$  by making use of a composite plate material model, as explained below. With all four plate constants in hand, a linear analytic plate model or a nonlinear finite element scheme is then used to compute the shape of the deflected region produced by a finite area static probe load. The point stiffness and space constant are determined from the result, and compared to that reported in the experimental data. The values of  $E_y$  and  $E_x$  are then adjusted,  $G_{xy}$  and  $\nu_{xy}$  recomputed, and the procedure repeated until a match with experiment is obtained.

Two sets of boundary conditions have been employed by previous authors modeling the cochlear partition. In some works, one edge is taken to be simply supported and the other clamped. This is motivated by Iurato's anatomical studies of the rat cochlea, in which he observed that the main supporting bundles of the spiral lamina (LAM) continue directly into the fibers of the basilar membrane [17], suggesting a clamped end condition. The fibers on the other side of the BM continue directly into the spiral ligament (LIG) but suddenly become thinner prior to joining the spiral ligament, which suggests a simply supported boundary condition. However, the movements at the boundaries of the BM are difficult to observe, thus leaving open the possibility for other boundary conditions. For this reason, and perhaps for simplicity, other authors have chosen to

use simply supported boundary conditions along both edges [26]. In order to explore the effect of changing boundary conditions on the material properties, we have carried out computations using both sets of boundary conditions: (SS) simply supported at both ends and (CS) clamped at the spiral lamina but simply supported at the spiral ligament.

## 2.4 Beam Model

The first step in our procedure is to make use of a beam model to produce an initial estimate of the local elastic modulus  $E_y$ . The width of the beam is taken to be the probe's diameter:  $10\mu\text{m}$  in [7],  $25\mu\text{m}$  in [9]. This is the same as assuming that the cochlear partition is perfectly orthotropic.

Figure 2.6 is a schematic of the beam model under probe load (with CS boundary conditions).

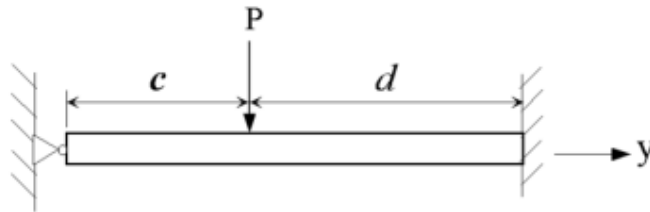


**Figure 2.6 Schematic of a beam model under load with one end simply supported and the other clamped**

The Elastic modulus calculated from the beam model [42] for CS boundary condition is

$$E = \frac{-dc^2 [3L(d^2 - L^2) + c(3L^2 - d^2)]}{12IL^3} k \quad (2.1)$$

and for SS boundary condition is

$$E = \frac{-dc(2c^2 - 2cL)}{6IL} k \quad (2.2)$$

where  $k$  is the point stiffness of the beam,  $L = c + d$  is the length of the beam,  $I = \frac{wh^3}{12}$  is the area moment of inertia of the beam,  $w$  is the beam width, taken to be the probe diameter, and  $h$  is the beam thickness. Both the thickness and length of the beam,  $h$  and  $L$ , are taken from BM thickness and width as measured by Schweitzer *et al* [28].

According to [7] Figure 5 Panel D, the stiffness decreases along the longitudinal direction from base to apex as

$$k(x) = \frac{5.755 N}{e^{0.31x} m} \quad (2.3)$$

According to [9] Figure 3 Panel A stiffness decreases as

$$k(x) = \frac{3.25 N}{e^{0.5x} m} \quad (2.4)$$

For both equations,  $x$  has dimension  $mm$ .

Material properties were computed at 3 locations along the BM according to the experimental data from [7]. These 3 locations are chosen because of the availability of experimental data for the dimensions of BM width and thickness for those locations in Schweitzer *et al* [28].

The first location is 1.14 mm from the base, the second is 3.99 mm from the base and the last one is 6.612 mm from the base. An additional

location 7.3 mm from the base is picked because it is the location at which the longitudinal coupling was measured by Emadi *et al* [9]. Though the dimensions of the BM at this location are not given explicitly in [28], width and thickness of the BM can be estimated from Panel A and B in Figure 5. Table 2.2 below shows the stiffness and radial elastic modulus computed using this procedure at the different locations.

**Table 2.2 Initial estimate of radial elastic modulus as determined from measured stiffness using a beam model**

<b>Location from Base (mm)</b>	<b>Beam Length L (<math>\mu m</math>)</b>	<b>Thickness h (<math>\mu m</math>)</b>	<b>Position of Applied Load c (<math>\mu m</math>)</b>	<b>Stiffness (N/m)</b>	<b>Boundary Conditions</b>	<b><math>E_y</math> (KPa)</b>
1.14 (Naidu & Mountain)	150	15.8	60	4.04	SS	79700
					CS	40600
3.99 (Naidu & Mountain)	194	17.3	78	1.67	SS	54300
					CS	27700
6.612 (Naidu & Mountain)	232	23.7	87	0.741	SS	15300
					CS	8060
7.3 (Naidu & Mountain)	242	25.3	91	0.599	SS	11500
					CS	6080
7.3 (Emadi <i>et al</i> )	242	25.3	91	0.08	SS	601
					CS	317

## 2.5 Plate Model

### 2.5.1 Composite Material Model

With an initial estimate of transverse elastic modulus in hand, we now move on to an orthotropic composite plate model. There are four independent material properties for the plate, but only two measurements at each location, requiring that additional assumptions be introduced. We use a composite plate model which allows us to reduce the number of unknowns. In particular, shear modulus,  $G_{xy}$ , and Poisson's ratio,  $\nu_{xy}$  are estimated using the volume fraction method [43].

In this method, the cochlear partition is treated as a fiber reinforced composite. The fibers are considered as an isotropic linear elastic material with elastic constants  $E_r$  and  $\nu_r$ , and the matrix another isotropic linear elastic material, with material properties  $E_m$  and  $\nu_m$ . The composite has volume fractions occupied by the fibers and matrix,  $V_r$ , which is the ratio of fiber area to the total area and  $V_m$ , which is the ratio of matrix area to the total area, respectively. The composite plate model is shown in Figure 2.7.

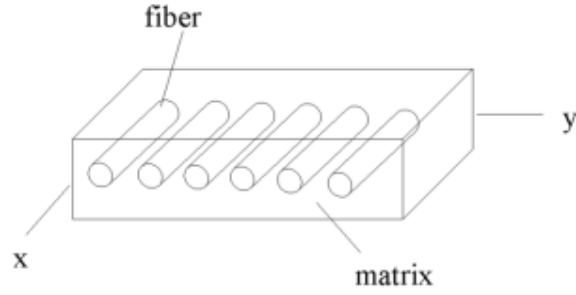


**Figure 2.7 Composite material with fibers and matrix**

The relationships between the elastic moduli of the component materials and the effective elastic moduli of the composite plate are [43],

$$E_x = \frac{E_r E_m}{V_r E_m + V_m E_r} \quad (2.5)$$

$$E_y = V_r E_r + V_m E_m$$

The lower and upper fiber band thicknesses can be estimated from Panel B and C in Figure 7 of [28]. We make the simplifying assumption that the fiber bands are fully dense. The fibers are then treated as uniformly distributed throughout the thickness, maintaining these volume fractions. From the information from [28], the cross-sectional areas of the fibers and matrix are estimated, leading to the volume fractions  $V_r$  and  $V_m$ , listed in Table 2.3 below.

**Table 2.3 Volume fractions at different locations taken from Schweitzer [28]**

<b>Location from Base(mm)</b>	<b>1.14</b>	<b>3.99</b>	<b>6.612</b>	<b>7.3</b>
$V_r$	0.192	0.089	0.05	0.041
$V_m$	0.808	0.911	0.95	0.959

We have an estimate of  $E_y$  based on the beam model, and have arbitrarily chosen  $E_x$  (recall for our procedure we chose an  $E_x$ , compute a space constant, and iterate to match experiment). We can therefore compute the required values of  $E_r$  and  $E_m$  as follows,

$$E_r = \frac{E_x V_r^2 - E_x V_m^2 + E_y}{2V_r} \pm \frac{\sqrt{E_x^2 V_r^4 - 2E_x^2 V_r^2 V_m^2 - 2E_x E_y V_r^2 + E_x^2 V_m^4 - 2E_x E_y V_m^2 + E_y^2}}{2V_r} \quad (2.6)$$

$$E_m = \frac{-E_x V_r^2 + E_x V_m^2 + E_y}{2V_m} \mp \frac{\sqrt{E_x^2 V_r^4 - 2E_x^2 V_r^2 V_m^2 - 2E_x E_y V_r^2 + E_x^2 V_m^4 - 2E_x E_y V_m^2 + E_y^2}}{2V_m} \quad (2.7)$$

The shear moduli of the component materials are then directly computed from [43],

$$G_r = \frac{E_r}{2(1+\nu_r)} \quad (2.8)$$

$$G_m = \frac{E_m}{2(1+\nu_m)}$$

So we have the shear modulus of the composite [43],

$$G_{xy} = \frac{G_r G_m}{V_r G_m + V_m G_r} \quad (2.9)$$

We still need to compute the Poisson ratio of the composite plate. The Poisson's ratio of tissue ranges widely. Two different sets of Poisson's ratios  $\nu_r = 0.2$  [44], which is estimated from Bovine Humeral articular cartilage, and  $\nu_r = 0.4$  [45], which is estimated from dog lung tissue, are investigated. Figure 2.8 shows that the choice of this parameter does not

have a major impact on our results. The ground substance behaves as a layer of incompressible fluid [32], so we take  $\nu_m = 0.5$ . From these two component Poisson ratios and the volume fractions, we can compute the two Poisson ratios for the composite orthotropic plate [43],

$$\begin{aligned} \nu_{yx} &= V_r \nu_r + V_m \nu_m \\ \nu_{xy} &= \frac{E_x}{E_y} \nu_{yx} \end{aligned} \quad (2.10)$$

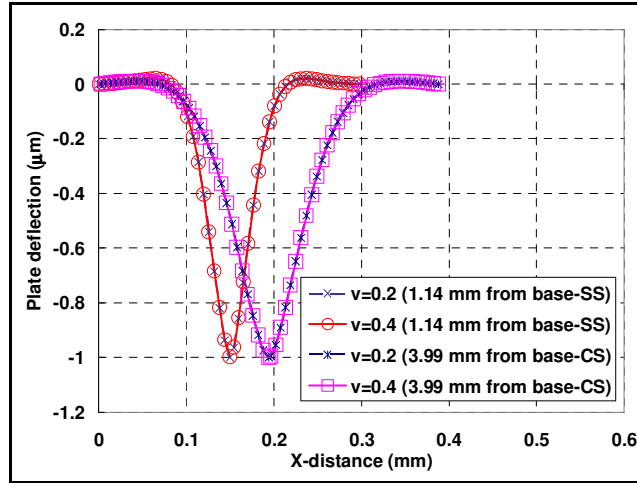


**Figure 2.8 Comparison of vertical displacement computed with different fiber Poisson's ratios for two different locations and boundary conditions.  
The Poisson ratio of the fiber has little impact on the result**

## 2.5.2 Analytic Linear Plate Model

At this point, all four plate properties are defined. It is now possible to proceed to an orthotropic linear plate solution and compared computed and measured stiffness and space constant. The governing equation for a linear orthotropic Kirchhoff plate under a distributed load is:

$$D_x \frac{\partial^4 w}{\partial^4 x} + 2D_{xy} \frac{\partial^4 w}{\partial^2 x \partial^2 y} + D_y \frac{\partial^4 w}{\partial^4 y} = q(x, y) \quad (2.11)$$

Where

$$D_x = \frac{E_x h^3}{12(1 - \nu_{xy} \nu_{yx})} \quad (2.12)$$

is the flexural rigidity of the plate in  $x$  direction,

$$D_y = \frac{E_y h^3}{12(1 - \nu_{xy} \nu_{yx})} \quad (2.13)$$

is the flexural rigidity of the plate in  $y$  direction, and

$$D_{xy} = \frac{E_x h^3 \nu_{yx}}{12(1 - \nu_{xy} \nu_{yx})} + \frac{G_{xy} h^3}{6} \quad (2.14)$$

is the tensional rigidity of the plate.  $q(x, y)$  is the normal load per unit area applied on the plate. The quantity  $h$  is the plate thickness, and  $E_x$ ,  $E_y$ ,  $G_{xy}$ ,  $\nu_{xy}$  and  $\nu_{yx}$  are the orthotropic plate material properties as described previously.

In the experiments, the load is applied on the middle of the pectinate zone. The load contact area is taken to be a circle whose diameter is the same as that of the probe.  $q(x, y)$  is taken to be a uniform pressure over that contact area. Figure 2.9 is a schematic for one of the two choices of boundary conditions (CS). Note that the simply supported boundary conditions at  $x = 0$  and  $x = a$  are chosen to be far enough away from the load that they have no impact on the result.

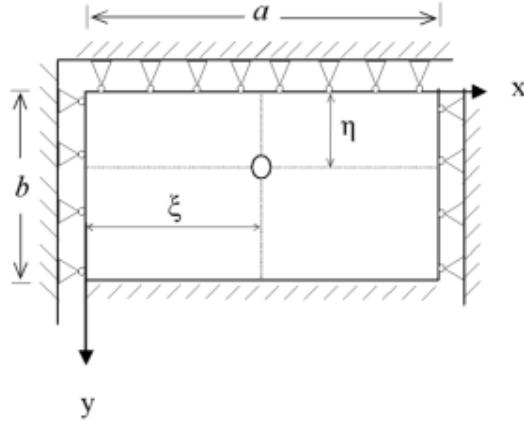


Figure 2.9 Schematic of plate boundary conditions and load area

The analytic displacement solutions for a circular region of distributed load with rectilinear boundary conditions have been derived based on plate theory (Szilard 2004; Whitney 1987; Ugural 1999). The solution for the simply supported plate under circular load can be written as

$$W = \sum_{m=1}^{\infty} \sum_{n=1}^{\infty} \left[ \frac{4P}{ab\pi^4} \int_0^{2\pi} \int_0^c \sin(\alpha) \sin(\beta) \rho d\rho d\theta \frac{\sin\left(\frac{m\pi x}{a}\right) \sin\left(\frac{n\pi y}{b}\right)}{D_x \frac{m^4}{a^4} + 2D_{xy} \frac{m^2 n^2}{a^2 b^2} + D_y \frac{n^4}{b^4}} \right] \quad (2.15)$$

Where

$$\alpha = \left( \frac{m\pi(\xi + \rho \cos(\theta))}{a} \right) \quad (2.16)$$

$$\beta = \left( \frac{n\pi(\eta + \rho \sin(\theta))}{a} \right)$$

where  $a$  is the length of the plate which is chosen to be large enough so that the length will have no impact on the result,  $b$  is the width of the plate,  $c$  is the radius of the circle of load,  $P$  is the total load,  $\xi = \frac{a}{2}$  is the

load location in the  $x$  direction,  $y$  is the load location in the  $y$  direction.

The solution for the one edge clamped and three edges simply supported with a circular load can be written as,

$$w = \sum_{m=1}^{\infty} \sum_{n=1}^{\infty} \left[ A \sin\left(\frac{m\pi\lambda_2 y}{a}\right) \cosh\left(\frac{m\pi\lambda_1 y}{a}\right) + B \cos\left(\frac{m\pi\lambda_2 y}{a}\right) \sinh\left(\frac{m\pi\lambda_1 y}{a}\right) + C \sin\left(\frac{n\pi y}{b}\right) \right] \cdot \sin\left(\frac{m\pi x}{b}\right) \quad (2.17)$$

Where  $\alpha$  and  $\beta$  are defined in Eqn. (2.16). The constants are

$$A = \frac{-C \sinh\left(\frac{m\pi\lambda_1 b}{a}\right) \cos\left(\frac{m\pi\lambda_2 b}{a}\right)}{\sin\left(\frac{m\pi\lambda_2 b}{a}\right) \cosh\left(\frac{m\pi\lambda_1 b}{a}\right)} \quad (2.18)$$

$$B = \frac{-C n a \cos(n\pi) \sin\left(\frac{m\pi\lambda_2 b}{a}\right) \cosh\left(\frac{m\pi\lambda_1 b}{a}\right)}{m b (-D + E - F)} \quad (2.19)$$

$$C = \sum_{m=1}^{\infty} \sum_{n=1}^{\infty} \left[ \frac{4P}{ab\pi^4} \int_0^{2\pi} \int_0^c \sin(\alpha) \sin(\beta) \rho d\rho d\theta \right] \left[ \frac{D}{x} \frac{m^4}{a^4} + 2D_{xy} \frac{m^2 n^2}{a^2 b^2} + D_y \frac{n^4}{b^4} \right] \quad (2.20)$$

$$\begin{aligned} D &= -\lambda_2 \sinh\left(\frac{m\pi\lambda_1 b}{a}\right) \cosh\left(\frac{m\pi\lambda_1 b}{a}\right) \\ E &= \lambda_1 \cos\left(\frac{m\pi\lambda_2 b}{a}\right) \sin\left(\frac{m\pi\lambda_2 b}{a}\right) \left[ \cosh\left(\frac{m\pi\lambda_1 b}{a}\right) \right]^2 \\ F &= \lambda_1 \sin\left(\frac{m\pi\lambda_2 b}{a}\right) \cos\left(\frac{m\pi\lambda_2 b}{a}\right) \left[ \sinh\left(\frac{m\pi\lambda_1 b}{a}\right) \right]^2 \end{aligned} \quad (2.21)$$

and  $\lambda_1$  and  $\lambda_2$  are two constants

$$\begin{aligned}\lambda_1 &= \text{Re} \left\{ \sqrt{\frac{D_{xy} \pm \sqrt{D_{xy}^2 - D_x D_y}}{D_y}} \right\} \\ \lambda_2 &= \text{Im} \left\{ \sqrt{\frac{D_{xy} \pm \sqrt{D_{xy}^2 - D_x D_y}}{D_y}} \right\}\end{aligned}\tag{2.22}$$

Figure 2.10 shows the results for an analytic model after iteration of the values of  $E_y$  and  $E_x$  to produce a match to the point stiffness and space constant reported in [7, 8] at  $x = 3.99 \text{ mm}$  from the base. Identical iterative procedures were applied at the other locations to produce the material properties shown in Table 2.4.

It is emphasized again that these are based on a *linear* composite analytic plate model. Note that the linear plate only deflects normal to its surface. Thus, in matching the space constant, it is necessary to use the assumption of Naidu and Mountain that the observed *lateral* deflections of the plate are proportional to *out of plane* deflections. It is to explore the validity of this assumption that we move on to the geometrically nonlinear plate model.

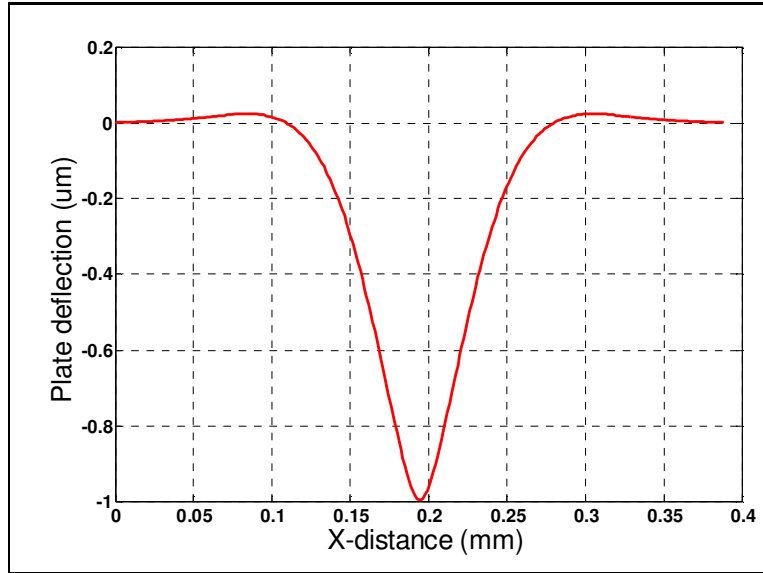


Figure 2.10 Deflection profile using linear model

### 2.5.3 Nonlinear Finite Element Model

In Figure 2 in [7], the stiffness stays constant when the BM deflection remains in the  $1\ \mu m$ - $3\ \mu m$  range. In addition, the displacements in this range ( $1$ - $3\ \mu m$ ) are small compared to the plate thickness ( $16$ - $25\ \mu m$ ). Thus, the use of a linear structural model for deflections of up to  $3\ \mu m$  appears to be justified. However, the space constant in [8] is based on the *lateral* displacement. A linear plate model gives no lateral displacements. On the other hand, a finite element analysis (FEA) solution using linear elastic material constitutive laws, but including *geometric nonlinearities*, will give non-zero lateral displacements. Such a solution was implemented in the finite element software package Abaqus™.

Figure 2.11 shows the mesh that was used at location  $1.14\ mm$  from the

base. The element used is S4R: a 4-node doubly curved thin or thick shell element with reduced integration and hourglass control for finite membrane strains. A half plate model is used since the plate model is symmetric about  $x=0$ . In order to reduce model size, the mesh is truncated in the x-direction in a way that makes the symmetric model square. A rectangular plate model whose length is twice its width was also tested to verify that the truncation does not affect the model results. Convergence was tested by increasing the number of elements. A mesh with characteristic element length  $0.6 \mu m$  is sufficient to produce a converged solution.

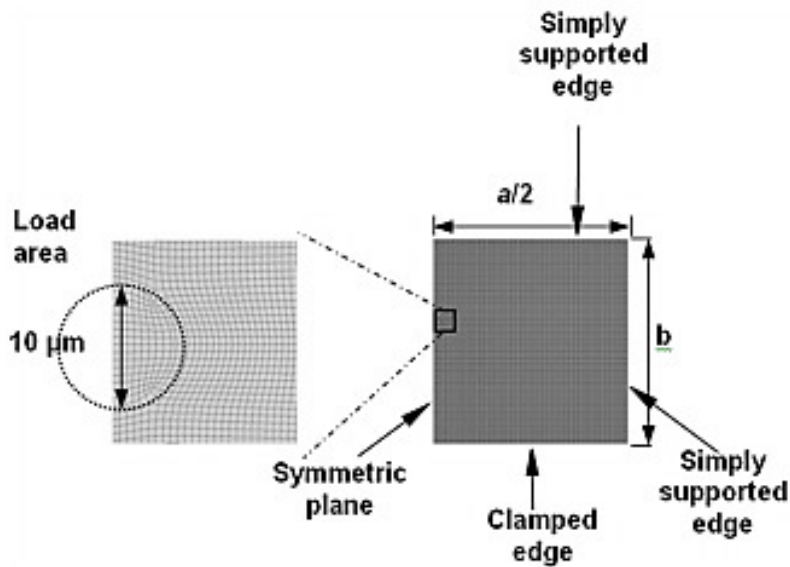


**Figure 2.11 A meshed symmetric plate model (at a position of 1.14 mm from the base) in Abaqus. 62158 elements are used for this model, and the model is truncated to produce a square model**

An identical iterative procedure to that used with the analytical linear

model is used with the nonlinear FEA model to compute moduli. In this case, however, the lateral (in-plane) deflection is compared to the experimental results to match space constant. Thus, no assumption of the proportionality between out-of-plane and in-plane deflection is made.

**Table 2.4 Material properties computed using the analytical linear model to match experimental point stiffness and space constant reported by Naidu and Mountain [7, 8].**

These results are based on the assumption of Naidu and Mountain, that the observed transverse displacements are linearly proportional to the out-of-plane displacements, an assumption we question in the next section

Distance from Base (mm)	Space Constant ( $\mu\text{m}$ )	b ( $\mu\text{m}$ )	$\eta$ ( $\mu\text{m}$ )	Thickness ( $\mu\text{m}$ )	Stiffness (N/m)	Boundary Conditions	Composite Plate Properties Determined by Matching Experiment			
							$E_x$ (KPa)	$E_y$ (KPa)	$G_{xy}$ (KPa)	$\nu_{xy}$
1.14 (Naidu & Mountain)	13.2	150	60	15.8	4.042	SS	106	21500	35.5	0.0022
	13.2					CS	82.7	13100	27.6	0.0028
3.99 (Naidu & Mountain)	23.8	194	77.6	17.3	1.671	SS	150	8100	50.0	0.0088
	23.8					CS	148	4430	49.0	0.016
6.612 (Naidu & Mountain)	33.5	232	87	23.7	0.741	SS	36.0	1920	12.0	0.0091
	33.5					CS	42.0	1000	14.0	0.021
7.3 (Naidu & Mountain)	36.0	242	91	25.3	0.599	SS	26.0	1400	8.60	0.009
	36.0					CS	30.0	735	10.0	0.02

## 2.6 Results and Discussions

### 2.6.1 Linearity vs. Nonlinearity

The geometrically nonlinear orthotropic plate model was first used to duplicate the previously conducted linear analytic analyses for both

boundary conditions (using the material properties and geometry shown in Table 2.4. A contour plot of the out-of-plane and lateral deflections computed with the nonlinear model are shown below in Figure 2.13. An example of a comparison of the result with the analytical solution is shown in Figure 2.12. The out-of-plane deflections are almost identical to the linear model results, verifying the FEA solution and demonstrating that the out-of-plane deflections are well captured by a linear model.

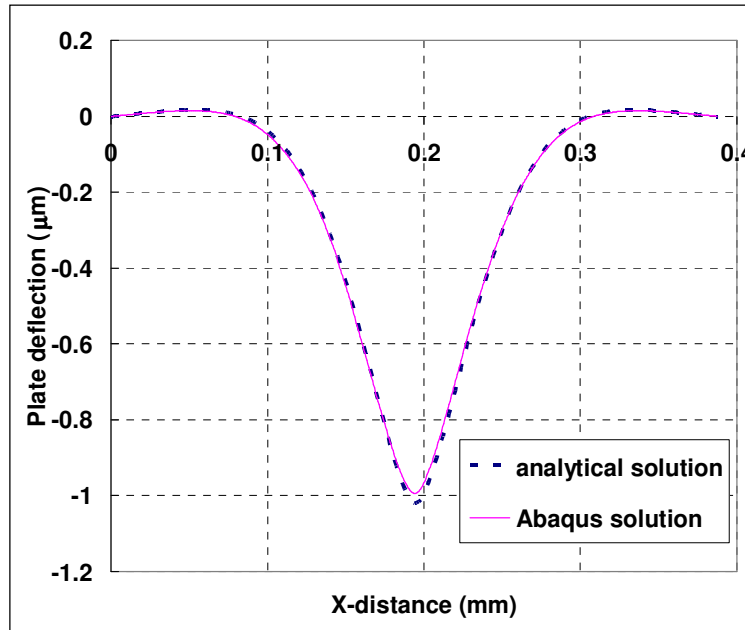


**Figure 2.12 Comparison of analytical solution with Abaqus solution for SS boundary conditions at a position 3.99 mm from the base of the BM**

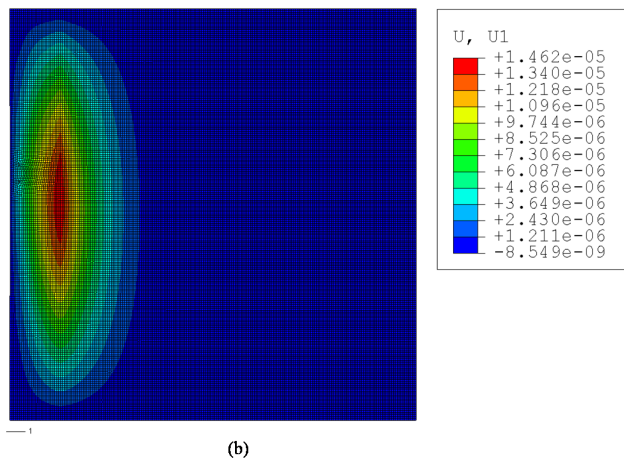
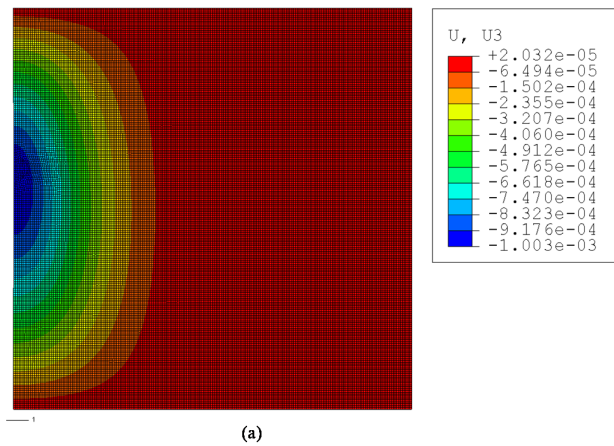


**Figure 2.13** Contour plot shows plate deflection at 1.14 mm from base. This is for an applied load of 4  $\mu\text{N}$  distributed uniformly over the 5  $\mu\text{m}$  radius contact region. (a) is the out-of-plane deflection in  $\text{mm}$  and (b) is the in-plane deflection in  $\text{mm}$

The lateral deflections, which are nonzero due to nonlinear geometric effects, are also shown. A cross-section of the lateral deflection and out-of-plane deflection curves in the longitudinal direction through the centroid of the load region are shown in Figure 2.14. The lateral deflections exhibit a different space constant than the out-of-plane deflections. It is the lateral deflection space constant that was measured by Naidu and Mountain.

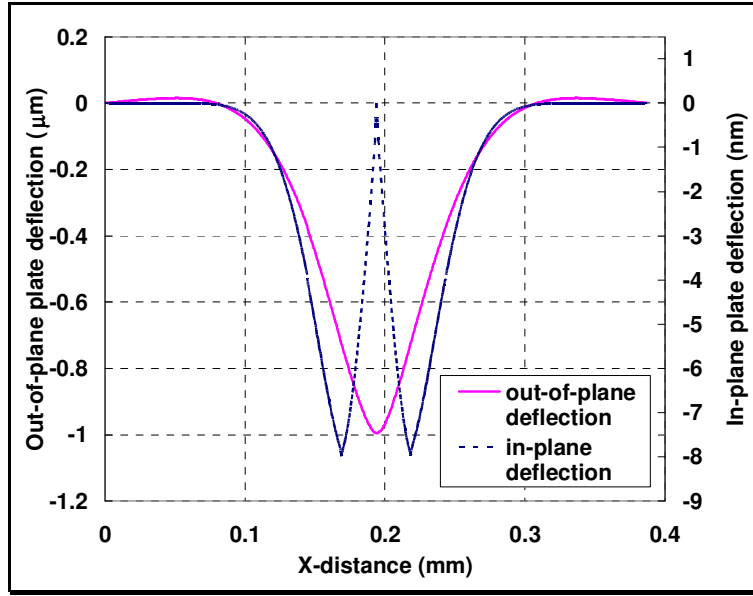
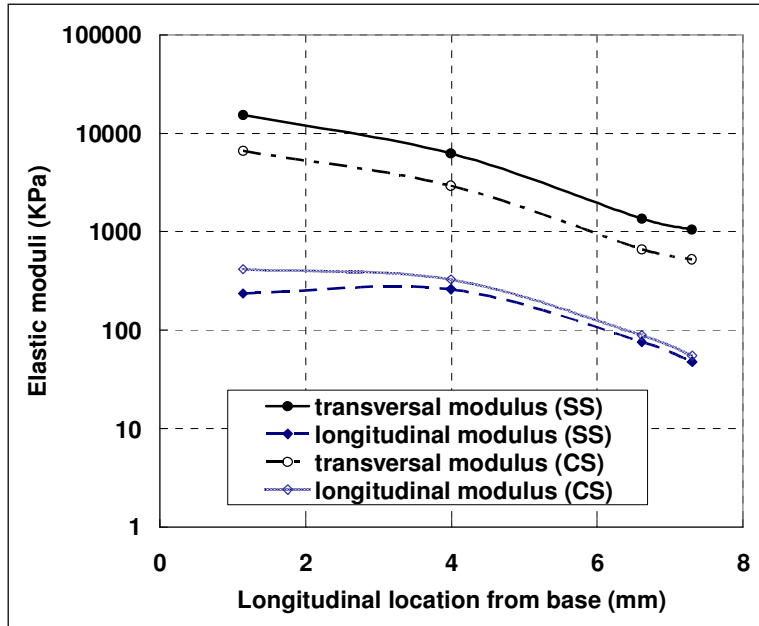


Figure 2.14 Comparison of out-of-plane deflection and in-plane deflection for SS boundary conditions at a position 3.99 mm from the base of the BM. Out-of-plane deflection uses left vertical axis and in-plane deflection uses right vertical axis. Note that the space constant for the out-of-plane deflection and in-plane deflection are different

Again the value of  $E_x$  and  $E_y$  in the geometrically nonlinear finite element model were iterated, starting from the linear results. The point stiffness and space constants reported by Naidu and Mountain were matched at each location along the BM. The space constant was now determined based on the *lateral* deflections. The shear modulus and Poisson ratio were determined using the volume fraction method described above. Table 2.5 shows the parameters used and the resulting effective plate properties. Figure 2.15 shows how the results of material properties in Table 2.5 vary along the longitudinal direction. The flexural rigidities of the plate were also calculated using effective plate properties and are presented in Table 2.5.



**Figure 2.15** Material property variations along the longitudinal direction for SS boundary condition, computed using nonlinear plate model.

**Table 2.5 Results for material properties to match stiffness and *lateral* space constant. These are computed using the geometrically nonlinear orthotropic plate FEA model**

Distance from Base (mm)	Space Constant ( $\mu\text{m}$ )	$b$ ( $\mu\text{m}$ )	$\eta$ ( $\mu\text{m}$ )	Thickness ( $\mu\text{m}$ )	Applied Pressure Load (KPa)	Stiffness (N/m)	Boundary Conditions	Composite Plate Properties Determined by Matching Experiment			
								$E_x$ (KPa)	$E_y$ (KPa)	$G_{xy}$ (KPa)	$\nu_{xy}$
1.14 (Naidu & Mountain)	13.2	150	60	15.8	51.5	4.042	SS	236	15300	78.6	0.0068
							CS	415	6640	138	0.028
3.99 (Naidu & Mountain)	23.8	194	77.6	17.3	21.27	1.671	SS	260	6240	86.7	0.020
							CS	326	2930	109	0.053
6.612 (Naidu & Mountain)	33.5	232	87	23.7	9.436	0.741	SS	76	1360	25.2	0.027
							CS	88.5	664	30.0	0.065
7.3 (Naidu & Mountain)	36.0	242	91	25.3	7.623	0.599	SS	47.7	1050	16.0	0.022
							CS	55.2	525	18.4	0.051

## 2.6.2 Comparison with Hemicochlea Experiment

In [9], the plateau stiffness at increasing distances from the upper middle turn (7.3 mm from the base) cut edge of a hemicochlea are measured. The authors used the change of stiffness very close to the cut edge to quantify the longitudinal coupling within the basilar membrane. They computed the space constant by fitting the plateau stiffness with an exponential rise to an asymptote. The space constant they computed is 21  $\mu\text{m}$ , which is smaller than a 40  $\mu\text{m}$  space constant reported by Naidu and Mountain [8], who pushed on the basilar membrane with a rigid probe and optically measured deflections of nearby structures. Thus, they stated there is relatively little longitudinal coupling within the pectinate zone of the basilar membrane in contrast to the intermediate levels of longitudinal coupling measured by Naidu and Mountain [8].

Since Emadi *et al* and Naidu and Mountain used different methods to measure the space constant, and, indeed, different definitions for what the space constant is, it is difficult to directly compare their interpretation. We employ our orthotropic finite element plate model with a cut (free) edge to obtain the plateau stiffness profile in Fig. 4B in [9]. From this, we extract material properties from Emadi *et al*'s experimental data. Figure 2.16 shows the stiffness profiles from Emadi *et al*'s hemicochlea experiment and Abaqus simulations for both types of boundary conditions. Stiffness measured by Emadi *et al* at the cut edge is

approximately an order of magnitude below the noise floor and so is treated in their work as effectively as zero. However, from a mechanics point of view, the stiffness at the edge can not be truly zero; thus the model results, which include no noise, will always show a nonzero stiffness at the edge. The asymptotic stiffness is  $0.07\text{ N/m}$  in [9], which we match. The variation of stiffness with distance from the cut edge is matched as closely as possible, giving a stiffness that gradually increases at distance increments up to the asymptotic stiffness, as shown in Figure 2.16.

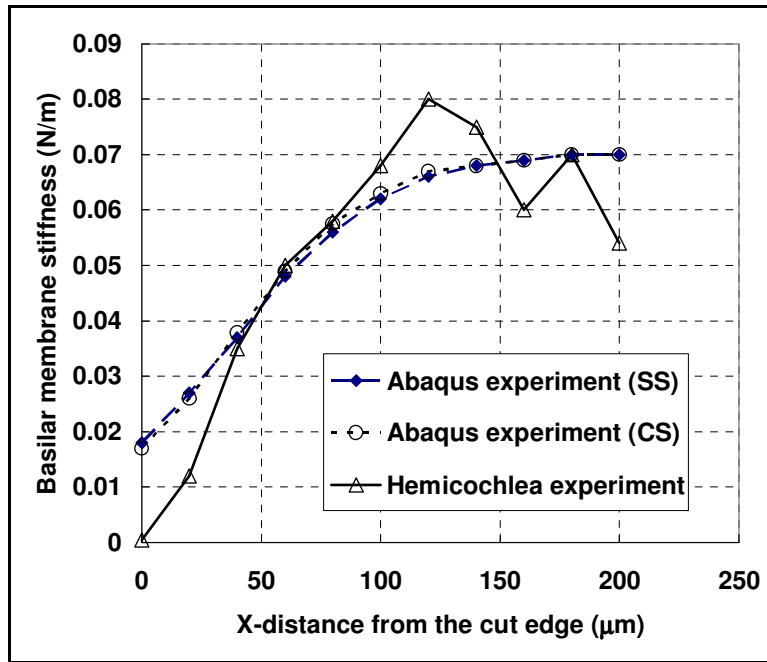


Figure 2.16 Comparison of stiffness profile in hemicochlea experiment and Abaqus experiments for different boundary conditions

Attempts had been made to use ABAQUS data to fit the hemicochlea data for the points close to the cut edge before we came to the final fit curve. When the cut edge and the measured point closest to the cut edge

are matched well with the hemicochlea data, the stiffness reduces and does not reach the stiffness far from the edge. We believe it is important to match the stiffness far from the edge. The discrepancy close to the cut edge can be explained by the possibility that the edge was damaged, whereas the cochlea was cut in half. In addition, the probe is  $25\ \mu\text{m}$  in diameter, which is relative large compared to the distance from the edge for the closest point. As the cut edge cannot support much force, it is also possible that the probe might slip.

The material properties determined to produce this matched result for the hemicochlea experiment are shown in Table 2.6. Using these material properties, we are then able to compute a Naidu and Mountain space constant from Emadi *et al's* experimental data. This space constant is  $185\ \mu\text{m}$  for SS boundary conditions and  $126\ \mu\text{m}$  for CS boundary conditions. These space constants demonstrate considerable longitudinal coupling is present in Emadi *et al's* results. Indeed, their results seem to suggest a greater degree of coupling than is present in Naidu and Mountain's data, where the space constant at this location was  $36\ \mu\text{m}$ .

**Table 2.6 Material properties obtained to match hemicochlea stiffness experiment [9]**

<b>Boundary Condition</b>	<b><math>E_x</math> (KPa)</b>	<b><math>E_y</math> (KPa)</b>	<b><math>G_{xy}</math> (KPa)</b>	<b><math>\nu_{xy}</math></b>
SS	26	48	8.69	0.2645
CS	23	25	7.7	0.4436

### 2.6.3 Probe Area

In an experiment the contact area of the probe with the BM may not be precisely known. The maximum contact area is the total size of the probe, a  $5\ \mu\text{m}$  radius for Naidu and Mountain's experiments, a  $12.5\ \mu\text{m}$  radius for Emadi *et al.* In order to investigate the sensitivity of the results to probe contact area, four different load areas, with radii  $2\ \mu\text{m}$ ,  $5\ \mu\text{m}$ ,  $8\ \mu\text{m}$ , and  $12.5\ \mu\text{m}$  were investigated in both analytical and finite element solutions. In all cases, the results indicate that the probes with radius from  $2\ \mu\text{m}$  to  $12.5\ \mu\text{m}$  have little effect on the shape of the deflected region. An example result is shown below in Figure 2.17.

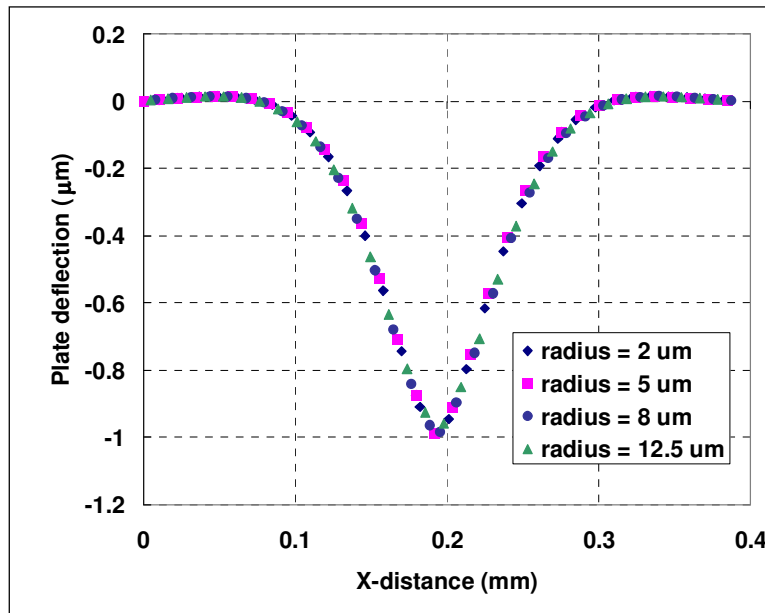


Figure 2.17 Comparison of contact area effect for Abaqus solution

In contrast, Geuta *et al* [46] indicated that two different research groups obtained similar indentation shape on the tectorial membrane when both

used nano-scale indenters but there was no agreement between the results when micro-scale indenters were used. They used a micro-scale indenter with diameter  $2 \mu m$  while the other group used  $10 \mu m$ . The  $10 \mu m$  indenter is about half size of the width of the tectorial membrane measured which caused significant difference from the results measured by a  $2 \mu m$  indenter, which is only 1/10 of the width of the tectorial membrane. This suggests that the probe size has little effect on the deflection shape when it is small enough compared with the dimensions of the object measured.

#### **2.6.4 Stiffness Linearity**

In Figure 2 in [7], the stiffness measured in the  $1 \mu m$ - $3 \mu m$  deflection range is approximately constant. That is to say, the deflection vs. applied force curve is linear. The stiffness linearity of the geometrically nonlinear FEA plate model was examined by applying double and triple the test load. Figure 2.18 below shows the FEA results for center point deflection for both boundary conditions. The geometric nonlinearity contributes approximately 10% nonlinear stiffening at a displacement of  $3 \mu m$ . This appears to be within the experimental error seen in Figure 2 of [7]. Hence the linearity of the stiffness curve, which the authors of [7] use as evidence for the linear nature of the problem, is not sufficient evidence to neglect

nonlinear geometric effects.

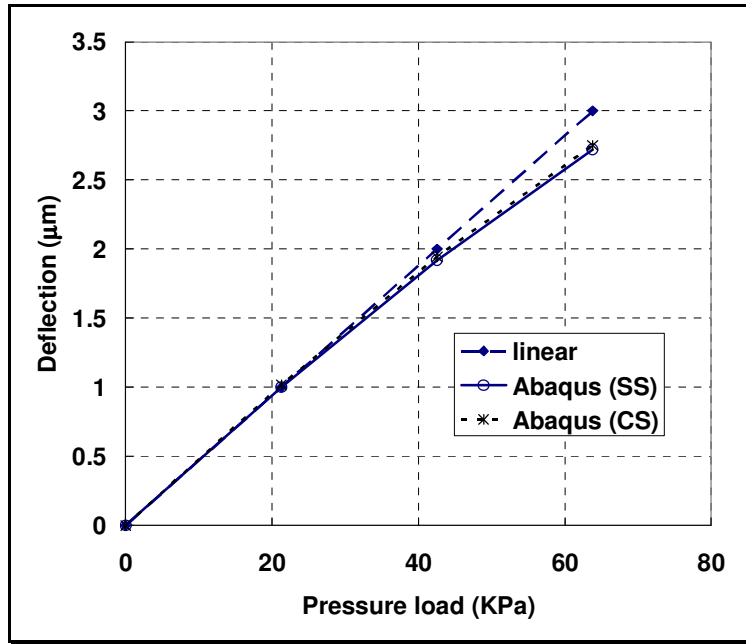


Figure 2.18 Plate model linearity in the constant stiffness range at 3.99 mm from base

## 2.6.5 Basilar Membrane Dimensions

The basilar membrane dimensions used in the models were reported by Schweitzer *et al* [28], which were derived from fixed tissue. The fixation process results in a decrease in the thickness of the basilar membrane. The reason we used Schweitzer *et al* dimension data for basilar membrane is that they also reported the fiber band dimensions which are essential for the volume fraction method. The basilar membrane does not have uniform thickness along radial direction but the curvature of the membrane is not known. To simplify the problem, we used uniform thickness for the plate model. The maximum thickness value in

Schweitzer *et al* is used as the uniform thickness of the plate. When applying the material properties calculated in this paper to model the BM as a plate, the reader should use the same thickness that we use for the computations. Alternatively, the reader can use the plate properties from Table 2.7.

**Table 2.7 Composite plate flexural rigidity computed using plate material properties**

Distance from Base (mm)	$b$ ( $\mu\text{m}$ )	Thickness ( $\mu\text{m}$ )	Boundary Conditions	Composite Plate flexural rigidity computed using plate material properties		
				$D_x$ (N·m)	$D_y$ (N·m)	$D_{xy}$ (N·m)
1.14 (Naidu & Mountain)	150	15.8	SS	$7.78 \times 10^{-11}$	$5.044 \times 10^{-9}$	$8.597 \times 10^{-11}$
			CS	$1.38 \times 10^{-10}$	$2.21 \times 10^{-9}$	$1.526 \times 10^{-10}$
3.99 (Naidu & Mountain)	194	17.3	SS	$1.133 \times 10^{-10}$	$2.72 \times 10^{-9}$	$1.29 \times 10^{-10}$
			CS	$1.443 \times 10^{-10}$	$1.297 \times 10^{-9}$	$1.628 \times 10^{-10}$
6.612 (Naidu & Mountain)	232	23.7	SS	$8.54 \times 10^{-11}$	$1.53 \times 10^{-9}$	$9.72 \times 10^{-11}$
			CS	$1.014 \times 10^{-10}$	$7.61 \times 10^{-10}$	$1.16 \times 10^{-10}$
7.3 (Naidu & Mountain)	242	25.3	SS	$6.51 \times 10^{-11}$	$1.43 \times 10^{-9}$	$7.47 \times 10^{-11}$
			CS	$7.64 \times 10^{-11}$	$7.265 \times 10^{-10}$	$8.67 \times 10^{-11}$
7.3 (Emadi <i>et al</i> )	242	25.3	SS	$4.03 \times 10^{-11}$	$7.44 \times 10^{-11}$	$4.313 \times 10^{-11}$
			CS	$3.95 \times 10^{-11}$	$4.29 \times 10^{-11}$	$3.98 \times 10^{-11}$

## 2.7 Conclusion

The effective material properties of the gerbil BM were determined from experimental data using a geometric nonlinear orthotropic plate model implemented using a finite element framework. It is important to recognize that an orthotropic plate model cannot capture the full complexity of the cochlea physiology. However, using a simple model reduces the number of free parameters, allowing them to be determined from available data. It is important that the reader understands the material properties are effective properties, which should be used only for a flat orthotropic plate of the same uniform thickness used to derive the properties. Alternatively, models can use the linear orthotropic plate properties shown in Table 2.7. The resulting model is useful as an effective plate, representing a combination of effects coming from the complex physiology. Some examples of the complexities that are subsumed into the plate model include: the effect of organ of Corti [7, 8], the effect of tectorial membrane [9] and the effect of the probe size [46]. A variety of computations were conducted to explore different possibilities related to *in vivo* experiments as detailed below.

Different probe sizes were investigated in the simulations and it was shown that the exact contact area between probe and BM does not affect the results for probes of radius  $2-12.5 \mu m$ . Under the same total load, by choosing a contact area radius of  $2-12.5 \mu m$ , the plate deformed similarly.

The space constant for the out-of-plane deflection, computed by both linear and geometrically nonlinear models, is very different than the space constant for in-plane deflections. Computation of the in-plane deflection requires a geometrically nonlinear model. The results from the geometric nonlinear model demonstrate that such a model is necessary to interpret Naidu and Mountain's experimental data, and thus produce an improved estimate of material properties for the BM. The assumption that *lateral* deflection is proportional to *vertical* deflection is inaccurate, and a purely linear model will produce imprecise estimates of material properties even for small deflections.

Using the point stiffness and space constant data from Naidu and Mountain, and Emadi *et al* [7-9], a complete set of orthotropic plate properties was determined using a geometrically nonlinear model and two possible boundary conditions. For both simple supported (SS) and clamped-simply supported (CS) boundary conditions, a decrease of radial modulus is observed from base to apex. For SS (CS) boundary conditions, the radial modulus varies from  $15 \text{ MPa}$  ( $6.6 \text{ MPa}$ ) to  $1 \text{ MPa}$  ( $0.5 \text{ MPa}$ ) from the base to the upper middle turn of gerbil cochlea; in the same region the longitudinal modulus decreases from  $0.2 \text{ MPa}$  ( $0.4 \text{ MPa}$ ) to  $0.05 \text{ MPa}$  ( $0.05 \text{ MPa}$ ). From these results, it can be seen that the orthotropy varies along the length of the cochlear partition from a maximum of 65 close to the base to a minimum of 10 in the upper middle

turn. This can be explained by the longitudinal decrease in thickness of fiber bands [28] which mainly contribute to the material properties in the transverse direction. For SS boundary conditions, both moduli are larger than for CS boundary conditions, as expected. The orthotropy ratio is similar for either choice of boundary conditions.

Naidu and Mountain observed that the BM of the gerbil is nearly isotropic at the apex and calculated an orthotropy ratio of 2 at the apex [26]. Our orthotropy ratio is about 20 for SS boundary conditions and 10 for CS conditions at the upper middle turn (two thirds of the distance to the apex), which is a similar result. Skrodzka used a longitudinal elastic modulus  $200\text{ KPa}$  and a transverse elastic modulus  $250\text{ KPa}$  for human basilar membrane [47], indicating a constant orthotropic ratio of 2.5 along the basilar membrane which is close to our orthotropy ratio toward the apex. Gross properties of chinchilla basilar membrane used in a three-dimensional nonlinear active cochlear model by Lim and Steele were taken as  $1.0\text{ GPa}$  for transverse modulus and  $0.01\text{ GPa}$  for longitudinal modulus along the entire length of the BM [48]. This 100 orthotropy ratio is close to our orthotropy ratio at the base of gerbil cochlea.

The different methods for measuring space constant by Emadi *et al* and Naidu and Mountain were reconciled through the plate model presented in this paper. Material properties were retrieved through matching a

stiffness profile in [9] and then used in the same model as that of Naidu and Mountain. The material properties determined from Emadi *et al's* experiment were used to simulate a Naidu and Mountain space constant. For Emadi *et al's* experimental data this resulted in a space constant of 185  $\mu m$  for SS boundary conditions, and 126  $\mu m$  for CS boundary conditions. Both of these results are considerably higher than the 36  $\mu m$  space constant measured by Naidu and Mountain at this location, demonstrating that Emadi *et al's* data also shows considerably longitudinal coupling.

Stiffness measured by Naidu and Mountain differ significantly from that by Emadi *et al.* The material properties estimated using these two sets of data thus differ dramatically. Upon close examination it appears that the major difference is in the radial elastic modulus. This suggests something fundamentally different between the considerably different experimental setups used by these two research group. Naidu and Mountain used isolated turn preparation for the cochlea experiments, in which the turn of interest was isolated while the adjacent turns were removed. The resulting preparation consisted of an entire cochlea turn with the OC and its attachments to the spiral lamina and spiral ligament intact. Emadi *et al* cut the cochlea from apex to base along the modiolar plane. The cut effectively removed one half of the cochlea and left behind a hemicoclea. As stated earlier, the difference is not caused by the probe sizes. Both

experimental data sets show considerable longitudinal coupling, but they cannot be completely reconciled by the model described in this paper. These results all appear to indicate that longitudinal coupling in the gerbil BM is significant, with orthotropy ratios on the order of 1 to 100, increasing from apex to base. Dynamic models of traveling wave motion in the passive cochlea demonstrate that low orthotropy ratios result in a more spatially distributed BM response, which would lead to less frequency discrimination. The next step in this work is to implement a dynamic model using these material properties. The details of how this will affect the modeled dynamic responses remain to be seen.

# Chapter 3

## **SCALED HYDROMECHANICAL GUINEA PIG COCHLEA MODEL**

The mammalian cochlear duct length is on the order of millimeters. It is difficult to build a life-size physical cochlear model to study cochlear dynamic response. A practical and scientific way to achieve this goal is to enlarge the dimensions of the cochlea in the prototype model without distorting the motion phenomena. The conditions necessary to obtain similarity between the cochlea model and the real cochlea are constrained by the *scaling law*, which is derived through dimensional analysis with *Buckingham Pi theorem*.

Fernandez [49] did thorough measurements on guinea pig cochlear geometries, including longitudinal variation of cochlear duct and basilar membrane length, width and thickness. The oval window area was also measured. These dimensions are essential for building an accurate physical cochlear model.

A guinea pig cochlear model scaled-up 16 times is designed and

fabricated based on the dimensions taken from [49]. Elasticity of the basilar membrane is one of the parameters needed for the scaling law. No quantified elasticity is available for guinea pig, so the orthotropic material properties of gerbil determined in chapter 2 are used to represent those of guinea pig. In future studies, it may be possible to incorporate the hair-like sensors described in chapters 4 through 6 into this scale model platform.

### **3.1 Background**

The response of the cochlea to vibratory stimulation was initially described for cadavers experiments by von Békésy [5]. The fluid motion in the cochlea models were investigated by [50] and many other researchers have been studying the pattern of traveling waves (e.g. [3, 51, 52]). A number of researchers have reported scaled-up hydromechanical models of simplified one- or two-duct cochlear models. Some built duct and BM with constant geometry and others with varying dimensions. The frequency-position mappings and phase accumulations were reported. A summary of scaled physical cochlea model is listed in Table 3.1.

**Table 3.1 Scaled physical cochlear models in the literature [12]**

<b>Author</b>	<b>Number of Duct</b>	<b>Directionality</b>	<b>Description</b>
Cannell [53] 1969	Two	Isotropic	Duct and BM plate dimensions varied longitudinally. The length of BM plate was 42cm. The experiment results showed frequency position mapping over 25-800 Hz band and maximum phase accumulation of $4\pi$ radians.
Helle [54] 1974	Two	Isotropic	BM plate was 20cm long. The duct and plate dimensions varied longitudinally. The frequency position mapping was 212-848Hz and maximum phase accumulation of $10\pi$ radians.
Chadwick [55] 1975	Two	Isotropic	The model was a 68cm long, 20cm high and 8cm wide box with a thin beam 63cm long. The beam represented BM and had uniform width. Experiments were carried out with different beam materials and fluid viscosities. The steady-state beam envelopes were measured and results were in agreement with theoretical predictions.
Cancelli [56] 1985	Three	Orthotropic	50 times scaled cochlear model with three channels and two membranes. Upper membrane was a 0.1mm thick nylon film representing Reissner's membrane. The lower membrane was a composite structure consisting of a 1mm thick rubber membrane, a rubber and some silicone wax. The measured frequency position mapping was 25-350Hz and phase accumulation was up to $14\pi$ radians.

**Table 3.1 Scaled physical cochlear models in the literature [12]--continued**

<b>Author</b>	<b>Number of Duct</b>	<b>Directionality</b>	<b>Description</b>
Lechner [57] 1993	One	Isotropic	A 14 times scaled human cochlea model with rubber membrane representing BM. The membrane varied in width longitudinally. The experiment results showed frequency position mapping over 40-400Hz band and phase accumulation up to $18\pi$ radians. PVDF transducers were used active feedback control and sharper tunings were observed with the feedback.
Dodson [32] 1999	One	Orthotropic	The duct was 100mm long by 25mm wide by 38mm deep. Different metal or graphite composite plate representing orthotropic BM and different BM widths were investigated. The results showed a frequency position mapping over 1.5-6KHz band and phase accumulation up to $8\pi$ radians.
Tam [58] 2011	One	Isotropic	3 times scaled human cochlea model with both straight and coiled duct were tested at 50, 500 and 5000 Hz. A traveling wave was observed at all three frequencies for both models. No standing waves and backward traveling waves were seen in the straight model but were observed in the coiled model.

In this chapter, we focus on the design and fabrication of the 16 times scaled guinea pig cochlear model and measurements of the cochlea response at different locations to a sweep sinusoidal stimulation. The physical model geometry and fluid properties were chosen in a way to satisfy *scaling law* which is derived from dimensionless analysis with *Buckingham Pi theorem*. By satisfying the *scaling law*, the scaled physical cochlear model can be used to study the guinea pig cochlea dynamic response. The experimental results are compared with mathematical results derived using WKB method. Two boundary conditions are investigated using the WKB method to accommodate the possible boundary conditions for the physical model.

In this chapter, the physical model's design and fabrication are described, followed by mathematical models using WKB method to predict the cochlea response at different locations to a sweep sinusoidal stimulation. The experiment setup is described in details and the experimental results and predicted behavior of the cochlea are compared. The results are presented and discussed at the end of this chapter.

### **3.2 Physical Model**

This physical cochlear model is intended to represent the passive cochlear dynamics. No active elements are included in the structure. The 16 times

scaled-up cochlear model has one duct which is built on an aluminum base as show in Figure 3.1 Cochlear duct and its base.

The duct's height and width vary with its length. A plastic thin film made of Polyoxymethylene (Delrin, DuPont) with thickness of  $76\mu m$  is used to represent basilar membrane (BM). Two clear plastic plates are made of cast acrylic and each has an identical opening slot which defines the shape of the BM. The width of the slot changes exponentially along its length. The Delrin membrane is sandwiched between two acrylic plates which represent spiral lamina and spiral ligament of cochlea and define the boundaries of BM. The open slot allows the membrane move out of the plane. The plate structure and dimensions (in *mm*) are shown in Figure 3.2 Cochlear membrane and its superstructure.

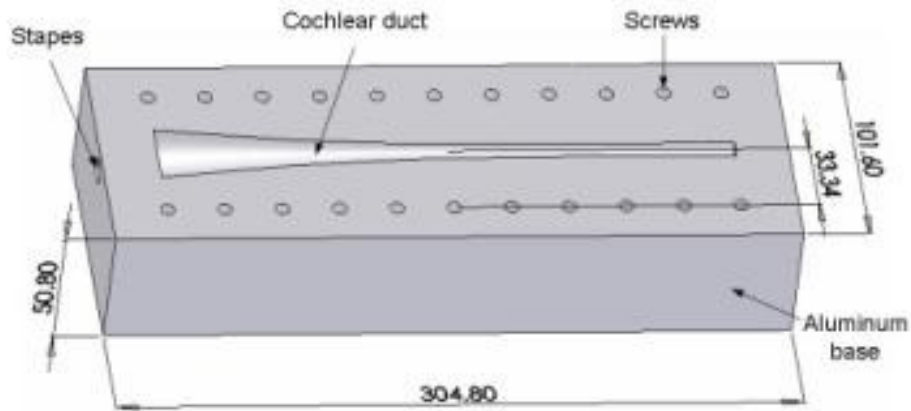


**Figure 3.1 Cochlear duct and its base**

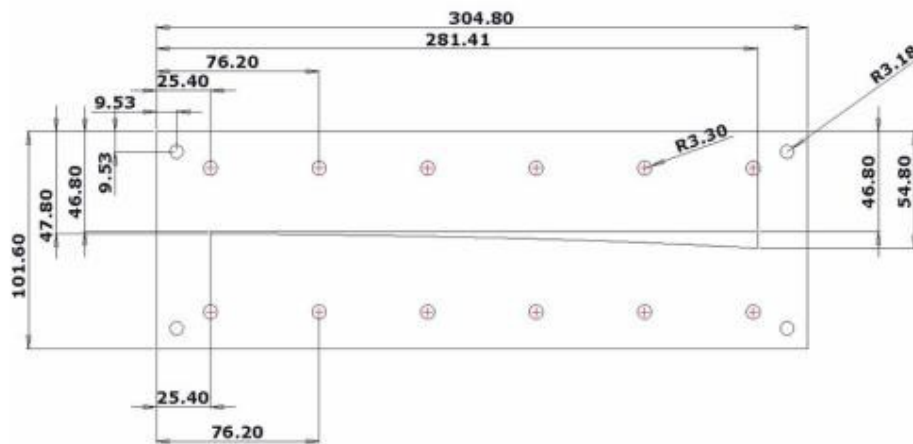


**Figure 3.2 Cochlear membrane and its superstructure dimensions**

The Delrin membrane and two acrylic plates are fixed in place using screws to the aluminum base with an aluminum cover. A rectangular rubber strip is placed between the aluminum base and the acrylic plate to seal the cochlear model from leaking. A small hole representing oval window (OW) of the cochlea opens up the aluminum base from one of the side walls, allowing communication between the cochlea duct and outside environment. A piece of rubber representing the OW membrane and covering the small hole is attached and fixed to the aluminum base. A screw with hemisphere head which represents the Stapes of the middle ear is used as the drive mechanism. A photograph of the cochlear model and shaker set up is shown in Figure 3.3.

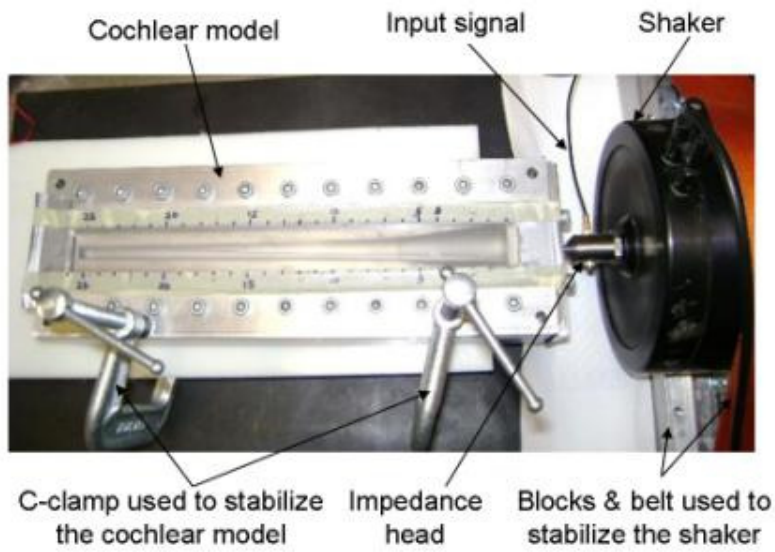


**Figure 3.3 Cochlear model and shaker set up**

All the physical parameters used in this analysis listed in Table 3.2.

Table 3.2 Parameters of cochlear model

Parameter	Value	Note
$E_p$	$2.5 \times 10^9 Pa$	Membrane modulus
$\mu$	$20 / 500 cSt$	Fluid viscosity
$d_e$	0.01	Hysteretic damping
$\rho_p$	$1384 kg / m^3$	Membrane density
$\rho_f$	$950 kg / m^3$	Fluid density
$\nu$	0.35	Poisson's ratio
$l$	$0.256 m$	Membrane length
$h$	$76 \times 10^{-6} m$	Membrane thickness
$b(x)$	$b(0) = 0.001 m$	Membrane width at the base
	$b(0)e^{\frac{x \ln(\frac{b(l)}{b(0)})}{l}} m$	$x$ is longitudinal direction of the Membrane Membrane width varies with $x$
	$b(l) = 0.008 m$	Membrane width at the apex
$L_1(x)$	$L_1(0) = 0.03 m$	Duct width at the base
	$L_1(\frac{4}{l}) = 0.0145 m$	Duct width at a quarter length from the base
	$L_1(l) = 0.0082 m$	Duct width at the apex $L_1(x)$ Linearly varying with $x$ between these three points

Table 3.2 Parameters of cochlear model—continued

Parameter	Value	Note
$L_2(x)$	$L_2(0) = 0.011m$	Duct height at the base
	$L_2(\frac{4}{l}) = 0.0056m$	Duct height at a quarter length from the base
	$L_2(l) = 0.0082m$	Duct height at the apex $L_2(x)$ Linearly varying with $x$ between these three points
$A_{st}$	$5.518 \times 10^{-5} m^2$	Stapes area

### 3.3 Mathematic Model Using WKB Method

Mathematical model are used to compare with the experimental results. The mathematical method implemented in the cochlear model is Wentzel-Kramers-Brillouin(WKB) method. The WKB theory is a method for approximating the solution of a differential equation of the form  $\frac{d^2y}{dx^2} + f(x)y = 0$ , where  $f(x)$  is slowly varying with respect of the solution. The WKB asymptotic method applied to the calculation of the cochlear model is derived by Steele and Taber, in which the fluid motion is fully three dimensional [25]. The fundamental mechanism of the cochlea is governed by geometric and physiologic variation with the distance from the Stapes. In the typical mammalian cochlea, this

variation is quite slow. Thus, the WKB asymptotic method is well suited for the treatment of this problem. The basic idea behind the WKB method is that when the wavelengths are sufficiently short, the properties can be taken as constant over the space of a wavelength. The basilar membrane was treated as a thin plate in [25], and the plate deflection is approximated as

$$w(x, y, t) = W(x)\eta(x, y)e^{i(\omega t - \int_0^x \lambda(x) dx)} \quad (3.1)$$

where the spatial variation of the solution in  $x$  has been expressed as the product of slowly varying envelope function,  $W(x)$ , and the oscillatory function,  $e^{-i \int_0^x \lambda(x) dx}$ . The plate cross-mode shape is a function of  $x$ . For simply supported boundaries,

$$\eta(x, y) = \sin(\pi y / b(x)) \quad (3.2)$$

For clamped edges,

$$\eta(x, y) = \sin^2(\pi y / b(x)) \quad (3.3)$$

$\lambda(x)$  is the wave number varying with  $x$ . It is solved through “eikonal” equation

$$F(\lambda, \omega) = \frac{1}{4} \omega^2 (2\rho_f H_{eq}(\lambda) + \rho_p h) - K(1 + id_E)\Gamma(\lambda) = 0 \quad (3.4)$$

where  $\rho_f, \rho_p$  are the fluid and plate density respectively,  $h$  is the thickness of the basilar membrane,  $d_E$  is the hysteretic damping for the viscoelastic basilar membrane property,  $H_{eq}(\lambda)$  is the equivalent fluid thickness related to structure and fluid mode shapes, cochlear dimensions and material properties,

$$H_{eq} = \left( \int_0^b \eta^2(y) dy \right)^{-1} \times \sum_{j=0}^{\infty} \left( \frac{A_j^2}{m_j L_1 (\tanh(m_j L_2) - m_j \beta_j^{-1})} \right) \times \begin{cases} 1 & j=0 \\ 2 & j=1,2,\dots \end{cases} \quad (3.5)$$

where  $A_j$  is the integration of structural mode shapes with fluid mode shapes,

$$A_j = \int_0^b \eta^2(y) \cos(j\pi y / L_1) dy \quad (3.6)$$

$$m_j = \sqrt{(j\pi / L_1)^2 + \lambda^2} \quad (3.7)$$

$$\beta_j = \sqrt{(m_j)^2 + i\rho_f \omega / \mu} \quad (3.8)$$

$K$  is the stiffness of the Basilar membrane,

$$K = \begin{cases} \frac{\pi^6 D}{8b^5} & \text{for simply supported edges} \\ \frac{8\pi^4 D}{b^5} & \text{for clamped edges} \end{cases} \quad (3.9)$$

where  $D$  is the bending stiffness of the plate.

$\Gamma$  is a function of the plate width,

$$\Gamma = \begin{cases} \frac{2b}{\pi^2} \left[ 1 + \left( \frac{\lambda b}{\pi} \right)^2 \right]^2 & \text{for simply supported edges} \\ \frac{b}{6} \left[ 1 + \frac{1}{2} \left( \frac{\lambda b}{\pi} \right)^2 + \frac{3}{16} \left( \frac{\lambda b}{\pi} \right)^4 \right] & \text{for clamped edges} \end{cases} \quad (3.10)$$

$W(x)$  is solved by ‘transport’ equation

$$W(x) = C \left( \frac{\partial F(\lambda, \omega)}{\partial \lambda} b(x) \right)^{-\frac{1}{2}} \quad (3.11)$$

where  $C$  is a constant.

It is convenient to normalize the plate amplitude with respect to that of

the Stapes. The ratio of the plate to the Stapes amplitude at the center of the basilar membrane cross section along x direction is

$$\begin{aligned} \frac{W(x, \frac{L_1}{2}, t)}{\delta_s t} &= \frac{W(x) e^{i(\alpha x - \int_0^x \lambda(x) dx)}}{-i(A_0 w(x) / \lambda A_{st})_{x=0} e^{i\alpha x}} \\ &= A_{st} \left( \frac{\lambda}{A_0} \right)_{x=0} \left[ \frac{(b(x) \frac{\partial F(\lambda, \omega)}{\partial \lambda})_{x=0}}{(b(x) \frac{\partial F(\lambda, \omega)}{\partial \lambda})} \right]^{\frac{1}{2}} e^{i\phi - \zeta} \end{aligned} \quad (3.12)$$

where  $A_{st}$  is the Stapes area,  $A_0$  is  $A_j$  when  $j=0$ , the phase is from the real part of the  $\lambda$

$$\phi = \frac{\pi}{2} - \int_0^x \text{Re}(\lambda) dx \quad (3.13)$$

and the damping factor is from the imaginary part of  $\lambda$

$$\zeta = -\int_0^x \text{Im}(\lambda) dx \quad (3.14)$$

From Eqn.(3.12), the displacement ratio of the basilar membrane to Stapes at different location under different frequency stimuli can be computed. The results can be used to compare with the experimental results. A Matlab<sup>®</sup> script for the computation can be found in Appendix A1.

### 3.4 Scaling Law

As mentioned in the beginning of the chapter, an enlarged cochlear model can resemble the real cochlea only by satisfying the *scaling law*. According to *scaling law*, based on the length of the BM  $l$ , if all other dimensions of the guinea pig cochlea can be expressed as ratios to  $l$ , and

if all the dimensions of the enlarged cochlear model have same ratios to a scaled-up membrane length (*i.e.*,  $16 l$ ) as those of the guinea pig cochlea, then these two cochlear models will themselves be alike. Also despite the change in dimensions, the equation of motion remains the same and their motions will be similar. The movement of the basilar membrane and the fluid in the cochlear duct is determined by some constants: the density  $\rho$  and viscosity  $\eta$  of the fluid, the stimuli frequency  $f$ , and the elasticity of the membrane  $E$ . The elasticity can be expressed as the volume compliance  $\epsilon$ , which is the volume displacement of the membrane per unit of length when a unit pressure is applied to one side. The constant  $\epsilon$  has the dimensions  $\epsilon = \text{volume}/(\text{length} \cdot \text{pressure}) = kg^{-1}m^3s^2$ , where  $kg$ ,  $m$ ,  $s$  are the units for mass, length and time respectively.

The equation of motion can be expressed in the form  $\phi(l, \rho, \eta, f, \epsilon) = 0$  ([5], page 406). According to the *Buckingham Pi theorem*, given a relation among five parameters of the form  $\phi(l, \rho, \eta, f, \epsilon) = 0$ , the five parameters can be grouped into two independent dimensionless ratios expressible in functional form by

$$\Phi\left(\frac{\rho fl^2}{\eta}, \frac{\eta^2 \epsilon}{\rho l^4}\right) = 0 \quad (3.15)$$

If the five constant parameters are chosen in a way that for both guinea pig cochlea and the enlarged cochlear model,  $\frac{\rho fl^2}{\eta}$ ,  $\frac{\eta^2 \epsilon}{\rho l^4}$  are the same,

then the equation of motion is the same and the movements of the both models are alike.

The basilar membrane length  $l$  of the physical cochlea is chosen to be 16 times of guinea pig basilar membrane length. The fluid density  $\rho$  and viscosity  $\eta$ , the stimuli frequency  $f$  can be chosen to ensure  $\frac{\rho fl^2}{\eta}$  is same as that of guinea pig. The volume compliance is a function of the membrane width  $w$  and height  $h$ . Once the height of the enlarged cochlear model membrane is chosen, by varying the width of the membrane, we will be able to decide the cochlear model membrane volume compliance  $\epsilon_m$  that can be used to represent the guinea pig cochlear membrane volume compliance  $\epsilon_g$ . The guinea pig cochlear membrane volume compliance  $\epsilon_g$  was not reported in the literature. However, gerbil BM material properties were reported in [41]. Guinea pig and gerbil have similar cochlea dimensions; thus we used gerbil BM properties, implemented with finite element method to compute the volume compliance of the guinea pig BM. Once the five parameters are chosen to satisfy the *Buckingham Pi theorem*, then the motion of the cochlear model can represent the motion of the guinea pig cochlea and can be observed through the experiments.

### 3.5 Scaling Parameters of the Cochlear Model

The human being cochlea fluid density is  $1034kg/m^3$  and viscosity is  $0.00197Pa \cdot s$  [5]. We assume guinea pig cochlear fluid has same density and viscosity as those of human being. The volume compliance  $\epsilon_g$  for the guinea pig is calculated using finite element commercial package COMSOL<sup>®</sup> at several locations along the basilar membrane and listed in Table 3.3. According to the *scaling law*, the two independent dimensionless ratios for the guinea pig cochlea are equal to those of the cochlear model,

$$\frac{\rho_g f_g l_g^2}{\eta_g} = \frac{\rho_m f_m l_m^2}{\eta_m} \quad (3.16)$$

$$\frac{\eta_g^2 \epsilon_g}{\rho_g l_g^4} = \frac{\eta_m^2 \epsilon_m}{\rho_m l_m^4} \quad (3.17)$$

where under script  $g$  represents properties for guinea pig and  $m$  represents for the physical cochlear model. The fluid used in the cochlear model has density  $950kg/m^3$  and kinematic viscosity  $500cSt$ , which is  $0.475Pa \cdot s$  dynamic viscosity. According Eqn.(3.16), when the guinea pig cochlea responds to the frequency  $f_g$ , the cochlear model has to operate at frequency  $f_m$  in order to have the same motion response,

$$f_m = \frac{\rho_g l_g^2 \eta_m}{\rho_m l_m^2 \eta_g} f_g = 0.9712 f_g \quad (3.18)$$

According Eqn.(3.17), the volume compliance of the cochlear model that satisfies the *scaling law* is,

$$\epsilon_m = \frac{\rho_m l_m^4 \eta_g^2}{\rho_g l_g^4 \eta_m^2} \epsilon_g = 1.154 \epsilon_g \quad (3.19)$$

The calculated volume compliance of the cochlear model is list in Table 3.3. Volume compliance has unit  $kg^{-1}m^3s^2$ . The location indicated in the table is the distance from the base of the cochlear model.

**Table 3.3 Parameters calculated from scaling law**

<b>Volume compliance</b>	<b>Guinea pig</b> $\left(\frac{m^3 s^2}{kg}\right)$	<b>Model</b> $\left(\frac{m^3 s^2}{kg}\right)$
$\epsilon(1.14mm)$	$1.22 \times 10^{-13}$	$1.41 \times 10^{-13}$
$\epsilon(3.99mm)$	$8.37 \times 10^{-13}$	$9.66 \times 10^{-13}$
$\epsilon(6.612mm)$	$3.79 \times 10^{-12}$	$4.37 \times 10^{-12}$
$\epsilon(7.3mm)$	$5.47 \times 10^{-12}$	$6.31 \times 10^{-12}$

### 3.6 Experiments

The experiment setup is shown in Figure 3.4 Setup for cochlear model experiment LabVIEW® is used to perform the data acquisition analysis. LabVIEW® commands are sent from a computer to a signal generator which produces a drive signal amplified by a power amplifier. The drive signal excites a modal exciter (*shaker*). An impedance head is mounted on the shaker. The signal is then sent to a charge amplifier through the

acceleration sensor on the impedance head. The charge amplifier changes the acceleration signal to a velocity signal which becomes the input signal sent to the data acquisition box. The impedance head driving by the shaker excites the stapes of the cochlear model. The vibration of the stapes sets the fluid in the cochlear duct and the membrane in motion. The motion of the membrane is detected by the laser vibrometry. The detected signal is then sent to the data acquisition box as an output signal. Both input and output signals are sent to the computer where they are analyzed by the LabVIEW<sup>®</sup> program. The results from the LabVIEW<sup>®</sup> are used to compare with the WKB mathematical results.

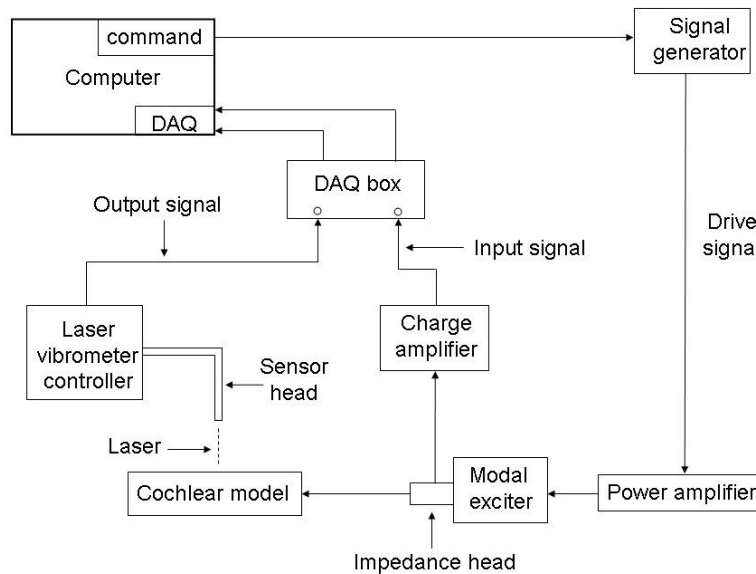


**Figure 3.4 Setup for cochlear model experiment**

Two different viscosities silicone oil,  $20cSt$  and  $500cSt$  are used as the fluid in the cochlear duct to investigate the influence of viscosity on the

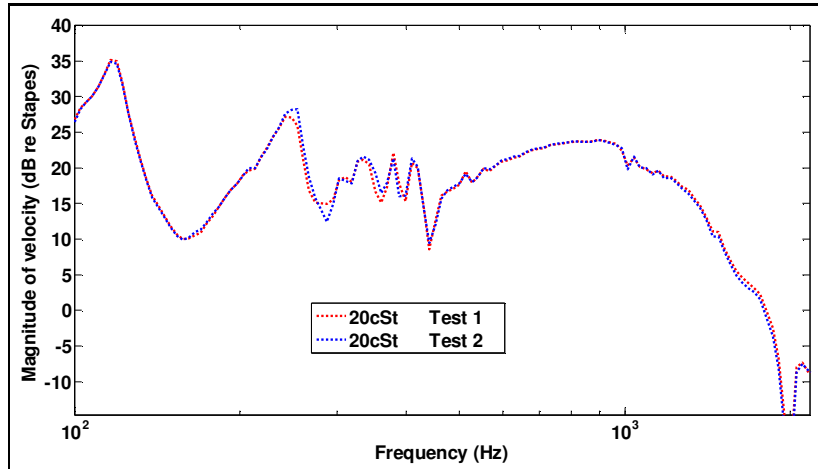
fluid motion. A sweep sinusoidal signal ranging from  $100\text{Hz}$  to  $20000\text{Hz}$  is used to stimulate the cochlea at different measuring locations. The membrane's responses to different frequency stimuli thus can be observed and, the characteristic frequency for a particular location can be identified.

## **3.7 Result and Discussion**

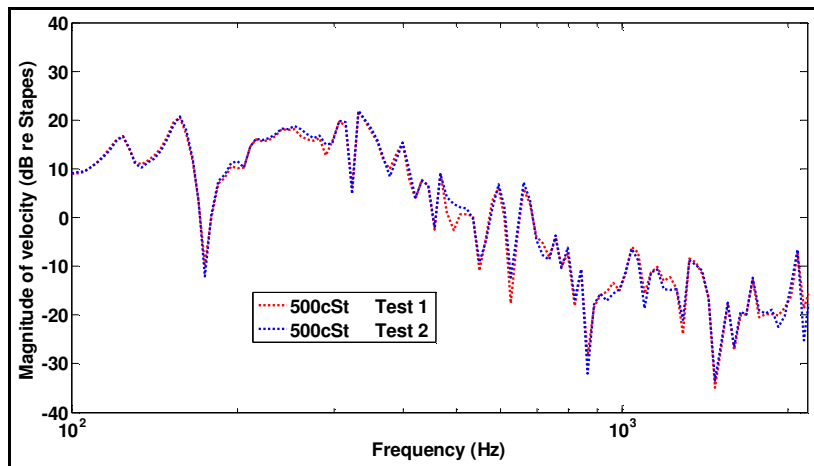
### **3.7.1 Experiment Repeatability of the Cochlear Model**

Repeatability of the experimental results is defined as the closeness of the agreement between the results of successive measurements of the same experiment carried out under the same conditions. The repeatability quantifies the reliability of the cochlear model. The repeatability test is carried out using two different silicone oils and at different locations.

For  $20\text{cSt}$  silicone oil, the experiment measurements are recorded at  $10\text{cm}$  from the base and the comparison for two tests is shown Figure 3.5(a). For  $500\text{cSt}$  silicone oil, the experiment measurements are recorded at  $18\text{cm}$  from the base and the comparison for two tests is shown Figure 3.5(b). The plots show the experiments are very repeatable at different locations for fluids of different viscosities.



(a)



(b)

**Figure 3.5 Repeatability of the cochlea model**  
 (a) For 20cst silicon oil (b) For 500cst silicon oil

### 3.7.2 Viscosity Influence on the Cochlear Model

20cSt and 500cSt silicone oils are used to investigate the influence of viscosity on the cochlear motion when subjected to the same stimuli. The experiments show that for these two particular silicone oils, the cochlear model does not demonstrate significant difference for the membrane

vibration. The comparison is shown in Figure 3.6.

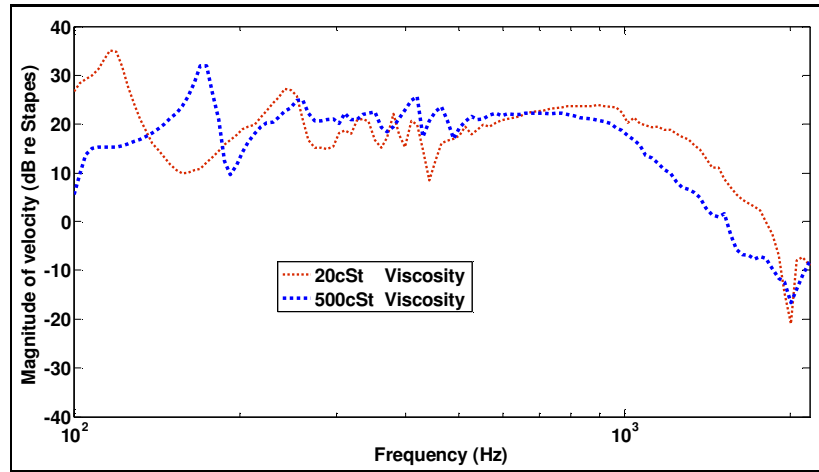
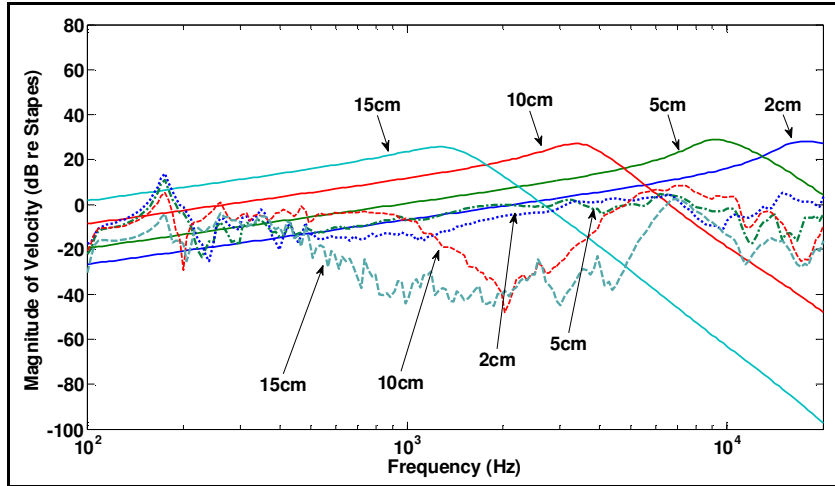


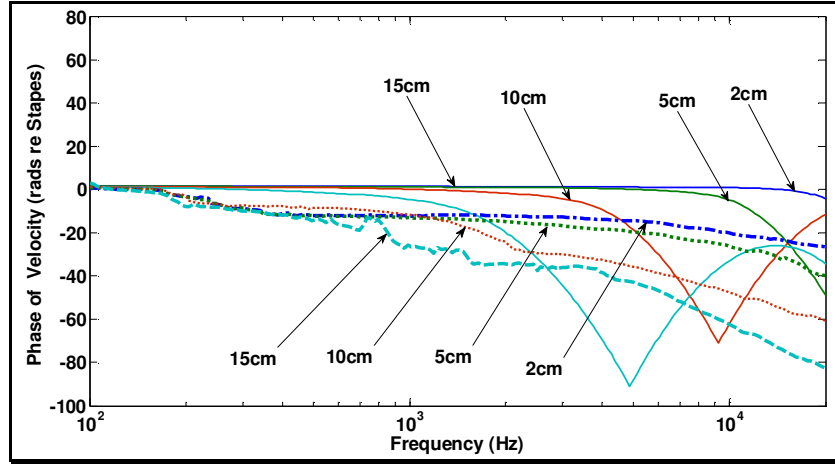
Figure 3.6 Viscosity influence on the cochlear model

### 3.7.3 Comparison of WKB with Experimental Results

The WKB method is implemented to verify the validity of the model by the comparison with some experimental results. Four locations are measured along the membrane,  $2\text{cm}$ ,  $5\text{cm}$ ,  $10\text{cm}$  and  $15\text{cm}$  from the base respectively. Two boundary conditions are investigated using WKB method to accommodate to the possibility of the boundary conditions for the cochlear model. One possible boundary condition is clamped edges because the membrane is sandwiched between two acrylic plates. The magnitude and phase comparison of the experimental results with clamped boundary conditions is shown in Figure 3.7.



(a)



(b)

**Figure 3.7 Comparison of WKB and experimental results for clamped boundary condition**

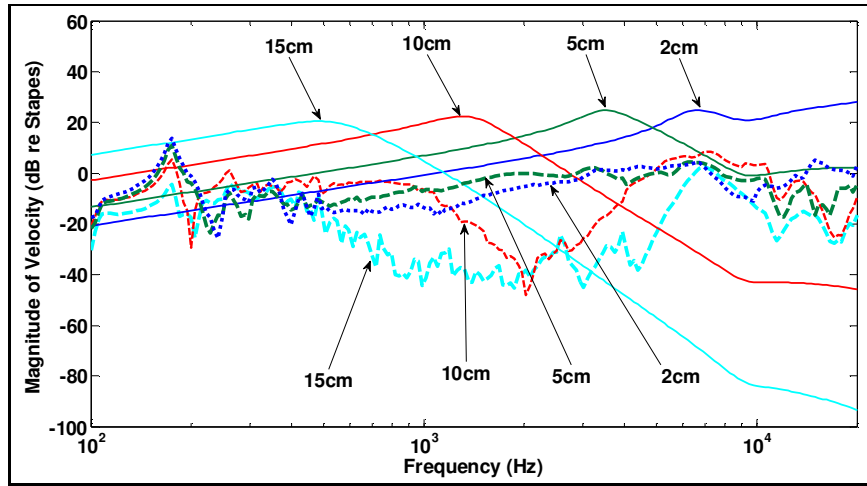
**(a) Magnitude of velocity (b) Phase of velocity**

The experimental results used here for the comparison are from  $500cSt$  silicone oil. The cochlear model exhibits a systematic resonance around  $200Hz$ , which can be seen from the plot for all four locations. The plot demonstrates the model system is unreliable above  $7000Hz$ . In Figure

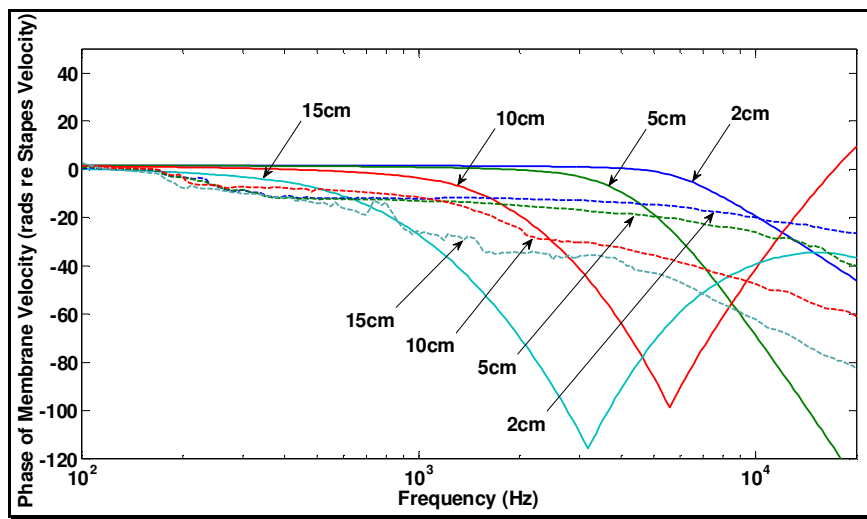
3.7, for the clamp edged boundary condition, at location  $2\text{cm}$  from the base, the WKB method calculated a characteristic frequency about  $16000\text{Hz}$  while the experiment shows a characteristic frequency is around  $7000\text{Hz}$ . At  $5\text{cm}$  from the base, WKB predicts a characteristic frequency of  $9000\text{Hz}$  and an experimental characteristic frequency of  $3000\text{Hz}$ . At  $10\text{cm}$  from the base, WKB has a characteristic frequency of  $3300\text{Hz}$  and an experimental characteristic frequency of  $1000\text{Hz}$ . At  $15\text{cm}$  from the base, WKB has a characteristic frequency of  $1300\text{Hz}$  and an experimental characteristic frequency of  $500\text{Hz}$ . The plot indicates large difference between characteristic frequencies calculated from WKB method and experimental results. The magnitudes of the ratio of membrane to stapes velocity calculated from WKB method are about  $10-20\text{dB}$  higher than those obtained from experiments. For both WKB and experimental results, the phase decreases drastically after the sweep frequencies pass its characteristic frequency.

Another possibility is a simply supported boundary condition. It is possible that the fluid in the cochlear duct permeate between the membrane and the acrylic plate which is immersed in the fluid. In Figure 3.8, for the simply supported boundary condition, at the location  $2\text{cm}$  from the base, the WKB method calculated a characteristic frequency about  $7000\text{Hz}$ , the same as that of the experimental characteristic frequency. At  $5\text{cm}$  from the base, WKB has a characteristic frequency of

3300Hz which is very close to an experimental characteristic frequency of 3000Hz . At 10cm from the base, WKB has a characteristic frequency of 1300Hz and an experimental characteristic frequency is 1000Hz . At 15cm from the base, WKB has a characteristic frequency of 500Hz and an experimental characteristic frequency of 400Hz . For the simply supported boundary condition, the experimental characteristic frequencies are very close to those computed using WKB method with differences from 100Hz to 300Hz at different locations. The magnitudes of the ratio of membrane to the Stapes velocity calculated from WKB method are about 15–25dB higher than those from experiments, similar to those from clamp edged boundary condition. The phases for WKB and experimental results are close.



(a)



(b)

**Figure 3.8 Comparison of WKB and experimental results  
for simply supported boundary condition  
(a) Magnitude of velocity (b) Phase of velocity**

The comparison of the results from two different boundary conditions is shown in Figure 3.9. The magnitudes of velocity ratio for simply supported boundary condition are *5dB* higher than those of the clamped boundary condition. The boundary conditions affect the

characteristic frequencies greatly. The simply supported boundary shifts the characteristic frequencies to the basal direction of the cochlear model significantly. The comparison of the WKB results with the experimental results indicates that the WKB method with simply supported boundary condition better resembles the experimental results than clamped boundary condition. The relative magnitudes of the membrane to the stapes are different by  $15-25\text{dB}$  and the characteristic frequencies are close for both WKB and experimental results. The WKB method does not fully capture all the aspects of the physical model and the two results are not in complete agreements. The differences could have been caused by many factors, including tension in the membrane. Naidu and Tam [26, 59] reported pretension in both gerbil basilar membranes and membranes of coiled physical cochlear models. The WKB method does not include the pretension of the membrane and thus the results cannot fully represent the physical models with tensioned membrane.

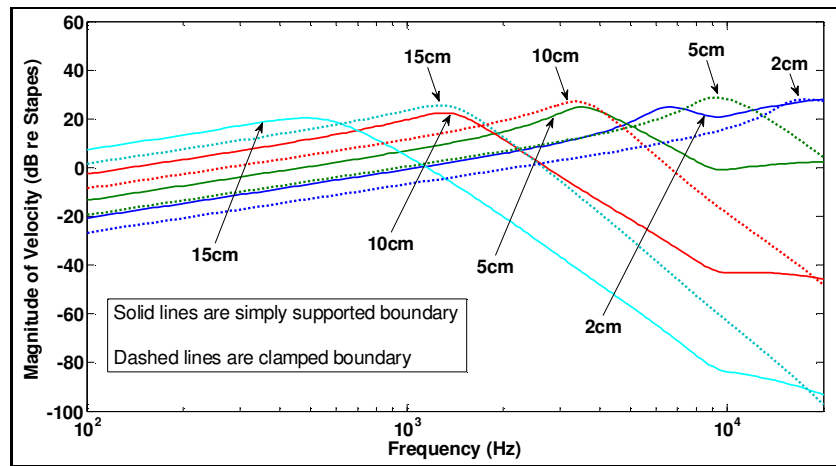


Figure 3.9 Comparison of results for simply supported and clamped boundaries

### 3.8 Conclusion

A 16 times scale hydromechanical cochlear model is designed and fabricated. A *scaling law* allows a scale-up cochlear model to have similar motion responses as those of guinea pig cochlea if the independent parameters are chosen in a way which satisfies *Buckingham Pi theorem*.

The operating frequency for the cochlear model and volume compliance of the basilar membrane that satisfy the *Buckingham Pi theorem* are calculated.

The cochlear model has only one duct. The cochlear duct's height and width linearly vary with its length analogizing the physiology of the guinea pig cochlea. The guinea pig basilar membrane is represented by a Delrin thin film and it is fixed in place by two acrylic plates. The drive force is applied by a screw head on a rubber piece which represents the oval window membrane of the cochlea. A sweep sinusoidal program is used to generate sinusoidal signals to drive the screw head to stimulate the cochlear model system. The membrane motion is detected by laser vibrometry and the relative magnitude and phase of the velocity between the membrane motion and the drive signal are recorded and plotted.

Repeatability is tested using different silicone oils at different locations. The results demonstrate the experiments are very repeatable for fluids with different viscosities at varying locations, affirming the reliability of the cochlea model.

Two boundary conditions are investigated using WKB method. The comparison of WKB results with experimental results shows that the WKB method with simply supported boundary condition better represents the experimental results than clamped boundary condition. The relative magnitudes between the output signal and the input signal calculated from WKB method are about  $15-25dB$  higher than those of experiments for simply supported boundary. The characteristic frequencies and the phase lagging computed from the WKB method are similar to the experimental results. The WKB method does not include effects caused by the pretension in cochlear membrane and thus did not produce results that fully represent the experiment results. A mathematic cochlear model including basilar membrane pretension would better represent the physical model. The next step involves finding such a mathematic model to compare with experiment results and construct a scaled gerbil cochlear model with orthotropic basilar membrane properties computed in chapter 2 using the *scaling law*. The future study will be investigating the traveling wave patterns and the mapping of the characteristic frequencies of gerbil cochlea through the enlarged gerbil cochlear model. Sensors can be embedded in the model to detect the flow forces in the cochlea fluid for the feedback control of the model.

# Chapter 4

## INTRODUCTION TO SHEAR SENSORS

A surface force and flow measurement hair-like sensor array using micro-electro-mechanical systems (MEMS) technology for aeroacoustic application is described in the next three chapters. The sensor array was inspired by the hair cells in the cochlea, but specifically designed for use in a wind tunnel test environment at Spirit AeroSystems, Inc. This particular facility currently operates at flow rates up to Mach 0.6. The goal is to have the sensor array measure surface shear stress underneath a turbulent boundary layer. In addition, the sensor will be used for investigating skin friction on aerodynamic structures that are manufactured and tested for commercial aircraft.

This chapter starts with the motivation and objective for the design of the hair-like shear sensors, followed by a literature review of the existing technology for surface force and shear stress measurements.

## 4.1 Motivation

Turbulence is an irregular, diffuse, three-dimensional vortical fluctuation following a continuum model and dissipates over various spatial length scales [60]. A turbulent boundary layer is characterized by a wavenumber-frequency spectrum which influences the degree and type of coupling between the exterior air and the fuselage. Effective design of the fuselage from an aeroacoustic perspective requires knowledge of the structure of the spectrum. Some features of the spectrum are known. The most notable is the presence of a strong convective ridge [61, 62]. However, the very high wavenumber and very low wavenumber portions of the spectrum have not been sufficiently explored, particularly at high Reynolds and Mach number, due to limitations in experimental and computational techniques.

For turbulent flow, boundary layer thickness can be on the order of hundreds of microns. For aerospace application, turbulent boundary layer thickness can be on the order of  $1\text{cm}$ . Small measurement devices with large bandwidth and spatial sizes, smaller than those of the turbulent structures, are required to accurately capture the full spectrum of the turbulent shear stress fluctuation, as well as to avoid disturbance of the boundary layer.

Conventional shear stress measurement techniques, which operate at large spatial scales, often fail to detect local time-resolved fluctuating

shear stress, which can be important for fluid mechanics-related applications. MEMS technology can micromachine sensors at the microscale, which allows shear stress sensors to be built with feature sizes on the order of microns, thus providing the necessary spatial resolution for turbulence measurements.

Previous work on MEMS shear stress sensors was reviewed by Lofdahl and Gad-el-Hak in 1999 [63]. Existing MEMS shear sensor designs fall into two categories: direct measurement sensors, i.e., floating element sensors [64-66], and indirect sensors, such as thermal element sensors [67, 68]. Thermal elements characterize shear stress using heat loss from a heated surface patch. Thermal shear stress sensors usually employ a thermal resistor operating at an over-heated temperature compared to the surrounding fluid. Heat transfer from the thermal resistor to the surrounding fluid is related to the wall shear stress to be measured. Specifically, the sensor output signal indicates the total heat transfer rate, which must then be converted to the corresponding shear-stress magnitude via an empirical relation. This measuring scheme has the advantage of no moving parts. However, as an indirect measure of shear stress, it can cause confusion when attempting to relate heat loss to flow properties for complicated turbulent flows. Floating element sensors perform a direct measurement of flow shear stress, but have only been demonstrated by a few authors [64-66]. Some concerns remain unresolved

that flow around complex geometries at the surface of the floating element sensor may affect the fidelity of the measurements [69]. In addition, floating element sensors tend to be fragile, and as such can be difficult to use in wind tunnels and in flight.

Inspired by the hair cell in the cochlea, which functions as a flow sensor, a third type of MEMS surface shear sensor was designed to use hair-like structures to sense surface flow. Arrays of hairs sitting on top of structures made of conductive material deflect in response to surface flow. This deflection is sensed at the hair base capacitively. The design has some similarities to hair-like sensor arrays developed by Engel, Chen, Fan, and others from C. Liu's group at the University of Illinois [70, 71], as well as the work by Grosse and Schroder [72-74], but uses a different fabrication process and sensing scheme. It is hoped that this will present a more robust structural sensor than the floating element sensors, and with less complex flow around the structure, but will be a more direct measure of shear stress and flow than the heated element sensors. The sensor arrays have been successfully designed, modeled, and fabricated. Characterization of sensitivity has been done using a laminar flow cell. The following section describes the objectives of hair-like shear stress sensors from engineering requirements.

## 4.2 Objective

Kolmogorov microscales are the smallest scales in turbulent flow. They describe the smallest turbulent eddies' length scale, time scale and velocity scale. Eddies smaller than the Kolmogorov scale dissipate very quickly. Kolmogorov microscales are the desired absolute scientific scales of interest for turbulent study.

Hair-like shear stress sensors are designed for use in a wind tunnel test environment at flow rates up to Mach 0.6 with average shear stress of approximately 50 Pa. For wind tunnel tests 3 meters down from the contraction section in a 6×6 wind tunnel duct at the Spirit AeroSystems Inc. with flow speed of Mach 0.6, the Reynolds number based on plate length is:

$$Re_L = \frac{\rho VL}{\mu} = \frac{1.177 \frac{kg}{m^3} \times 206 \frac{m}{s} \times 3m}{1.846 \times 10^{-5} \frac{kg}{m \cdot s}} = 3.94 \times 10^7 \quad (4.1)$$

where  $\rho$  is the density of air,  $V$  is the velocity of the free stream fluid,  $L$  is the distance the fluid travelled and  $\mu$  is dynamic viscosity of air.

The turbulent boundary layer thickness is:

$$\delta = \frac{0.382 \times L}{\sqrt[5]{Re}} = \frac{0.382 \times 3m}{\sqrt[5]{3.96 \times 10^7}} = 0.035m \quad (4.2)$$

The Kolmogorov microscales can be calculated as:

$$\begin{aligned}
\eta &= \left( \frac{\nu^3}{\varepsilon} \right)^{\frac{1}{4}} = \left( \frac{\nu^3}{u^3 / \delta} \right)^{\frac{1}{4}} = \left( \frac{(1.59 \times 10^{-5})^3}{206^3 / 0.035} \right)^{\frac{1}{4}} = 1.6 \mu m \\
\tau &= \left( \frac{\nu}{\varepsilon} \right)^{\frac{1}{2}} = \left( \frac{\nu}{u^3 / \delta} \right)^{\frac{1}{2}} = \left( \frac{1.59 \times 10^{-5}}{206^3 / 0.035} \right)^{\frac{1}{2}} = 0.25 \mu s \\
v &= (\nu \varepsilon)^{\frac{1}{4}} = (\nu (u^3 / \delta))^{\frac{1}{4}} = \left[ (1.59 \times 10^{-5}) (206^3 / 0.035) \right]^{\frac{1}{4}} = 7.9 m / s
\end{aligned} \tag{4.3}$$

$\eta$  : length scale

$\tau$  : time scale

$v$  : velocity scale

$\nu$ : kinematic viscosity of the fluid

$\varepsilon = u^3/x$  is the energy dissipation rate

$u$ : free stream fluid flow speed

$x$ : turbulent boundary layer thickness

For our targeted wind tunnel tests, the Kolmogorov length scale is  $1.6 \mu m$ , time scale is  $0.25 \mu s$  and velocity scale is  $7.9 m / s$ . An ideal shear sensor should have the spatial and time resolution to match the Kolmogorov length and time scale, in order to detect the wall shear stress generated by the smallest and fastest eddies in a turbulent boundary layer. For our application, a sensor with spatial resolution of  $2 \mu m$  having a dynamic measurement up to  $4 MHz$  can meet Kolmogorov microscales requirements. Current MEMS sensors are far from reaching the spatial resolution of  $2 \mu m$ . Also from an engineering perspective, turbulence frequencies above  $20 kHz$  may not be particularly significant, since the sounds generated by

such eddies will be above the frequency range of human hearing.

Over the last decades, numerous experiments have been conducted on wall shear stress measurements. Time-resolved turbulent flow measurement is a desired measure of unsteady structures in the flow. To date, however, the quantitative time-resolved direct measurement of fluctuating shear stress has not been realized [75]. Though time-averaged turbulent flow measurement cannot capture the unsteady structures in the flow, it can be used to determine body-averaged properties such as skin friction drag.

No commercial MEMS shear stress sensors which are capable of measuring mean shear stress of turbulent flow are available yet. Thus, the first goal of this research is to develop a robust hair-like MEMS shear stress sensor for time-averaged turbulent flow measurements. The second goal is to design the sensor to have high dynamic range, and high bandwidth for turbulent boundary layer measurement.

The hair-like shear sensors use a differential capacitance scheme. An 8 by 8 array, with a total of 64 sensors, will be fabricated on a  $10.1\text{mm}$  by  $10.1\text{mm}$  polysilicon chip. The sensor array is designed to measure shear stress up to  $100\text{Pa}$  with a bandwidth larger than  $20\text{kHz}$ . The sensor array was successfully fabricated using the PolyMUMPs foundry process and was tested in a laminar flow cell.

## **4.3 Existing Technologies of Flow Measurement Sensors**

This section reviews the techniques used for shear stress sensor measurements. This review covers conventional and modern techniques for shear stress measurements, especially emphasizing MEMS shear stress sensors.

### **4.3.1 Conventional Techniques for flow measurements**

All the techniques for measuring shear stress can be divided into two categories: direct and indirect methods of measurement. An indirect technique depends on the measurement of other fluid properties, such as temperature or pressure, and the correlation of the measured fluid property to the shear stress. Indirect methods are not the preferred method for measuring shear stress since they require the use of empirical correlation relationships that are only applicable to very specific conditions.

Direct measurement techniques are more attractive since no assumptions must be made about the relationship between the wall shear stress and the measured fluid properties. However, indirect methods are widely used for their easy fabrication and easy usage. Direct methods are desired but

have many drawbacks of their own.

This section will present a brief discussion on conventional shear stress measurement techniques and their advantages and disadvantages.

Figure 4.1 shows the categorization of traditional shear measurement techniques by Haritonidis [76].

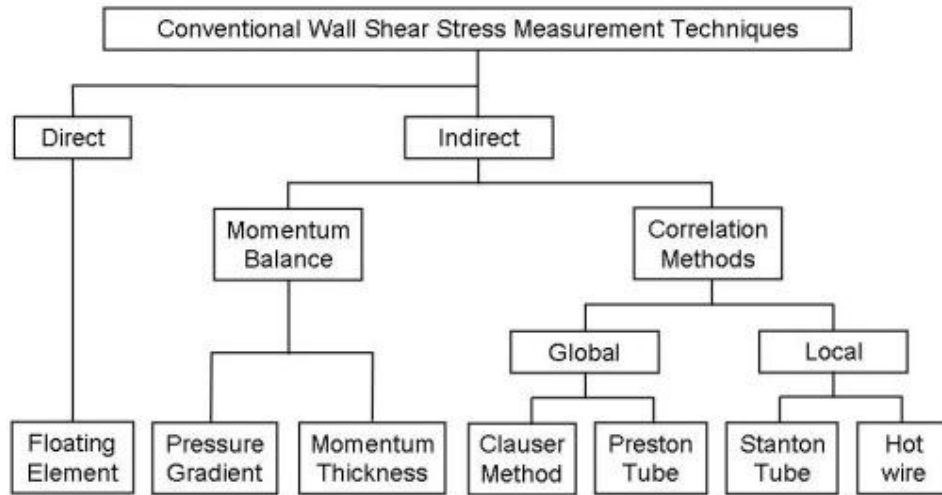


**Figure 4.1 Classification of wall shear stress measurements [76]**

Several authors [76-78] have written reviews on the conventional techniques used to measure wall shear stress. Hanratty and Campbell [77] summarized six principle methods used for measuring local shear stress.

The six principles are listed below:

1. The Stanton tube
2. Direct measurement
3. Thermal method
4. The Preston tube

5. The sublayer fence

6. The electrochemical technique

The earliest wall shear stress measurement was done using the Stanton tube method.

This method was reported in a historic paper by Stanton and his co-workers [79]. The Stanton tube [79], Preston tube [80] and sublayer fence [81] are surface obstacle devices whose presences interfere with the flow; thus though easy to fabricate and use, these devices are used in thick turbulent boundary layers. They have poor spatial resolution because of their sizes and poor accuracy because they rely on empirical correlation between a 2-D turbulent boundary layer profile and the property measured. They can measure mean shear stress, but are unable to measure time-resolved fluctuating shear stress.

Shear stress sensors based on heat/mass transfer principles, including hot-film sensors and hot-wire sensors remain widely used. Their advantages include simple structure, fast response and high sensitivity, and they are able to measure fluctuations in the wall shear stress as well as the mean shear stress. Small thermal elements can be flush mounted on the wall, causing minimal interference with the flow. But they have disadvantages of their own. They represent an indirect measurement of shear. Shear stress is inferred based on the Reynolds analogy hypothesis that the heat-transfer is proportional to the shear stress. In turbulent

flow, this assumption is invalid except in fully developed boundary layer conditions. Heat/mass transfer sensors are sensitive to temperature drift and suffer calibration repeatability problems because of heat loss to the substrate and air [75].

Reiss and Hanratty [82, 83] developed a device using the electrochemical technique. In this scheme, an electrochemical reaction is carried out on the surface of an electrode mounted flush with the wall. The current flowing through the electrode circuit is proportional to the rate of mass transfer at the electrode surface, and the rate of mass transfer is related to the velocity gradient at the surface. This device has the advantages of being calibrated analytically and can be easily applied to situations which require complicated sensor configurations. Also this technique does not interfere with the flow since it is flush mounted but it requires a liquid flow of specific chemistry.

The direct measurement schemes are known as skin friction balance or floating element balances. The floating element method is attractive for turbulent boundary layer measurements because it is a direct measurement; does not require any assumption about the flow field above the device; and no correlation between the different properties is necessary. Since it satisfies the need for aerodynamic measurement of shear stress in high-speed flows, floating element devices have been used in wind tunnel measurements since the early 1950s.

Winter [78] listed disadvantages of the direct shear stress measurement.

They are stated as the following:

1. The compromise between the sensor spatial resolution and the minimum detectable forces.
2. The effect of the necessary gaps around the element.
3. The error associated with misalignment of the element with respect to the surrounding surface.
4. Forces generated through pressure gradients.
5. The effects of heat transfer.
6. The use with boundary layer injection or suction.
7. The effects of gravity or acceleration if the device is used in a moving vehicle.
8. The effects of temperature change.
9. The effects of leaks.
10. The effects of the whole system in the presence of large transients.

In addition to the problems mentioned by Winter, Harittonidis added two more disadvantages of traditional floating element devices [76].

1. Poor frequency response due to large size, making them unsuitable for fluctuating shear stress measurements
2. Difficulties associated with the handling and installation of the devices due to their delicate structure.

Modern technology dealt with some of the issues mentioned above and

aimed to improve sensor performance. Modern techniques used for shear stress measurement can be broadly categorized as micro-electro-mechanical systems (MEMS) based shear sensors, oil-film interferometry and liquid crystal coatings. Naughton and Sheplak reviewed these techniques, and summarized the theory, development, limitations, uncertainties and misconceptions surrounding these techniques in 2002 [75]. In the following section, various MEMS shear sensors with different sensing schemes are presented in great detail.

### **4.3.2 MEMS Sensors for flow measurements**

MEMS is a technology that can be defined as miniaturized mechanical and electro-mechanical elements that are made using the techniques of microfabrication. This technology enables fabrication of sensors and actuators in micro-scale, which can perform in a way that is not possible with traditional mechanical fabrication techniques. MEMS technology is able to integrate sensors with signal processing circuitry on the same substrate, decreasing costs for making additional signal processing circuitry.

The measurement of time-resolved fluctuating shear stress in a turbulent boundary layer is always very important for fluid mechanics related applications. But conventional shear stress measurement techniques often

failed to detect this desired fluid property. MEMS technology confers many advantages for fluid flow research due to the small size of the devices. The boundary layer thickness in fluid flow can be on the order of millimeters; and for turbulent flow, boundary layer thickness can be on the order of hundreds of microns. To accurately capture the full spectrum of the turbulent shear stress fluctuation, a large bandwidth and spatial dimensions that are sufficiently smaller than the turbulent structure are required for the measuring device. MEMS sensors can meet these requirements because micromachined sensors can be fabricated on the same order of magnitude of the Kolmogorov microscale which are the smallest scales in turbulent flow [84]. For example, given a turbulent flow with relatively low Reynolds number, a boundary layer thickness of  $5\text{cm}$  and an edge velocity of  $50\text{m/s}$ , the Kolmogorov spatial scale is approximately  $100\mu\text{m}$  and time scale  $2\text{ms}$  [75]. For aerospace applications, the boundary layer thickness is on the order of  $1\text{cm}$  and the Kolmogorov spatial scale approximately  $1\mu\text{m}$ . Such small spatial and time resolution requirements can only be met by micromachined sensors.

Like conventional wall shear stress sensors, MEMS sensors can be divided into direct and indirect measurement techniques. According to different measuring schemes and device structures, MEMS sensors can be further divided into different categories. The following subsections describe different shear sensors in detail.

### 4.3.2.1 Direct Shear Stress Measurements

Direct sensors measure the shear force produced by the wall shear stress on the model surface directly. This is typically achieved by a flush mounted movable floating element. The floating element is attached either to a displacement transducer or is part of a feedback force-balance configuration. Based on the sensing scheme, floating element sensors can be categorized to capacitive, piezoresistive and optical shear stress sensors. A schematic view of a typical floating element sensor is shown in Figure 4.2. A summary and comparison of the direct MEMS sensors in the literature is listed in Table 4.1.

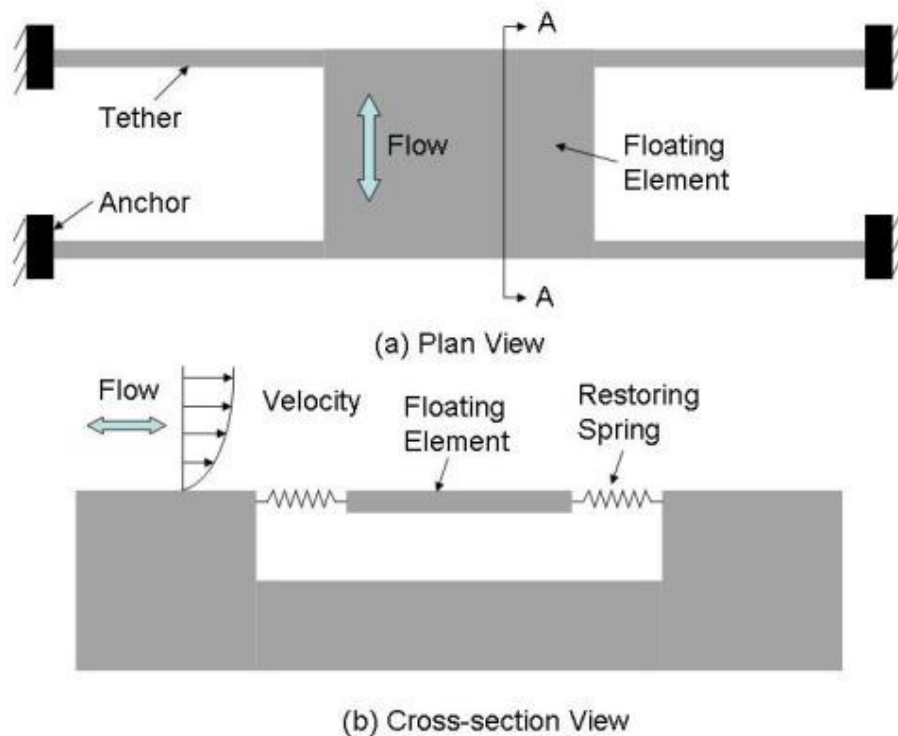
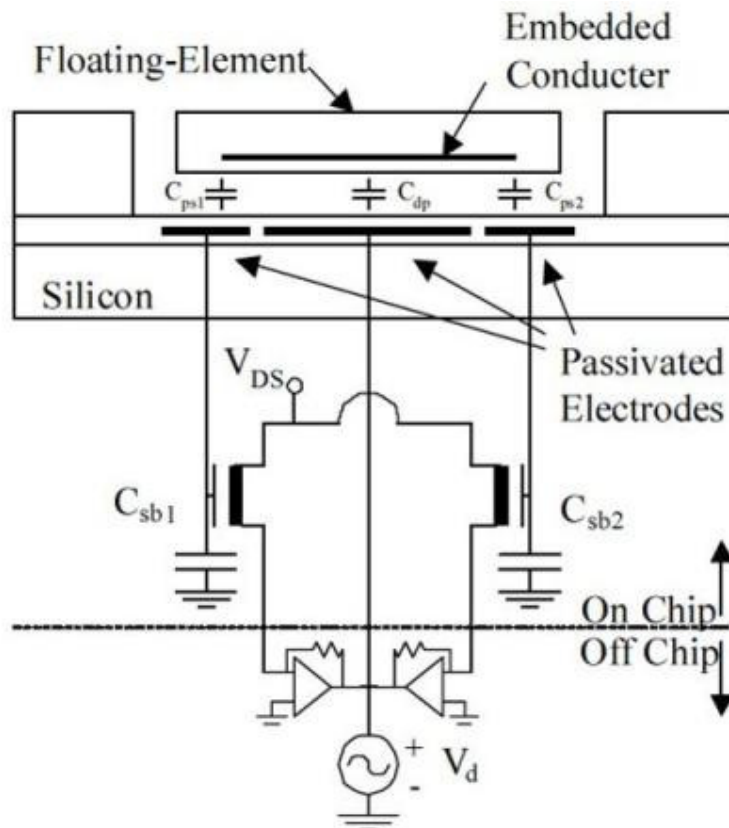


Figure 4.2 Schematic view of a typical floating element sensor

## Capacitive Shear Stress Sensors

A capacitive floating element sensor usually consists of a sensing element, compliant tethers, and inter-digitized capacitive comb fingers. Schmidt *et al* [85] were the first ones to develop a micromachined floating element sensor with an integrated readout for applications in low speed turbulent boundary layers. Figure 4.3 shows a schematic view of the first capacitive floating element sensor developed by Schmidt *et al*.



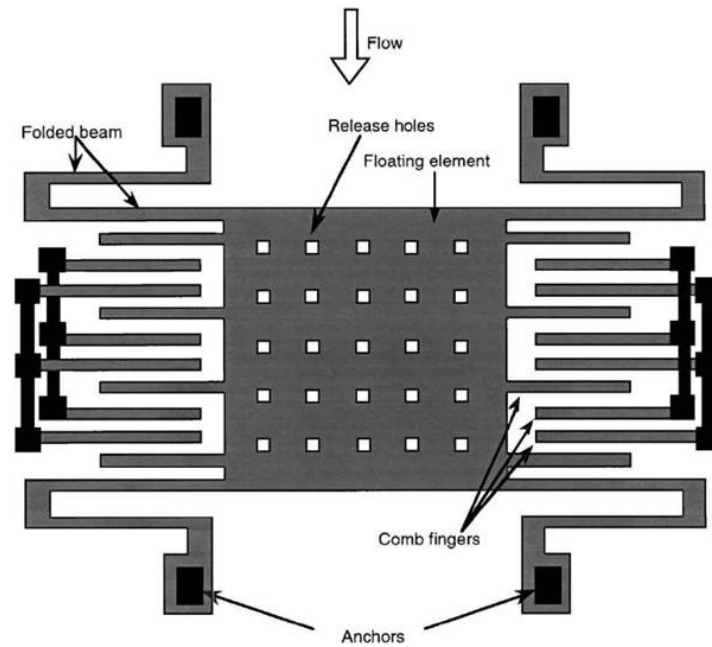
**Figure 4.3 Schematic cross-section view of differential capacitive floating element sensor by Schmidt *et al* [85]**

The designed sensor had a floating element with dimensions of  $500\mu m \times 500\mu m$  and a thickness of  $30\mu m$ . The floating element was suspended by four tethers with lengths of 1mm and widths varying from 10 to  $20\mu m$ . The device was fabricated using a polyimide/aluminum surface micromachine technique and the movement of the floating element was detected using a differential capacitive scheme. The sensor was designed to have a dynamic range of  $0.01-1.0Pa$  and was calibrated in a laminar flow cell using dry compressed air up to a shear stress of  $1Pa$ . The sensor displayed a sensitivity of  $52\mu V / Pa$ . The achieved minimum detectable shear stress was  $0.1Pa$  with a bandwidth of  $10kHz$ . The measured response was in agreement with the design model. Polyimide was chosen as the structure material due to several advantages it held. Polyimide fabrication provided a smooth surface for the flow, its tensile residue stress helped the device to release and provided mechanical restoring forces for the floating element and it is a low temperature material that can allow the integration of electronics. Despite the advantages polyimide offered, the sensor suffered from sensitivity drift due to changes in the polymer mechanical properties caused by humidity changes in the experimental environment. Also, the sensor was sensitive to electromagnetic interference (EMI) because of the high impedance input of the sensor.

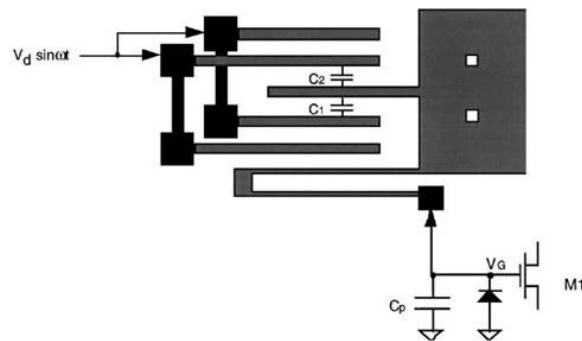
Pan *et al* [64, 65] designed, fabricated and calibrated three different

floating element sensors using a differential capacitance measuring scheme with inter-digitized fingers. For both the first and second designs, the floating elements were suspended by folded beams instead of the simple four-beam suspensions used by Schmidt [85]. The advantages of the folded beams over the simple four-beam suspensions are that they relieve the internal residue stresses of the structure and are more flexible, thus providing higher sensitivity for the device. In their first design, the electrodes for detecting the sensing signal were fabricated on a chip but no amplification was applied. The capacitance changes of the device under flow were only on the order of several femto-farads, which was too weak to overcome the noise introduced by external measurement equipment and parasitic capacitances. This floating element was measured optically with 500 magnifications. The sensitivity of the devices was measured to be  $0.11\mu\text{m}/\text{Pa}$  for the  $100\mu\text{m}$ -beam device which had resonant frequencies of  $16\text{kHz}$ , and  $0.18\mu\text{m}/\text{Pa}$  for the  $120\mu\text{m}$ -beam device with resonant frequencies of  $11\text{kHz}$ . Their second design includes the monolithic integrated NMOS differential amplifier circuit. The tested voltage output is in a non-linear relationship with shear stress change which is in agreement with the predicted sensitivity. Figure 4.4 shows a schematic representation of the second design of the force-feedback floating element by Pan *et al.* Their third design of shear stress sensor was achieved by modifying an existing commercial accelerometer. The

accelerometer proof-mass element was replaced with a floating element that was sensitive to shear stress. On-chip circuitry provided force-feedback operations for the sensors. These devices demonstrated a high sensitivity of  $1.02V/Pa$  with a dynamic range of  $0.5-3.8Pa$ .



(a) Schematic plan-view of second generation floating element



(b) Schematic illustration of the sense capacitors of shear stress sensors

**Figure 4.4 Schematic representation of second generation floating element by Pan *et al* [65]**

Zhe *et al* [86] developed a floating element shear stress sensor based on a cantilever-beam-like structure using a differential sensing scheme as shown in Figure 4.5. The beam was designed to have a high thickness/width ratio to make the floating element sensitive to shear stress but insensitive to the pressure. The sensor was fabricated on an ultra-thin  $50\mu m$  silicon wafer using wafer bonding and deep-reactive ion etching (DRIE) techniques. The sensor consisted of two sensing electrodes, two actuation electrodes, a floating element with dimensions of  $200\mu m$  in width and  $500\mu m$  in length and a cantilever beam  $3mm$  long. The deflection of the cantilever beam caused by shear stress changed the capacitance detected using a commercial differential capacitance measurement chip called *MS3110* Universal Capacitive Readout IC. The sensor was tested in a controlled laminar flow channel. The reported sensitivity is  $337mV/Pa$ . The sensor can detect stress as low as  $0.04Pa$  with an accuracy of  $8\%$  up to  $0.2Pa$ .

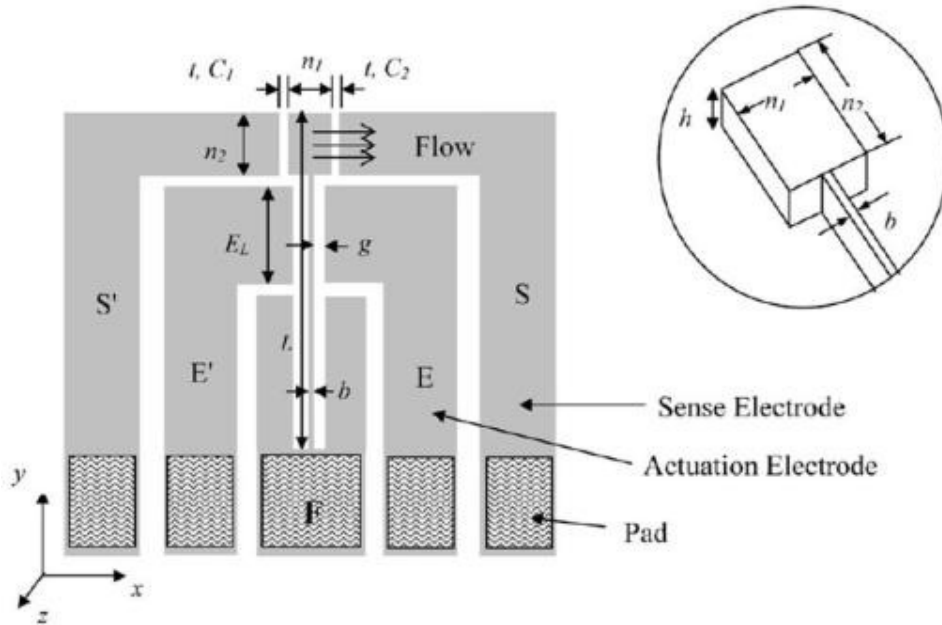


Figure 4.5 Schematic top view of capacitive floating element.

The inset shows 3D floating element [86]

### Piezoresistive Shear Stress Sensors

Ng *et al* [87] extended Schmidt's work [85] to make a floating element using the piezoresistive transduction scheme. This design had a wide dynamic range from  $1kPa$  to  $100kPa$  which is intended to be used in fluid environments. The sensor consisted of a rectangular floating element measuring  $120\mu m$  by  $140\mu m$  and four tethers that were  $10\mu m$  by  $30\mu m$ , as shown in Figure 4.6. When a shear stress acted on the sensor, the floating element was displaced and it moved the tethers in the flow direction which caused a change of resistance in the sensor due to the piezoresistive properties of the doped silicon. Two tethers experienced compressive stress and the other two experienced tensile stress. The two

compressed tethers and two elongated tethers were connected into a half bridge configuration which converted the shear stress to an electrical output. The symmetrical structure and electrical configuration made the sensor insensitive to non-axial flows because both of the half bridge resistors experienced the same change. The device was also intended to be able to sustain high pressures up to  $6000\text{psi}$  and temperatures on the order of  $300^\circ\text{C}$ . The device was tested in pressures up to  $5000\text{psi}$  and temperatures up to  $220^\circ\text{C}$  without suffering any mechanical degradation. The reported sensitivity is  $13.7\mu\text{V}/\text{V}-\text{kPa}$ .

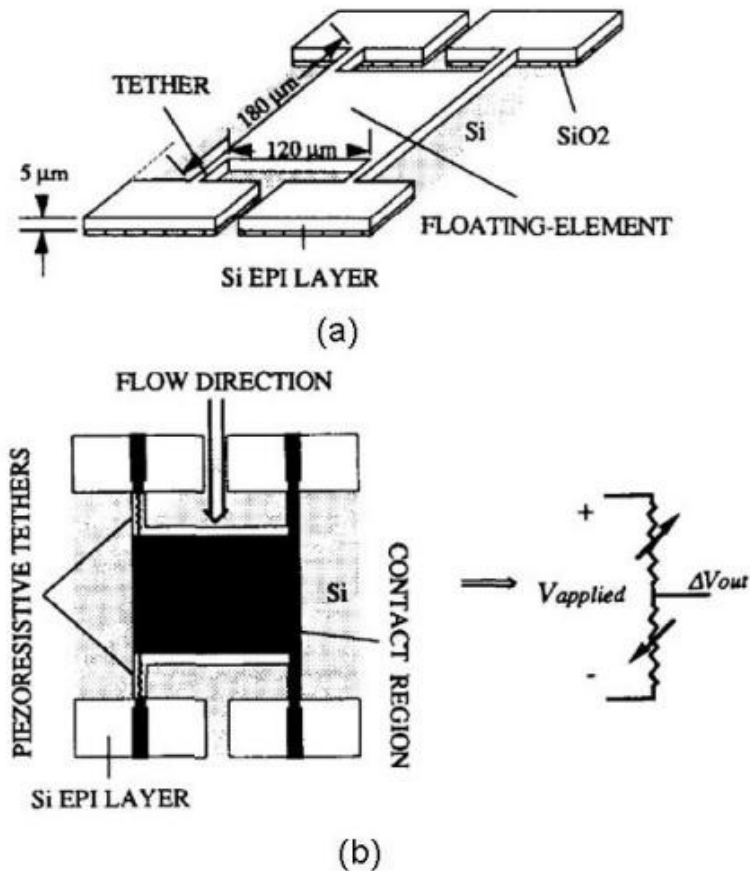


Figure 4.6 Piezoresistive shear stress sensor developed by Ng *et al* [87]

(a) Schematic view of floating element

(b) Schematic top view of the floating element and the electrical readout configuration

Barlian *et al* [88] developed a piezoresistive shear stress sensor for the direct measurement of shear stress underwater. The sidewall-implanted piezoresistors measured the lateral integrated shear force, and the top-implanted piezoresistors measured normal pressure. A variety of sensors were designed with different geometries of the floating elements and tethers and different gap sizes. A nominal designed sensor with a floating element of  $500\mu m$  by  $500\mu m$  and a  $10\mu m$  tether width and thickness was tested. The sensor was calibrated using a microfabricated piezoresistive silicon cantilever force sensor. The displacement of the floating element was detected using a Wheatstone bridge. When a shear force was applied to the floating element by the cantilever force sensor, the output voltage was recorded. The same experiment was repeated five times to show the trend and repeatability of the five sequential measurements of the shear stress sensor. The experimental measurements indicated the in-plane force sensitivity was in the range of  $0.052 \pm 0.011 mV / Pa$  , compared with the predicted sensitivity of  $0.068 mV / Pa$  . The detected out-of-plane normal stress sensitivity is  $0.001 mV / Pa$  indicating low sensitivity to off-axis loads. Dynamic analysis was realized by mounting the sensor on a micro-slide and driven in out-of-plane motion by a piezoelectric shaker with a frequency sweep from  $500 Hz$  to  $50 kHz$  . The out-of-plane velocity was detected using a laser Doppler vibrometer. The resonant frequency was found to be

18.2kHz , higher than the predicted 13.4kHz . The sensitivity of the top-implanted piezoresistor to normal force was 0.04mV / Pa .

Li *et al* [89] presented a sensor structure which integrates laterally-implanted diffused piezoresistors into the sidewall of the sensor tethers for detecting the floating element deflection via a strain-induced resistance change. The sensor was optimally designed using a nonlinear electromechanical model. Preliminary experimental characterization indicates a sensitivity of 4.24 $\mu$ V / Pa and a noise floor of 11.4  $\frac{mPa}{\sqrt{Hz}}$  (for a 1Hz bin centered at 1kHz) for a bias voltage of 1.5V . The tested device is linear up to the maximum testing range of 2Pa and possesses a flat dynamic response up to the frequency testing limit of 6.7kHz .

## Optical Shear Stress Sensors

Padmanabhan *et al.* developed two generations of floating element shear stress sensors using an optical sensing scheme [90, 91]. Two geometries were designed and fabricated. One was a 500 $\mu$ m by 500 $\mu$ m square floating element with a thickness of 7 $\mu$ m , and the other was a 120 $\mu$ m by 120 $\mu$ m square floating element with a thickness of 7 $\mu$ m . The floating element was fabricated using wafer-bonding technology. The first generation sensor is shown in Figure 4.7. A pair of photodiodes was located under the floating element on the leading and trailing edges. The

sensor was under uniform illumination from a laser source. When no flow passed the floating element, the exposed areas of the two photodiodes were the same and produced zero differential photocurrent. When subjected to a shear flow, the displacement of the floating element changed the exposed area of the photodiodes and thus produced finite differential photocurrent. The  $500\mu\text{m}$  by  $500\mu\text{m}$  floating element sensor was tested in a laminar flow cell and in a low-turbulent wind tunnel. Both tests resulted in the same sensitivity of  $0.3\text{V}/\text{Pa}$  (measured from sensitivity plot [90]) with a minimum detectable shear stress of  $0.01\text{Pa}$ .

The second generation sensor addressed the issue encountered in the first generation sensor which was the sensitivity to intensity variations across the floating element. The second generation design was improved by using a split diode scheme which reduced the sensitivity to intensity variation by  $40\text{dB}$ . The second generation sensor was subjected to dynamic measurement and the dynamic response of the sensor was quantified up to the characterization limit of  $4\text{kHz}$ . The dynamic range of the sensor is from  $1.4\text{Pa}$  to  $10\text{Pa}$ . The lowest measurable shear stress of  $0.0014\text{Pa}$  was three orders smaller than  $0.1\text{Pa}$  reported in [85]. The sensor showed very good repeatability and minimal drift. Furthermore, the sensor was insensitive to EMI and stray charging compared to the capacitive detection scheme. The main drawback to this sensor was the

remote mounting of the incident light source from the sensor which resulted in sensitivity to any mechanical movement of the light source relative to the sensor.

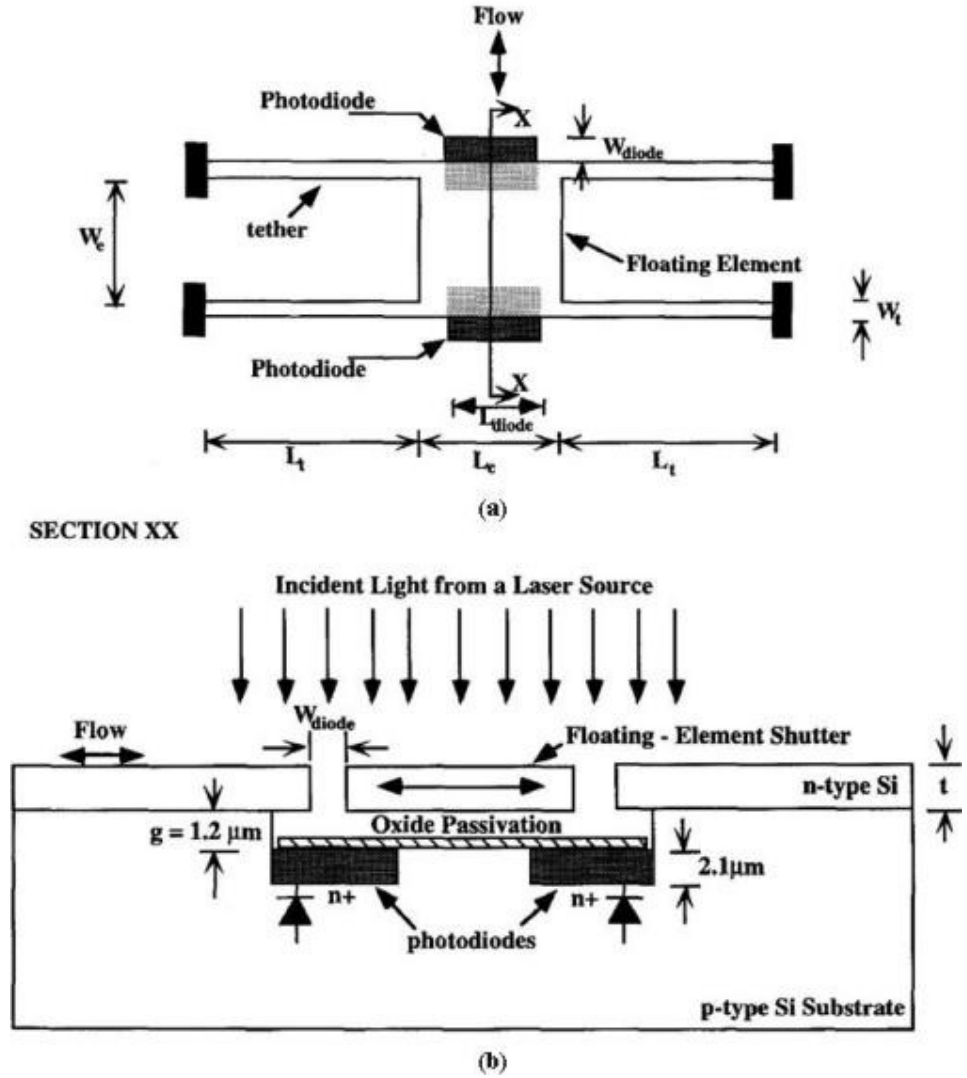
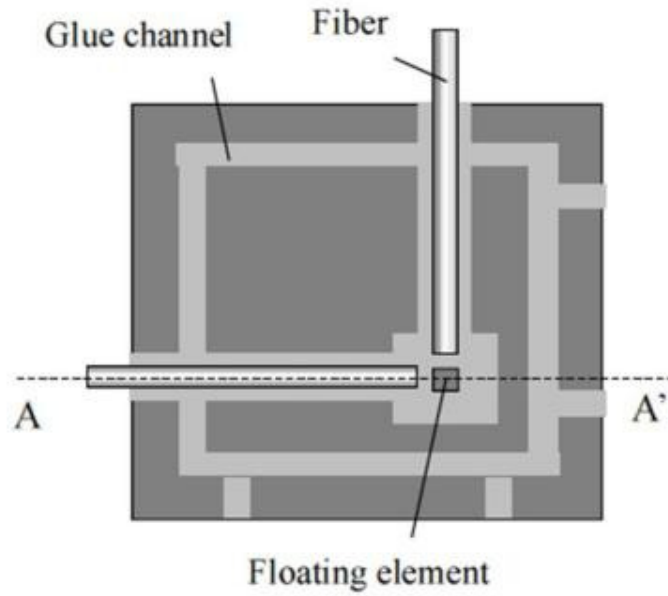


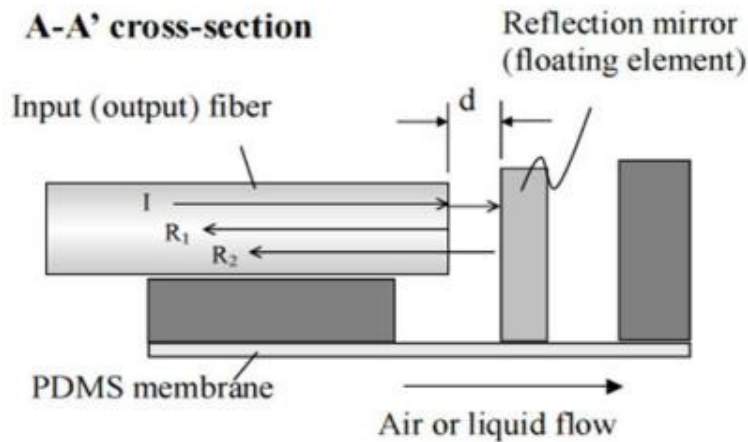
Figure 4.7 Optical shear stress sensor by [90] (a) Schematic top-view of floating element (b) Schematic side-view of the floating element shows sensing principle

Tseng and Lin reported a novel optical shear stress sensor using a flexible membrane and SUS polymer and optical fibers [92]. The flexible membrane made of silicone rubber served as protection to the inner

sensing parts and a support to the floating element displacement measurement, enabling sensor measurement for both air and liquid environments. A double SU8 resist fabricated using UV lithography served as a floating element ( $200\mu m$  by  $200\mu m$  square with a height of  $400\mu m$ ) with Au coating on one of the side-walls used as a moving micro-micro. The structure and sensing scheme of this sensor is shown in Figure 4.8. The displacement of the floating element induced by the wall shear stress on the flexible membrane was detected via an optical fiber using a Fabry-Perot interferometer. Static calibration tests in laminar flow showed the sensitivity of the sensor is  $0.65Pa/nm$  with a resolution minimum detectable shear stress of  $0.065Pa$ . This sensor was immune to EMI but had a high noise level of  $2-3nm$ .



(a)



(b)

**Figure 4.8 Optical shear stress by [92] (a) Schematic top-view  
(b) Schematic cross-section-view of the floating element shows sensing principle**

Chen *et al* [93] developed a floating-element shear stress sensor based on the geometric Moire interferometer. The sensor consisted of a silicon floating element suspended by four tethers on a silicon support structure

which is bonded to a Pyrex support structure. Two sets of aluminum optical gratings were fabricated on both the floating element and the Pyrex structure. Each set of gratings had a slightly different pitch that resulted in a Moire fringe pattern as illustrated in Figure 4.9.

When the floating element displaced under the influence of a shear flow, the displacement of the aluminum grating on the floating element changed the Moire fringe pattern, which in turn can be used to determine the displacement of the floating element and shear stress that caused the displacement of the floating element. In this paper, a design of the Moire amplification which is determined by the Moire fringe pattern spatial period  $G$  over the pitch  $g_2$  of the gratings on the Pyrex support structure was set to be 100. The sensor was calibrated in a laminar flow cell. A digital camera was used in the experiment to capture the Moire fringe pattern through a microscope. Under  $5Pa$  shear stress, a  $2kHz$  shear stress yielded a sensitivity of  $59nm/Pa$  in the laminar flow. Though the Moire transduction scheme can amplify the mechanical motion in the floating element and effectively increase the sensitivity of the sensor. Like other optical sensing technology, the size of the optical package is typically bulky and inappropriate for anything but benchtop measurements.

This research attempted to minimize the size of the optical components to enable shear stress measurements for practical applications. To realize

this goal, the microscope was replaced by optical fibers. The optical fibers not only enabled the fibers to be attached directly to the Moire sensor but also enabled the optoelectronic components to be located remotely from the sensor. Figure 4.10 shows an overview of the optical setup using the fiber bundle configuration and photographs of the fiber sensor. This minimized optical configuration was tested using an optical test-bed. The shear stress sensor was derived by a nano-positioner controller and the Moire fringe pattern was recorded at several nano-positioner displacements. The computed Moire amplification from the experimental data was 91-93 using different mathematical models, compared with theoretical amplification of 100.

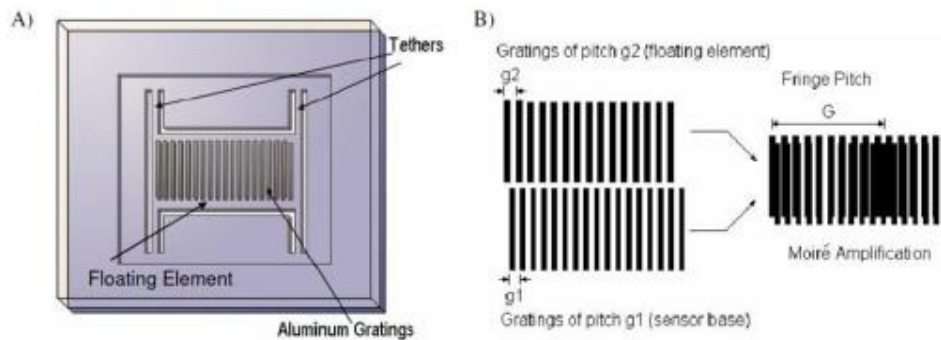


**Figure 4.9 Optical Moireshear stress sensor and sensing scheme [93]**

**(A) Schematic top-view of the sensor (B) Graphical illustration of Moire effect**

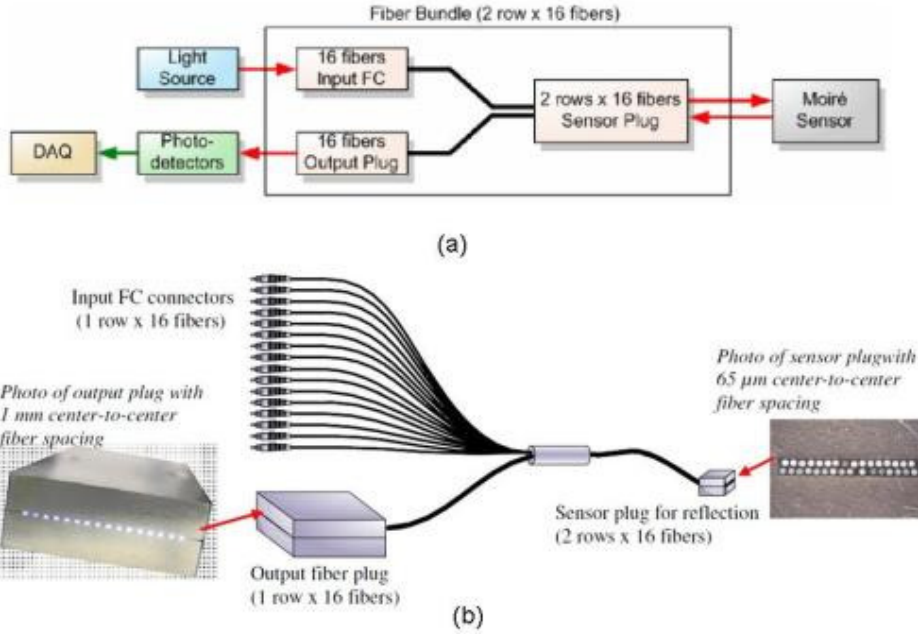


**Figure 4.10 Photographs of the fiber configuration at the sensor plug and drawing of the optical fiber bundle [93]**

A whispering gallery modes (WGM) optical sensing technology was used to detect wall shear stress by Ayaz *et al* [94]. This sensor consisted of a microsphere made of PDMS, a silica beam which acted as a lever and a flat plate that served as the sensing surface. Schematic views of the sensor are shown in Figure 4.11 A shear sensor using WGM optical sensing technology [94]. When a shear flow passed by the sensor, the sensing surface was displaced, causing the silica beam to rotate about the pivot. A flat plate was attached to the beam to suppress the PDMS sphere. The shear stress transmitted from the flow to the sphere deformed the sphere slightly, causing a shift in the WGM in the sphere.

The sensor was static calibrated using a cantilever beam mounted on a

micro-translational stage. The other end of the cantilever beam was in contact with the sensing surface. The moving of the stage exerted force through the beam. The force acted on the sensor was computed using beam theory. The sensitivity of the sensor with harder PDMS (base to curing agent mixing ratio 40:1) sphere of diameter  $700\mu m$  is  $15pm/Pa$ ; the sensitivity of the sensor with softer PDMS (base to curing agent mixing ratio 60:1) sphere of diameter  $750\mu m$  is  $231pm/Pa$ . The dynamic range of the sensor with PDMS (base to curing agent mixing ratio 60:1) sphere of diameter  $900\mu m$  was larger than  $100dB$ . The frequency range for softer PDMS material (base to curing agent mixing ratio 60:1) was up to  $3.5kHz$ , but was only less than  $300Hz$  for harder PDMS (base to curing agent mixing ratio 40:1). The calibrated sensor was tested in a 2-D Poiseuille's flow and the results validated the static calibration.

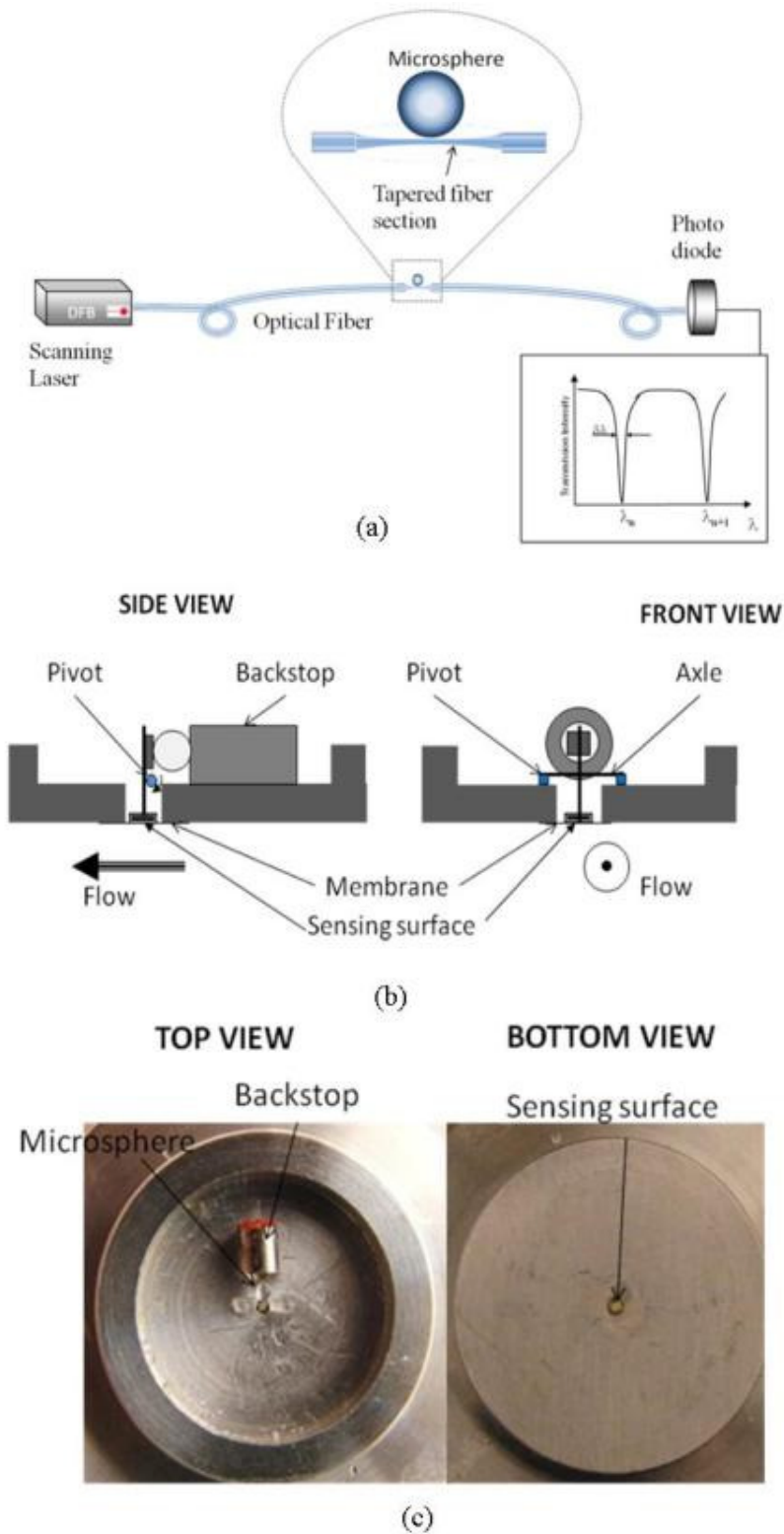


Figure 4.11 A shear sensor using WGM optical sensing technology [94]

Table 4.1 Summary of direct shear stress measurement MEMS sensors

Author	Sensing Scheme	Sensor Dimensions	Sensitivity
Schmidt [85] 1988	Capacitive	$500\mu m \times 500\mu m$ Floating element	$52\mu V / Pa$
Pan [64, 65] 1999	Capacitive	$100\mu m \times 100\mu m$ Floating element	$1.02V / Pa$
Zhe [86] 2005	Capacitive	$500\mu m \times 200\mu m$ Floating element	$337mV / Pa$
Ng [87] 1991	Piezoresistive	$120\mu m \times 140\mu m$ Floating element	$13.7\mu V / V - kPa$
Barlian [88] 2007	Piezoresistive	$500\mu m \times 500\mu m$ Floating element	$0.052 \pm 0.011mV / Pa$
Li [89] 2008	Piezoresistive	$150\mu m \times 150\mu m$ Floating element	$4.24\mu V / Pa$
Padmanabhan [90, 91] 1996, 1997	Optical	$500\mu m \times 500\mu m$ Floating element	$0.3V / Pa$
Tseng [92] 2003	Optical	$200\mu m \times 200\mu m$ Floating element	$0.65Pa / nm$
Chen [93] 2003	Optical	$1000\mu m \times 1500\mu m$ Floating element with $9.9\mu m$ and $10\mu m$ in pitch	$59nm / Pa$
Ayaz [94] 2011	Optical	$700\mu m$ in diameter Sphere	mixing ratio 40:1 $15pm / Pa$ mixing ratio 60:1 $231pm / Pa$

### 4.3.2.2 Indirect Shear Stress Measurements

An indirect method of measurement relies on the measurement of another parameter such as temperature or pressure and the correlation of that parameter to the shear stress. In this section, we will discuss in detail each technique's operating principles and shear stress sensors that have been reported over the years.

#### Thermal Shear Stress Sensors

Thermal shear stress sensors operate on heat transfer principles which transduce temperature measured to voltage. A typical thermal sensor consists of a thin-film sensing element which is comprised of a material possessing desirable temperature-resistance characteristics flush mounted on the surface. When the shear flow passes by a thermal sensor, the sensing element is resistively heated to a temperature greater than the fluid temperature defined by the non-dimensional thermal overheat ratio

$$\alpha_T = \frac{T_s - T_f}{T_f} = \frac{\Delta T}{T_f} \quad (4.4)$$

where  $T_s$  is the absolute sensor temperature and  $T_f$  is the absolute temperature of the fluid. When the temperature of the sensor varies with changes in the flow environment due to convective heat transfer, the sensor resistance changes and hence, the Joulean heating rate changes. The convection of heat from the sensor is measured by monitoring changes

in the resistance of the sensing element. The temperature-dependent resistance is approximately:

$$R_s = R_r[1 + \alpha(T_s - T_r)] \quad (4.5)$$

where  $R_s$  is the sensor resistance,  $\alpha$  is the thermal coefficient of resistance,  $T_s$  is the sensor temperature and  $T_r$  is a reference temperature corresponding to a sensor reference resistance  $R_r$ . Since the thermal sensor essentially measures heat-transfer rate, a theoretical or/and empirical correlation is required to relate the Joulean heating rate to the wall shear stress [75].

One of the major drawbacks of the thermal sensor is the reduction in sensitivity and complications in the dynamic response due to frequency-dependent conductive heat transfer into the substrate.

Ho and Thai and their co-workers developed a novel polysilicon-based sensor on a silicon nitride membrane over a vacuum cavity designed to reduce conductive heat lost to the substrate [95-97]. Figure 4.12 shows a schematic view of a typical thermal shear stress sensor [97]. In this design, the heating and heat-sensing element was a phosphorous-doped polysilicon resistor  $2\mu m$  wide and  $0.45\mu m$  thick. The resistors' length varied from  $20-200\mu m$  in different designs. The resistor was located at the center of a cavity diaphragm, which is  $200\mu m$  by  $200\mu m$  square. The thickness of the vacuum cavity is  $2\mu m$ . The sensor was calibrated within a wind tunnel using three different driving modes: CC (constant

current), CV (constant voltage) and CT (constant temperature) for a shear stress range of  $0-1.0 Pa$ . The response curves agree with theoretical analysis well. CT mode operations showed highest shear-stress sensitivity and fastest frequency response. When compensated by a custom-built constant current circuit, the entire sensing system demonstrated a sensitivity of  $15 mV / Pa$ .

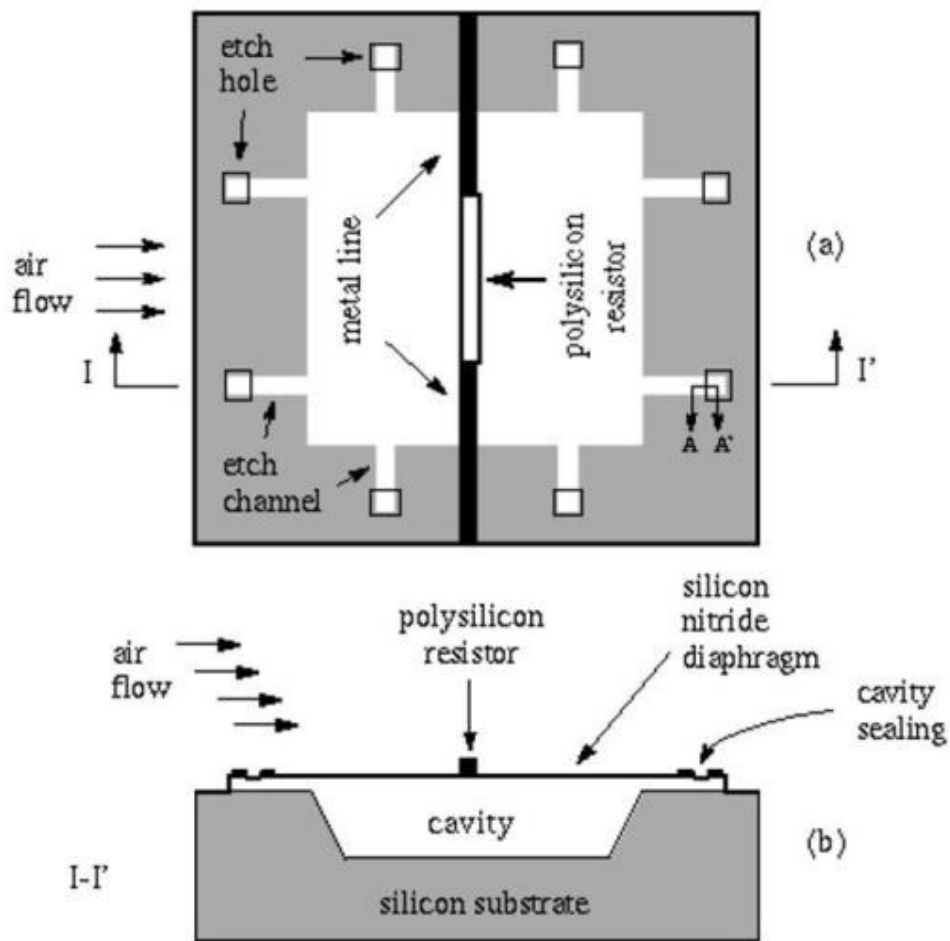


Figure 4.12 Schematic view of a thermal shear-stress sensor

(a) top-view (b) side-view [97]

The vacuum cavity sensor design was later incorporated into a novel

flexible skin sensor array process that allows for shear stress measurement on a curved surface. Jiang *et al* [98, 99] invented a flexible skin technology that is compatible with both IC and MEMS fabrications. The flexible skin technology involves creating many individual silicon islands used as MEMS electronic devices which are connected together by polyimide film. The thermal shear stress sensor was made on silicon substrate. After the sensor was successfully fabricated, silicon substrate was wet etched from the backside to form a thin diaphragm, then a RIE (reactive ion etching) etching creates silicon islands.

Each silicon island is an individual thermal shear stress sensor. Silicon islands were sandwiched between  $7\mu m$  thick polyimide on the front side of the silicon and  $10\mu m$  thick polyimide on the backside of the silicon. Figure 4.13 shows a photograph of a flexible skin shear stress sensor array wrapped around a semi-cylindrical block. The sensor was calibrated within a wind tunnel. The sensors on the flexible skin have been found to behave the same as those on a rigid substrate. When driven in CT mode, the sensitivity is about  $100mV / Pa$  with an overheat ratio of 10%.

The flexible skin sensors array was also used to detect the separation-point in a flow. Data for flow over a circular cylinder show that the separation-point position was exactly in agreement with documented results. The flexible sensor array was also used to detect instantaneous separation lines on the leading edges of a delta wing. For

the first time the shear-stress distribution along the rounded leading edges of a delta wing was successfully measured by the flexible sensor array.

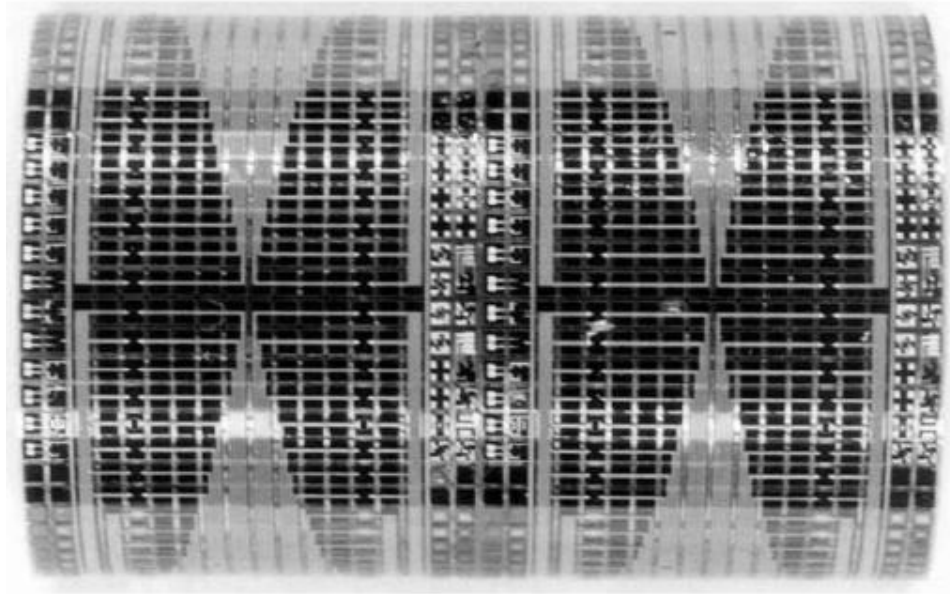


**Figure 4.13 Photograph of flexible skin shear stress sensor array wrapped around a semi-cylindrical block [99]**

Kalvesten *et al* [100] developed a novel surface micromachined thermal shear stress sensor. The sensor consisted of a  $6\text{mm} \times 4\text{mm} \times 0.5\text{mm}$  substrate chip with a  $1.5\text{mm} \times 1.5\text{mm} \times 0.03\text{mm}$  membrane where the active part of the shear sensor, a  $300\mu\text{m} \times 60\mu\text{m} \times 30\mu\text{m}$  heated chip, was located. The chip was electrically heated by a polysilicon resistor and thermally insulated by polyimide filled KOH-etched trenches in the membrane. Two diodes were integrated to measure temperatures. One diode was located near the heated chip to measure the sensor temperature. The other diode was located at the edge of the substrate to

measure the temperature of the flow. Power was supplied to the heater in order to maintain the chosen temperature difference between the sensor and the fluid. A Pitot tube and a Clauser plot were used to determine the time-averaged wall shear stress and the power that was provided to maintain the sensor at a constant temperature was measured. The wall shear stress fluctuations were tested in a wind tunnel for a frequency range from  $10\text{Hz}$  to  $10\text{kHz}$ . The power spectra of wall shear stress fluctuations of the turbulent boundary layer at free stream velocities of 0 and  $40\text{m/s}$  were reported.

Sheplak *et al* [101] reported an extensive characterization of a silicon micromachined thermal shear stress sensor. The sensor consisted of a  $200\mu\text{m}\times 4\mu\text{m}\times 0.15\mu\text{m}$  platinum heating/sensing element on top of a  $0.15\mu\text{m}$  thick silicon nitride membrane. A vacuum cavity with a  $200\mu\text{m}$  diameter and a  $10\mu\text{m}$  depth prevented heat transfer to the substrate. The reasons these researchers chose platinum-based sensors over polysilicon-based sensors are the higher thermal coefficient of resistance, higher thermal operating range, lower impedance, reduced  $1/f$  noise, and no piezoresistive-induced pressure sensitivity the platinum has compared to polysilicon.

The sensor was operated in a constant current (CC) mode and characterized using a four-point probe configuration in order to isolate the sensor response from the effects of external compensating circuitry.

Static sensor calibration was performed in two different environments at various overheat ratios, in a plane wave tube which provided the maximum mean shear stress of  $0.08Pa$  and in a laminar flow channel which provided the maximum mean shear stress of  $1.7Pa$ . The maximum sensitivity was  $11mV/Pa$  at an overheat ratio of 1. The sensor pressure sensitivity was measured to be negligible. The dynamic response was measured up to  $7kHz$ . Noise floor measurement indicated a minimum detectable shear stress of  $9\mu Pa/Hz$ , resulting in a sensor dynamic range over  $100dB$ .

### **Micro-Pillar Shear Stress Sensors**

Grosse *et al* developed micro-pillar sensors for two dimensional shear stress measurements [72-74, 102, 103]. The sensors consisted of flexible micro-pillars manufactured from the elastomer poly-dimethylsiloxane (PDMS). The micro-pillars protruded into the viscous sublayer and were bent in reaction to the fluid flow forces. The deflections of the micro-pillars' tips were detected optically. The wall-shear stress is derived from the relation between the detected velocity gradient in the viscous sublayer and the local surface friction. A single pillar and pillar array are shown in Figure 4.14.

The symmetric geometry of the micro-pillars, which had no preferred

sensitivity direction allowed two-dimensional measurement of shear stresses. The static sensor calibration was performed in a plate-cone rheometer. A plate-cone rheometer was chosen because such devices can generate a plane linear shear flow with a constant shear rate over a sufficiently wide spatial region and velocity range such that the drag force distribution exerted on the sensor structure is identical to that in the viscous sublayer of a turbulent boundary layer.

The sensitivity of the sensor was expressed as the ratio of pillar tip deflection under fluid forces over the pillar length. In linear pillar deflection range the sensitivity was 0.07. The dynamic calibration was performed by magnetically exciting the micro-pillars in a fluid [103]. Since micro-pillars were made of non-magnetic material PDMS, a thin permanent magnetic layer had to be attached to the tip of the pillars in order to be excited magnetically. An electro-magnetic coil was used to excite the pillars at different frequencies.

The calibration results are in excellent agreement with the findings of a second-order analytical approximation based on experimentally determined damped Eigen-frequencies and damping coefficients. Measurements at different sensor geometries and in different fluids showed the sensor possessed a flat dynamic response up to several hundred hertz, allowing measurement of turbulent fluctuations. Turbulent measurement was conducted in a square-cross-sectioned duct

flow facility [74]. Due to the insufficient time span of the recordings, the characteristics of the turbulent flow were not possible to be investigated. However, the results demonstrated the micro-pillar sensor technique was capable of multidirectional detection of the two-dimensional wall shear stress distribution in turbulent flows. The wall shear stress distributions in both streamwise and spanwise directions were reported.

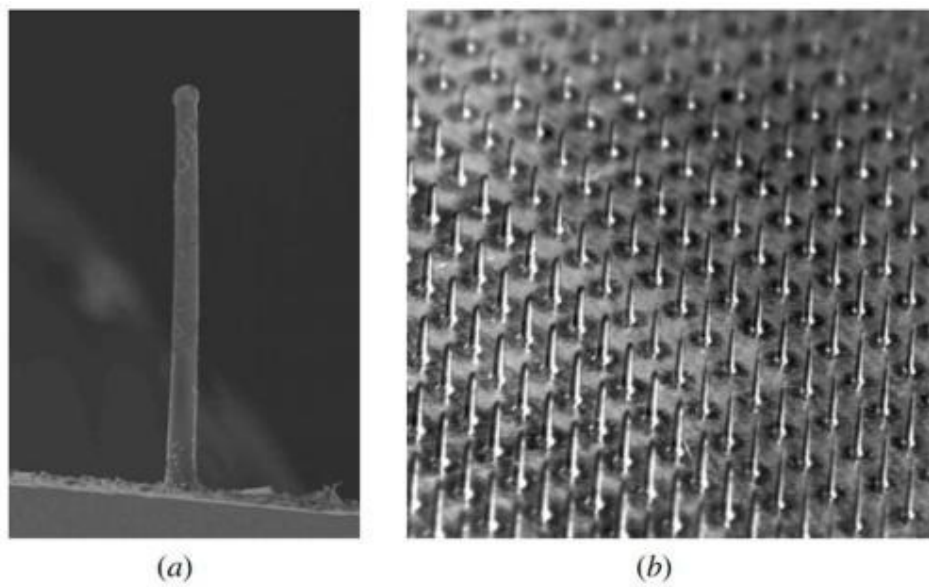


**Figure 4.14 Images of micro-pillar shear sensors by Grosse *et al* [72]**

**(a) Single hair (b) Hair array**

Liu's group used hair pillar structure sensor array to detect force generated by a flow [104-106]. In their design, carbon-impregnated polyurethane elastomer was used as force sensitive resistors. Sitting on top of the force resistors were  $3000\mu m$  tall,  $500\mu m$  in diameter polyurethane hair posts. The force sensors were bidirectional and can detect forces coming from different directions with on-axis sensitivity of

$590\mu V / \mu m$  and off-axis sensitivity of  $115\mu V / \mu m$  . Devices were successfully fabricated on rigid glass as well as flexible polyimide substrates. Figure 4.15 shows photos of the sensor array.

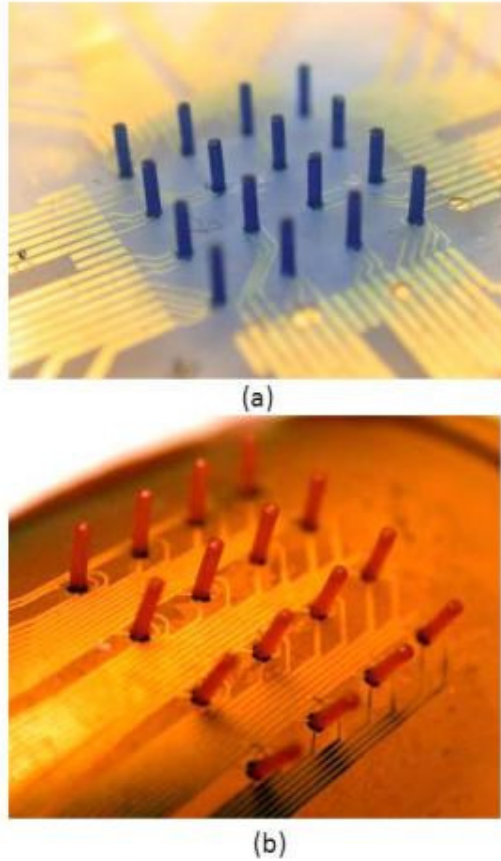


**Figure 4.15 Photos of hair-like force sensor array [105]**  
**(a) on glass substrate (b) on flexible polyimide substrate**

A summary of indirect shear stress and force measurement MEMS sensors is listed in Table 4.2.

Many shear measurement techniques are reviewed in this chapter. In the following chapter, the modeling and design of the flow sensors for aeroacoustic application will be presented.

**Table 4.2 Summary of MEMS Sensors for Indirect Shear Measurements**

<b>Author</b>	<b>Sensing Scheme</b>	<b>Sensor Dimensions</b>	<b>Sensitivity</b>
Ho [95-97] 1997-1999	Thermal	$200\mu m \times 200\mu m$ Diaphragm	$15mV / Pa$
Jiang [98, 99] 2000, 1997	Thermal	$200\mu m \times 200\mu m$ Diaphragm	$100mV / Pa$
Kalvesten [38] 1996	Thermal	$1.5mm \times 1.5mm$ Membrane with $300\mu m \times 60\mu m \times 30\mu m$ Heated chip	Power spectra of wall shear stress fluctuations of the turbulent boundary layer at free stream velocities of 0 and $40m / s$ were reported.
Sheplak [39] 2002	Thermal	$200\mu m$ diameter diaphragm $200\mu m \times 4\mu m \times 0.15\mu m$ Heating element	$11mV / Pa$
Grosse [72-74, 102, 103] 2008-2009	Micro-pillar	$260\mu m$ tall, $22\mu m$ in diameter hair array	The wall shear stress distributions in both streamwise and spanwise directions were reported.
Liu [104-106] 2005-2007	Micro-pillar	$3000\mu m$ tall, $500\mu m$ in diameter Hair array	on-axis sensitivity $590\mu V/\mu m$ and off-axis sensitivity $115\mu V/\mu m$

# Chapter 5

## MODELING and DESIGN

As mentioned in the previous chapter, MEMS sensors for flow measurements are categorized as direct and indirect measurements. To date, direct measurement technology uses a floating element to detect the flow passing from its surface. The sensor described in this dissertation is inspired by cochlea hair cell which has many stereocilia protruding from the top surface of the hair cell acting as a sensory organ. This is a direct flow measurement sensor based on hair posts sitting on top of a conductive plate. Figure 5.1 shows the schematic view of this concept.

A conductive plate on which hair posts are fabricated forms two capacitors,  $C_1$  and  $C_2$ , with two electrodes underneath it, shown in Figure 5.1(a). The top plate acts as a movable diaphragm and is separated from the bottom electrodes (fixed to a substrate) by an air gap, shown in Figure 5.1(b). The top plate is fixed by its edge to the substrate. When a flow passes by the hair posts, the shear force generated by the flow rotates the hair posts at their bases, which in turn, bend the top plate.

The top plate deflects as show in Figure 5.1(c). The deformation of the top plate changes the capacitance of the capacitors.

From Figure 5.1, the air gap in  $C_1$  increases due to the deflection of the diaphragm, resulting in a decrease of the capacitance for  $C_1$ . Air gap in  $C_2$  decreases, resulting in an increase of capacitance for  $C_2$ . The change of the capacitance is a function of shear stress generated by the flow. By measuring the change of the capacitance of the sensor, through calibration, shear stress can be determined. The sensing scheme is to measure the differential capacitance change of the sensor. The total capacitance change for the sensor is  $\Delta C_2 - \Delta C_1$ . When two electrodes are placed symmetrically about the center of the sensor, two features can be realized: (1) the sensitivity is doubled by measuring differential capacitance change compared with using only one capacitor, and (2) it can also filter out the capacitance change induced by the pressure on the sensor.

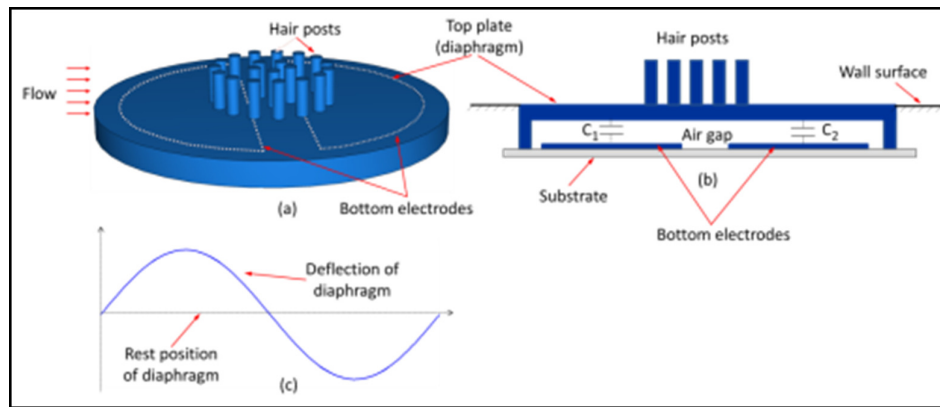


**Figure 5.1 Schematic of hair-like sensor**

**(a) Structure of hair-like shear sensor (b) Parallel plates act as a capacitor**

**(c) Deflection of op plate of the sensor due to the bending of the hair posts**

Two capacitors can detect one directional flow using the differential capacitance sensing scheme. Four capacitors, if placed symmetrically, can detect bidirectional flows. This concept is shown in Figure 5.2. The capacitor formed between the diaphragm and top electrode as well as the capacitor formed between the diaphragm and bottom electrode can sense vertical flow. Similarly, capacitors formed between the diaphragm and left and right electrodes can sense horizontal flow. This sensing scheme allows detecting two dimensional flows with one sensor. The sensor designed in this dissertation takes advantage of both these features and is used for bidirectional flow testing.

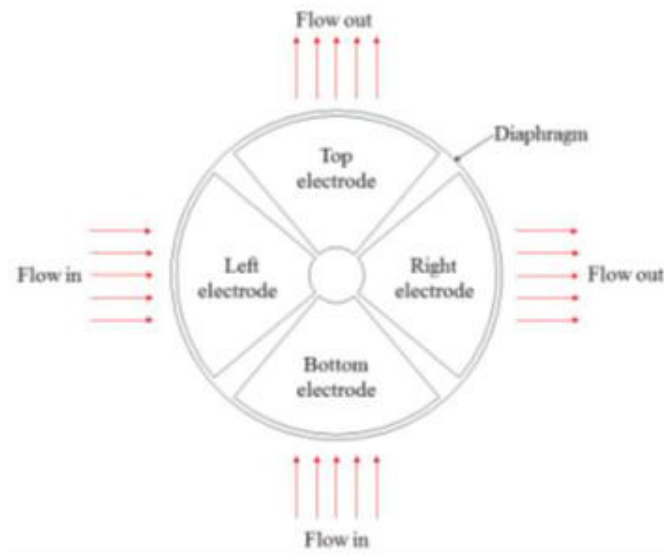


**Figure 5.2 Concept of bidirectional flow sensor**

In this chapter, we start with an analytical plate modeling which simulates the diaphragm deflection under a point moment load caused by

the rotation of a hair post. The computation result is verified by a finite element plate model. The following section uses the plate model to find the best locations to place hair posts. Knowing the best locations for hair posts, the sensor layout is determined. The sensor will be tested in a laminar flow cell. In section 5.4 the design of the flow cell is presented. Then a fluid and a structural FEA model are used to predict the sensitivity of the sensor. The models are described and results are discussed. The last section of this chapter focuses on the electronics that are used for sensor characterization.

## **5.1 Plate Modeling**

Analytical and numerical methods are implemented to simulate the hair sensor performance for flow measurements. This section describes the plate models used to compute the deflection of diaphragm.

### **5.1.1 Analytical Kirchoff Plate Model**

A Kirchoff thin plate model (thickness of the plate is smaller than 1/10 of plate diameter) is used to simulate the diaphragm deflection under a point moment load that is generated by a hair post. A Mindlin plate model, which takes into account of first-order shear strain, is created in a finite element analysis (FEA) commercial package Comsol<sup>®</sup>. The FEA

Mindlin plate model results are compared with the analytical Kirchoff plate model. The comparison can testify if a Kirchoff plate model is sufficient for the analysis and demonstrate how much shear strain is present in the deformed plate.

The governing differential equation for a flat thin circular plate is

$$\frac{d^4 w}{dr^4} + \frac{2}{r} \frac{d^3 w}{dr^3} - \frac{1}{r^2} \frac{d^2 w}{dr^2} + \frac{1}{r^3} \frac{dw}{dr} = \frac{p(r)}{D} \quad (5.1)$$

where

$$D = \frac{Eh^3}{12(1-\nu^2)} \quad (5.2)$$

is the flexural rigidity of the plate,  $p(r)$  is an applied transverse load per unit area,  $r$  is the cylindrical coordinate and  $w$  is the displacement of the plate. The displacement of the plate is axisymmetric when subject to uniform pressure or a concentrated load at the center of the plate, which is only a function of radial coordinate  $r$ . When a concentrated force is applied at a point  $A$  at a distance  $b$  from the center  $O$  of the plate, the displacement  $w$  becomes a function of both radial coordinate  $r$  and azimuthal coordinate  $\theta$ . Figure 5.3 shows the schematic of a clamped circular plate under a point force, where  $a$  is the radius of the plate.

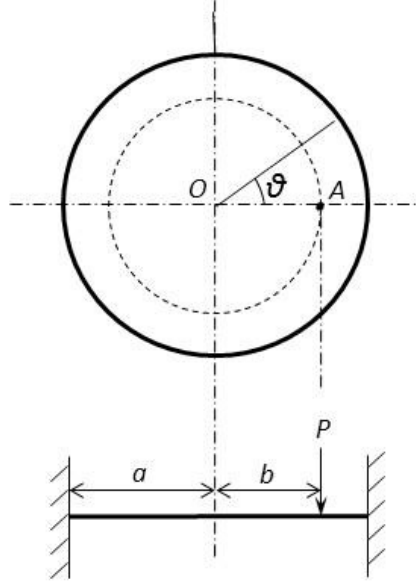


Figure 5.3 Schematic of a clamped circular plate subject to point force  $P$  at  $A$

Dividing the circular plate into two parts by the cylindrical section of radius  $b$  by the dashed line as shown in Figure 5.3, we denote the circle inside of the dashed line inner part and the donut shape outside the dashed line outer part. The displacement of the circular plate outer part is: ([107], page 260)

$$w = R_0 + \sum_{m=1}^{\infty} R_m \cos(m\theta) \quad (5.3)$$

where

$$\begin{aligned} R_0 &= A_0 + B_0 r^2 + C_0 \ln(r) + D_0 r^2 \ln(r) \\ R_1 &= A_1 r + B_1 r^3 + C_1 r^{-1} + D_1 r \ln(r) \\ &\vdots \\ &\vdots \\ &\vdots \\ R_m &= A_m r^m + B_m r^{-m} + C_m r^{m+2} + D_m r^{-m+2} \end{aligned} \quad (5.4)$$

For a clamped boundary condition, the constants in the displacement

solution are:

$$R_0 = \frac{P}{(8\pi D)} \left[ (r^2 + b^2) \ln \frac{r}{a} + \frac{(a^2 + b^2)(a^2 - r^2)}{(2a^2)} \right] \quad (5.5)$$

$$R_1 = -\frac{Pb^3}{16\pi D} \left[ \frac{1}{r} + \frac{2(a^2 - b^2)r}{a^2 b^2} - \frac{(2a^2 - b^2)r^3}{a^4 b^2} - \frac{4r}{b^2} \ln \frac{r}{a} \right] \quad (5.6)$$

$$R_m = \frac{Pb^m}{8m(m-1)\pi D} \times \left\{ \frac{r^m}{a^{2m}} \left[ (m-1)b^2 - ma^2 + (m-1)r^2 - \frac{m(m-1)}{m+1} \frac{b^2 r^2}{a^2} \right] + \frac{1}{r^m} \left( r^2 - \frac{m-1}{m+1} b^2 \right) \right\} \quad (5.7)$$

The displacement for the inner part of the circular plate has similar expressions:

$$w' = R'_0 + \sum_{m=1}^{\infty} R'_m \cos(m\theta) \quad (5.8)$$

with

$$\begin{aligned} R'_0 &= A'_0 + B'_0 r^2 + C'_0 \ln(r) + D'_0 r^2 \ln(r) \\ R'_1 &= A'_1 r + B'_1 r^3 + C'_1 r^{-1} + D'_1 r \ln(r) \\ &\vdots \\ &\vdots \\ &\vdots \\ R'_m &= A'_m r^m + B'_m r^{-m} + C'_m r^{m+2} + D'_m r^{-m+2} \end{aligned} \quad (5.9)$$

For the clamped boundary condition,

$$R'_0 = \frac{P}{(8\pi D)} \left[ (r^2 + b^2) \ln \frac{b}{a} + \frac{(a^2 + r^2)(a^2 - b^2)}{(2a^2)} \right] \quad (5.10)$$

$$R'_1 = -\frac{Pb^3}{16\pi D} \left[ \frac{2(a^2 - b^2)r}{a^2b^2} + \frac{(a^2 - b^2)^2 r^3}{a^4b^4} - \frac{4r}{b^2} \ln \frac{a}{b} \right] \quad (5.11)$$

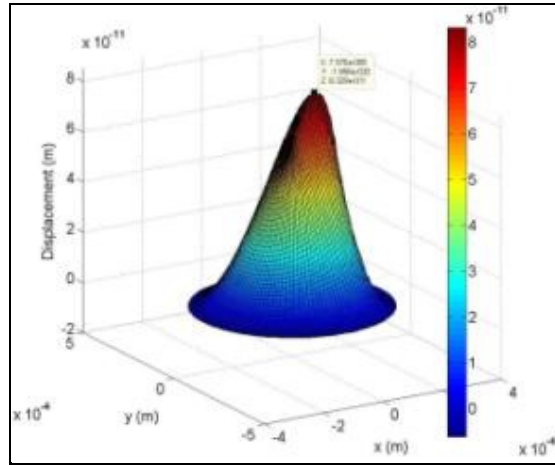
$$R'_m = \frac{Pb^m}{8m(m-1)\pi D} \times \left\{ \frac{r^m}{a^{2m}} \left[ (m-1)b^2 - ma^2 + \frac{a^{2m}}{b^{2m-2}} \right] + (m-1) \frac{r^{m+2}}{a^{2m}} \left[ 1 - \frac{m}{m+1} \frac{b^2}{a^2} - \frac{1}{m+1} \left( \frac{a}{b} \right)^{2m} \right] \right\} \quad (5.12)$$

When substituting the constants into the two displacement equations, the displacement profile of the circular plate can be computed and plotted. Using the superposition law, the displacement of the circular plate under a couple, two point forces acting in opposite directions and separated by a distance, which form a pure moment representing the moment generated by the hair post on the structure plate underneath it, can be computed. Matlab<sup>®</sup> is used to compute the analytical solution. Figure 5.4 (a) is a 3D Matlab<sup>®</sup> plot showing displacement distribution of a circular plate with a diameter of  $600\mu m$  when under a couple of  $1\mu N$ . The couple is applied at locations  $150\mu m$  and  $155\mu m$  from the center of the plate.

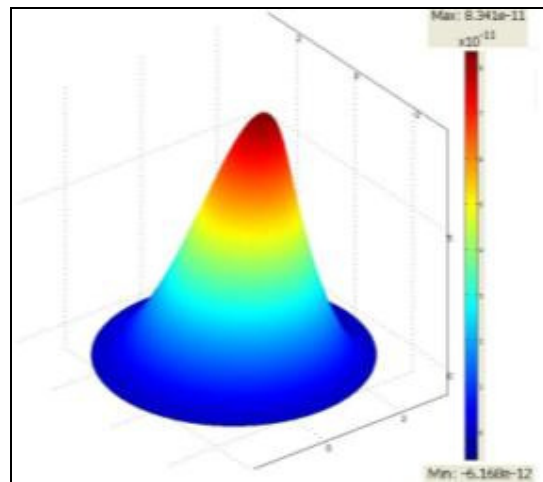
### 5.1.2 FEA Mindlin Plate Model

The Finite element analysis (FEA) and the analytical analysis can be used to validate each other. Often, an analytical analysis is necessary to

verify a finite element model (FEM) before the model is used for more complicated problems. FEA in turn can affirm an analytical result. A Mindlin plate model is created in Comsol<sup>®</sup> to compute the displacement of the plate structure under the same forces and at the same locations as those in the analytical model. The results are shown in Figure 5.4 (b). The maximum displacement is  $8.329 \times 10^{-11} m$  for the analytical solution, very close to  $8.341 \times 10^{-11} m$  computed using FEA model. The results show that a Kirchhoff thin plate model is sufficient for point moment analyses and thus used for the optimization of locations for the hair posts.



(a)



(b)

Figure 5.4 Comparison of plate deflection

(a) Analytical result computed using Matlab® (b) FEA result computed using Comsol®

## 5.2 Hair Post Location and Diameter Optimization

One of the most critical processes of MEMS device fabrication is to release the device. This is where the sacrificial layer (that eventually becomes the air gap) is chemically etched away at the final step of the

sensor fabrication and the structure is released from sacrificial material. A capacitive MEMS microphone array chip fabricated using PolyMUMPs foundry process used for turbulent boundary layer pressure measurement has been successfully fabricated and released in our research group [108]. The chips consist of 64 sensors and each sensor has a diaphragm of  $600\mu m$ . The shear sensor presented in this dissertation uses the same PolyMUMPs foundry process and the microphone diaphragm dimension for the structure plate of the shear sensor to ensure the successful release of the chip.

With the capacitor diaphragm diameter determined, the next step is to determine the locations of the hair posts on the diaphragm. The hair posts can be placed at any location on the diaphragm. A question arises: Is there a best location that the hair posts, when subjected to flow, can maximally deflect the plate, and thus produce the largest sensitivity for the sensor? Also, will the diameter of the hair posts affect the sensitivity of the sensor? In order to answer these questions, a series of simulations were carried out to compute the sensitivity of the sensor for the different sizes of hair posts placed at different locations. These simulations are carried out in Matlab<sup>®</sup> using a Kirchhoff plate model. Figure 5.5 demonstrates the optimization process.

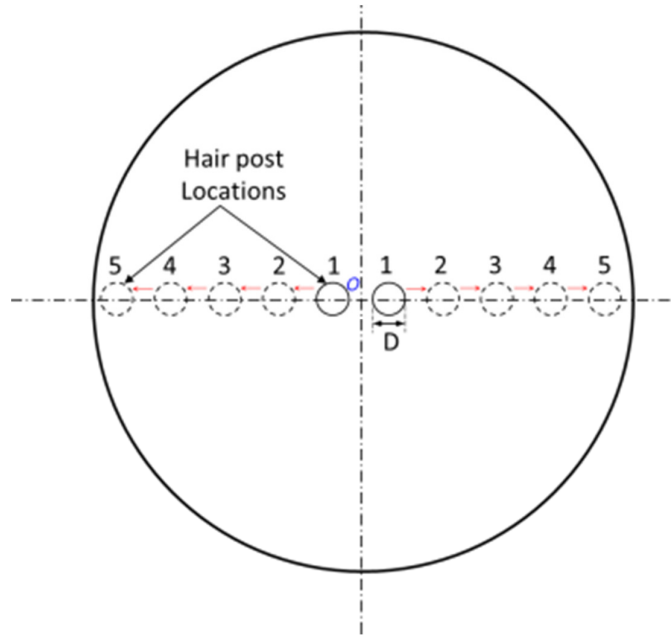


**Figure 5.5 Investigation of hair post locations**

In the optimization process, a hair post with diameter of  $D$  is placed at location 1 which is very close to the center of the diaphragm  $O$ . Another same sized post is placed at a location symmetric to the first post about  $O$ . A couple is applied to the post edge to form a bending moment. The plate deflection and the differential capacitance changes are computed for location 1. Then the post is moved to location 2, then 3, and so on, until to the edge of the plate. The differential capacitance changes are computed for every location. In addition to changing the post locations, the size of the hair posts are varied to investigate the effect of the hair post diameters on sensor sensitivity. The results are shown in Figure 5.6.

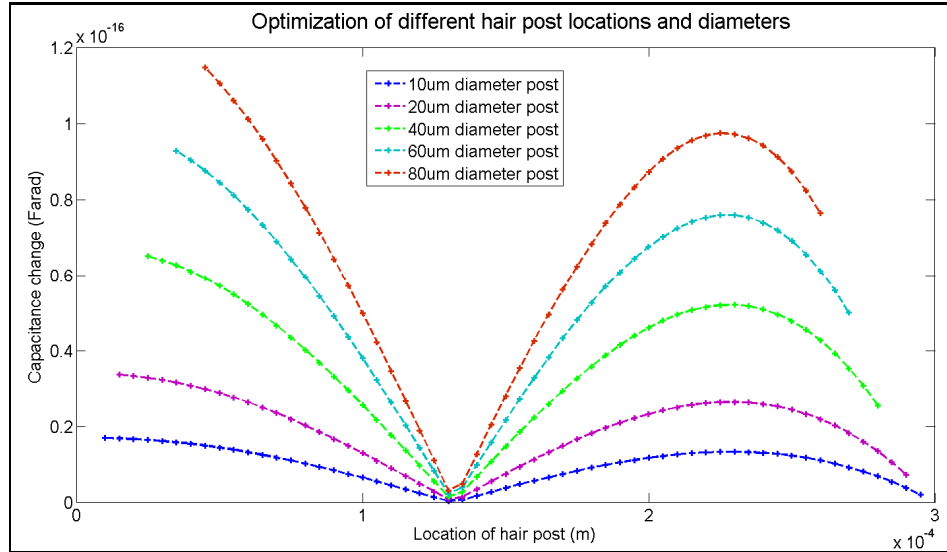


**Figure 5.6 Optimization of hair post locations and the effect of post diameter**

Figure 5.6 shows that for the same diameter hair post, when it is placed near the center of the plate, the sensor is most sensitive. The sensitivity decreases as the post moves away from the center and reaches the lowest capacitance change at  $130\mu\text{m}$  from the center. The sensitivity increases as the post moves away from this lowest capacitance change distance and reaches its second highest value at  $230\mu\text{m}$  from the center of the plate and decreases again as the post approaches to the edge of the plate. The figure also demonstrates that the larger the diameter is, the higher the sensitivity of the sensor is.

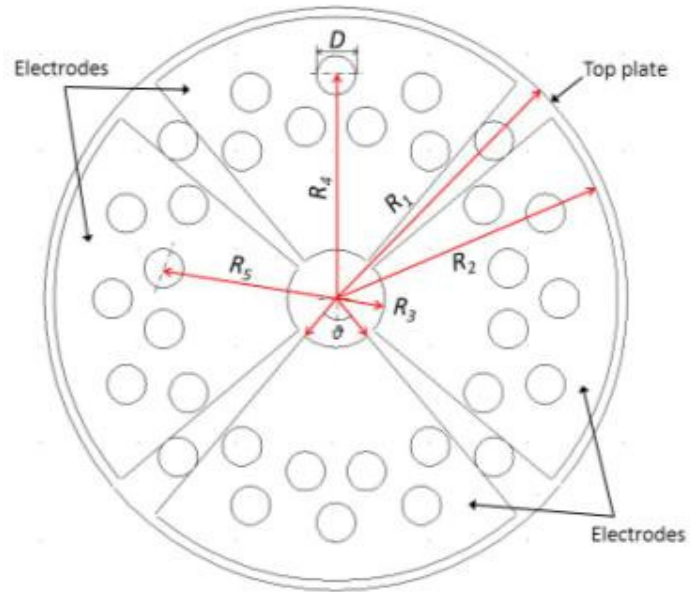
Figure 5.6 shows that the best location to place the hair post is at the center of the plate and the second best position is  $230\mu\text{m}$  away from the center. Only one hair post can be placed in the middle of the plate, but many same sized posts can be placed at a circle of radius of  $230\mu\text{m}$ . The

Matlab<sup>®</sup> script for the optimization can be found in Appendix A2.

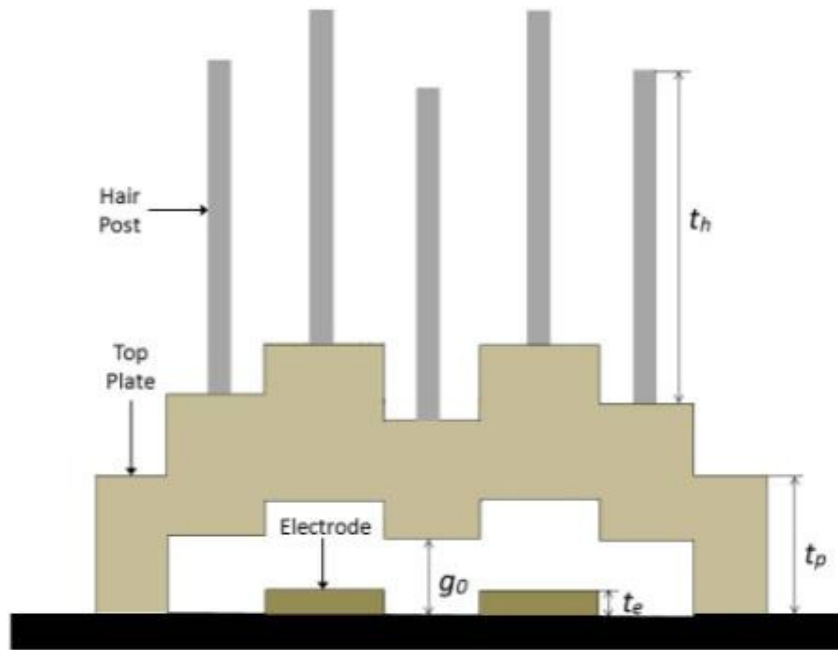
Figure 5.6 also shows that the larger the post diameter is, the larger the sensitivity of the sensor is. But the choice of the diameter of the post is also affected by the post material properties and fabrication capabilities. SU8-2025 is used to fabricate the hair posts on the sensor. The maximum thickness SU8-2025 can produce without sacrificing film uniformity is about  $80\mu m$ . An aspect ratio of two is commonly applied for SU8 structures, so the hair posts diameter of  $40\mu m$  was selected.

### **5.3 Sensor and Array Layout**

The designed hair posts layout is shown in Figure 5.7(a). 16 posts are evenly placed at the best location  $230\mu m$  from the center of the plate. Another 16 posts are placed at  $180\mu m$  from the center but each post is situated in between outside posts so that the flow can directly contact the posts without being blocked by outside posts. Figure 5.7(b) shows a side view of the sensor structure. All geometrical parameters are labeled and the values are listed in Table 5.1.



(a)

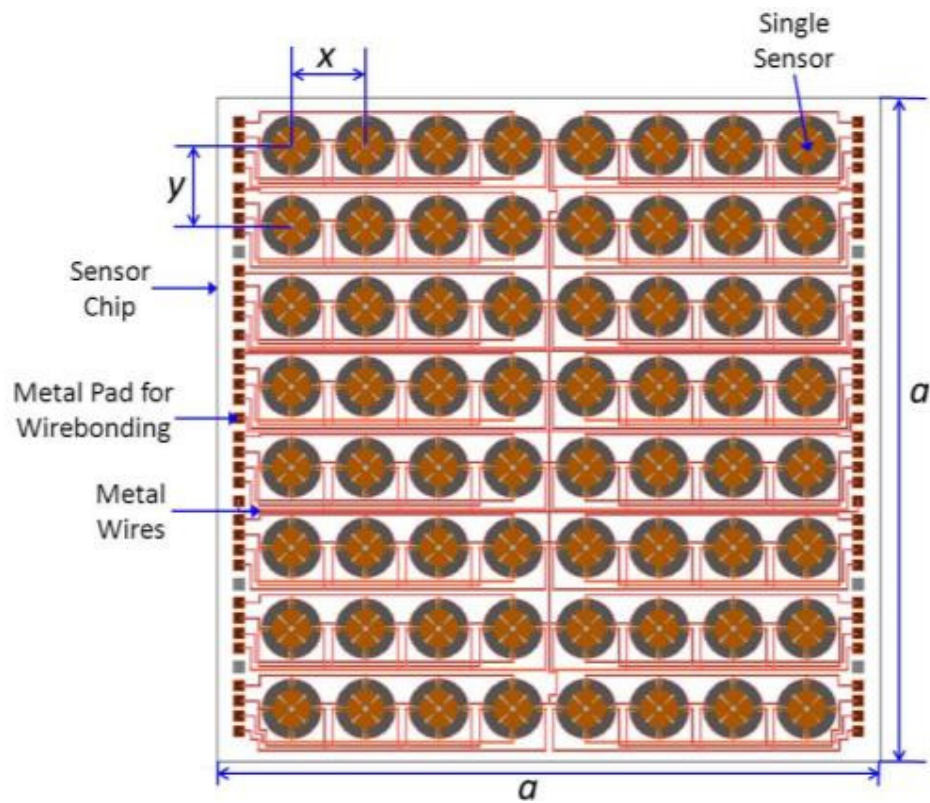


(b)

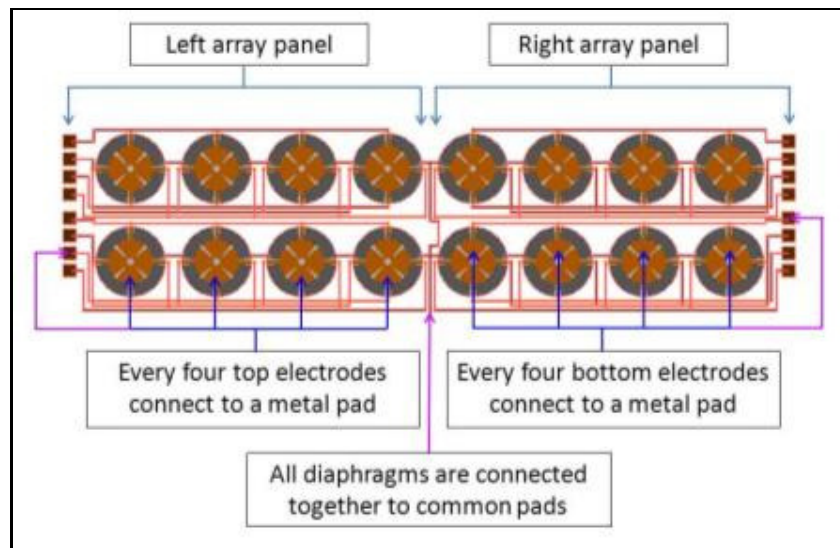
**Figure 5.7 Single hair-like sensor layout (a) Top view (b) Side view**

An  $8 \times 8$  array, total 64 sensors are fabricated on  $10.1\text{mm} \times 10.1\text{mm}$  square polysilicon chip as shown in Figure 5.8. Every four sensors in a row are

grouped together. In each group, the top electrodes from four different sensors are wired together and connected to a metal pad that is designated for wirebonding. In the same way, the bottom electrodes, left electrodes and right electrodes in each group are wired together and connected to three different metal pads. All the diaphragms of the sensors are wired together and connected to a metal pad which is called the common pad. The diaphragm and four electrodes underneath form four capacitors. The pitches of the sensor array are listed in Table 5.1.



(a)



(b)

**Figure 5.8 Hair-like sensor array layout**

**(a) Whole array (b) Close-up two rows of sensors**

**Table 5.1 Geometry and structure parameters of sensor and array**

<b>Parameter</b>	<b>Value</b>	<b>Note</b>
$R_1$	$300\mu m$	Capacitor top plate radius
$R_2$	$290\mu m$	Capacitor electrode outer radius
$R_3$	$50\mu m$	Capacitor electrode inner radius
$R_4$	$230\mu m$	Outer ring of hair posts position
$R_5$	$180\mu m$	Inner ring of hair posts position
$D$	$40\mu m$	Hair post diameter
$\theta$	$80^\circ$	Fan-shaped electrode angle
$t_p$	$3.5\mu m$	Thickness of top plate
$t_e$	$0.5\mu m$	Thickness of electrodes
$t_h$	$80\mu m$	Hair post height
$g_0$	$2\mu m$	Initial air gap between top plate and electrode
$x$	$1120\mu m$	X direction pitch of sensor array
$y$	$1204\mu m$	Y direction pitch of sensor array
$a$	$10.1mm$	The size of sensor chip

## 5.4 Design of Flow Cell

The sensor array will be tested in a flow cell with laminar flow. The flow chamber is designed as a rectangular box as show in Figure 5.9.

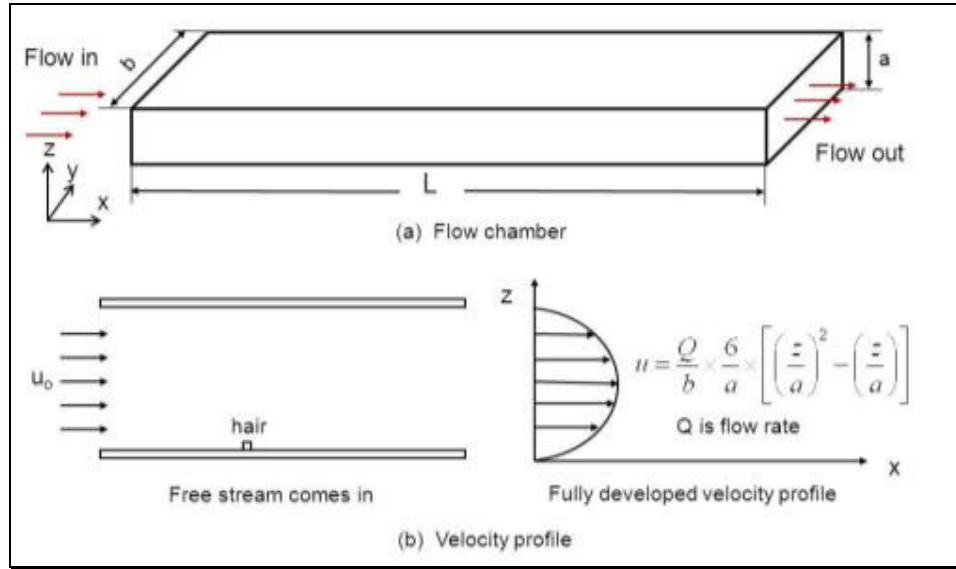


Figure 5.9 Laminar flow in a flow chamber

The flow in the chamber can be modeled as internal flow between two infinite parallel plates. The fully developed velocity varies with the height of the chamber:

$$u(z) = \frac{Q}{b} \times \frac{6}{a} \times \left[ \left( \frac{z}{a} \right)^2 - \left( \frac{z}{a} \right) \right] \quad (5.13)$$

where

$u(z)$  is flow velocity at height  $z$

$Q$  is flow rate

$a$  is flow chamber height

$b$  is flow chamber width

The pressure drop at  $x$  direction is

$$\frac{\partial P}{\partial x} = -\frac{Q}{b} \cdot \frac{12\mu}{a^3} \quad (5.14)$$

The shear stress distribution along the height of the chamber is

$$\tau(z) = a \cdot \frac{\partial P}{\partial x} \cdot \left( \frac{z}{a} - \frac{1}{2} \right) = \frac{12Q\mu}{a^2b} \cdot \left( \frac{z}{a} - \frac{1}{2} \right) \quad (5.15)$$

The geometry of the flow cell is determined based on several criteria and limitations: the length  $L$  is sufficient for the flow to fully develop before reaching hair sensors, the width of the chamber is constrained by the sensor package, and the height of the flow chamber influences both entrance length and wall shear stress in the chamber. First the width of the chamber is chosen to be  $19.8mm$  based on the sensor package size.

The entrance length for an internal laminar flow can be estimated as [109]

$$Le \simeq 0.06 Re \cdot D \leq 0.06 \cdot 2300 \cdot D = 138D \quad (5.16)$$

where  $Le$  is the entrance length,  $Re$  the Reynolds number and  $D$  the hydraulic diameter. Under normal condition, transition from laminar flow to turbulence occurs at  $Re \approx 2300$  for flow in pipes. For wide rectangular duct, the hydraulic diameter is  $D = 2a$ . According to Eqn.(5.16), the entrance length is  $Le = 8.4cm$ . The final length of the flow cell is chosen to be  $L = 15cm$ . The height of the flow chamber is determined by the height of the shim. The components of the flow cell are shown in Figure 5.10 and flow cell assembly in Figure 5.11. All the components were laser cut to their geometry shape. The top, middle and

bottom plate are PMMA plate. The shim is supposed to be  $0.01in$  thick Nylon sheet but the actual measured thickness is  $305\mu m$ . The bottom plate is mounted on sensor package through screws, the top of the middle plate is flush with the surface of the sensor, the shim defines the flow chamber size and the top plate encloses the flow chamber. An open hole on the top plate allows air to enter the flow cell. Pressure taps are assembled on the top plate to measure the pressures at different locations along the length of the flow cell. Thanks to Zhengxin Zhao, my co-worker, who helped to design and fabricate the flow cell. The measured pressure drop can be compared with computed pressure drop and the results will be presented and discussed in next chapter.

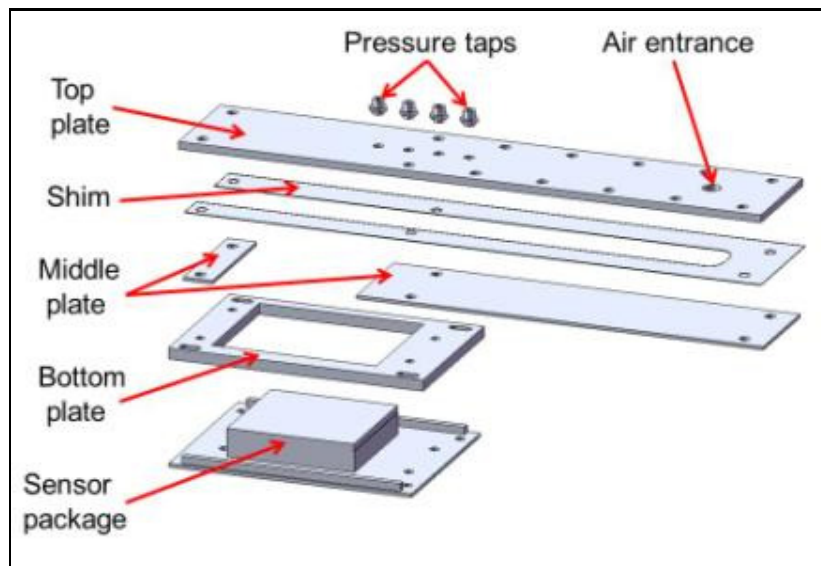


**Figure 5.10 Flow cell components**

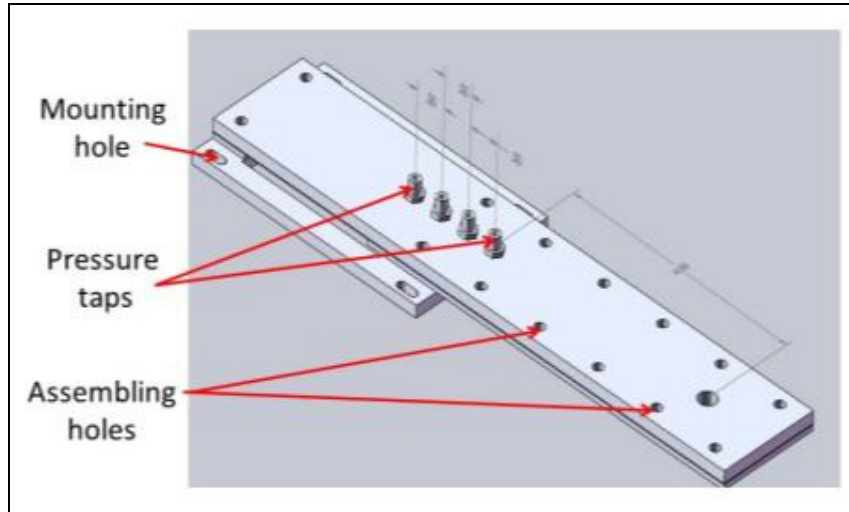


Figure 5.11 Assembled flow cell

## 5.5 Predicted Sensitivity

It is important to know the expected sensitivity for the hair-like sensor giving the specific design and flow condition mentioned earlier. An ideal simulation would be to create a 3D coupled fluid-displacement model using FEA and including both capacitors and hair posts. Attempts were made to create a 3D model and solve it in Comsol<sup>®</sup>. However, due to the big difference in dimensions for the model (smallest dimension is  $2\mu m$  and biggest dimension is  $600\mu m$ ), a large amount of elements are needed to solve this coupled problem. The commercial software Comsol<sup>®</sup> does not have the capacity to solve all the equations generated by the large amount of nodes. Instead, two separate models were created in order to compute the capacitance change. The first model is a 3D fluid mechanics model, in which a single hair post is modeled as a rigid body immersed in

a fluid domain. The total moment that is generated on the post due to the flow can be computed from this fluid model. The second model is a 2D Mindlin plate, in which the moment is applied on each hair location and the bending of the plate is simulated and capacitance change is computed. The two FEA models are described in detail in the following sections.

### **5.5.1 Fluid Mechanics Analyses of Hair Post**

A FEA fluid mechanics model is used to simulate the fluid passing a hair post. A rectangular box of size  $80\mu\text{m}\times 160\mu\text{m}\times 160\mu\text{m}$  represents a fluid domain as shown in Figure 5.12. The fluid enters as fully developed flow from the front surface of the fluid domain and exits from the back surface. The incoming flow velocity is a function of flow duct height  $z$ . The top surface of the domain has a constant velocity of  $9.5\text{m/s}$  computed from Eqn. (5.13). The bottom surface is a rigid wall. The  $80\mu\text{m}$  tall hair post is modeled as a rigid body object that is intruded in the fluid domain. Since this problem is symmetric about the center line of the hair post, to reduce the computation cost, a semi-post model is used and symmetric boundary is applied. The left and right surfaces are modeled as symmetric boundaries.

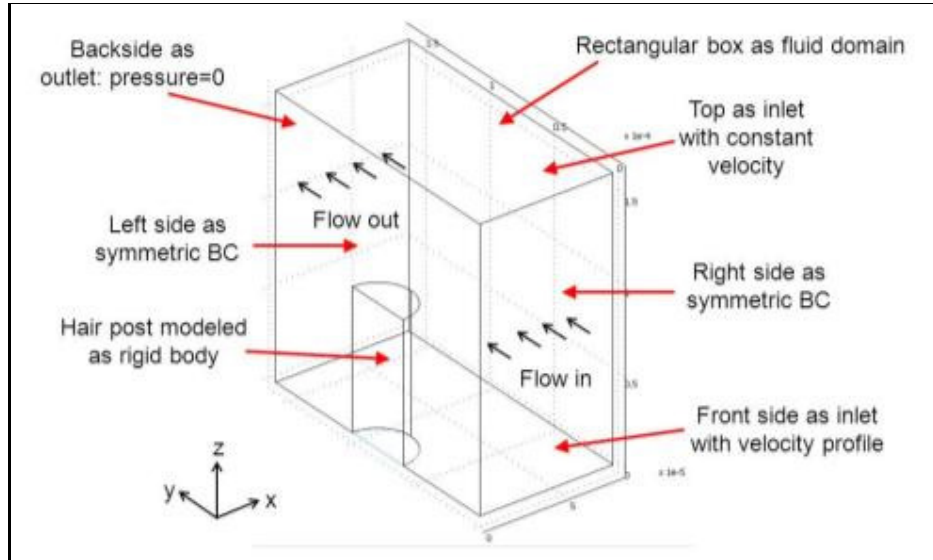


Figure 5.12 FEA model of fluid domain

A flow rate of  $Q = 5CFH$  (cubic foot per hour), which is equal to  $Q = 3.95 \times 10^{-5} m^3 / s$  is applied to the model. The boundaries and values applied to the model are listed in Table 5.2 and dimensions and material properties are listed in Table 5.3.

**Table 5.2 Fluid mechanics FEA model boundaries**

	Face	Boundary Condition	Value
Rectangular box	Front	Inlet	$u = -\frac{Q}{l} \cdot \frac{6}{a} \left[ \left( \frac{z}{a} \right)^2 - \left( \frac{z}{a} \right) \right]$
	Back	Outlet	$pressure = 0$
	Top	Inlet	$u_{top} = -\frac{Q}{l} \cdot \frac{6}{a} \left[ \left( \frac{160\mu m}{a} \right)^2 - \left( \frac{160\mu m}{a} \right) \right]$
	Bottom	Wall	$u_{bot} = 0$
	Left	Symmetric	-
	Right	Symmetric	-
Hair post	Right half	Wall	Treated as rigid body

**Table 5.3 Parameters used in fluid mechanics FEA model**

Parameter	Value	Note
$x$	$80\mu m$	Fluid domain dimension in $x$ direction
$y$	$160\mu m$	Fluid domain dimension in $y$ direction
$z$	$160\mu m$	Fluid domain dimension in $z$ direction
$a$	$305\mu m$	Flow chamber height
$b$	$2.03cm$	Flow chamber width
$Q$	$3.95 \times 10^{-5} m^3 / s$	Flow rate
$\mu$	$1.846 \times 10^{-5} kg / (m \cdot s)$	Dynamic viscosity of air
$\rho$	$1.177kg / m^3$	Density of air

Tetrahedral elements are used for the computation. A finer mesh is

applied for the post and the total elements in the model are 42717. Figure 5.13 FEA mesh for the fluid mechanics model shows the mesh for the model.

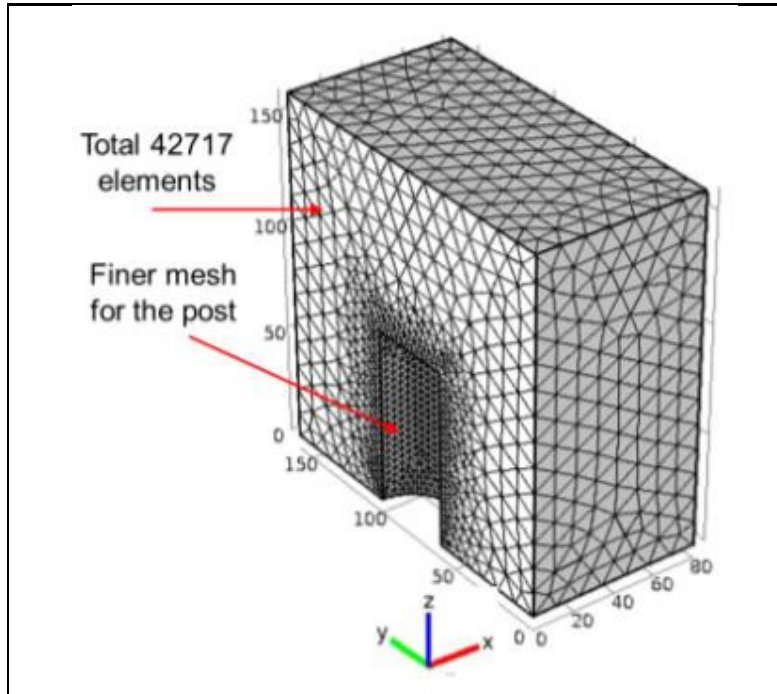
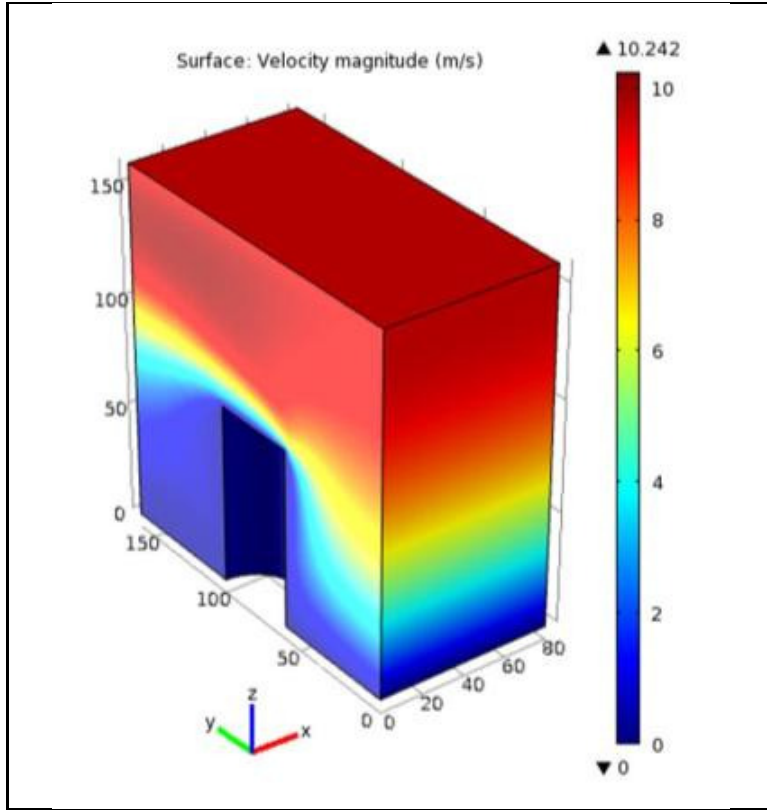


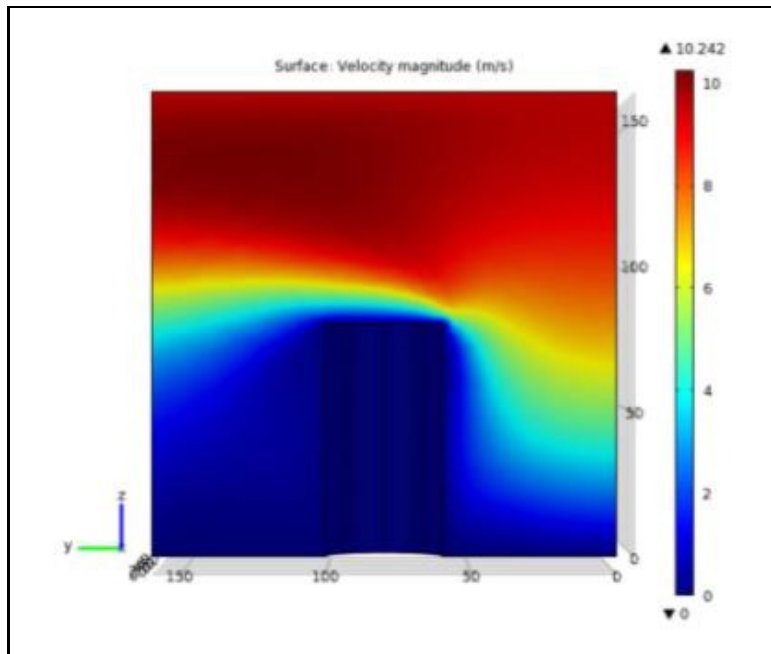
**Figure 5.13 FEA mesh for the fluid mechanics model**

After applying air properties and the boundaries to the model, a laminar flow analysis was run in Comsol®. The computed fluid velocity distribution is shown in Figure 5.14 and shear stress distribution is shown in Figure 5.16 for the model with 42717 elements. The convergence of the FEA model is verified by comparing the computation results of a model which has 32689 elements with those in the 42717 elements model. The velocity profile for 32689 elements model is shown in Figure 5.15. The velocity distribution and magnitude were very close for these two models,

indicating the 42717 elements are sufficient for the analyses.



(a)



(b)

Figure 5.14 Velocity distribution in the fluid domain for 42717 elements model

(a) Isometric view (b) Side view

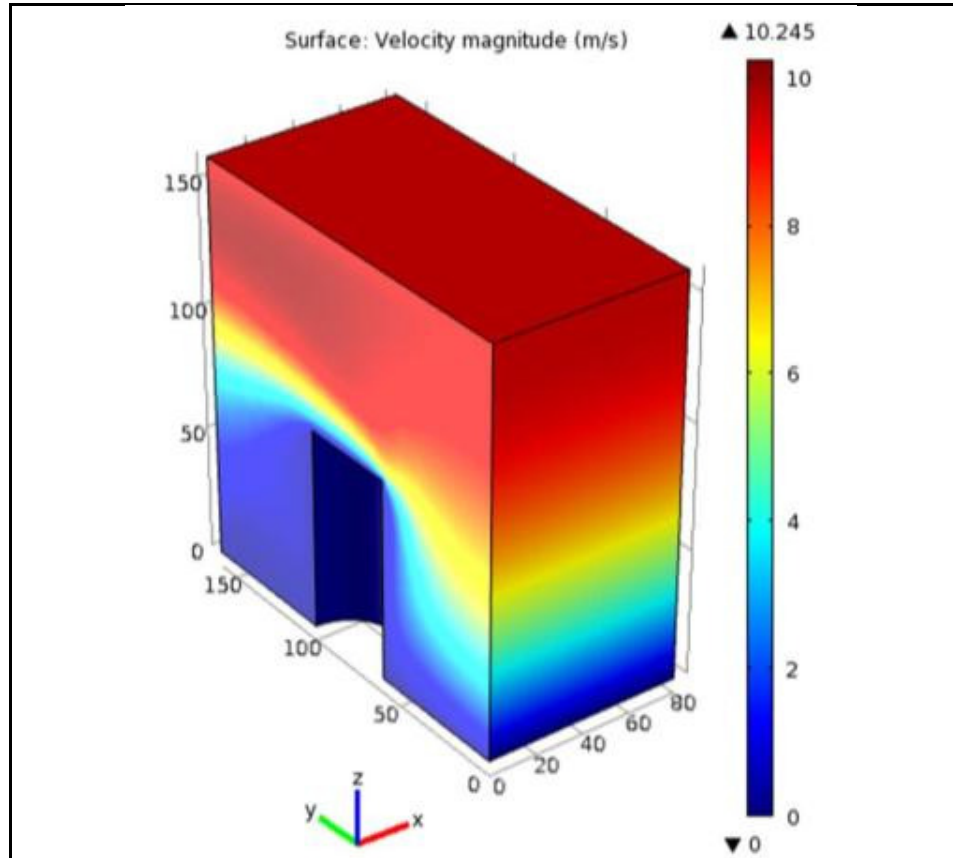


Figure 5.15 Velocity distribution in the fluid domain for 32689 elements model

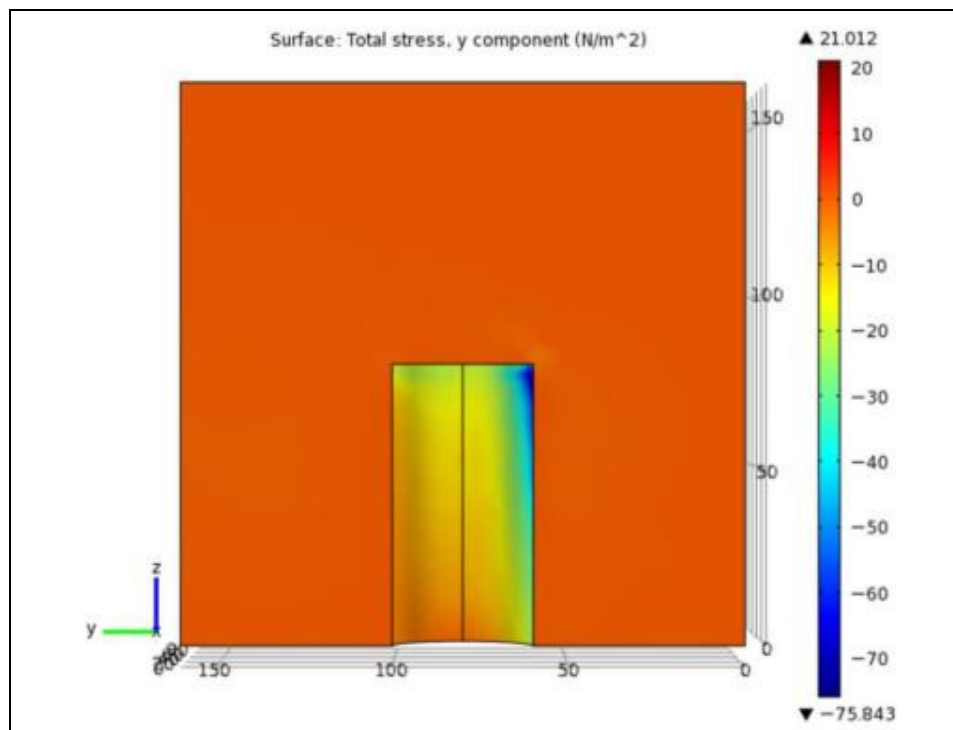


Figure 5.16 Shear stress distribution on the hair post for 42717 elements model

Shear stress distributed on the hair post was integrated over the post surface and total moment about the base of the post was computed,

$$M = \int_0^A z \cdot \tau dA \quad (5.17)$$

Where  $M$  is the total moment generated by the shear stress on the hair post,  $\tau$  is the shear stress,  $A$  is the total area of the half post and  $z$  is the distance from  $dA$  to the base of the post. The moment was calculated using Comsol<sup>®</sup> post-processing tool. The moment generated by the flow on the half post is  $4.7725 \times 10^{-12} N \cdot m$ . The total moment of the whole post is  $M = 9.545 \times 10^{-12} N \cdot m$

### **5.5.2 Structure Mechanics Analyses of Mindlin Plate**

With moment applied on the post in hand, we can proceed to compute the plate deflection under those moments. A 2D FEA Mindlin plate model is created for this simulation. The geometrical dimensions of the plate structure are listed in Table 5.1. The other properties that are needed for the computation are listed in Table 5.4. The moment was applied on the plate by applying a couple of concentrated forces normal to the plate with the arm of the couple equal to post diameter.

**Table 5.4 Properties used in Mindlin plate model**

<b>Parameter</b>	<b>Value</b>	<b>Note</b>
$E_{poly}$	$158 \times 10^9 Pa$	Young's modulus of polysilicon
$\nu_{poly}$	0.22	Poisson's ratio of polysilicon
$t_{poly}$	$3.5 \mu m$	Thickness of polysilicon plate
$E_{post}$	$4 \times 10^9 Pa$	Young's modulus of SU8 photoresist
$\nu_{post}$	0.22	Poisson's ratio of SU8 photoresist
$t_{total}$	$83.5 \mu m$	Thickness of polysilicon plate and hair post
$F_z$	$0.2369 \mu N$	Applied couple force
$d$	$40 \mu m$	Arm of the couple

The mesh of the plate is shown in Figure 5.17 The mesh of 2D Mindlin plate model with 27696 elements The mesh consists of 27696 triangular elements. The convergence of the model was investigated and confirmed.

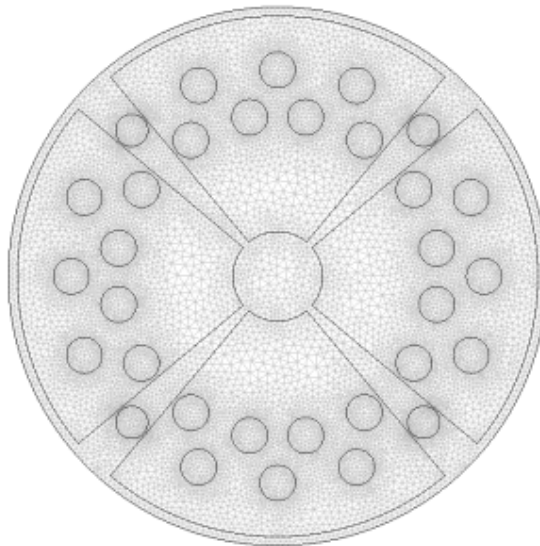
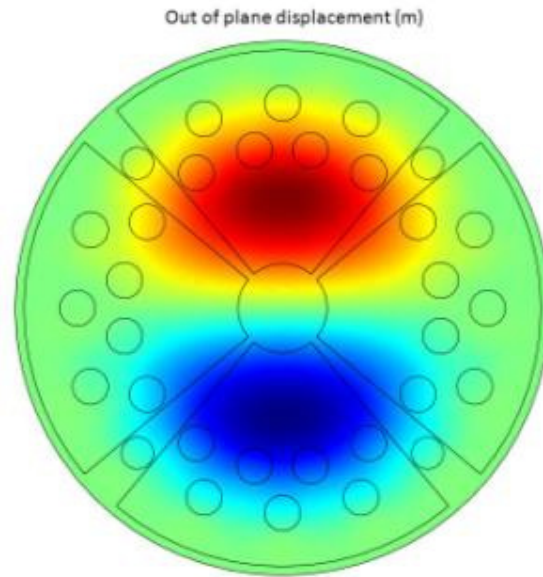
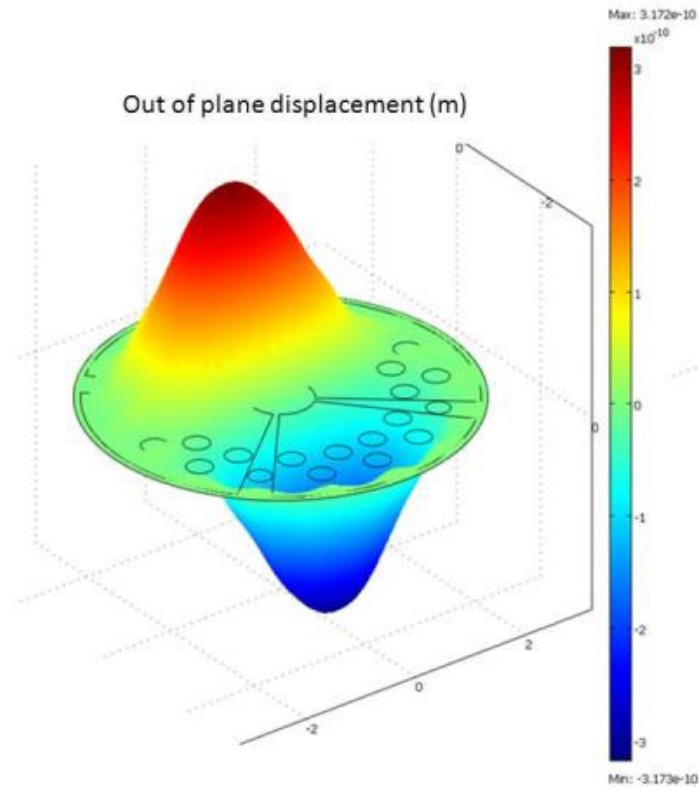


**Figure 5.17 The mesh of 2D Mindlin plate model with 27696 elements**

The out of plane displacement of the plate is shown in Figure 5.18.



(a)



(b)

**Figure 5.18 Top plate deflection (a) 2D view (b) 3D view**

The capacitance change is

$$\begin{aligned}\Delta C &= C_{final} - C_{original} \\ &= \varepsilon_o \int_0^A \left( \frac{1}{g_o - w(x, y)} - \frac{1}{g_o} \right) dA\end{aligned}\quad (5.18)$$

where

$\Delta C$  is the capacitance change for one electrode

$C_{original}$  is the capacitance before the plate deformation

$C_{final}$  is the capacitance after the plate deformation

$g_o$  is the initial air gap of the capacitor

$w(x, y)$  is the out of plane displacement of the plate when subjected to load, which is a function of plate location at coordinate  $x$  and  $y$

$A$  is the total area of the electrode

In this simulation, the flow direction is passing through the bottom electrode to the top electrode. Using Comsol<sup>®</sup> post-processing tool, the computed capacitance change for both the top electrode and bottom electrode capacitors are  $\Delta C = 1.652 \times 10^{-17} \text{ Farad}$  but with opposite sign.

So the total capacitance change for the sensor is

$\Delta C_{total} = 3.304 \times 10^{-17} \text{ Farad}$ . The computed wall shear stress is  $2.3 \text{ Pa}$

from the fluid model for  $Q = 3.95 \times 10^{-5} \text{ m}^3 / \text{s}$  flow rate. So the sensitivity

for a single sensor is

$$\begin{aligned}
 S_{single} &= \frac{\Delta C}{\tau} = \frac{3.304 \times 10^{-17} \text{ Farad}}{2.3 \text{ Pa}} \\
 &= 1.437 \times 10^{-17} \frac{\text{Farad}}{\text{Pa}}
 \end{aligned}
 \tag{5.19}$$

## 5.6 Electronics Design

In the last section, the predicted sensitivity of the sensor was calculated. A commercial MS3110 Universal Capacitive Readout™ IC chip is used to measure the actual differential capacitance change of the sensor in a laminar flow cell. MS3110 is a 16 pin small-outline integrated circuit (SOIC) surface mounted chip. A photograph of the chip and pin-out diagram is shown in Figure 5.19.

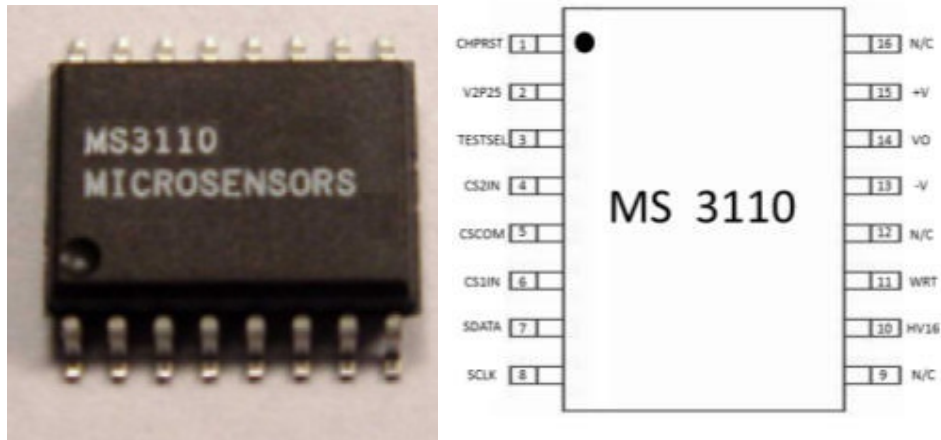


**Figure 5.19 MS3110 capacitive readout sensor and pin-out diagram [110]**

The chip is powered by 5V DC voltage through pin 13 and 15. The output of the chip  $V_o$  is a voltage in the range of 0-5V, detected through pin 14.

The functional block diagram is shown in Figure 5.20. The transfer function of the sensor is

$$V_o = Gain \times V_{2P25} \times 1.14 \times (CS_{2T} - CS_{1T}) / CF + V_{REF} \quad (5.20)$$

Where:

$V_o$  is the output voltage

$Gain$  is 2 or 4V/V

$V_{2P25}$  is a reference voltage 2.25V

$$CS_{2T} = CS_{2IN} + CS_2$$

$$CS_{1T} = CS_{1IN} + CS_1$$

$CF$  is an adjustable feedback capacitance to the amplifier in MS3110

$V_{REF}$  is 0.5V or 2.25V

$CS_{2IN}$  is one of the capacitances detected by MS3110. For our application, it is the capacitance between bottom electrode and diaphragm of hair-like sensor

$CS_{1IN}$  is the other capacitances detected by MS3110. For our application, it is the capacitance between top electrode and diaphragm of hair-like sensor

$CS_1$  and  $CS_2$  are internal adjustable capacitances that are used to balance the capacitance difference of the external capacitances to ensure the circuit is operating in the normal range and the output is within 0-5V.

The MS3110 sensor has a low pass filter that is programmable between 500Hz-8000Hz. The sensor's resolution is  $4.0aF / \sqrt{Hz}$ . For the minimum

bandwidth  $500\text{Hz}$ , the minimum detectable capacitance change is  $90\text{aF}$ .

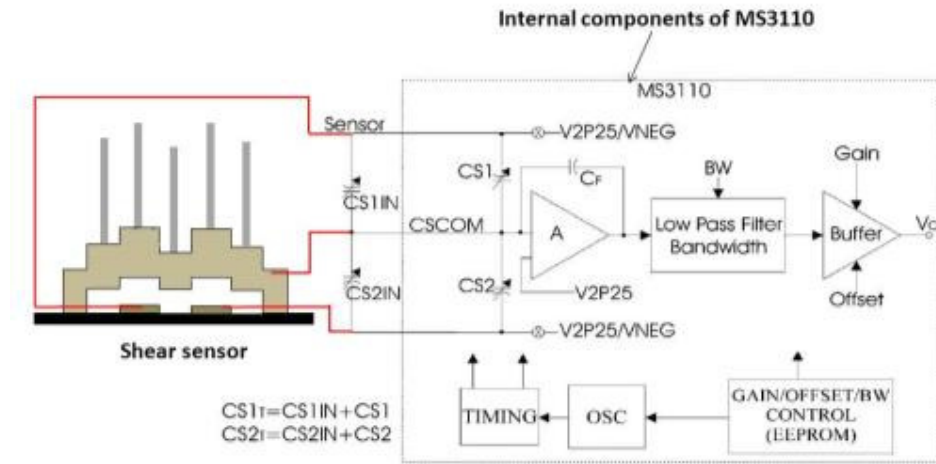


**Figure 5.20 MS3110 functional block diagram and connection with hair-like sensor [110]**

There are many parameters in the MS3110 sensor that are adjustable. Labview<sup>®</sup> was used to program the sensor parameters for different applications. MS3110 has two different programming modes: temporary programming mode, which is also called volatile register write mode and permanent programming mode, which is also called EEPROM write mode. In the temporary mode, the adjustable parameters values are loaded into the on-chip shift register through Labview<sup>®</sup> via a data acquisition board. The shift register can be readout through Labview<sup>®</sup> program to verify that the right values were written into the register. The temporary programming does not require extra power except the 5V that is needed to power the chip. As long as the chip's power is on and the chip is not reset, the temporary programming data is stored in the shift register and the MS3110 sensor chip functions as it is temporarily

programmed. However, once the power is off or the chip is reset, all the temporary programming data in the shift register will be lost and data stored in EEPROM memory map will be sent into shift register. The sensor chip functions according to permanent programming that was written in EEPROM memory map. The temporary programming is used for the tuning of the MS3110 chip until it performs as desired. Once the settings are determined for one application, the sensor then can be permanently programmed. The permanent programming requires a 16V power supply to write the data into EEPROM memory map. Four pins are required for the permanent programming: HV16, SDATA, SCLK and WRT. Three pins are required for temporary programming: SDATA, SCLK and TESTSEL. The EEPROM permanent program write mode timing diagram is shown in Figure 5.21.

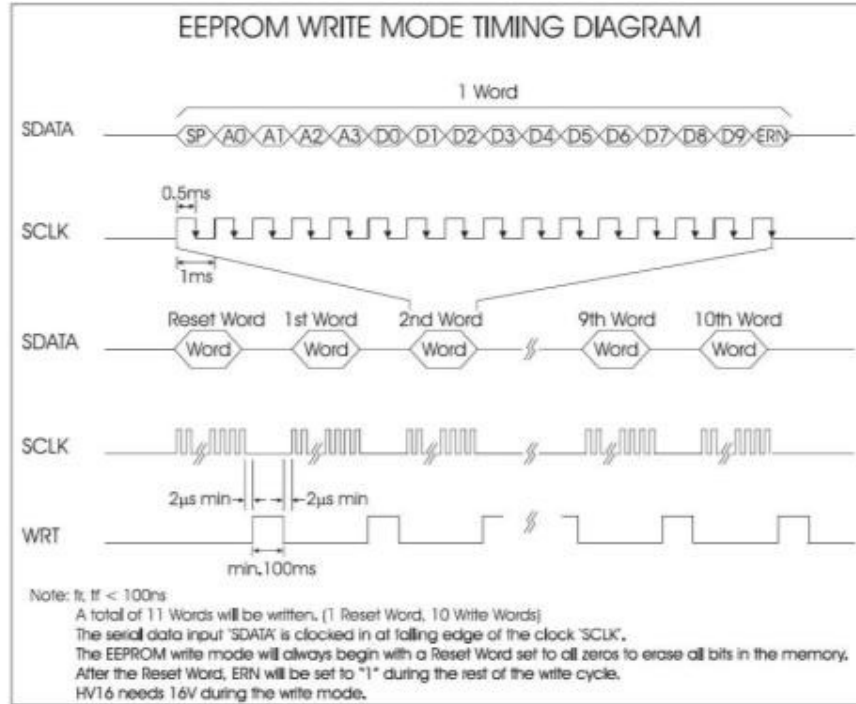
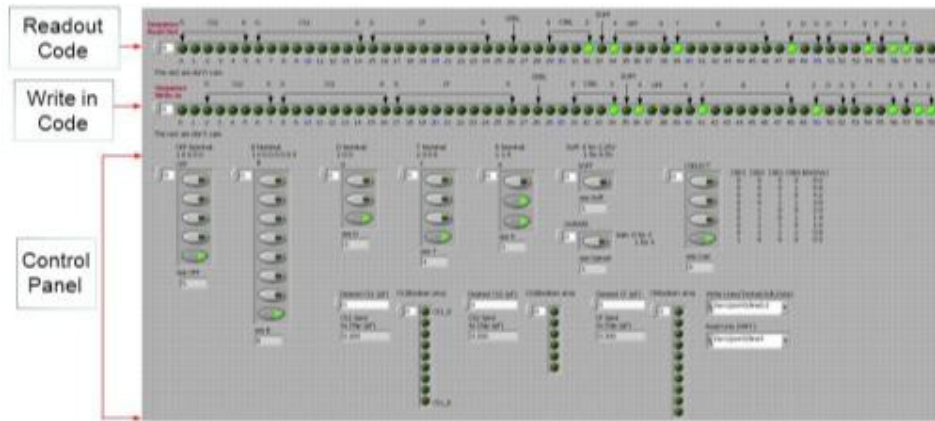


**Figure 5.21 EEPROM permanent write mode timing diagram [110]**

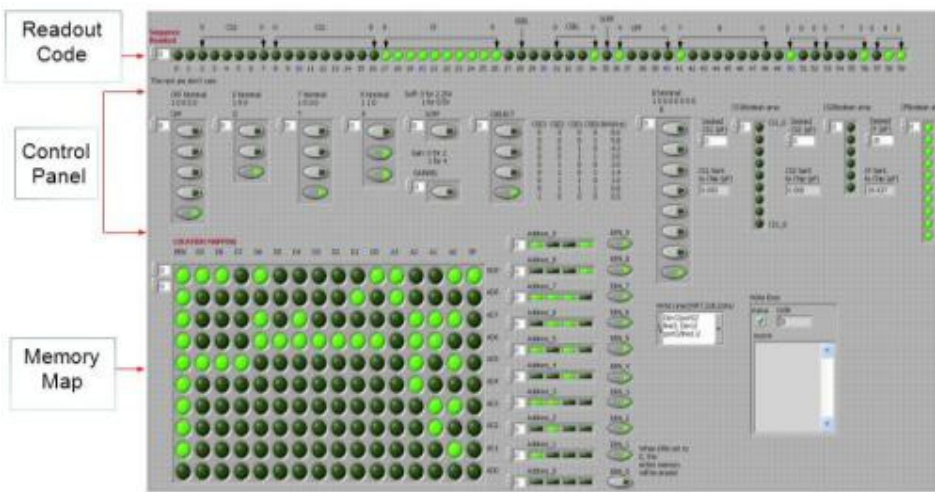
The parameters are adjusted using a Labview<sup>®</sup> program control panel.

The Labview<sup>®</sup> interface is shown in Figure 5.22. The Labview<sup>®</sup> block

diagrams can be found in Appendix B.



(a)



(b)

**Figure 5.22 Labview® program interface**

**(a) Temporary programming (b) Permanent programming**

An electrical board prototype was built to test and debug the Labview® program. The photo of the prototype is shown in Figure 5.23.

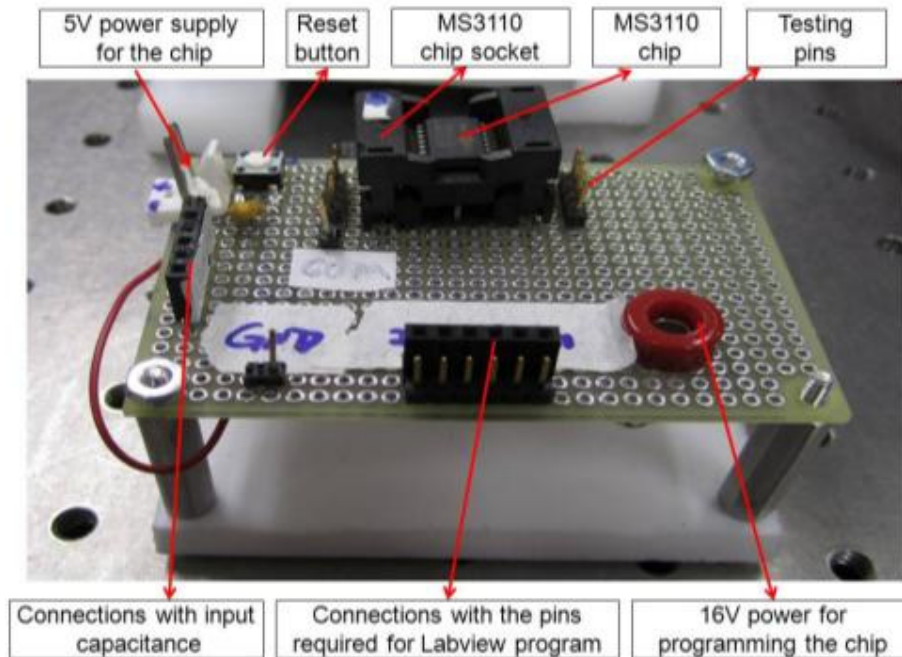
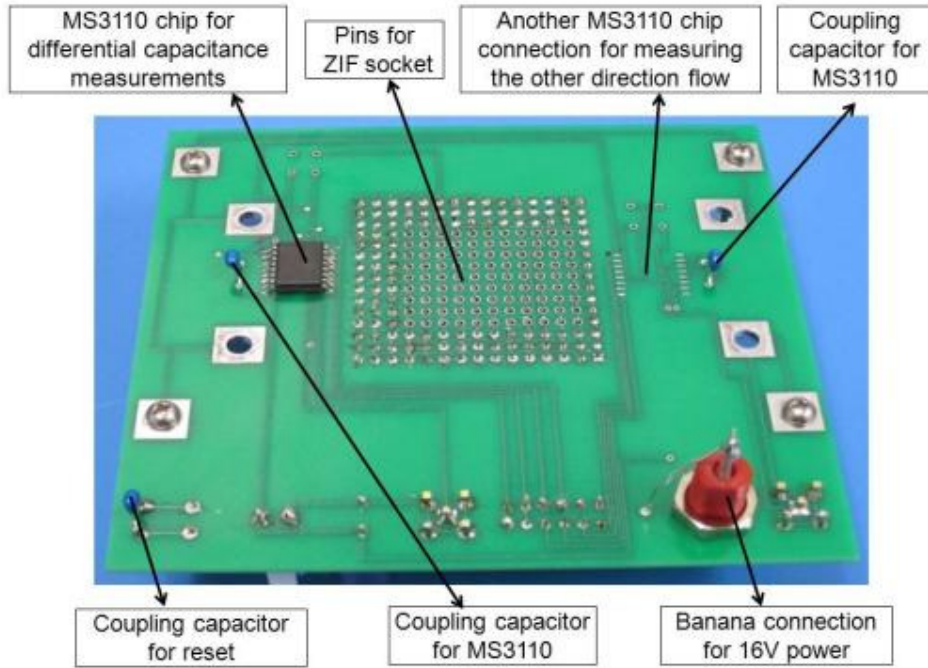


**Figure 5.23 Programming board prototype**

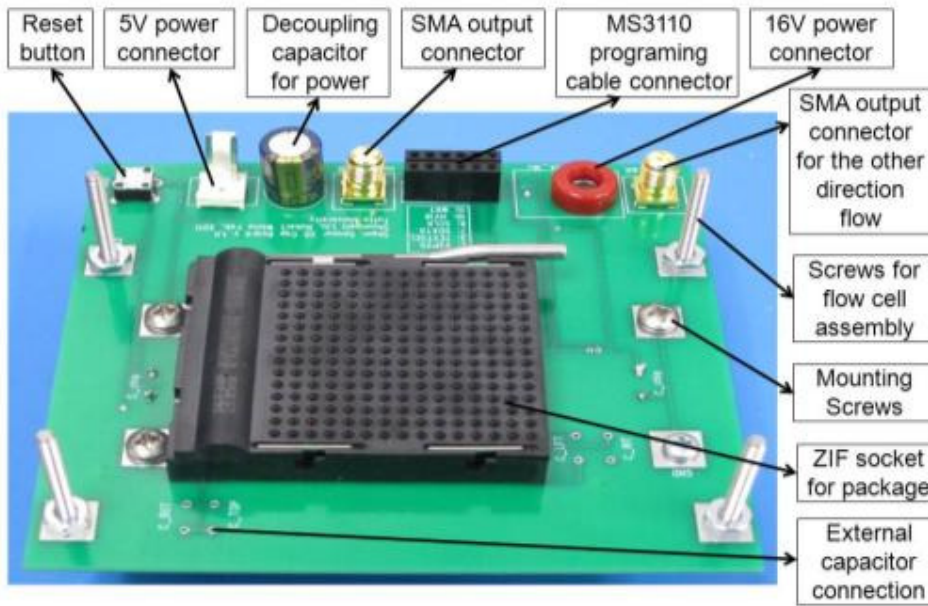
On the programming board, a zero insertion force (ZIF) socket was soldered on a protoboard. The MS3110 can be easily mounted and dismounted from the ZIF socket. Testing pins were used to monitor the program parameters. Both 5V and 16V power supplies were provided for temporary and permanent programming. Connections with required programming pins allow communication between Labview<sup>®</sup> program and the MS3110 Chip via a data acquisition board which is not shown in the figure. A reset button was used to verify that the control data was written in EEPROM memory permanently.

After the Labview<sup>®</sup> program was tested and proven to work properly, the next step was to integrate the MS3110 sensor chip with the hair-like shear

sensor on an electronic board so that the shear sensor could be tested in a laminar flow cell. The electronic board is a two-layer printed circuit board (PCB) assembled with MS3110 chip along with various passive components, power connectors, output connectors and cable connectors used for MS3110 programming. The size of the PCB is  $3.7in \times 4.3in \times 0.062in$ . The electronic board is shown in Figure 5.24.



(a)



(b)

**Figure 5.24 Electrical board for hair-like sensor testing**

**(a) Back side of the board (b) Front side of the board**

A ZIF socket was soldered on the PCB. The hair sensor package can be inserted into the ZIF socket. All top electrodes in the sensor array are connected together through the PCB wires and connected to one of the MS3110 input capacitance pins,  $CS1IN$ . The same concept applies to all the bottom electrodes which are connected to the other MS3110 input capacitance pin,  $CS2IN$ . The output pin of the MS3110 was connected to a SubMiniature version A (SMA) connector which is connected to a precision voltage meter for capacitance readout.

An  $100\mu\text{F}$  aluminum electrolytic capacitor was connected to the power supply works as local energy storage and filters the AC signal superimposed on the DC power line. The  $1\mu\text{F}$  ceramic capacitors performed the same function to MS 3110 chips and to a reset button. A Molex male pin connector was soldered on the PCB. This connector was used to connect with external 5V external power supply. A banana connector was used to connect to 16V power supply for the permanent programming of the MS3110 chip. A rectangular six pin female socket was used to connect with the data acquisition board for MS3110 programming. A reset button was soldered on PCB to refresh the program in MS3110.

This chapter described the design and modeling of the sensor and the apparatus needed for the sensor testing. In the next chapter, the sensor fabrication, packaging and testing will be presented.

# Chapter 6

## FABRICATION, PACKAGING and TESTING

### 6.1 Shear Sensor Fabrication

#### 6.1.1 PolyMUMPs™ Foundry Process Fabrication

PolyMUMPs™ is one of the MUMPs® MEMS manufacturing processes provided by MEMSCAP Inc. MUMPs® stands for Multi-User MEMS Processes, a commercial foundry program for MEMS manufacturing based on fixed processes. The process uses seven deposited layers, including three polysilicon layers, two sacrificial layers, one metal layer and one isolation layer, built on top of a silicon wafer substrate. The process requires specific design rules and the thickness of every deposited layer is not subject to change. This limits the choices of the structure design. However, it provides good uniformity and alignment, a smooth surface and minimal residual stresses. The final products of this process are MEMS devices on  $10.1\text{mm} \times 10.1\text{mm}$  square chips with structural layers unreleased. Upon receiving the diced chips from MEMSCAP,

post-processing includes SU8 hair post fabrication on the square chips and structure release through HF etching of sacrificial layers. The post-processing is done at Tufts Micro-Nano Facility (TMNF).

A thorough PolyMUMPs™ process overview and design rules can be found in [111]. A brief overview of the process is presented here and the process is diagrammed in Figure 6.1.

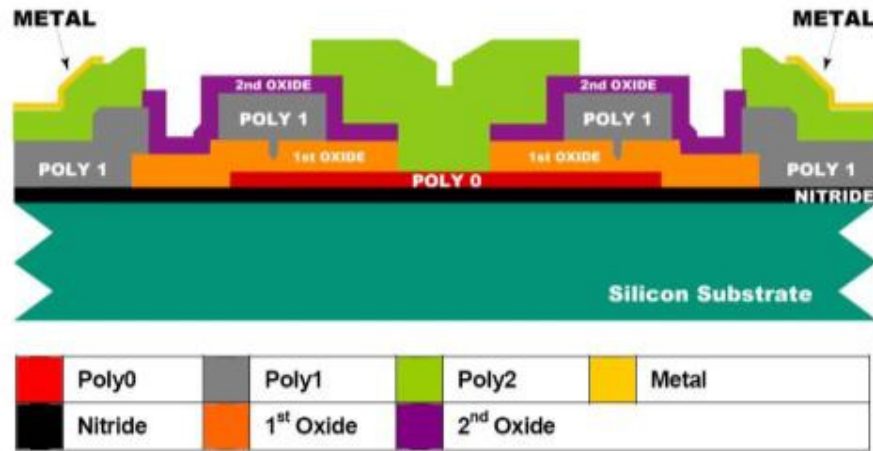


Figure 6.1 Overview of PolyMUMPs™ process [111]

Table 6.1 lists all the manufacturing layer names and the associated thickness for each layer, the residual stresses generated during film depositions, and the minimal features that are allowed in each layer. In addition, the masks used for each process are listed in Table 6.1. The mask layout can be found in Appendix C1.

Table 6.1 PolyMUMPs™ process layers, material properties and requirements

(Positive stress is tensile stress)

Layer Name	Layer Thickness	Residual Stress	Mask Name	Minimum Feature
Silicon Nitride	0.6 $\mu\text{m}$	90MPa	—	—
Poly 0	0.5 $\mu\text{m}$	-25MPa	POLY0	2 $\mu\text{m}$
First Oxide	2 $\mu\text{m}$	—	DIMPLE	3 $\mu\text{m}$
			ANCHOR1	3 $\mu\text{m}$
Poly 1	2 $\mu\text{m}$	-10MPa	POLY1	2 $\mu\text{m}$
			HOLE1	3 $\mu\text{m}$
Second Oxide	0.75 $\mu\text{m}$	—	POLY1_POLY2_VIA	3 $\mu\text{m}$
			ANCHOR2	3 $\mu\text{m}$
Poly 2	1.5 $\mu\text{m}$	-10MPa	POLY2	2 $\mu\text{m}$
			HOLE2	3 $\mu\text{m}$
Metal	0.5 $\mu\text{m}$	50MPa	METAL	3 $\mu\text{m}$

The process begins with preparing n-type (100) silicon wafers with a diameter of 150mm. The surfaces of the wafers then are heavily doped with phosphorus using a phosphosilicate glass (PSG) as the dopant source. The purpose of this doping is to reduce or prevent charge feedthrough to the substrate from electrostatic devices on the surface. Next, a 0.6 $\mu\text{m}$  silicon nitride layer is deposited on the wafers using a low pressure chemical vapor deposition (LPCVD) process. The silicon nitride

serves as an electrical isolation layer between MEMS device and doped silicon substrate.

Next, the first of the three polysilicon film layers, a  $0.5\mu\text{m}$  Poly0 layer, is deposited using LPCVD. The Poly0 layer is patterned by photolithography using mask POLY0 and undesired polysilicon is etched away using plasma etching. On top of the patterned Poly0, a  $2\mu\text{m}$  PSG sacrificial layer is deposited by LPCVD and annealed at  $1050^\circ\text{C}$  for 1 hour in argon gas. This PSG layer is called First Oxide layer and along with Second Oxide layer will be removed at the end of the process to free the mechanical structure layers of polysilicon. It also serves as a dopant source which heavily phosphorus dopes Poly0 during the anneal.  $0.75\mu\text{m}$  tall dimples are created on the First Oxide layer through photolithography with the DIMPLES mask, and are reactive ion etch (RIE) into the First Oxide layer. Using mask ANCHOR1, certain parts of the First Oxide layer are etched away, exposing Poly0 or the Silicon Nitride layer directly to the Poly1 layer, providing anchors for Poly1 structures.

Subsequently, the first structural layer of polysilicon, a  $2\mu\text{m}$  thick Poly 1 layer, is deposited on top of the First Oxide layer. The dimple pattern on the First Oxide layer is transferred to Poly1. A  $0.2\mu\text{m}$  layer of PSG is deposited over Poly1 and the wafer is annealed at  $1050^\circ\text{C}$  for 1 hour. The anneal serves two purposes: first, it dopes the polysilicon with

phosphorus from the PSG layers both above and below it; second, the annealing significantly reduces the net stress in the Poly1 layer. The polysilicon Poly1 layer and the thin PSG layer which serves as a masking layer are lithographically patterned using mask POLY1. The thin PSG layer is etched to produce a hard mask for the subsequent polysilicon etch. Then the unwanted Poly1 layer is chemically etched away. The hard mask is more resistant to the polysilicon etch chemistry than the photoresist and ensures better transfer of the pattern into the polysilicon. Afterward, the hard mask is removed by RIE.

On top of patterned Poly1, a  $0.75\mu\text{m}$  Second Oxide PSG layer is deposited and annealed. Two different masks are used to pattern the Second Oxide layer. The POLY1\_POLY2\_VIA mask is used to etch away certain parts of the Second Oxide layer to expose the Poly1 layer underneath it. This process provides a mechanical and electrical connection between the Poly 1 and Poly 2 layers. The ANCHOR2 level is provided to etch both the First and Second Oxide layers in one step, thereby eliminating any misalignment between separate etch steps. Both The POLY1\_POLY2\_VIA and ANCHOR2 are lithographically patterned and etched by RIE.

The second structural layer, a  $1.5\mu\text{m}$  thick Poly 2 layer, is then deposited followed by the deposition of a  $0.2\mu\text{m}$  thin PSG layer. This thin PSG layer serves as both an etch mask and dopant source for Poly 2.

The wafer is annealed for one hour at 1050 C to dope the polysilicon and reduce the residual film stress. The Poly2 layer is lithographically patterned with mask POLY2. The PSG and polysilicon layers are etched by plasma and RIE processes, similar to those used for Poly 1.

The final step of the PolyMUMPs process is to deposit a  $0.5\mu\text{m}$  thick gold metal layer. The metal layer can be used for probing, wirebonding and electrical routing. The wafer is patterned lithographically with the last mask. METAL and the metal is deposited and patterned using lift-off. After all the layers are deposited and patterned, the wafers are diced, sorted and shipped to the PolyMUMPs<sup>TM</sup> users.

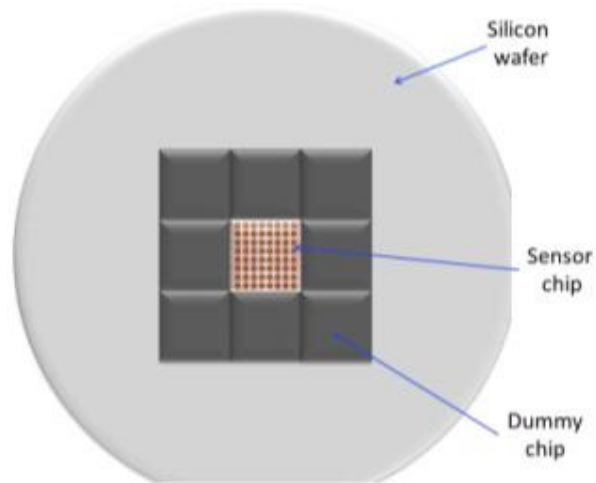
### **6.1.2 Hair Posts Fabrication**

Upon receiving the diced chips, hair posts were fabricated on top of the Poly2 structure layer at Tufts Micro-Nano Facility. The hair posts are fabricated using SU8-2025, an epoxy based negative photoresist product by MicroChem Corp. Fabricating SU8, which has high viscosity, on a  $10.1\text{mm} \times 10.1\text{mm}$  chip, was challenging for several reasons. First, the polysilicon chip is too small to be used on the OAI Mask Aligner for feature alignment and SU8 photoresist exposing. Second, the edge bead effect of SU8 makes it difficult to achieve the desired film thickness. When SU8 photoresist is spin coated on a wafer, the SU8 thickness at the

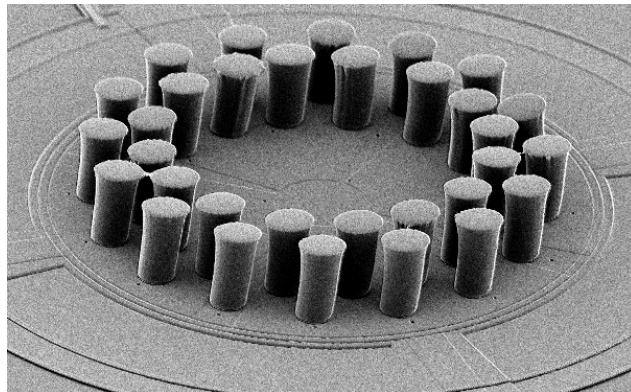
edge of the wafer is thicker than the rest on the wafer. This phenomenon is called the “edge bead effect”. Due to its small size, the spin coated SU8 on the chip has very non-uniform thickness.

Several steps were taken to solve the fabrication difficulties mentioned above. First, a 4" silicon wafer was spin-coated with SPR3.0 photoresist. SPR3.0 is a positive photoresist that is easily dissolved in Acetone. Then, before the photoresist dries, a  $10.1\text{mm} \times 10.1\text{mm}$  polysilicon sensor chip is placed at the center of the wafer on photoresist. Eight dummy chips which have the same size and thickness are placed closely around the sensor chip as show in Figure 6.2. The wafer is placed on a  $120^{\circ}\text{C}$  hotplate for 5 minutes to let the photoresist dry. The photoresist acts as a glue to secure the chips on the wafer. The wafer with chips on it can then be spin-coated with SU8-2025 for the hair posts fabrication. When SU8 is spin-coated on the wafer, the edge bead effect is observed at the edge of the eight dummy chips, ensuring uniform film thickness on the central sensor chip. Also, since the chips are secured on the wafer, the sensor chip can be easily handled on the OAI aligner through the wafer. By adjusting the wafer position, the polysilicon sensor chip can be aligned with the hair post mask. After the SU8 photoresist is exposed and developed, the wafer is soaked in a glass beaker full of acetone. The sensor chip and dummy chips are removed from the wafer. A fully fabricated sensor chip SEM picture is shown in Figure 6.3 and a light microscope imagine of the

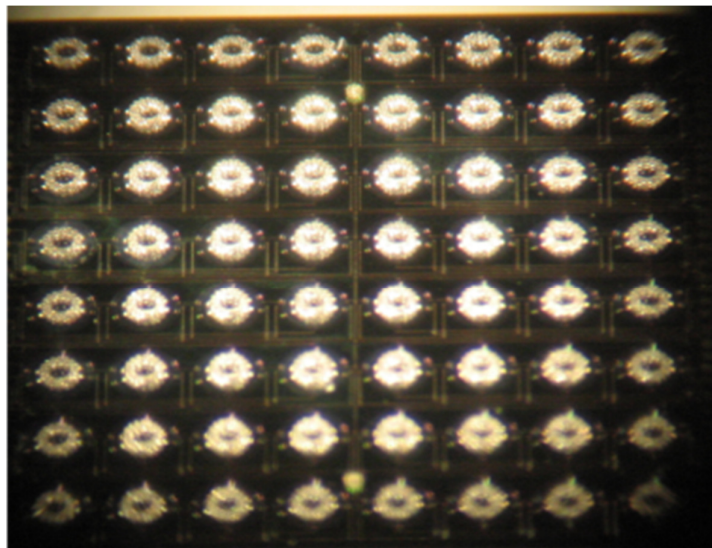
entire sensor chip is shown in Figure 6.4.



**Figure 6.2 Chips layout on silicon wafer**

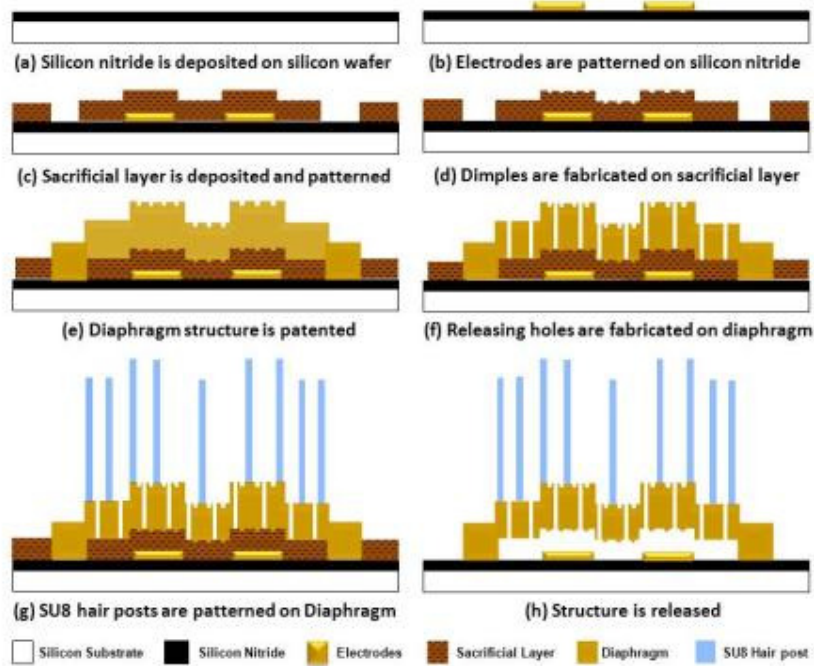


**Figure 6.3 SEM of hair-like shear sensor**



**Figure 6.4 Microscope image of hair-like sensor chip**

A complete hair-like shear sensor fabrication flow chart is shown in Figure 6.5.



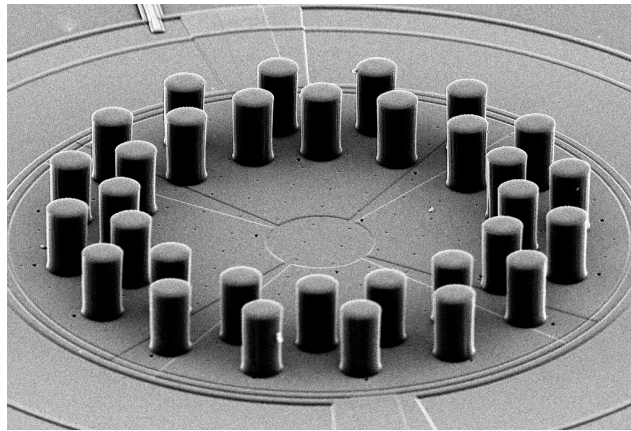
**Figure 6.5 Hair-like shear sensor fabrication flow chart**

Figure 6.3 shows that posts are not completely separated, because the actual size of the posts is larger than the designed size. The posts are also bigger at the top than at the bottom. This effect is called “T-topping”. The poor quality of the hair posts is due to the UV light exposure process of SU8. SU8 photoresist exposure is optimized near UV wavelengths of  $350-400\text{nm}$ . It is insensitive to light above  $400\text{nm}$  wavelength, but absorbs light below  $350\text{nm}$ . Excessive dose below  $350\text{nm}$  results in over-exposure of the feature, especially the top portion of SU8 film. This over-exposure causes the enlargement of features and the T-topping effect.

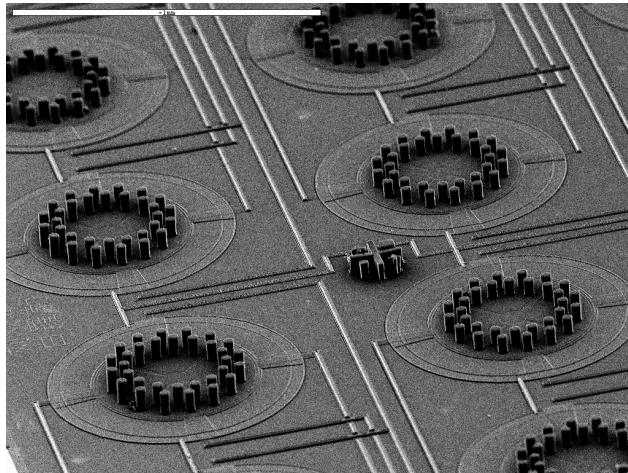
To solve this problem, a UV-filter was placed on top of the hair post mask.

This filter can filter out UV light below  $350\text{nm}$ , ensuring the SU8 photoresist only absorbs  $350 - 400\text{nm}$  wavelength UV light.

Figure 6.6 shows the SEM picture of hair posts fabricated using the UV-filter. The hair posts quality is much better than the ones without using UV-filter. Figure 6.6 (a) is a SEM image of a single hair-like sensor and (b) is an array of sensors.



(a)



(b)

**Figure 6.6 SEM of hair-like shear sensors applied with UV-filter**

**(a) A single sensor (b) Sensor array**

After the hair posts are fabricated on the sensor chip, the last step in the fabrication is to release the sensor structure to form capacitors.

### 6.1.3 Sensor Releasing

The PolyMUMPs™ handbook suggests 49% hydrofluoric acid (HF) etching of the PSG sacrificial layers. Experiments were done in the TMNF to release the sensor in undiluted HF. A profilometer was used to verify whether the structure was released or not. Figure 6.7 shows the sensor membrane deflections after release for 2 hours under different stylus loads using a Dektak surface profiler.

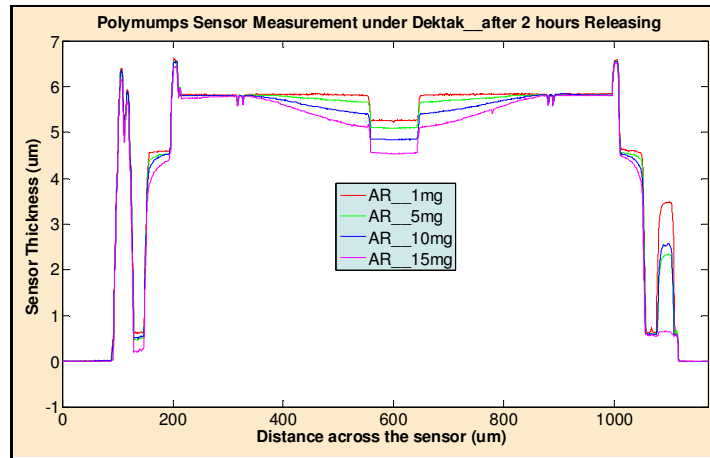


Figure 6.7 Sensor membrane deflections under different loads after releasing

Figure 6.7 demonstrates that the heavier the load, the greater the deflection of the membrane, indicating a released structure. The frequency response of a sweep sine voltage with frequency range from 50Hz to 1MHz was applied across the sensor electrodes. The frequency

response showed the sensor membrane was not moving under electrostatic drive. Further testing showed while Poly1 and Poly2 layer are electrically conducting, Poly0 is not conducting. Experiments in [112] demonstrated that galvanic attack occurs on polysilicon structures attached to gold in an HF solution, resulting in polysilicon discoloration and increased electrical resistance. In our design, the metal layer is directly deposited on the Poly0 layer for electrode wiring. The galvanic corrosion made the Poly0 wires not conducting. [112] demonstrated that releasing polysilicon structure in a 4:1 ratio of 49% HF and 39% HCl (hydrochloric acid) mixture can prevent galvanic attack on the grain boundaries of the polysilicon. This formula was adopted for hair-like shear sensor releasing. The releasing starts with immersing the hair-like sensor in the 4:1 mixture of HF and HCl solution for 50 minutes. Then the sensor is taken out and soaked in 4:1 ratio of methanol and DI water mixture for 10 minutes, allowing diluting and removing any residual HF and HCl solution. Then the sensor is soaked in pure methanol for 15 minutes followed by an air drying process.

During the releasing process, adhesion can occur after the sacrificial oxide material is dissolved. Since the device-to-substrate gap is so small, when the suspended sensor membrane is exposed to an aqueous rinse and dry cycle, strong attractive capillary forces can develop during the dehydration causing the structure collapses and subsequent pinning to

the substrate. Methanol is chosen as the last aqueous rinse because it has low surface tension, thus producing small capillary forces during the drying process. The same collapse can develop when the device is exposed to high humidity conditions due to same reason.

After methanol rinse, the sensor is placed in a dry box which is filled with dry air with a relative humidity of  $\leq 25\%$ , lower than relative humidity of  $\approx 49\%$  in the cleanroom. This helps to reduce adhesion related failures.

Figure 6.8 shows the difference of a single sensor without hairs before and after release.

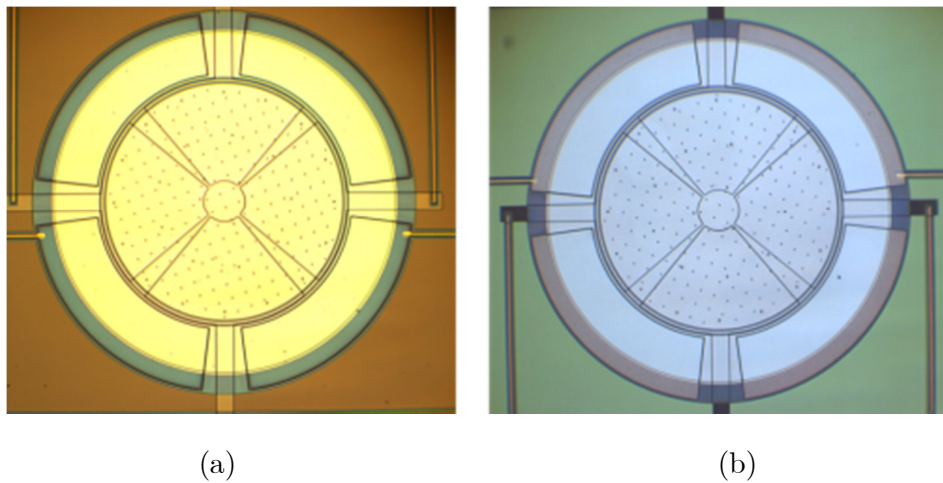


**Figure 6.8 Microscope images of single sensor without hair**

**(a) Before release (b) After release**

The hair posts' fabrication and sensor releasing run sheet can be found in Appendix D.

## 6.2 Sensor Packaging

The released hair-like shear sensor is packaged in a ceramic pin grid package (CPGA) from Spectrum Semiconductor Materials, Inc. The package is shown in Figure 6.9. The CPGA has 144 finger pads that are electrically connection to the sensor pads through a wirebonding process. The finger pads that are on the top surface of the package are connected to the pins on the bottom surface of the package. Every finger pad corresponds to one specific pin. Those pins can be inserted into a CPGA ZIF socket, which can be connected to an electronic testing board for sensor characterizations.

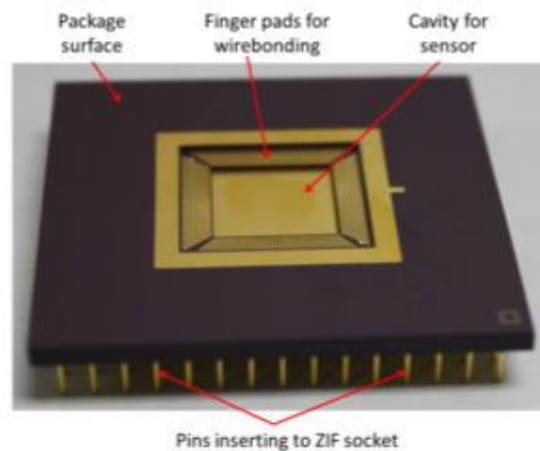
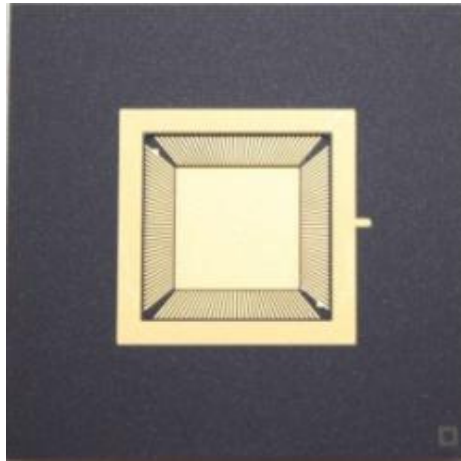
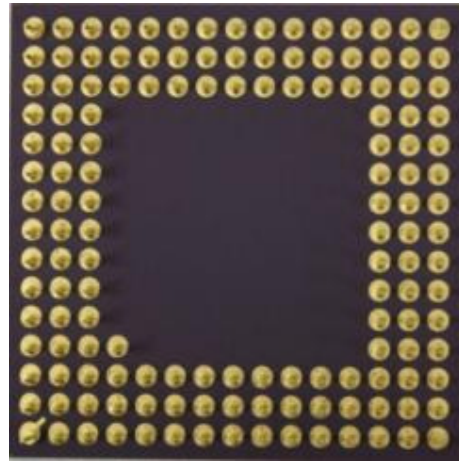


**Figure 6.9** Ceramic pin grid package (CPGA) for hair-like sensor

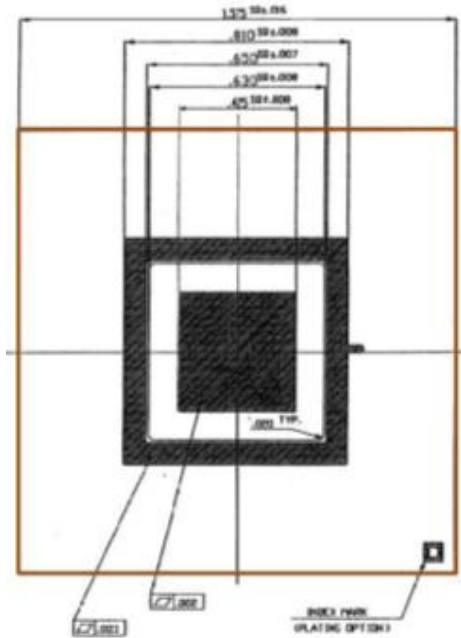
Figure 6.10 shows the top and bottom views of the package and geometry specification. The center cavity where the sensor chip will be placed is a  $10.8mm \times 10.8mm$  square.



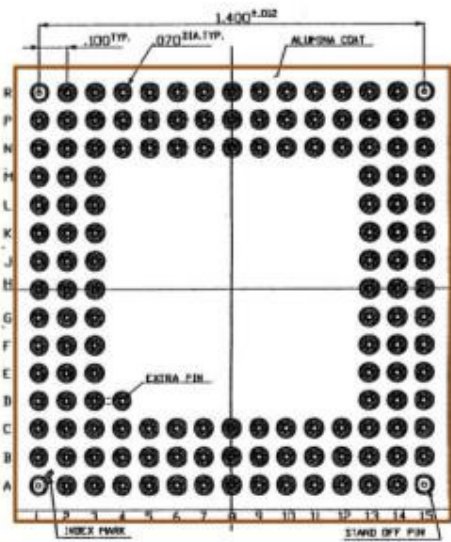
(a) Package top view



(b) Package bottom view



(c) Specification on top surface



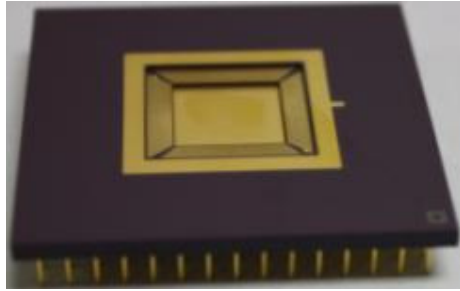
(d) Specification on bottom surface

**Figure 6.10 Package top and bottom view  
and dimensions specification (Dimensions in inch)**

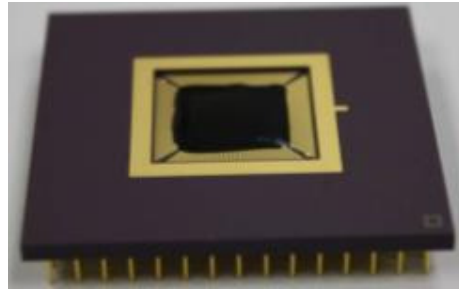
Photos in Figure 6.11 show the main steps in the packaging process. The hair-like sensors are designed for surface flow measurement, so it is critical that the sensor surface is flush with the package surface, in order

that the package will not disturb the flow. To achieve this goal, epoxy is filled in the package cavity as shown in Figure 6.11 (b) and then milled to the desired thickness shown in Figure 6.11 (c). The epoxy used is Namics Chipcoat G8345-6, which has a low coefficient of thermal expansion of  $15ppm/^{\circ}C$  and high resistivity of  $3 \times 10^{13} \Omega \cdot cm$ . When the sensor is fixed on the milled epoxy, the total thickness of the sensor chip and the epoxy is equal to the depth of the cavity, making the sensor surface flush with the package surface (Figure 6.11 (d)). Then the sensor is electrically connected to the package via wirebonding (Figure 6.11 (e)). The gap between the sensor the package is filled with epoxy (Figure 6.11 (f)). The finished package has a flat surface with the sensor embedded.

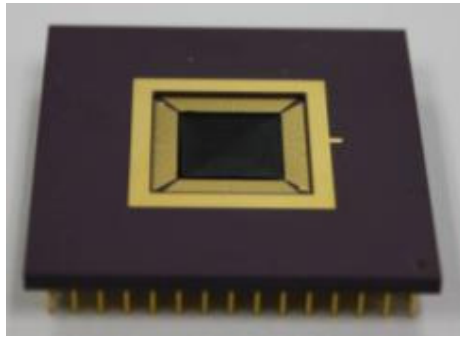
The detailed packaging process flow chart can be found in Table 6.2.



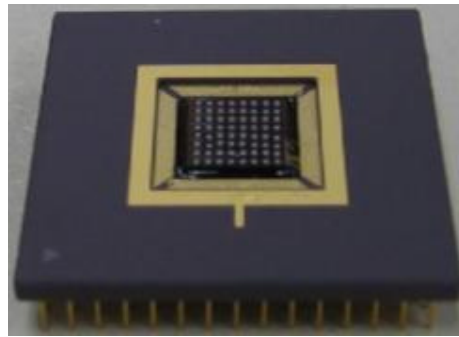
(a) Plain package



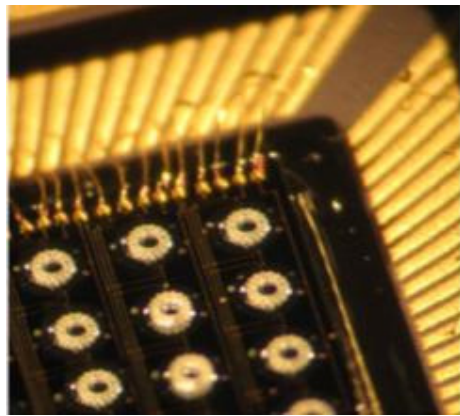
(b) The cavity is filled with epoxy



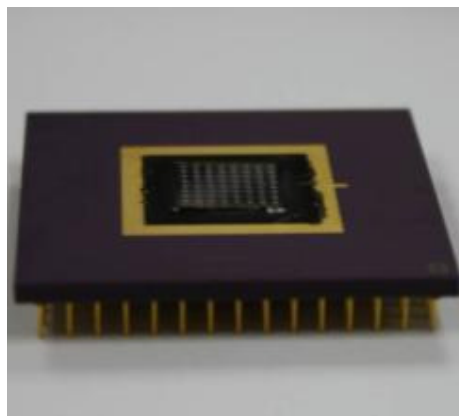
(c) Epoxy is milled to desired thickness



(d) Sensor chip is fixed on package



(e) Chip is wirebonded on package



(f) Finished sensor package

**Figure 6.11 Photos show the packaging process**

**Table 6.2 Sensor packaging process**

<b>Step</b>	<b>Description</b>
1	Clean a new package surface with isopropanol to remove any particles and dust (Figure 6.11 (a)).
2	Fill the package cavity with Chipcoat G8345-6. The epoxy should not overflow to cover the finger pad on the package (Figure 6.11 (b)).
3	Cure the epoxy at 1 hour at 90°C, followed by another hour at 160°C.
4	After cure, the epoxy is milled using a computer numerically controlled (CNC) milling machine to the desired thickness (Figure 6.11 (c)).
5	Place small amount of Chipcoat G8345-6 on the milled epoxy in the cavity of package. Center the sensor chip on top of Chipcoat G8345-6. An 80g force is applied on the center of the chip through a capillary tip using a wirebond machine to make sure the chip is flush with the package. The epoxy is cured under the same condition as in step 3. The epoxy functions as a glue, secure the sensor chip in place (Figure 6.11 (d)).
6	Another epoxy Chipcoat G8345D is painted on the edge of the sensor chip near the bonding pads on the chip. The strip of Chipcoat G8345D can prevent wirebonds from touching the edge of the chip and thus short the sensors. The same curing procedure is applied to Chipcoat G8345D.
7	Wirebonding through ultrasonic transduction using 25 $\mu$ m diameter gold wire between metal pads on sensor chip and finger pads on the package (Figure 6.11 (e)).
8	Fill the gap between the chip and the package surface with Chipcoat G8345-6. Make the epoxy as flat to the surface as possible. Cure the epoxy as indicated in step 3. The last filled epoxy protects wirebonds as well as makes the finished package surface flush to the sensor chip surface (Figure 6.11 (f)).

A printed circuit breakout board was design and fabricated for the purpose of testing the sensors. The breakout board is shown in Figure 6.12. A ZIF socket is soldered at the middle of the board. The sensor package is to be inserted into the socket. Each pad on the sensor chip is electrically connected to a pin on a row of male header pins connector through package and ZIF socket. The ZIF socket pin connection with the breakout board is shown in Figure 6.13. By connecting the pins on the breakout board to the testing equipment, the characterization of the sensor can be performed.

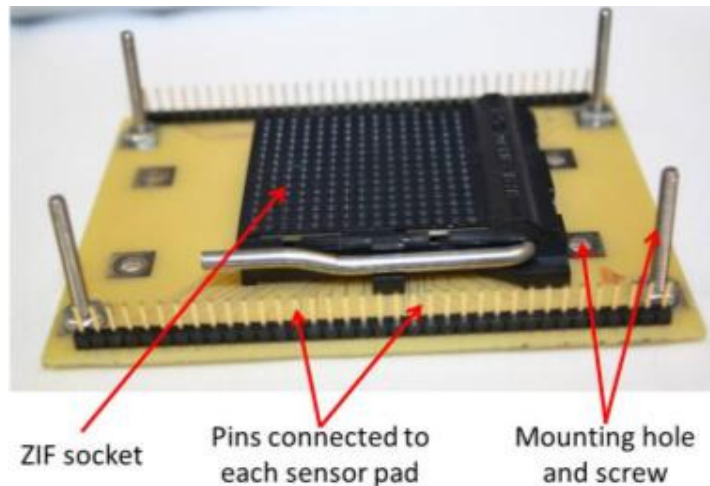


**Figure 6.12 Sensor testing breakout board**

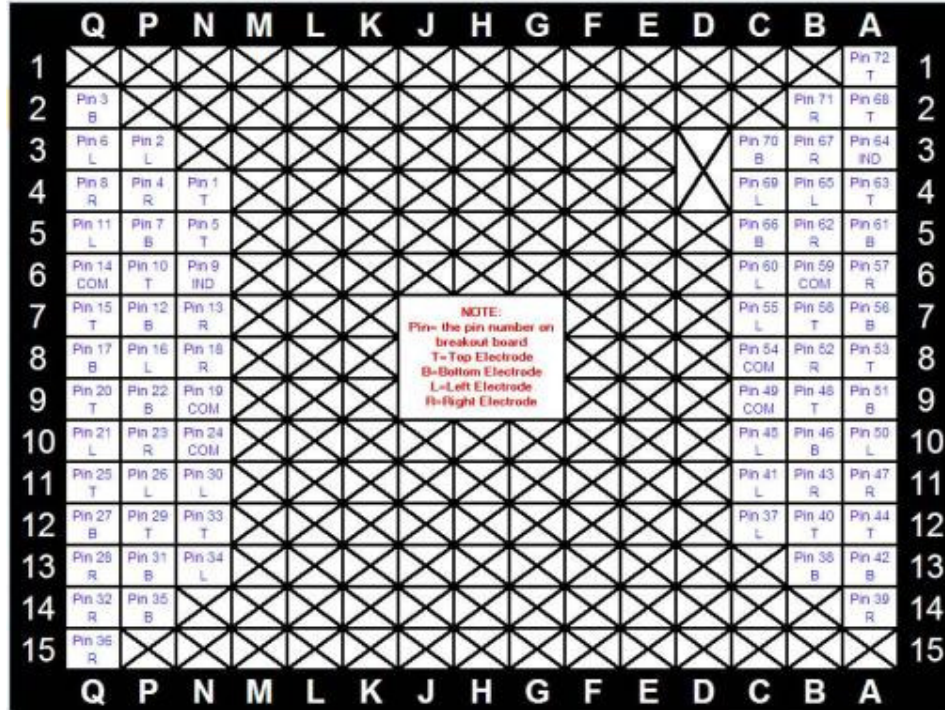


Figure 6.13 ZIF socket pin connection with breakout board layout (back-view)

## 6.3 Dynamic Characterization

### 6.3.1 Capacitance and Resistance Measurement

The sensor capacitance consists of two parts, the active capacitance which is the capacitance between the electrode and the membrane, and stray capacitance which is mainly from the capacitors formed by the silicon substrate and the anchors, metal pads, and wires that are separated by the thin silicon nitride. The stray capacitance varies from channel to channel due to the different lengths of the wires. The computed active capacitance between four electrodes of a group of four sensors and the membranes of those sensors is  $1pF$  and computed stray

capacitances are between  $42 - 52 pF$  . The computed stray capacitance is significant larger than the active capacitance of the sensor. The capacitances and resistances were measured using an LCR meter (Inductance (L), Capacitance (C), and Resistance (R)) for each group of four electrodes that are connected together. The measured capacitances between top/bottom electrodes and sensor membranes for sensor chip 10 are listed in Table 6.3.

Table 6.3 Measured capacitance and resistance of the sensors

Top Electrodes			Bottom Electrodes		
Pin	Capacitance	Resistance	Pin	Capacitance	Resistance
1	58.752 pF	12.8 MΩ	3	3.46 nF	964 Ω
5	60.029 pF	455 MΩ	7	9.00 pF	1.7 GΩ
10	60.167 pF	441 MΩ	12	64.152 pF	422 MΩ
15	7.201 pF	2 GΩ	17	62.971 pF	444 MΩ
20	8.152 pF	1.8 GΩ	22	1.336 nF	228 Ω
25	60.512 pF	441 MΩ	27	65.065 pF	410 MΩ
29	61.198 pF	442 MΩ	31	1.142 nF	278 Ω
33	60.998 pF	449 MΩ	35	65.788 pF	406 MΩ
40	60.239 pF	457 MΩ	38	64.362 pF	428 MΩ
44	60.126 pF	448 MΩ	42	64.549 pF	417 MΩ
48	60.055 pF	455 MΩ	46	64.176 pF	431 MΩ
53	58.931 pF	464 MΩ	51	63.892 pF	425 MΩ
58	13.206 pF	113 MΩ	56	63.872 pF	407 MΩ
63	60.247 pF	435 MΩ	61	65.146 pF	407 MΩ
68	63.390 pF	392 MΩ	66	134.393 pF	198 MΩ
72	1.762 nF	256 Ω	70	23.1 pF	1.2 kΩ

For pin 1, 3, 22, 31, 58, 70 and 72, the low resistances indicate that the membrane and the electrodes are shorted due to the collapse of the membrane. For pin 7, 15 and 20, the low capacitances but high resistance are due to the failure of the wirebonding that the sensor pads are not connected to the pins on the breakout board. For pin 66, the capacitance doubled and resistance is about half of what it should be. It is because pad 66 and pad 67 on the sensor are electrically connected during wirebonding process, making these two groups of sensors in series.

Since the sensor package will be measured in flow cell by detecting differentially capacitance change, only those sensors whose both top electrodes and bottom electrodes have proper capacitance and resistance can be considered as working sensors. Whether the sensor works properly or not will be further verified by their frequency response. Highlighted in Table 6.3 are the eight groups of sensors that can be considered as working sensors.

### **6.3.2 Frequency Response**

An Agilent 33220A function generator was used to excite a single sensor through the header pins on the breakout board. A 9V square wave voltage was sent to the sensor. The bias was applied to one of the electrodes on the bottom of the sensor and the membrane of the sensor. A

Polytec OFV 3001 Laser Doppler Vibrometer (LDV) was used to detect the motion of the membrane. The response was captured using Agilent DSO3062 oscilloscope show in Figure 6.14. Under the step input, the membrane was excited at its natural frequency. The measured natural frequency is around  $420\text{kHz}$ . This method is used to verify if a sensor is fully released and it can identify the first natural frequency of the sensor structure.

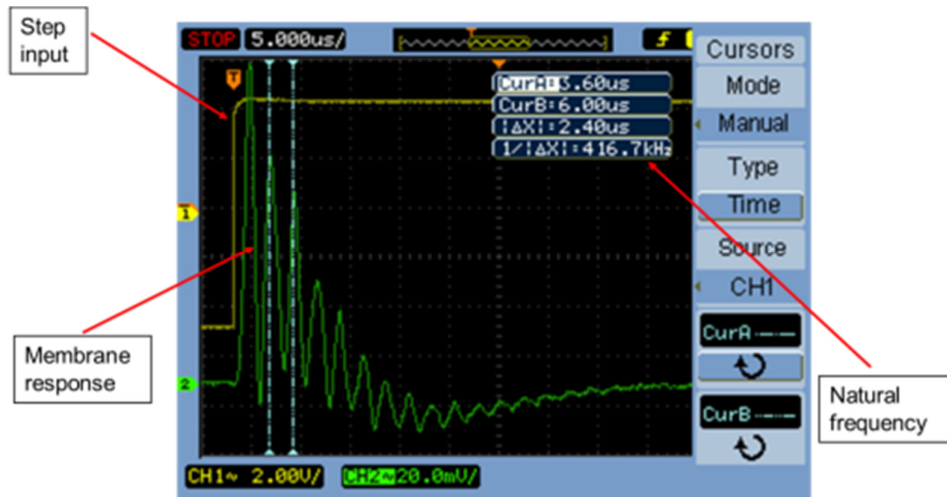


Figure 6.14 Sensor membrane vibration under a step input captured on oscilloscope

A Labview<sup>®</sup> program was used to plot frequency response of the sensors. A sweep sine voltage from  $50\text{kHz}$  to  $1000\text{kHz}$  was applied on one of the sensor on the chip through function generator. The membrane response was detected by LDV at every frequency and the detected signal was sent back to computer. The response of the membrane of one sensor was plotted as shown in Figure 6.15. The first natural frequency is about  $420\text{kHz}$ , similar to that detected on a oscilloscope.

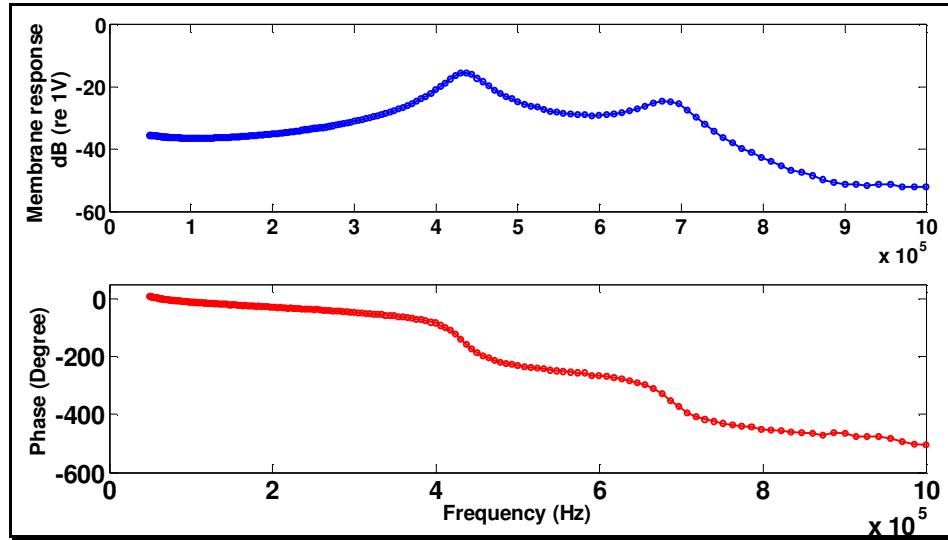
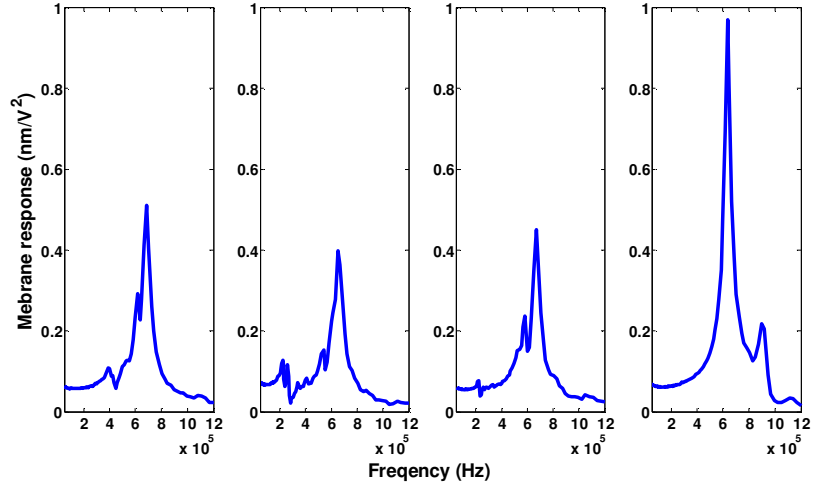


Figure 6.15 Frequency response of a single sensor group

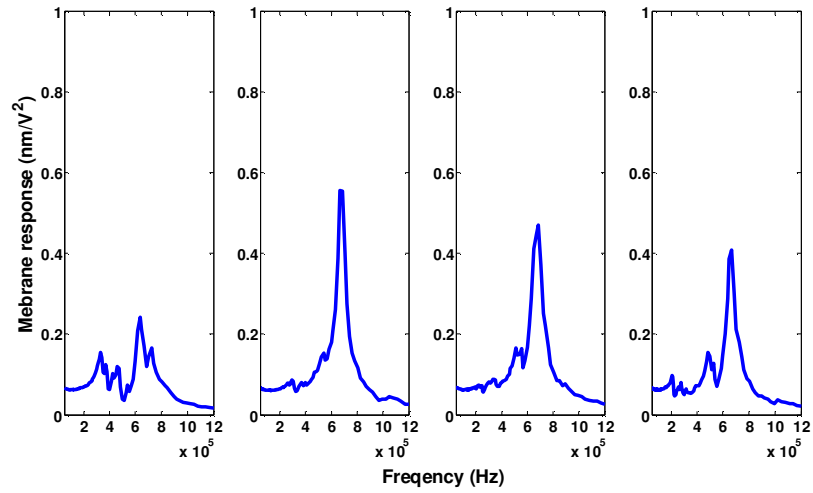
As mentioned above, frequency response can be used to verify whether a sensor is working properly or not. A Newport Universal Motion Controller/Driver is used to move the LDV laser sensor in a controlled way through a Labview<sup>®</sup> program. The program performs a sweep sine frequency response test on one sensor and the membrane's motion is monitored at its center by the laser sensor of LDV. Then the program commands the motion controller to move the LDV laser sensor to the center of another sensor until it finishes frequency response test for all 64 sensors on the chip. The drive signal is 2V peak to peak sine wave with  $V_{dc} = 9V$  DC offset. Root-mean-square (RMS) values for both stimulus and response were recorded by the Labview<sup>®</sup> program. The LDV has a displacement sensitivity of  $DS = 50nm/V^2$ . Figure 6.16 shows the membrane response of the sensors that are highlighted in Table 6.3, in

which the membrane response is expressed as  $\frac{RMS\_response \times DS}{RMS\_stimulus \times Vdc}$ . The

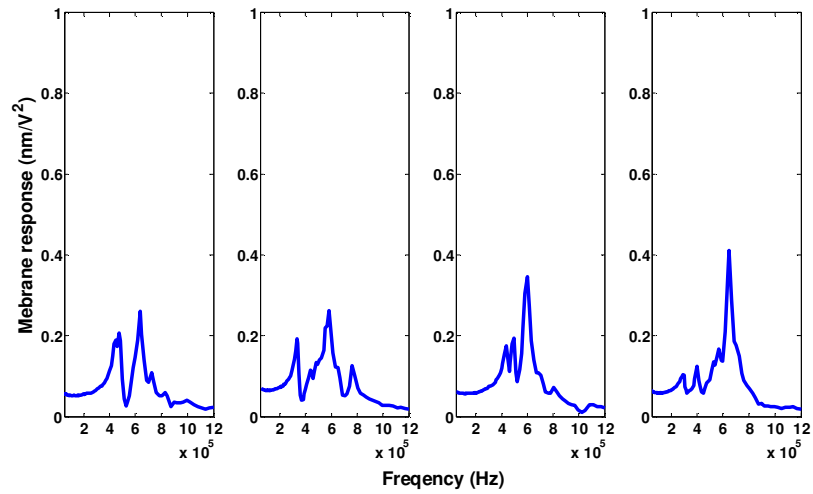
plot indicates all the sensor membranes responded to the stimulation though the amplitudes of the response vary from sensor to sensor. This could be caused by the laser not focusing on the center of the sensor membrane when moved by motion controller.



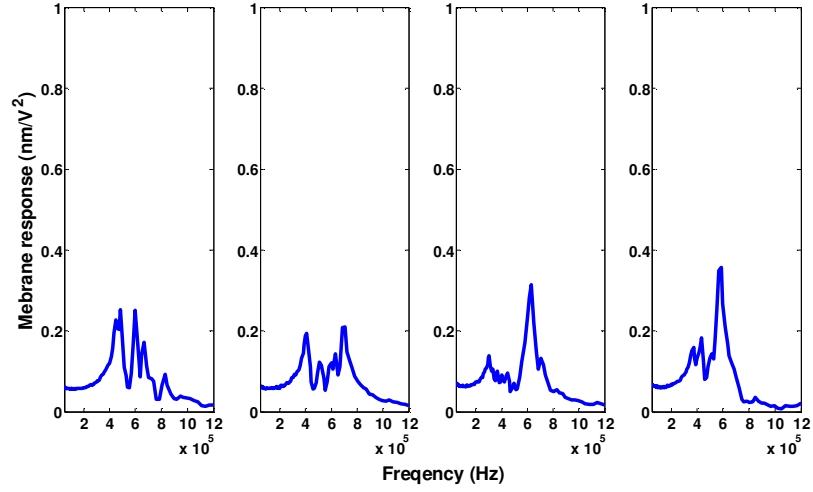
(a) Sensors connected to pin 10 & 12



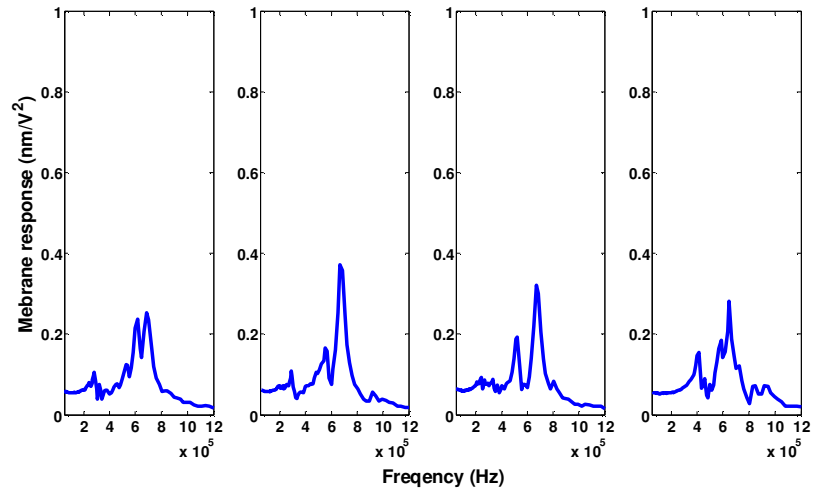
(b) Sensors connected to pin 25 & 27



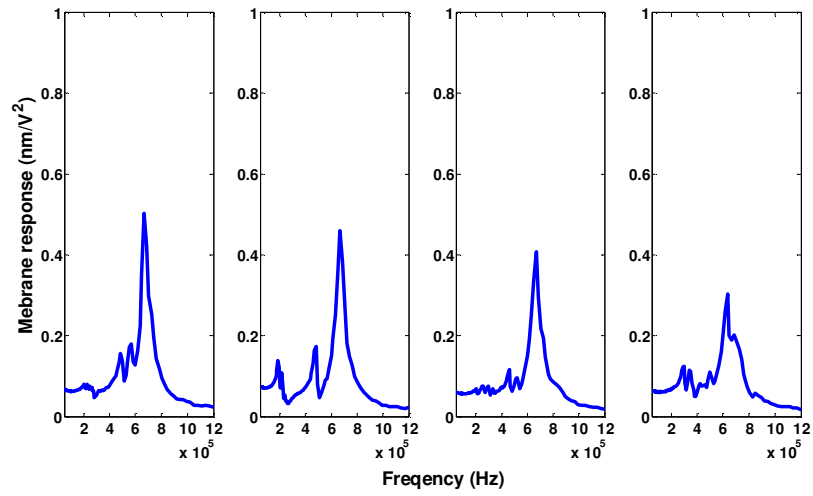
(c) Sensors connected to pin 33 & 35



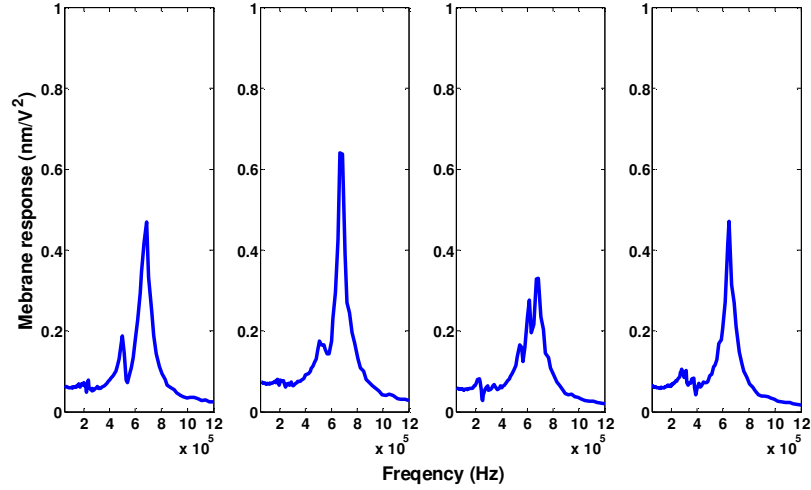
(d) Sensors connected to pin 40 & 38



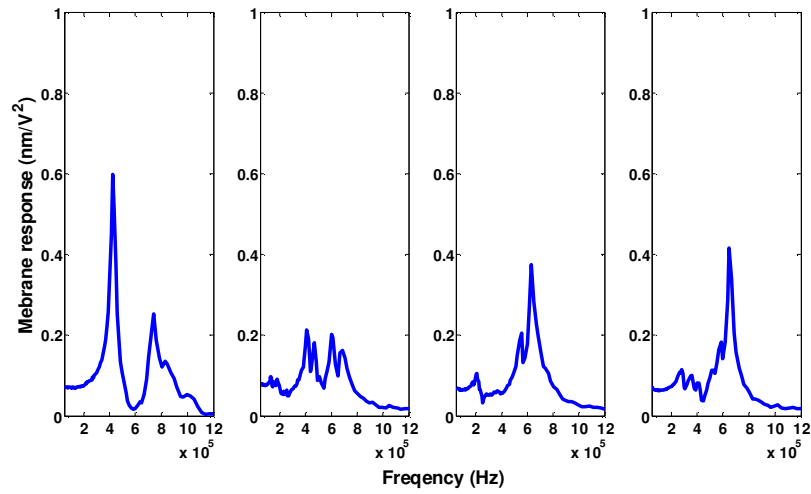
(e) Sensors connected to pin 44 & 42



(f) Sensors connected to pin 48 & 46



(g) Sensors connected to pin 53 & 51



(h) Sensors connected to pin 63 & 61

**Figure 6.16** Frequency response of different sensor groups

A reference sensor chip, chip8, was fabricated and packaged. This reference chip has no hair posts on it. It serves as a benchmark for hair-like shear sensor. It is tested along with the hair sensor and their results are often compared.

## **6.4 Laminar Flow Cell Testing**

The flow cell described in chapter 5 is used for hair-like shear sensor sensitivity tests. Two different kinds of test were carried out. The first is to use the LCR meter to measure sensor capacitances at different flow rates; the second is to use the electronic boards described in chapter 5 to measure the sensor differential capacitance change for different flow rates.

### **6.4.1 Wall Shear Stress in the Flow Cell**

The wall shear stresses in the flow cell can be computed using Eqn. (5.14) and (5.15) at different flow rates according to the flow chamber geometry. Pressure taps were also installed on the top plate of the flow cell to measure pressure drops at the flow cell wall. The shear stress can be computed from the pressure gradient. The shear stresses computed from flow rate and from pressure gradient are compared and plotted in Figure 6.17. For the flow range from 10–40CFH (Cubic Foot/Hour), the two computed stresses are very close and they increase linearly with the increase of flow rates. Computed shear stresses are listed in Table 6.4 at different flow rates.

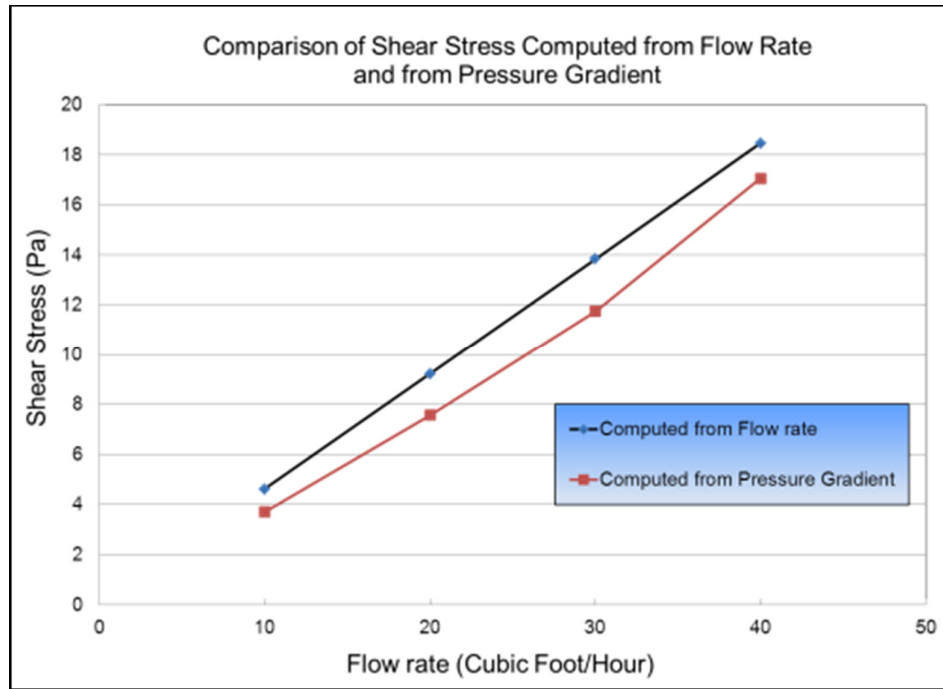


**Figure 6.17 Comparison of shear stress computed from flow rate and from pressure gradient**

**Table 6.4 List of shear stress computed from flow rate and from pressure gradient**

<b>Flow rete (CFH)</b>	<b>Flow rate (M<sup>3</sup>/s)</b>	<b>Computed from flow rate (Pa)</b>	<b>Computed from pressure gradient (Pa)</b>
5	$3.93 \times 10^{-5}$	2.3080	1.7831
10	$7.87 \times 10^{-5}$	4.6160	3.7026
20	$15.73 \times 10^{-5}$	9.2319	7.5662
30	$23.6 \times 10^{-5}$	13.8479	11.7518
40	$31.46 \times 10^{-5}$	18.4638	17.0643

### **6.4.2 LCR Capacitance Testing**

The breakout board was used for the flow cell LCR test. Since the LCR meter can only measure one capacitance at a time, the capacitance of the top and bottom electrodes of the sensors have to be measured separately. The breakout board has individual pin out connection as shown in Figure 6.12. All the top electrodes were connected together and all the bottom electrodes were connected together so that we can measure all working sensors on the chip simultaneously for maximum sensitivity. Two thin strips of PCB were designed and fabricated for this purpose. In these PCBs, all the top electrodes pin connections are connected together, as well as all bottom electrodes, right and left electrodes. These strips of PCB were soldered on female sockets which can be inserted in the pins on the breakout board. The soldered PCBs with female sockets inserted in the breakout board are shown in Figure 6.18 Breakout board for LCR capacitance test. The male pins that are soldered on the strips are used for test connections. Jumper wires are used to connect the two strips together. For the sensors which are not working properly, their connections to the breakout board pins were cut off by clipping off their corresponding pins on the bottom of the package.

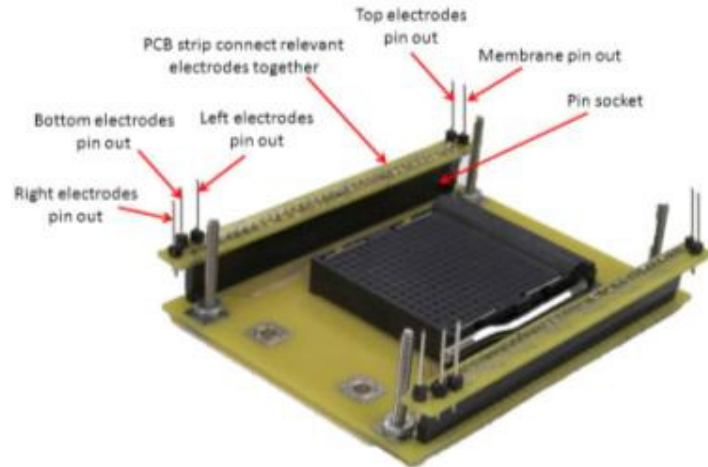


**Figure 6.18 Breakout board for LCR capacitance test**

Figure 6.19 is a Abaqus<sup>®</sup> simulation of the deformation of a sensor under flow. When the flow blows from the bottom electrode to top electrode direction, which is the situation for the flow cell test, the sensor membrane bends down at the bottom electrode position and goes up at the top electrode position. This deformation suggests that capacitance of the top electrode should decrease as flow rate increases, and the capacitance of the bottom electrode should increase.

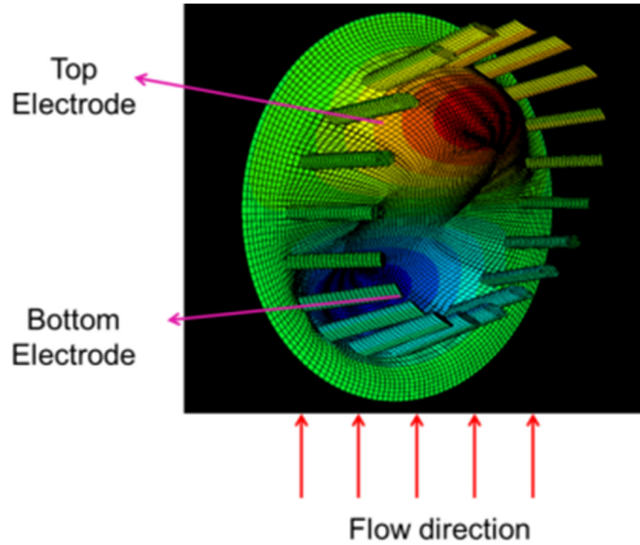


**Figure 6.19** Deformation shape of the sensor when subject to flow

Sensors without hair posts were used as a benchmark for the sensors with hair posts. Sensor chip 10 has hair posts and sensor chip 8 has no hair posts. Both chips' top electrodes and bottom electrodes capacitance change at different flow rates were recorded respectively. For every test, the flow rate was increased from  $10CFH$  to  $40CFH$  in  $10CFH$  steps, and decreased from  $40CFH$  to  $10CFH$  in  $10CFH$  steps. The following figures plot the capacitance changes vs. shear stress and sensitivities are shown on the plot for each test. The sensitivity for each test are listed results are compared in Table 6.5.

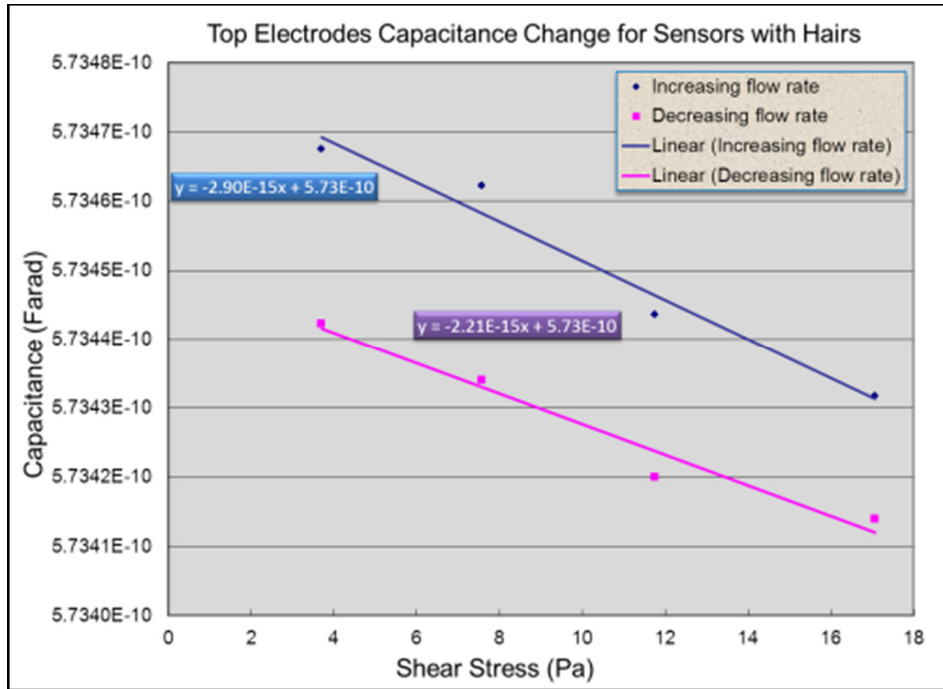


Figure 6.20 Top electrodes capacitance change for sensors with hairs at different flow rates (32 sensors in parallel)

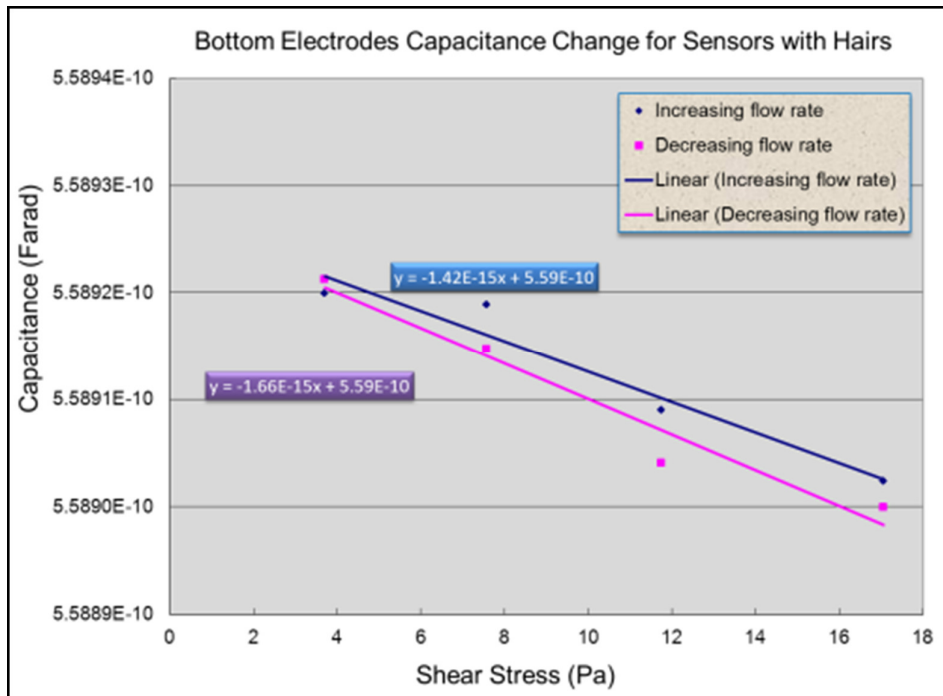


Figure 6.21 Bottom electrodes capacitance change for sensors with hairs at different flow rates (32 sensors in parallel)

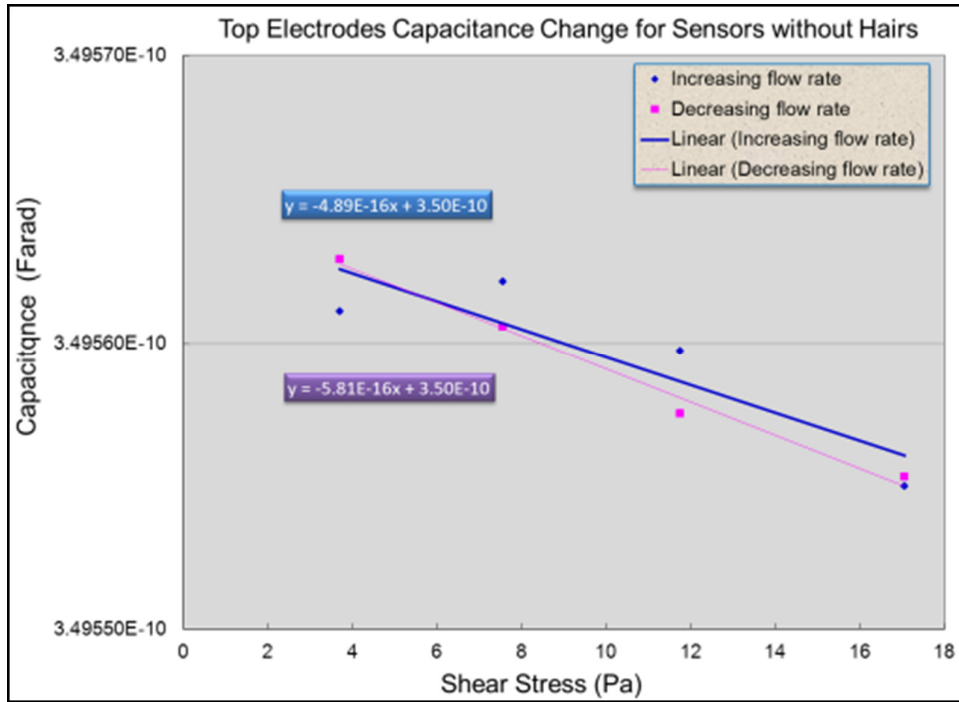


Figure 6.22 Top electrodes capacitance change for sensors without hairs at different flow rates (24 sensors in parallel)

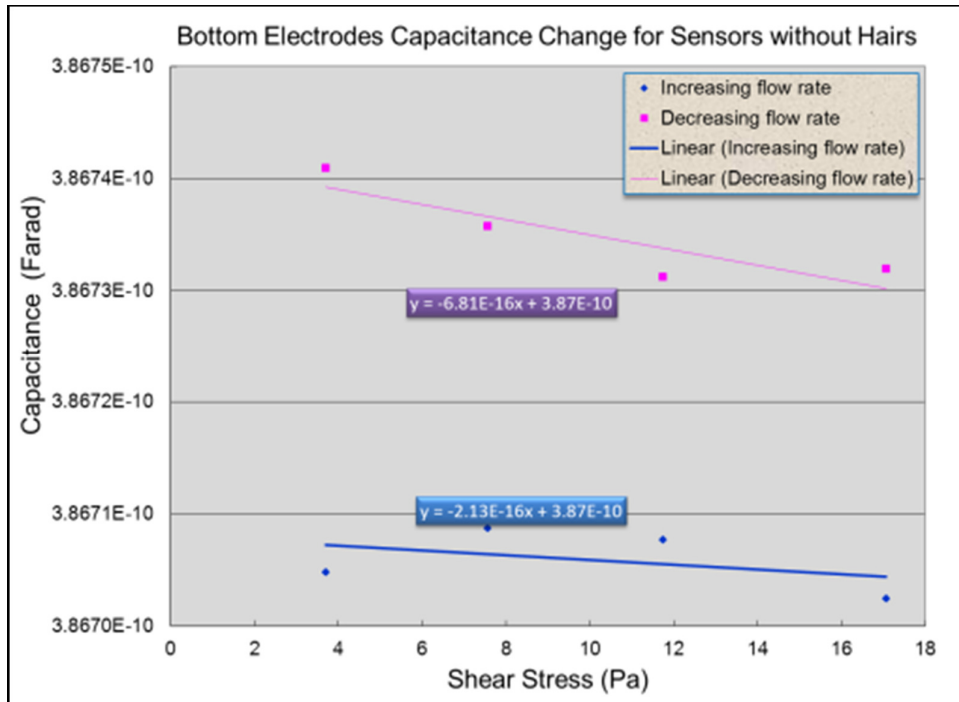


Figure 6.23 Bottom electrodes capacitance change for sensors with hairs at different flow rates (20 sensors in parallel)

**Table 6.5 Comparison of Sensitivity for sensors with hairs and without hairs using LCR**

	<b>Sensors with Hairs</b>		<b>Sensors without Hairs</b>	
	<b>Top Electrodes</b>	<b>Bottom Electrodes</b>	<b>Top Electrodes</b>	<b>Bottom Electrodes</b>
Average sensitivity ( <i>Farad/Pa</i> )	$-2.56 \times 10^{-15}$	$-1.54 \times 10^{-15}$	$-0.54 \times 10^{-15}$	$-0.46 \times 10^{-15}$
Number of sensors	32	32	24	20
Sensitivity per sensor ( <i>Farad/Pa</i> )	$-8 \times 10^{-17}$	$-5 \times 10^{-17}$	$-2.3 \times 10^{-17}$	$-2.3 \times 10^{-17}$

From Figure 6.19, we expect negative sensitivity for the top electrodes, (i.e. the capacitance decreases as flow rate increases) and positive sensitivity for the bottom electrodes. But the test results show that both the top electrode and the bottom electrode have negative sensitivity. However, the top electrode has a higher sensitivity than the bottom electrode. For sensors without hairs, we expect little or no sensitivity. But the test results show that for hairless sensors, both the top and the bottom electrode have the same negative sensitivity.

The proposed explanation for this phenomenon is that the whole surface of the sensor membrane is lifted up when flow passes by, as shown in Figure 6.24. The bulged membrane explains the negative sensitivity for both top and bottom electrodes for sensors without hairs. For sensors with hairs, the bending effect of the hairs shown in Figure 6.19 is superimposed on top of the bulged membrane, resulting in the actual

membrane deflection demonstrated in Figure 6.24. This explains the observed negative sensitivity for both top and bottom electrodes, with the top electrode exhibiting a higher sensitivity than the bottom electrode.

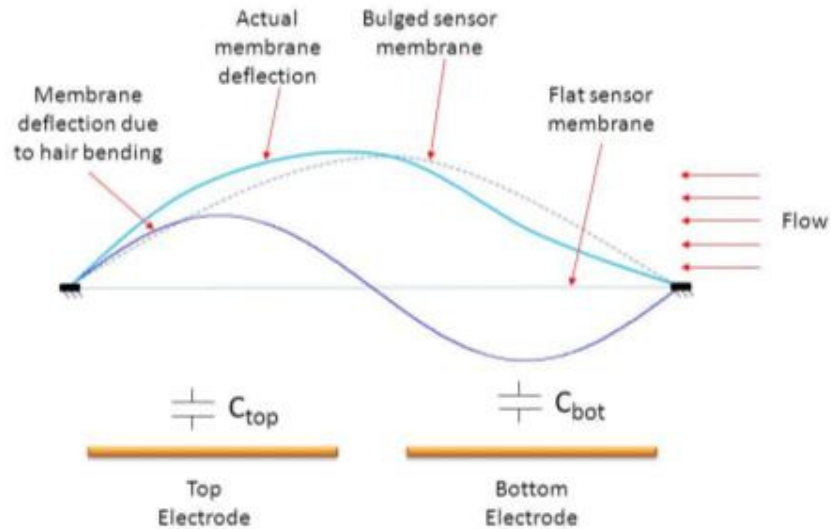


**Figure 6.24 Hypothesis of shear sensor deformation under flow**

The LCR meter test results discovered that the sensor membrane was lifted under flow. This unexpected phenomenon demonstrated the importance of using a differential testing scheme, whose test results will not be affected by the bulged membrane. Differential testing is described in next section.

## 6.4.3 Integrated System Testing

### 6.4.3.1 Experiment Setup

Figure 6.25 shows the experimental setup for the test. A Labview® controls the DAQ board through a GPIB adapter. Thin wires are inserted to the DAQ board. Those wires are soldered on a male D-subminiature connector DE9 on the other end. This male DE9 is connected a female DE9 which is soldered with wires that are connected to Molex pins that are inserted in the Molex female sockets on electronic board. These connections allow the computer to program the MS3110 chip to desired settings through the Labview® program.

A DC power supply provided 5V and 16V powers for temporary and permanent programming of MS3110.

Dry house air is sent to the flow cell through a plastic tube that connects the flow cell and an adjustable flow meter. The flow meter controls the volume flow rate. The differential capacitance changes are sensed by the MS3110 sensor and readout as voltages using a precision voltage meter. The voltage meter is connected to a SMA connector on the electronic board through a BNC to Banana plug adapter and a BNC to SMA cable. The voltage meter is connected to the computer through a GPIB adapter and cable. The Labview® program records the change of the voltages. At every flow rate, the measured time is 2 minutes and 182 voltage points

are recorded.

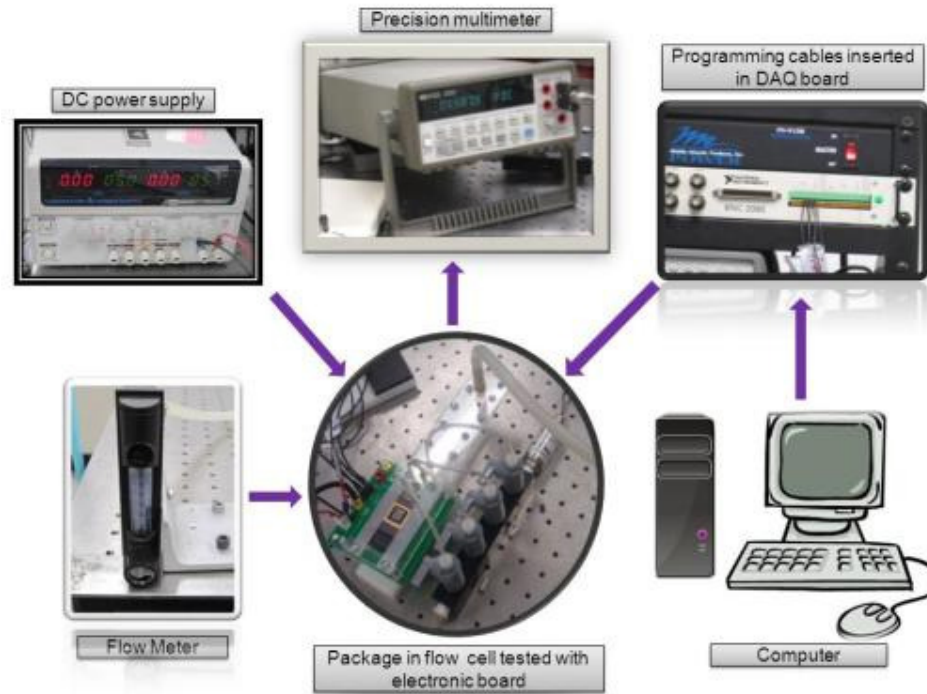


Figure 6.25 Experiment setup for hair sensor flow cell test using electronic board

### 6.4.3.2 Sensor Sensitivity Testing

According to the MS3110 transfer function Eqn. (5.21), for  $CF = 0.019 pF$ , the sensor sensitivity is  $\frac{\Delta C}{V} = 0.3 pF / V$ . A test was done using the programming board to measure the actual sensitivity of MS3110 sensor. A known capacitor was connected to  $CS2IN$  input terminal of a MS3110 sensor. The readout voltage was recorded for this capacitor. Then different capacitors were connected to  $CS2IN$  and voltages were recorded for each input capacitor. The capacitor vs. voltage is plotted in Figure 6.26. The plot shows a measured sensitivity

$\frac{\Delta C}{V} = 9.3pF / V$  , which is 30 times smaller than the data sheet stated.

The smaller sensitivity of MS3110 makes the detecting small changes more difficult but does not change hair sensor sensitivity in terms of capacitance vs. shear stress.

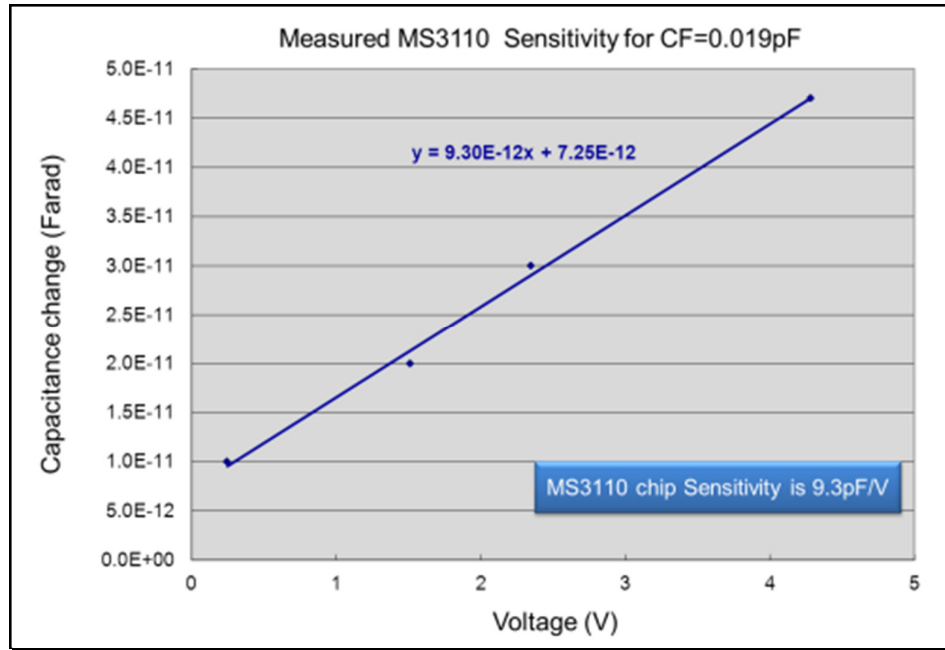


**Figure 6.26 Measured MS3110 sensitivity when CF=0.019pF**

Tests were done in the flow cell for both sensors with hairs and sensors without hairs. Flow rate was increased and then decreased for both sensor chips, in the same manner as the LCR meter tests. The readout voltages were converted to capacitance using the measured MS3110 sensitivity. The capacitance changes at different flow rates were plotted in Figure 6.27. The average differential hair-like shear sensor sensitivity is  $2.37 \times 10^{-16} \text{ Farad} / \text{Pa}$  for 32 sensors. The single sensor sensitivity is  $0.74 \times 10^{-17} \text{ Farad} / \text{Pa}$  , which is reasonably close to the predicted

sensitivity of  $1.437 \times 10^{-17} \text{ Farad} / \text{Pa}$ .

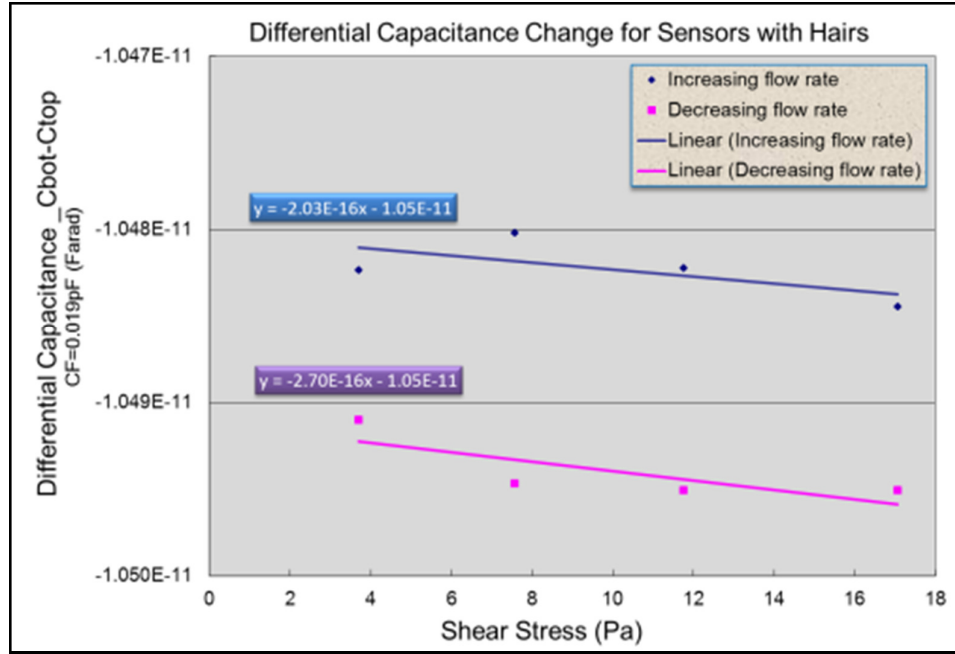


**Figure 6.27 Differential capacitance change for sensors with hairs at different flow rate (32 sensors in parallel)**

Figure 6.28 shows the differential capacitance test for sensors without hairs. The average sensitivity is  $0.7 \times 10^{-16} \text{ Farad} / \text{Pa}$  for 28 sensors. The single sensor sensitivity is  $0.025 \times 10^{-17} \text{ Farad} / \text{Pa}$ , which is 30 times less than the sensitivity of hair-like sensor.

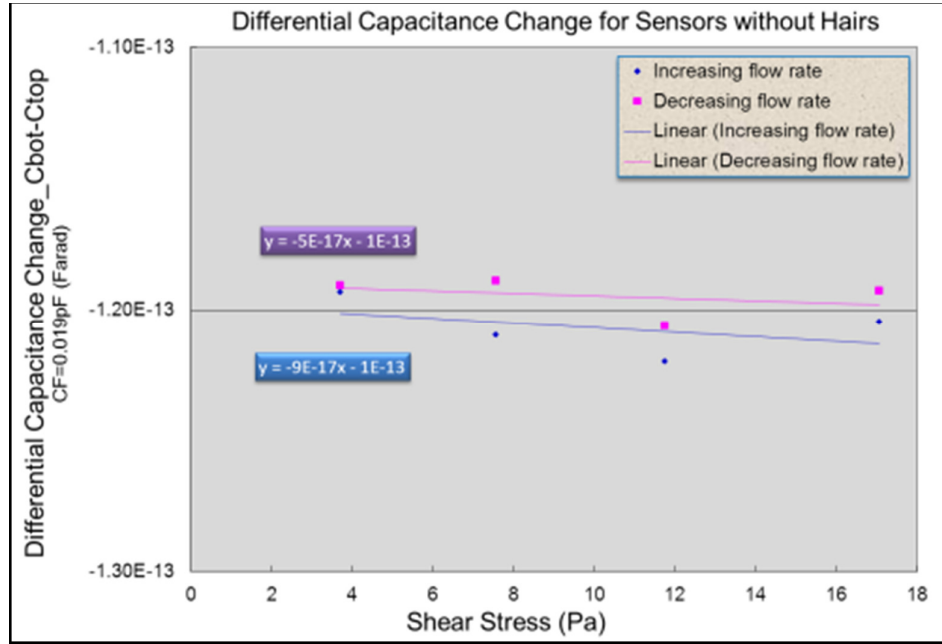


**Figure 6.28 Differential capacitance change for sensors without hairs at different flow rate (28 sensors in parallel)**

## 6.5 Discussion

Drift and noise are common problems of electronic measurements. In this section, their effects on sensor measurements are discussed. The repeatability of the measurement is discussed and the performances of current sensor array is compared with previous work.

### 6.5.1 Noise

The noise for chip 10 is shown in Figure 6.29 for flow rates from 10CFH to 40CFH . As flow rate increases, the averaged voltage decreases, indicating the sensor is measuring capacitance change for the flow

change.

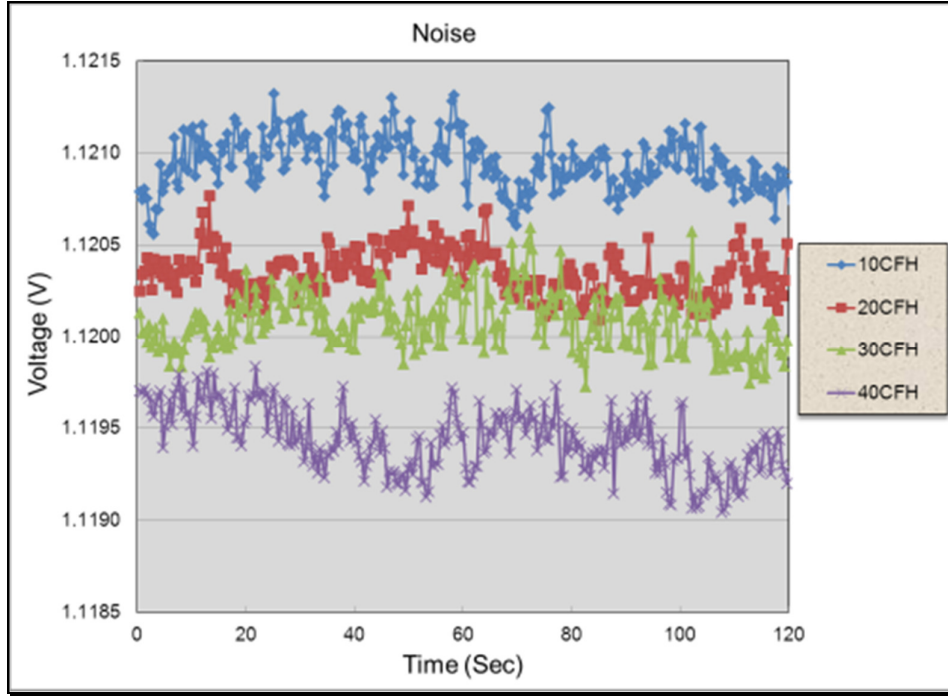


**Figure 6.29 Sensor noise at different flow rates**

Noise is stochastic variations of the measured signal about the averaged signal. The averaged noise density is calculated for 10CFH flow as follow:

$$P_{noise} = \frac{RMS[V_{measured} - Average(V_{measured})]}{\sqrt{F_{measured}}} \frac{V}{\sqrt{Hz}}$$

Where  $P_{noise}$  is averaged noise density,  $V_{measured}$  is the measured voltage at 10CFH as shown in Figure 6.29.  $F_{measured}$  is the Nyquist frequency of the sampled data. There are 182 samples taken in 120 seconds time period.

So the measured frequency is computed as:

$$F_{measure} = 1 / \frac{120}{281} / 2 = 1.17Hz$$

The computation starts with calculating the average of measured voltage.

Then the measured voltage at every time point is subtracted from the

$$P_{noise} = \frac{1.43 \times 10^{-4} V}{\sqrt{1.17}} = 1.3 \times 10^{-4} \frac{V}{\sqrt{Hz}}.$$

The RMS resolution of the sensors in a 1Hz band for 32 sensors in parallel is:

$$\begin{aligned} R_{rms-1Hz} &= P_{noise} \times \sqrt{1Hz} \times \frac{1}{Sensitivity\_32sensors} \times Sensitivity\_MS3110 \\ &= 1.3 \times 10^{-4} \frac{V}{\sqrt{Hz}} \times \sqrt{1Hz} \times \frac{1}{2.37 \times 10^{-16} F / Pa} \times 9.3 \times 10^{-12} \frac{F}{V} \\ &= 5.1 Pa \end{aligned}$$

For our measurements, the sampling data are averaged over 120 seconds, so the RMS resolution for  $1/120\text{sec}/2=0.00417\text{Hz}$  band is

$$R_{rms-1Hz} \times \sqrt{0.00417} = 5.1 \times 0.065 = 0.33 Pa.$$

### 6.5.2 Drift

Drift occurs when the voltage is measured under a fixed flow rate for a long period time, the voltage changes slowly. The sensor drift measured at 10CFH flow rate for 2000 seconds for hair sensor chip 10 using electronic board is shown in Figure 6.30, which has the same measurement settings as data shown in Figure 6.29.

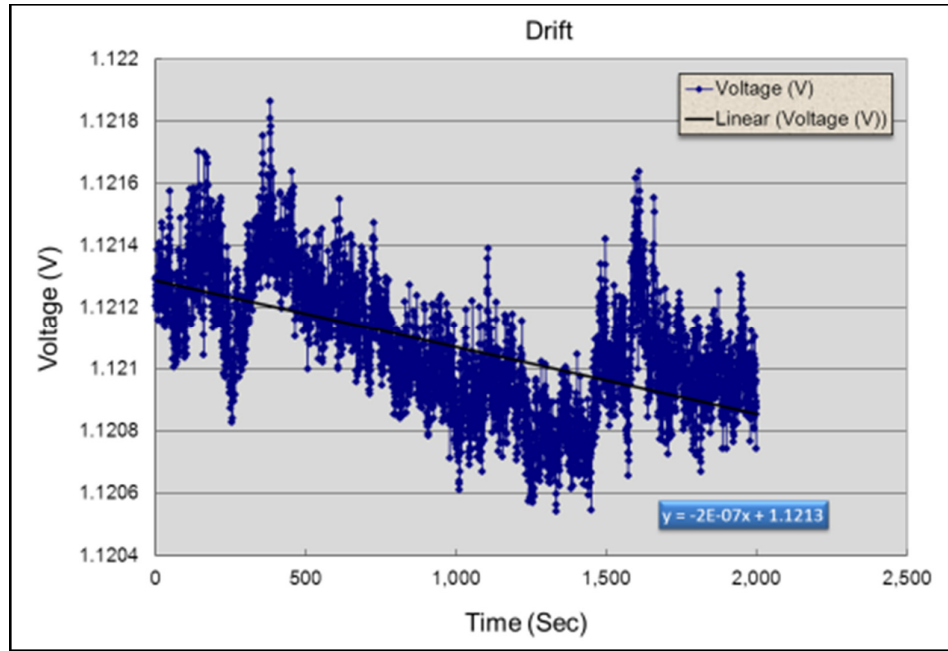


**Figure 6.30 Sensor drift measurement at 10CFH**

The drift slope is approximately  $2 \times 10^{-7} V / s$ , as seen from Figure 6.30.

In terms of shear stress, the drift is:

$$\begin{aligned}
 \text{Drift} &= 2 \times 10^{-7} V / s \times \frac{1}{2.37 \times 10^{-16} F / Pa} \times 9.3 \times 10^{-12} F / V \\
 &= 7.8 \times 10^{-3} Pa / s
 \end{aligned}$$

In order to drift 5.1Pa, it will take 654 seconds, which is 11 minutes. Thus if measuring in a 1 Hz bandwidth, the noise will be more significant than the drift for measurements of less than 11 minutes. If the measurement time is longer than 11 minutes, drift may become more significant than noise.

### 6.5.3 Repeatability

The repeatability of the sensor array was tested. Figure 6.31 shows multiple tests in an aluminum flow cell mentioned in chapter 7 for flow rate from 10–40CFH with an interval of 5CFH. This data was taken nine months after the previous data set. This sensitivity tested is very close to those shown in Figure 6.27. Though the test results show some noise, they demonstrate that the sensor array sensitivity is repeatable.

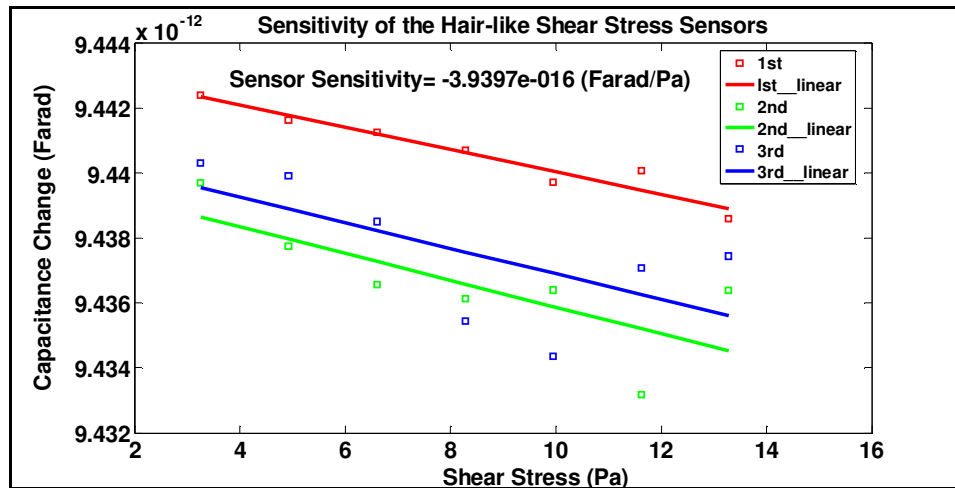


Figure 6.31 Sensitivity tests for sensors with hairs at different flow rate (32 sensors in parallel)

### 6.5.4 Comparison of current work with previous work

The performances of the hair-like shear stress sensor are compared with some of the previous reported shear sensors and are listed in Table 6.6.

Table 6.6 Sensor performances comparison chart

Author	Sensitivity	Bandwidth	Dynamic Range (Pa)	Dynamic Range (dB)
CURRENT WORK 2011	$26\mu V / Pa$	$420kHz$	0.33 to $>17$	$>34$
Li [89] 2008	$4.24\mu V / Pa$	$6.7kHz$	0.0114 to $>2$	$>45$
Schmidt [85] 1988	$52\mu V / Pa$	$10kHz$	0.01-1	20
Pan [64, 65] 1999	$1.02V / Pa$	$16kHz$	0.5-3.8	18
Zhe [86] 2005	$337mV / Pa$	$0.53kHz$	0.04-0.2	14
Barlian [88] 2007	$0.052mV / Pa$	$19kHz$	-	-
Padmanabhan [90, 91] 1996, 1997	$0.3V / Pa$	$4kHz$	0.0014-10	77
Grosse [72-74, 102, 103] 2008-2009	-	$2kHz$	0.01-0.85	38
Liu [104-106] 2005-2007	$590\mu V/\mu m$	DC	50nN-25 $\mu$ N	54

Compared with other shear stress sensors, the current hair-like shear stress sensor has largest bandwidth of  $420kHz$ . It also has a large dynamic range of  $34dB$ . For the current laminar flow cell tests, the sensor can measure a linear response up to  $17Pa$  before flow becomes turbulent. It has maximum measurable shear stress among the sensors listed. The sensitivity of the sensor is  $26\mu V / Pa$ , which can be increased using an amplifier. The resolution of the sensor,  $5Pa$  in a  $1Hz$  band, is the worst

of all surveyed sensors. But this is due to the higher maximum measurable stress. Since flow stresses in the wind tunnel are expected to reach  $100Pa$ , it is critical that the sensor respond well at high stresses.

## 6.6 Conclusion

The second part of this dissertation, from chapter 4 to chapter 6, described the development of a hair-like shear stress sensor array. The sensor array was successfully designed, fabricated, packaged and tested in a laminar flow cell.

The sensor array was designed to measure shear stresses up to  $100Pa$  for a wind tunnel testing environment. Laminar flow cell tests demonstrated that the sensor array can measure shear stresses up to  $17Pa$ , before the flow becomes turbulent. Figure 6.32(b) shows that under  $5CFH$  flow, which generate  $1.8Pa$  wall shear stress, in the current flow cell, the sensor membrane maximum deformation is  $0.3nm$ , which is only  $0.01\%$  of the membrane thickness of  $3.5\mu m$ . Let us assumed that a plate deforms linearly when the maximal deformation of the plate is  $1\%$  of the plate thickness. According to the deformation of the sensor membrane, the hair-like shear stress sensor array is able to measure shear stresses up to  $180Pa$ , which exceeds our goal of  $100Pa$ .

As mentioned in chapter 4, from an engineering perspective, for the

turbulence boundary layer measurement for the aeroacoustic applications, a shear stress sensor with bandwidth of  $20kHz$  is sufficient. The hair-like sensor has a bandwidth of  $420kHz$ , which also exceeds the engineering requirement for this aeroacoustic application.

# Chapter 7

## CONCLUSIONS AND FUTURE WORK

In this chapter, the research goals, objectives, and key results are summarized. Recommendations for future work on physical cochlear models and the hair-like shear sensors' designs and testing are provided.

### 7.1 Conclusions

Orthotropic material properties of the gerbil basilar membrane were computed using finite element method based on point stiffness and space constant data. Two boundary conditions were investigated: simply supported boundaries for both spiral ligament and spiral lamina, and simply supported boundary for spiral ligament and clamped boundary for spiral lamina. The material properties were quantified at different locations along the length of basilar membrane for both boundary conditions. For both simply supported boundary conditions, the computed radial modulus varies from  $15MPa$  to  $1MPa$  from the base to the upper middle turn of gerbil cochlea and the longitudinal modulus

decreases from  $0.2MPa$  to  $0.05MPa$ . For clamped and simply supported boundary conditions, the computed radial modulus varies from  $6.6MPa$  to  $0.5MPa$  in the same region and the longitudinal modulus decreases from  $0.4MPa$  to  $0.05MPa$ . The orthotropy varies along the length of the gerbil basilar membrane from a maximum of 65 close to the base to a minimum of 10 in the upper middle turn.

These quantified properties provide essential information for more accurate understanding of the motion of cochlear structures and the pattern of the travelling wave, both for mathematical models and physical cochlear models.

A 16 time scaled one-duct guinea pig cochlear model was designed and fabricated. The goal of this research is to verify if a scaled model using scaling law can capture the cochlear response compared with mathematic model based on WKB method. Two boundary conditions were explored: clamped and simply supported boundaries. The experimental data showed that simply supported boundary conditions agreed with WKB results better than clamped boundary. The characteristic frequencies are about 100-300Hz difference for experimental results from WKB results and the magnitudes of the ratio of membrane to Stapes velocity are about 15-25dB lower than those calculated from WKB method. The WKB model did not produce very similar simulation results compared with experimental results. The differences might be caused by the pretension

in the membrane of cochlear model, which was not presented in WKB method.

A novel hair-like sensor for direct measurement of shear stress was designed, fabricated and tested. The sensors were fabricated using PolyMUMPs™ foundry process and hair posts were fabricated at TMNF. The sensors were successfully released and packaged in CPGA. A series test textures were designed and fabricated, including breakout board, program evaluation board, electronic board and flow cell. The sensors were tested in a flow cell at different flow rates using both LCR meter and MS3110 chip. The test results were compared with benchmark sensors without hair posts. LCR meter tests showed a bulged sensor membrane under flow. Differential capacitance measurements using MS3110 showed higher sensitivities for the hair sensors than sensors without hairs. The measured single hair sensor sensitivity is  $0.74 \times 10^{-17} \text{ Farad} / \text{Pa}$ , about half of the predicted sensitivity  $1.856 \times 10^{-17} \text{ Farad} / \text{Pa}$ . The RMS resolution is  $0.33 \text{ Pa}$  with 120 seconds of averaging.

## **7.2 Future Work for Cochlear Models and Hair-like Shear Sensors**

With the available quantified gerbil basilar membrane properties, the next step is to build a scaled gerbil cochlear model and implement the

orthotropic material properties using scaling law to study gerbil cochlear mechanics. Active elements can be added in the physical model by adding sensors and actuators on the membrane to study the active response of cochlea through feedback circuits.

For hair-like shear sensors, there are some issues that affect the performance of the sensors. They are addressed as below:

1. The post fabrication of hair posts on the polysilicon surface of PolyMUMPs<sup>TM</sup> sensors was difficult. The hair posts are made of SU8 photoresist. SU8 is very sticky. After features were aligned, during the photoresist exposing process, which uses soft contact exposing method, SU8 can easily stick on the mask when the mask and sensor chip were brought to close contact. When the mask and the wafer were separated after expose, it often resulted in partial SU8 tearing from the sensor chip, which left some sensors without hair posts on the chip. However, when the mask and sensor chips were not brought close enough, the gap between them often resulted in larger and not separated hair posts. It is difficult to bring the mask and sensor chips to just right contact that a perfect expose can be performed.

2. The adhesion between SU8 posts and polysilicon surface was not strong. The hair posts can be knocked out from the sensor chips during post process steps, such as sensor release, packaging and wirebonding. This adhesion problem affects the robust performing of the sensors. Note,

however, that no hairs came off during flow testing.

3. The capacitance changes caused by the environment greatly affect test results. The test setting should not be disrupted during the testing process. However, current test set up requires a testing person to adjust the flow rate and computer operation, which inevitably interrupt the test settings.

4. Though the shear sensors were designed for bidirectional flow test, a flow cell that produces bidirectional flows was not designed. Bidirectional tests will be addressed and studied in future work.

To address the issues mentioned above and improve the sensor performance, a new design was created. The layout of the design is shown in Figure 7.1. This new design has sensors built on a glass substrate, which will significantly reduce the stray capacitance. The sensor layers and parameters as listed in Table 7.1.

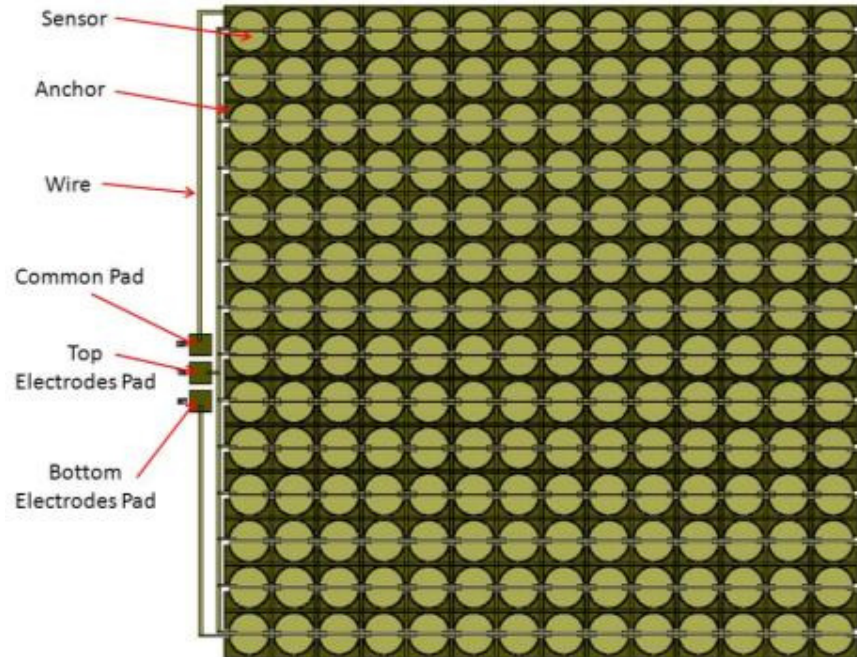


Figure 7.1 New design layout

Table 7.1 New design process parameters

Layer Name	Materials	Thickness	Process
Electrodes Layer	Chrome/Gold	$0.3\mu m$	Sputter + Lift off
Sacrificial Layer	Titanium/Copper	$2\mu m$	Sputter + Lift off
Structural Layer	Nickel	$3\mu m$	Plating
Hairpost Layer	Nickel	$20\mu m$	Plating

This new design has 296 sensors on one chip, which is more than four and half times of those in current design. The sensor size is kept the same. In this design, a differential capacitance scheme is used to eliminate any effect caused by flow pressure. The new design has only top and bottom electrodes to measure one directional flow. In this way, the single electrode size is doubled. Also, all the sensors are connected together. Only three pads need to be wirebonded, the top and bottom electrode

pads and the common pad that connects all sensor membranes together.

All the fabrication will be done at TMNF.

The new design starts with a  $0.3\mu\text{m}$  gold layer which defines the top and bottom electrodes, and all the routing wires. A  $2\mu\text{m}$  copper is used as a sacrificial layer. A  $3\mu\text{m}$  nickel layer is plated as sensor membrane layer, and it is anchored on the glass substrate. All the membranes are connected through the anchors. Lastly,  $20\mu\text{m}$  tall hair posts are nickel plated on top of the nickel membrane. The nickel plated hair posts have a much stronger bond with the sensor membranes than the SU8 posts. The nickel plated hair posts will solve the difficult fabrication and fragility issue of SU8 posts.

A new flow cell was designed and fabricated as shown in Figure 7.2. This new flow cell is made of aluminum which has only two parts. Instead of using a shim to create the flow chamber, the new design has the flow chamber milled in the top plate of the flow cell as shown in Figure 7.2 (b). The new bottom plate combined the previous middle and bottom plates. The new design is easier to assemble and thus has less chance for misalignments. Since Aluminum is conducting, it can reduce the EMI effect by dissipating charges to ground through the electronic testing board. The new flow cell will be used to test the hair-like shear stress sensor array with an amplifier to increase the voltage signal. The CAD drawing of the new flow cell is in Appendix C2.

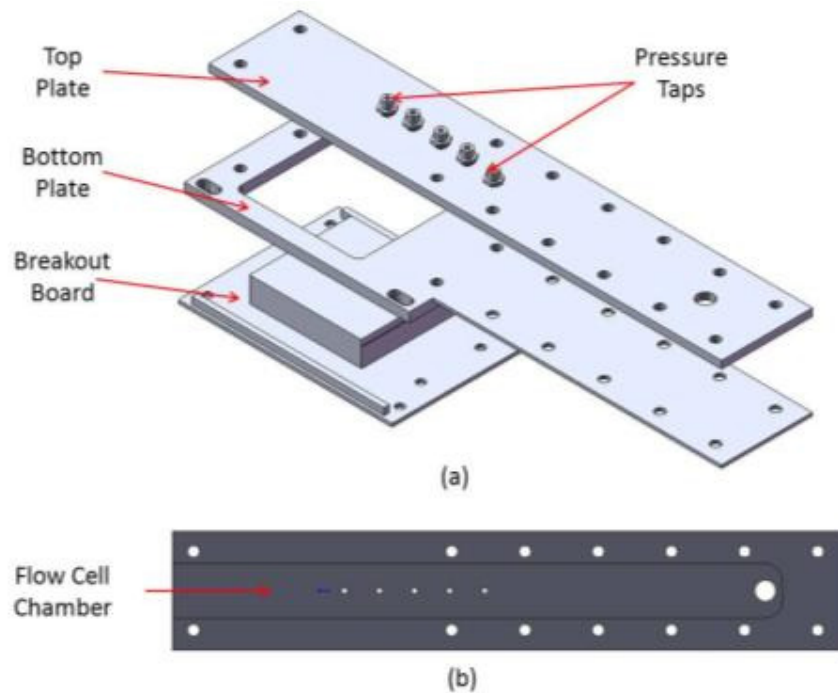


**Figure 7.2 Aluminum flow cell**

**(a) Exploded view of flow cell assembly (b) Bottom view of flow cell top plate**

A digital electronic flow meter will replace the current manually adjusted flow meter. The electronic flow meter can be controlled and adjusted using a Labview<sup>®</sup> program. No personnel is needed during the test, making it possible to have undisturbed environment for the whole test process.

## APPENDIX A: MATLAB® SCRIPTS

### A1 WKB Calculation for Cochlear Duct Response

#### Main Function

```
%This file implements a WKB solution to the three dimensional fluid filled
%duct problem, as described in Steele and Taber's paper "Comparison of WKB
%calculations and experimental results for a three- dimensional cochlear
%model" for clamped boundary.
1 clear lambda w x Disp Mag Phase xi phi dF zeta Aj h b eta i j
2 global Rho visc fluidmodes omega Ajlocal mode_sq_int_inv_local Rhop z
3 global h Cap_Gamma_coeff D L1 L2
   %Add the functions subdirectory to the matlab path:
4 path(path,'Z:\sliu\ASME 2008\cochlea model\WKB\SteeleWKB\functions');
   %Number of fluid cross-modes to use
5 fluidmodes=15;
   %Create vector of excitation frequencies to solve at
6 numfreqs=200;
7 startfreq=100; %Hertz
8 endfreq=20000; %Hertz
   %Number of x positions to solve at
9 numlocs=300;
10 z=1;
   %Number of transverse positions to compute structural mode shape for
   %numerical integration
11 widthmesh=100;
   %Maximum allowable tolerance in lambda (local wavenumber)
12 lambda_tol=0.01;
   %Set up model geometric properties (unit in mks)
13 l=0.256; %total length of the BM
14 x1=1/4; %Location of change in linear taper (fraction)
   %Width of the duct
15 L10=2.954e-2; %width at base
16 L1m=1.448e-2; %Width at 1/4 of base
17 L1f=0.8255e-2; %width at apex
   %Varying width along the duct
18 L1_vary=interp1([0 x1 1],[L10 L1m L1f],linspace(0,1,numlocs),'linear');
   %Effective height of the duct. The duct is treated as rectangular but has
   %the same cross area as the original guinea pig duct
19 L20=11e-3; %Fluid height at base (m)
```

```

20 L2m=5.6e-3;    %Fluid height at 1/4 of base (m)
21 L2f=3.25e-3;    %Fluid height at apex (m)
    %Varying height along the duct
22 L2_vary=interp1([0 x1 1],[L20 L2m L2f],linspace(0,1,numlocs),'linear');
    %Membrane dimensions
23 b0=1e-3;        %membrane width at base x=0 (m)
24 bfinal=8e-3;    %membrane width at apes x=1 (m)
    %Membrane width varies along the duct
25 b_vary=b0*exp(linspace(0,1,numlocs)*log(bfinal/b0));
26 c_vary=(L1_vary-b_vary)/2;
27 h=0.076E-3;    %membrane thickness
    %Stapes area [m^2]
28 Ast=pi*(0.33*0.0254/2)^2;    %drive screw has diameter 0.33 inches
    % Material properties
29 Rho=950*2;      %density of fluid and times 2 to consider as two duct
30 Rhop=1384;     %density of plate
31 de=0.01;       %hysteretic damping from material
32 pois=0.35;     %Poisson's ratio for the membrane
33 orth=1;        %orthotropy of the membrane material
34 visc=0.48;     %viscosity of the fluid
35 E=2.5e9;       %Young's modulus of the membrane
    %To do with membrane stiffness, including hysteretic damping:
36 D=((h.^3)/12)*(E*(1+i*de)/(1-(pois^2)));
    %-----END OF USER DEFINED CONSTANTS-----
    %Set up position and Circular frequency vectors:
37 w=logspace(log10(startfreq),log10(endfreq),numfreqs)*2*pi;
38 x=linspace(0,1,numlocs);
    %Produce Aj at each location by integrating structural mode shapes with
    %fluid mode shapes.
39 eta=zeros(numlocs,widthmesh);
40 xi=zeros(size(eta));
41 for i_x=1:numlocs,
42     blocal=b_vary(i_x);
    %Coordinate of the membrane varying from 0 to b
43     xi(i_x,:)=linspace(0,blocal,widthmesh);
    %Shpae function of membrane at cross section for clamped boundary
44     eta(i_x,:)=(sin(pi*xi(i_x,:)/blocal)).^2;
45 end
    %Get the inverse of the integral of the mode shape squared at each location
    %x, which appears in Heq, and also the Fourier coefficients Aj for each
    %location. For hinged and clamped boundary conditions there is an
    %analytical expression, otherwise integrate numerically.

```

```

46 for i_x=1:numlocs,
47 L1=L1_vary(i_x);
    %Aj and mode_sq_int_inv are different for each fluid cross-mode,
    %different at each location
48 for j_m=0:fluidmodes-1,
49 if j_m==0,
50 Aj(i_x,1)=b_vary(i_x)/2;
51 else
52 if (pi*(j_m*(-j_m^2*b_vary(i_x)^2+4*L1^2)))==0
53 Aj(i_x,j_m+1)=Inf;
54 else
55 Aj(i_x,j_m+1)=((2*L1^3)/(pi*(j_m*(-j_m^2*b_vary(i_x)
56 ^2+4*L1^2))))*(sin(pi*j_m*(b_vary(i_x)+c_vary(i_x))/L1)-sin(pi*j_m*c_vary
57 (i_x)/L1));
58 end
59 end
60 mode_sq_int_inv(i_x)=8/(3*b_vary(i_x));
61 end %End j_m loop
62 end %End i_x loop
    %A small fix to deal with numerical errors produced by the formulas for
    %hinged and clamped mode shapes for certain conditions:
63 inf_Aj=find(isinf(Aj));
64 num_inf=length(inf_Aj);
65 i_xlist=rem(inf_Aj,numlocs);
66 i_xlist=i_xlist+numlocs*(i_xlist==0);
67 j_mlist=floor(inf_Aj/numlocs)-(i_xlist==numlocs);
68 for cnt1=1:num_inf,
69 i_x=i_xlist(cnt1);
70 j_m=j_mlist(cnt1);
71 Aj(i_x,j_m+1)=trapz(xi(i_x,:),eta(i_x,:).*cos(j_m*pi*(xi(i_x,.)+c(i_x))./
72 L1_vary(i_x)));
73 end
    %Loop through frequencies and x locations and determine the local
    % wavenumbers, lambda, which will be complex. This is done using the
    % Eikonal eqn. given in equation 48A, derived from Hamiltons principle and
    %the averaged Lagrangian. F depends on both Heq(lambda) and Cap_Gamma
    % (lambda). So, these will have to be in the function used in the Newton
    % Raphson procedure, equation 48. See file eqn48A.m for the function
    % definition
74 for i_w=1:numfreqs, %frequency counter
75 omega=w(i_w); %driving frequency
76 for i_x=1:numlocs, %location counter

```

```

    %Some properties at this location
77  X=x(i_x);           %current X location
78  blocal=b_vary(i_x); %local membrane width
79  L1=L1_vary(i_x);   %local duct width
80  L2=L2_vary(i_x);   %local duct height
81  Ajlocal=Aj(i_x,:); %local Aj
82  mode_sq_int_inv_local=mode_sq_int_inv(i_x);
    %Now from this we can get the local wavenumber, lambda, from the
    %Eikonal equation
83  if i_x ==1          %first guess near Stapes
    %Use a 1-D simplification (Steele eqn. 15c and 25a), and assume
    %Cap_Gamma can be approximated by its constant term,
84  G=1.3333*(pi^4)/(blocal^4);
    %Try different first guess
85  guess=sqrt(((4*Rho*blocal*omega^2)/(L2*pi^2))*(D*G-0.25
86  *Rhop*h*omega^2)^-1);
    %Initial guess of lambda from 1-D approximation near stapes
87  lambda(i_w,i_x)=guess;
88  else
    %If this isn't the first time through, use last locations
    %lambda for the initial guess for root finding
89  guess=lambda(i_w,i_x-1);
90  end
    %If the root finder failed last time don't bother continuing
91  if isnan(guess)
92  lambda(i_w,i_x)=NaN;
93  dF(i_w,i_x)=NaN;
94  else
95  Cap_Gamma_coeff=[0.25*orth 0 +(2*pi^2/(3*blocal^2))*orth 0 4*pi^4/
96  (3*blocal^4)];
    %Error at current guess:
97  ERR=eqn48A_single([],guess); %ERR=F
98  numiters=0;
    %If the while loop is bigger than 100, assume it isn't converging, break
    %out the loop, and set lambda to NaN. Usually it takes only 3 or 4 iterations to
    %converge on the things tried so far
99  while(norm(ERR)>norm(lambda_tol) && numiters<100),
100 numiters=numiters+1;
    %First, we need to compute the Jacobian matrix at our current
    %guess It's much faster not to use the numerical numjac routine:
101 R=(eqn48A_single([],guess+real(guess)/1000)-ERR)*(1000/real(guess));
102 I=(eqn48A_single([],guess+imag(guess)/1000*i)-ERR)*(1000/imag(guess));

```

```

103 J=[real(R) real(I);imag(R) imag(I)]; %This is the Jacobian matrix
    %This Jacobian tells us how we expect the computed error to change if we
    %vary the real and imaginary parts of lambda. So, to head towards zero, we
    %want to solve J*delta=-E where delta is needed change in [real(guess)
    %imag(guess)] to send E to zero
104 delta=J\(-[real(ERR); imag(ERR)]);
    %Now change our guess by this amount
105 guess=guess+delta(1)+delta(2)*j;
106 rec(numiters,i_w,i_x)=guess;
    %And re-compute error with backtracking:
107 ERR_old=ERR;
108 ERR=eqn48A_single([],guess);
109 end
    %If it was not converging(i.e. the number of iterations exceeded 100) then
    %set lambda to NaN
110 if numiters>=100
111 guess=NaN;
112 end
    %Lambda for this membrane position
113 lambda(i_w,i_x)=guess;
114 dF(i_w,i_x)=(eqn48A_single([],guess+real(guess)/1000)-ERR)*(1000/real
115 (guess));
116 end
117 end %End the location index loop
118 end %End the driving frequency index loop
    %Initialize phi and zeta
119 phi=zeros(size(lambda));
120 zeta=zeros(size(lambda));
121 for i_w=1:numfreqs,
122 omega=w(i_w);
123 %Just integrating real part now use eqn. 54 for zeta
124 phi(i_w,:)=pi/2-cumtrapz(x,real(lambda(i_w,:)));
    %Just integrating imaginary part
125 zeta(i_w,:)=cumtrapz(x,imag(lambda(i_w,:)));
    %The membrane displacement relative to stapes displacement
126 Disp(i_w,:)=(Ast)*(lambda(i_w,1)/Aj(1,1)).*(((b_vary(1)*dF(i_w,1))./(b_vary.
127 *dF(i_w,:)).^0.5).*exp(j*phi(i_w,)-zeta(i_w,:)));
    %The membrane velocity relative to stapes displacement
128 v(i_w,:)=j*omega*Disp(i_w,:);
129 end
    %Unwrap the phase of velocity in radians, relative to Stapes velocity
130 for cnt=1:numfreqs,

```

```

131 Phase(cnt,:)=unwrap(angle(v(cnt,:)));
132 end
    %Define frequency for plotting purpose
133 freq=w/(2*pi);
    %Plot the results:
134 figure;
    %This figure plots magnitude of velocity at 2cm,5cm, 10cm and 15cm
135 semilogx(freq,[20*log10(abs(v(:,25))),20*log10(abs(v(:,60))),20*log10(abs(v(:,
136 118))),20*log10(abs(v(:,177)))]
137 title('WKB Results')
138 xlabel('Frequency (Hz)')
139 ylabel('Magnitude of Membrane Velocity (dB re Stapes Velocity)')
140 axis([startfreq endfreq -100 80])
141 legend('2cm', '5cm', '10cm','15cm')
142 figure;
    %This figure plots phase of velocity at 2cm,5cm, 10cm and 15cm
143 semilogx(freq,[unwrap(angle(v(:,25))),unwrap(angle(v(:,60))),unwrap(angle(v(:,
144 118))),unwrap(angle(v(:,177)))]);
145 title('WKB Results')
146 xlabel('Frequency (Hz)')
147 ylabel('Phase of Membrane Velocity (rads re Stapes Velocity)')
148 axis([startfreq endfreq -100 80])

```

## Called Equation eqn48A\_single

```
1  %This file shows explicit definition of Eikonal dependence on
2  %complex lambda for use in Newton-Raphson method for Eqn. 48A in
3  %Steele and Taber, "Comparison of WKB calculations and
4  %experimental results for a three-dimensional cochlear model",
5  function F=eqn48A_single(Params,lambda)
6  global Rho visc fluidmodes omega Ajlocal mode_sq_int_inv_local Rhop z
7  global h Cap_Gamma_coeff D L1 L2 orth
8  %From equation 8, due to separation of variables on Laplace's equation:
9  mj=sqrt(((0:fluidmodes-1).*pi./L1).^2 + lambda^2);
10 %The equivalent fluid height including viscous effects in Eqn. 23
11 Heq=mode_sq_int_inv_local*(sum((((z*Ajlocal.^2)./(mj.*L1)).*(1./((tanh
12 (mj*L2)-(mj.*sqrt(visc./(i*omega*Rho+(mj.^2)*visc)))))).*(ones(fluidmodes,1)
13 +[0; ones(fluidmodes-1,1)]')));
14 %Compute Cap_Gamma from its coeffs:
15 Cap_Gamma=Cap_Gamma_coeff(1)*lambda^4 + Cap_Gamma_coeff(3)
16 *lambda^2 +Cap_Gamma_coeff(5);
17 %Compute F(lambda)
18 F=(omega^2)*(Rho*Heq+0.5*Rhop*z*h)-2*z*D*Cap_Gamma;
```

## A2 Optimization of Hair Posts Locations

```
1 % Optimization of hair post location for hair-like shear sensor
2 %This file computes the deflection of a clamped circular plate under
3 %two coupled forces, representing the moment caused by hair posts. These
4 %two coupled forces are symmetric about the center of the plate,
5 %representing two hairs stand on the two sides of the center of the
6 %plate symmetrically. The coupled forces are applied in a way to form a
7 %counter-clockwise moment.
8 %The deflection of the plate under a concentrated force is in the form:
9 % $w(r,\theta)=R_0+\sum(R_m*\cos(m*\theta))$ ;where  $m=1\dots\infinite$   $R_0$  and  $R_m$  are
10 %the coefficient of the solution which are functions of  $(r,\theta)$  and
11 %defined in the following sections The electrode deflection and the
12 %change of the capacitance are computed as well
13 clear all
14 %% The geometry and material properties of the plate (unit in MKS)
15 a=300e-6; %the radius of the polysilicon plate
16 h=3.5e-6; %thickness of the plate (poly1:2um + poly2:1.5um)
17 electrode_in=50e-6; %the inner radius of electrode, which is a torus shape
18 electrode_out=290e-6; %the outer radius of electrode, which is a torus shape
19 electrode_angle=40; %the half angle of the electrode, in degree
20 E=158e9; %Young's modulus of Polysilicon
21 v=0.22; %Poisson's ratio of Polysilicon
22 D=E*h^3/(12*(1-v^2)); %Stiffness of the plate
23 %distance between b1 and b2; i.e. the moment arm of the coupled force
24 c=[10e-6 20e-6 40e-6 60e-6 80e-6];
25 interval=5e-6; %intervals distance between every calculation
26 g0=2e-6; %initial gap between top and bottom electrodes
27 ep0=8.854e-12; %F/m, permittivity of the air
28 %% Circular plate deflection under the first coupled forces
29 for j=1:5
30 clearvars -except c j
31 %parameters
32 P1=1e-6; %N, applied force on b1
33 P2=-1e-6; %N, applied force on b2;
34 d=0; % Force P1 and P2 are applied at angle d with distance c apart;
35 e=d+2*pi; %e is the full angle of the plate
36 %The location of one of the applied concentrated force P1;
37 %It changes along the line of angle d, so that the
38 %effect of the location of the coupled force could be observed
39 b1=[c(j)+5e-6:interval:a];
40 %The location of the other applied concentrated force P2;
```

```

41 %it keeps distance c from b1
42 b2=b1-c(j);
43 %computation starts
44 N=50; %grid number
45 n=500;%grid number
46 for i=1:ceil((a-c(j))/interval)
47 %This part computes the deflection of the plate under one of
48 %the concentrated forces P1 of the first coupled force; P1 is
49 %applied on location b1
50 %The grid between force P1 and the outer(clamped) edge of the plate
51 Rout1=linspace(b1(i),a,N);
52 %The grid between the center of the plate and force P2
53 %It does not start from zero because this value will appear as the
54 %denominator. Zero will make the computation invalid. Instead, a very
55 %small value is chosen to make the computation valid. This defect is
56 %fixed by the reshape and remesh command later
57 Rin1=linspace(1e-8,b1(i),N);
58 Theta1=linspace(d,e,N);%the angle grid of the plate
59 [rout1,theta1]=meshgrid(Rout1,Theta1); %make the grid to 2D meshgrid
60 [rin1,theta1]=meshgrid(Rin1,Theta1); %make the grid to 2D meshgrid
61 %coefficient R0 for outer part of the plate
62 R0_out1=P1/(8*pi*D)*((rout1.^2+b1(i)^2).*log(rout1./a)+(a^2+b1(i)^2)*
63 (a^2-rout1.^2)./(2*a^2));
64 %coefficient R0 for inner part of the plate
65 R0_in1=P1/(8*pi*D)*((rin1.^2+b1(i)^2)*log(b1(i)/a)+(a^2+rin1.^2)*(a^2-b1
66 (i)^2)./(2*a^2));
67 %coefficient R1 for outer part of the plate
68 R1_out1=-P1*b1(i)^3/(16*pi*D)*(1./rout1+2*(a^2-b1(i)^2)*rout1/(a^2*b1
69 (i)^2)-(2*a^2-b1(i)^2)*rout1.^3/(a^4*b1(i)^2)-4*rout1./b1(i)^2.*log(a./rout1));
70 %coefficient R1 for inner part of the plate
71 R1_in1=-P1*b1(i)^3/(16*pi*D)*(2*(a^2-b1(i)^2)*rin1/(a^2*b1(i)^2)+(a^2-
72 b1(i)^2)^2*rin1.^3/(a^4*b1(i)^4)-4*rin1./b1(i)^2*log(a/b1(i)));
73 %initialize coefficient Rm
74 Rm_out1=0;Rm_in1=0;
75 %This part computes the coefficient Rm for both outer and inner part of
76 %the plate
77 for m=2:30
78 Rm_out1=Rm_out1+P1*b1(i)^m/(8*m*(m-1)*pi*D)*(rout1.^m./a^(2*m).
79 *((m-1)*b1(i)^2-m*a^2+(m-1)*rout1.^2-m*(m-1)/(m+1)*b1(i)^2*rout1.^2/a^2)
80 +1./rout1.^m.*(rout1.^2-(m-1)/(m+1)*b1(i)^2)).*cos(m*theta1);

```

```

81 Rm_in1=Rm_in1+P1*b1(i)^m/(8*m*(m-1)*pi*D)*(rin1.^m./a^(2*m)).*
82 ((m-1)*b1(i)^2-m*a^2+a^(2*m)/b1(i)^(2*m-2))+m-1)*rin1.^(m+2)./a^(2*m)).*
83 (1-m/(m+1)*b1(i)^2/a^2-1/(m+1)*(a/b1(i))^(2*m))).*cos(m*theta1);
84 end
85 %The deflection of the outer part of the plate
86 w_out1=R0_out1+R1_out1.*cos(theta1)+Rm_out1;
87 %The deflection of the inner part of the plate
88 w_in1=R0_in1+R1_in1.*cos(theta1)+Rm_in1;
89 %Combine the outer part with the inner part Cartesian grid; this is a
90 %N*2N matrix
91 r1=[rin1 rout1];
92 th1=[theta1 theta1];
93 w1=[w_in1 w_out1];
94 %Make the N*2N matrix to a row vector in order to use griddata
95 %command to get uniform grid
96 R1=reshape(r1,1,N*2*N);
97 Th1=reshape(th1,1,N*2*N);
98 W1=reshape(w1,1,N*2*N);
99 %make uniform grid
100 [RI1,ThI1]=meshgrid([linspace(1e-8,a,n)],[linspace(0,2*pi,n)]);
101 WI1=griddata(R1,Th1,W1,RI1,ThI1); %deflection at uniform grid
102 WI1(isnan(WI1))=0;
103 %This part computes the deflection of the plate under the other
104 %concentrated force P2 of the first coupled force; P2 is applied on location b2
105 % The grid between the applied force P2 and the outer(clamped) edge of the plate
106 Rout2=linspace(b2(i),a,N);
107 %The grid between the center of the plate and the applied force P2
108 %It does not start from zero because this value will appear as the
109 %denominator. Zero will make the computation invalid. Instead, a small
110 %value is chosen to make the grid between the applied force and the
111 %outer edge of the plate
112 Rin2=linspace(1e-8,b2(i),N);
113 Theta2=linspace(d,e,N); %the angle grid of the plate
114 [rout2,theta2]=meshgrid(Rout2,Theta2); %make the grid to 2D meshgrid
115 [rin2,theta2]=meshgrid(Rin2,Theta2); %make the grid to 2D meshgrid
116 %Coefficient R0 for outer part of the plate
117 R0_out2=P2/(8*pi*D)*((rout2.^2+b2(i)^2).*log(rout2./a)+(a^2+b2(i)^2)*
118 (a^2-rout2.^2)/(2*a^2));
119 %Coefficient R0 for inner part of the plate
120 R0_in2=P2/(8*pi*D)*((rin2.^2+b2(i)^2)*log(b2(i)/a)+(a^2+rin2.^2)*(a^2-b2
121 (i)^2)/(2*a^2));

```

```

122 %Coefficient R1 for outer part of the plate
123 R1_out2=-P2*b2(i)^3/(16*pi*D)*(1./rout2+2*(a^2-b2(i)^2)*rout2/(a^2*b2
124 (i)^2)-(2*a^2-b2(i)^2)*rout2.^3/(a^4*b2(i)^2)-4*rout2./b2(i)^2.*log(a./rout2));
125 %Coefficient R1 for inner part of the plate
126 R1_in2=-P2*b2(i)^3/(16*pi*D)*(2*(a^2-b2(i)^2)*rin2/(a^2*b2(i)^2)+(a^2-
127 b2(i)^2)^2*rin2.^3/(a^4*b2(i)^4)-4*rin2./b2(i)^2*log(a/b2(i)));
128 %Initialize coefficient Rm
129 Rm_out2=0;Rm_in2=0;
130 %This part computes the coefficient Rm for both outer and inner part of the plate
131 for m=2:30
132 Rm_out2=Rm_out2+P2*b2(i)^m/(8*m*(m-1)*pi*D)*(rout2.^m./a^(2*m).
133 *((m-1)*b2(i)^2-m*a^2+(m-1)*rout2.^2-m*(m-1)/(m+1)*b2(i)^2*rout2.^2/a^2)
134 +1./rout2.^m.*(rout2.^2-(m-1)/(m+1)*b2(i)^2)).*cos(m*theta2);
135 Rm_in2=Rm_in2+P2*b2(i)^m/(8*m*(m-1)*pi*D)*(rin2.^m./a^(2*m).*
136 ((m-1)*b2(i)^2-m*a^2+a^(2*m)/b2(i)^(2*m-2))+m*(m-1)*rin2.^(m+2)./a^(2*m).*
137 ((m-1)*b2(i)^2-m*a^2+a^(2*m)/b2(i)^(2*m-2))+m*(m-1)*rin2.^(m+2)./a^(2*m).*
138 (1-m/(m+1)*b2(i)^2/a^2-1/(m+1)*(a/b2(i))^(2*m))).*cos(m*theta2);
139 end
140 %The deflection of the outer part of the plate
141 w_out2=R0_out2+R1_out2.*cos(theta2)+Rm_out2;
142 %The deflection of the inner part of the plate
143 w_in2=R0_in2+R1_in2.*cos(theta2)+Rm_in2;
144 %Combine the outer part with the inner part Cartesian grid; this is a N*2N matrix
145 r2=[rin2 rout2];
146 th2=[theta2 theta2];
147 w2=[w_in2 w_out2];
148 %Make the N*2N matrix to a row vector in order to use griddata
149 %command to get uniform grid
150 R2=reshape(r2,1,N*2*N);
151 Th2=reshape(th2,1,N*2*N);
152 W2=reshape(w2,1,N*2*N);
153 %Make uniform grid
154 [RI2,ThI2]=meshgrid([linspace(1e-8,a,n)],[linspace(d,e,n)]);
155 WI2=griddata(R2,Th2,W2,RI2,ThI2); %deflection at uniform grid
156 WI2(isnan(WI2))=0;
157 %% Circular plate deflection under the second coupled forces parameters
158 P3=-1e-6; %N, applied force on b3
159 P4=1e-6; %N, applied force on b4
160 %P3 and P4 are applied at the same angle of d and rotate angle f.
161 %If f=pi, then after rotation, P3 and P4 generate counter clock moment
162 %which is same as that generated by P1 and P2. Force P3 and P4 are
163 % applied at angle f with distance c apart; g is the full angle of the plate

```

```

164 f=pi; g=f+2*pi;
165 %The location of one of the applied concentrated force P3;
166 %It changes along the line of angle f, so that the
167 %effect of the location of the coupled force could be observed
168 b3=[c(j)+5e-6:interval:a];
169 %The location of the other applied concentrated force P2
170 %It keeps same distance c to b3
171 b4=b3-c(j);
172 %Computation starts
173 N=50;           %grid number
174 n=500;         %grid number
175 %This part computes the deflection of the plate under one of the
176 %concentrated forces P1 of the first coupled force; P3 is applied on location b3
177 %The grid between the applied force P3 and the outer edge of the plate
178 Rout3=linspace(b3(i),a,N);
179 %The grid between the center of the plate and the applied force P3
180 Rin3=linspace(1e-8,b3(i),N);
181 %It does not start from zero because this value will appear as the
182 %denominator. Zero will make the computation invalid. Instead, a small
183 %value is chosen to make the computation valid. This defect is fixed by the
184 %reshape and remesh command
185 %The angle grid of the plate; it rotates the force P3 and P4 by angle f
186 Theta3=linspace(f,g,N);
187 %Make the grid to 2D meshgrid
188 [rout3,theta3]=meshgrid(Rout3,Theta3);
189 [rin3,theta3]=meshgrid(Rin3,Theta3);
190 %Coefficient R0 for outer part of the plate
191 R0_out3=P3/(8*pi*D)*((rout3.^2+b3(i)^2).*log(rout3./a)+(a^2+b3(i)^2)*
192 (a^2-rout3.^2)./(2*a^2));
193 %Coefficient R0 for inner part of the plate
194 R0_in3=P3/(8*pi*D)*((rin3.^2+b3(i)^2)*log(b3(i)/a)+(a^2+rin3.^2)*(a^2-b3
195 (i)^2)./(2*a^2));
196 %Coefficient R1 for outer part of the plate
197 R1_out3=-P3*b3(i)^3/(16*pi*D)*(1./rout3+2*(a^2-b3(i)^2)*rout3/(a^2*b3
198 (i)^2)-(2*a^2-b3(i)^2)*rout3.^3/(a^4*b3(i)^2)-4*rout3./b3(i)^2.*log(a./rout3));
199 %Coefficient R1 for inner part of the plate
200 R1_in3=-P3*b3(i)^3/(16*pi*D)*(2*(a^2-b3(i)^2)*rin3/(a^2*b3(i)^2)+(a^2-
201 b3(i)^2)^2*rin3.^3/(a^4*b3(i)^4)-4*rin3./b3(i)^2*log(a/b3(i)));
202 %Initialize coefficient
203 Rm_out3=0;Rm_in3=0;

```

```

204 %This part computes the coefficient Rm for both outer and inner part of the plate
205 for m=2:30
206 Rm_out3=Rm_out3+P3*b3(i)^m/(8*m*(m-1)*pi*D)*(rout3.^m./a^(2*m).*
207 ((m-1)*b3(i)^2-m*a^2+(m-1)*rout3.^2-m*(m-1)/(m+1)*b3(i)^2*rout3.^2/a^2)
208 +1./rout3.^m.*(rout3.^2-(m-1)/(m+1)*b3(i)^2)).*cos(m*theta3);
209 Rm_in3=Rm_in3+P3*b3(i)^m/(8*m*(m-1)*pi*D)*(rin3.^m./a^(2*m)).*((m-1)
210 *b3(i)^2-m*a^2+a^(2*m)/b3(i)^(2*m-2))+m-1)*rin3.^(m+2)./a^(2*m)).*(1-m/
211 (m+1)*b3(i)^2/a^2-1/(m+1)*(a/b3(i)^(2*m))).*cos(m*theta3);
212 end
213 %The deflection of the outer part of the plate
214 w_out3=R0_out3+R1_out3.*cos(theta3)+Rm_out3;
215 %The deflection of the inner part of the plate
216 w_in3=R0_in3+R1_in3.*cos(theta3)+Rm_in3;
217 %Combine the outer part with the inner part Cartesian grid; this is a N*2N matrix
218 r3=[rin3 rout3];
219 th3=[theta3 theta3];
220 w3=[w_in3 w_out3];
221 %Make the N*2N matrix to a row vector in order to use griddata command to
222 %get uniform grid
223 R3=reshape(r3,1,N*2*N);
224 Th3=reshape(th3,1,N*2*N);
225 W3=reshape(w3,1,N*2*N);
226 %Make uniform grid
227 [RI3,ThI3]=meshgrid([linspace(1e-8,a,n)],[linspace(f,g,n)]);
228 WI3=griddata(R3,Th3,W3,RI3,ThI3); %deflection at uniform grid
229 WI3(isnan(WI3))=0;
230 %This part computes the deflection of the plate under the other
231 %concentrated force P4 of the second coupled force; P4 is applied on location b4
232 %The grid between the applied force P4 and the outer(clamped) edge of the plate
233 Rout4=linspace(b4(i),a,N);
234 %The grid between the center of the plate and the applied force P4
235 Rin4=linspace(1e-8,b4(i),N);
236 %The angle grid of the plate; it rotates the force P3 and P4 by angle f
237 Theta4=linspace(f,g,N);
238 [rout4,theta4]=meshgrid(Rout4,Theta4); %make the grid to 2D meshgrid
239 [rin4,theta4]=meshgrid(Rin4,Theta4); %make the grid to 2D meshgrid
240 %Coefficient R0 for outer part of the plate
241 R0_out4=P4/(8*pi*D)*((rout4.^2+b4(i)^2).*log(rout4./a)+(a^2+b4(i)^2)*
242 (a^2-rout4.^2)/(2*a^2));
243 %Coefficient R0 for inner part of the plate
244 R0_in4=P4/(8*pi*D)*((rin4.^2+b4(i)^2)*log(b4(i)/a)+(a^2+rin4.^2)*(a^2-b4
245 (i)^2)/(2*a^2));

```

```

246 %Coefficient R1 for outer part of the plate
247 R1_out4=-P4*b4(i)^3/(16*pi*D)*(1./rout4+2*(a^2-b4(i)^2)*rout4/(a^2*b4
248 (i)^2)-(2*a^2-b4(i)^2)*rout4.^3/(a^4*b4(i)^2)-4*rout4./b4(i)^2.*log(a./rout4));
249 %Coefficient R1 for inner part of the plate
250 R1_in4=-P4*b4(i)^3/(16*pi*D)*(2*(a^2-b4(i)^2)*rin4/(a^2*b4(i)^2)+(a^2-
251 b4(i)^2)^2*rin4.^3/(a^4*b4(i)^4)-4*rin4./b4(i)^2*log(a/b4(i)));
252 %Initialize coefficient Rm
253 Rm_out4=0;Rm_in4=0;
254 %This part computes the coefficient Rm for both outer and inner part of the plate
255 for m=2:30
256 Rm_out4=Rm_out4+P4*b4(i)^m/(8*m*(m-1)*pi*D)*(rout4.^m./a^(2*m).
257 *((m-1)*b4(i)^2-m*a^2+(m-1)*rout4.^2-m*(m-1)/(m+1)*b4(i)^2*rout4.^2/a^2)
258 +1./rout4.^m.*(rout4.^2-(m-1)/(m+1)*b4(i)^2)).*cos(m*theta4);
259 Rm_in4=Rm_in4+P4*b4(i)^m/(8*m*(m-1)*pi*D)*(rin4.^m./a^(2*m).*
260 ((m-1)*b4(i)^2-m*a^2+a^(2*m)/b4(i)^(2*m-2))+m-1)*rin4.^(m+2)./a^(2*m).*
261 ((m-1)*b4(i)^2-m*a^2+a^(2*m)/b4(i)^(2*m-2))+m-1)*rin4.^(m+2)./a^(2*m).*
262 (1-m/(m+1)*b4(i)^2/a^2-1/(m+1)*(a/b4(i))^(2*m))).*cos(m*theta4);
263 end
264 %The deflection of the outer part of the plate
265 w_out4=R0_out4+R1_out4.*cos(theta4)+Rm_out4;
266 %The deflection of the inner part of the plate
267 w_in4=R0_in4+R1_in4.*cos(theta4)+Rm_in4;
268 %combine the outer part with the inner part Cartesian grid; this is a N*2N matrix
269 r4=[rin4 rout4];
270 th4=[theta4 theta4];
271 w4=[w_in4 w_out4];
272 %make the N*2N matrix to a row vector in order to use griddata command to
273 %get uniform grid
274 R4=reshape(r4,1,N*2*N);
275 Th4=reshape(th4,1,N*2*N);
276 W4=reshape(w4,1,N*2*N);
277 %make uniform grid
278 [RI4,ThI4]=meshgrid([linspace(1e-8,a,n)],[linspace(f,g,n)]);
279 WI4=griddata(R4,Th4,W4,RI4,ThI4); %deflection at uniform grid
280 WI4(isnan(WI4))=0;
281 %% Capacitance change calculation
282 %This part computes the capacitance change under coupled force
283 %Superposition of deflection for under both coupled forces
284 WI=WI1+WI2+WI3+WI4;
285 % Define the area of the ipsilateral electrode from angle zero to
286 % electrode_angle/2 with the applied coupled force through radius
287 % and angle; find the deflection of the corresponding area

```

```

288 r_ips1=RI1(RI1>=electrode_in & RI1<=electrode_out & (ThI1<=
289 (electrode_angle/180*pi));
290 th_ips1=ThI1(RI1>=electrode_in & RI1<=electrode_out & (ThI1<=
291 (electrode_angle/180*pi));
292 w_ips1=WI(RI1>=electrode_in & RI1<=electrode_out & (ThI1<=
293 (electrode_angle/180*pi));
294 THING=(RI1>=electrode_in & RI1<=electrode_out & (ThI1<=
295 (electrode_angle/180*pi));
296 TEST=find(THING==1);
297 MyM=sum(THING(:,ceil(min(TEST)/size(THING,2))));
298 MyN=sum(THING(mod(min(TEST),size(THING,1)),:));
299 RR1=reshape(r_ips1,[MyM MyN]);
300 TH1=reshape(th_ips1,[MyM MyN]);
301 WW1=reshape(w_ips1,[MyM MyN]);
302 % Capacitance change of ipsilateral capacitor with the applied
303 % coupled force from angle zero to electrode_angle/2
304 delta_C_ips1(i)=ep0*trapz(RR1(1,:),RR1(1,:).*trapz(TH1(:,1),1./(g0+WW1)
305 -1./g0)) ;
306 % Define the area of the ipsilateral electrode from minus
307 % electrode_angle/2 to angle zero with the applied coupled force
308 % through radius and angle; find the deflection of the corresponding area
309 r_ips2=RI1(RI1>=electrode_in & RI1<=electrode_out & (ThI1>=((360-
310 electrode_angle)/180*pi));
311 th_ips2=ThI1(RI1>=electrode_in & RI1<=electrode_out & (ThI1>=((360-
312 electrode_angle)/180*pi));
313 w_ips2=WI(RI1>=electrode_in & RI1<=electrode_out & (ThI1>=((360-
314 electrode_angle)/180*pi));
315 THING=(RI1>=electrode_in & RI1<=electrode_out & (ThI1>=((360-
316 electrode_angle)/180*pi));
317 TEST=find(THING==1);
318 MyM=sum(THING(:,ceil(min(TEST)/size(THING,2))));
319 MyN=sum(THING(mod(min(TEST),size(THING,1)),:));
320 RR2=reshape(r_ips2,[MyM MyN]);
321 TH2=reshape(th_ips2,[MyM MyN]);
322 WW2=reshape(w_ips2,[MyM MyN]);
323 % Capacitance change of ipsilateral capacitor with the applied
324 % coupled force from angle zero to electrode_angle/2
325 delta_C_ips2(i)=ep0*trapz(RR2(1,:),RR2(1,:).*trapz(TH2(:,1),1./(g0+WW2)
326 -1./g0)) ;
327 delta_C_ips(i)=delta_C_ips1(i)+delta_C_ips2(i);

```

```

328 % Define the area of the contralateral electrode with the applied
329 % coupled force through radius and angle; find the deflection of
330 % the corresponding area
331 r_con=RI1(RI1>=electrode_in & RI1<=electrode_out & (ThI1>=((180-
332 electrode_angle)/180*pi)...
333 & ThI1<=((180+electrode_angle)/180*pi));
334 th_con=ThI1(RI1>=electrode_in & RI1<=electrode_out & (ThI1>=((180-
335 electrode_angle)/180*pi)...
336 & ThI1<=((180+electrode_angle)/180*pi));
337 w_con=WI(RI1>=electrode_in & RI1<=electrode_out & (ThI1>=((180-
338 electrode_angle)/180*pi)...
339 & ThI1<=((180+electrode_angle)/180*pi));
340 THING=(RI1>=electrode_in & RI1<=electrode_out & (ThI1>=((180-
341 electrode_angle)/180*pi)...
342 &ThI1<=((180+electrode_angle)/180*pi));
343 TEST=find(THING==1);
344 MyM=sum(THING(:,ceil(min(TEST)/size(THING,2))));
345 MyN=sum(THING(mod(min(TEST),size(THING,1)),:));
346 R_con=reshape(r_con,[MyM MyN]);
347 TH_con=reshape(th_con,[MyM MyN]);
348 W_con=reshape(w_con,[MyM MyN]);
349 % Capacitance change of contralateral capacitor with the applied coupled force
350 delta_C_con(i)=ep0*trapz(R_con(1,:),R_con(1,:).*trapz(TH_con(:,1),1./
351 (g0+W_con)-1./g0)) ;
352 %Total delta_C
353 delta_C_plus(i)=delta_C_ips(i)+delta_C_con(i);
354 delta_C_minus(i)=delta_C_ips(i)-delta_C_con(i);
355 end
356 plot(b2+(b1-b2)/2,abs(delta_C_minus),'--+', 'linewidth',2, 'markersize',6);hold on
357 title('Optimization of Location for Differential Capacitance Change of
358 Polymumps Sensor','fontsize',20)
359 xlabel('Location of Hair Post (m)','fontsize',16)
360 ylabel('Capacitance Change (Farad)','fontsize',16)
361 legend('delta__C for diameter post')
362 end

```

## APPENDIX B: LABVIEW® BLOCK DIAGRAM

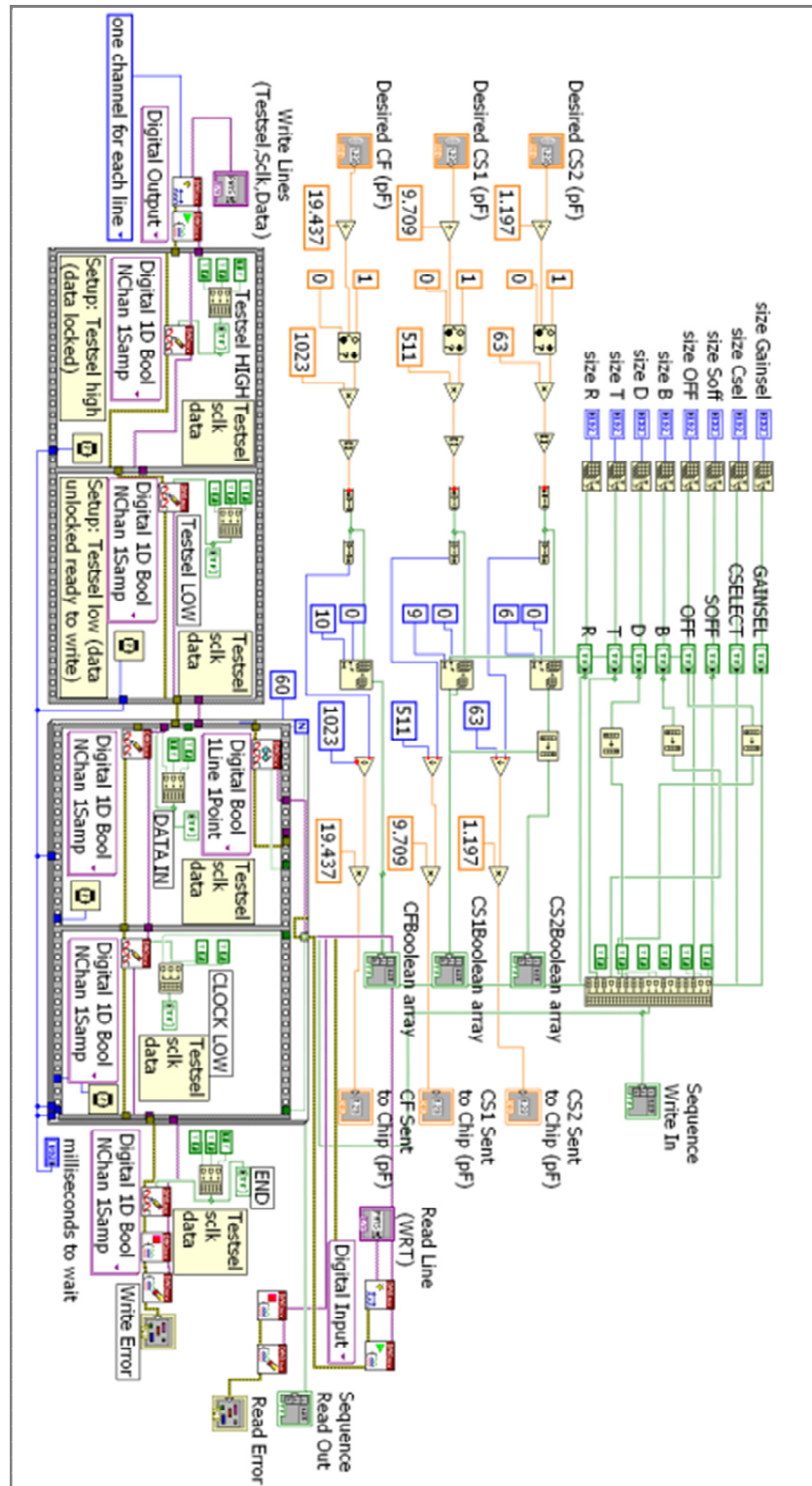
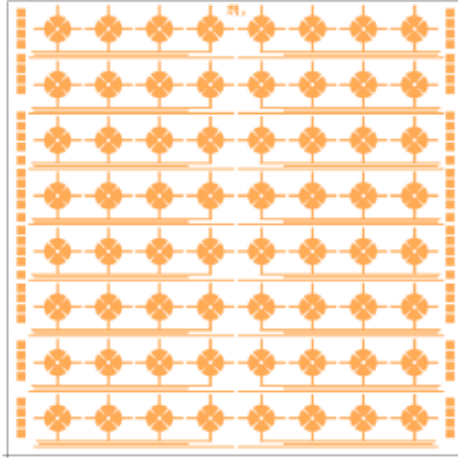


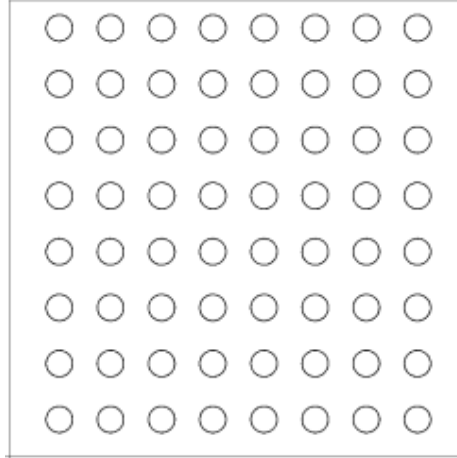
Figure B.1 Labview® block diagram for temporary programming of MS3110 chip

## APPENDIX C: CAD DRAWING

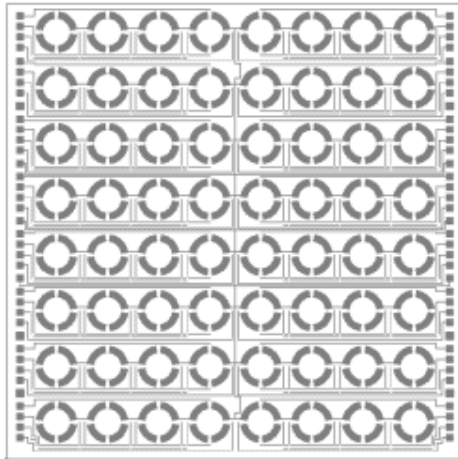
### C1 Hair Sensor Masks Layout



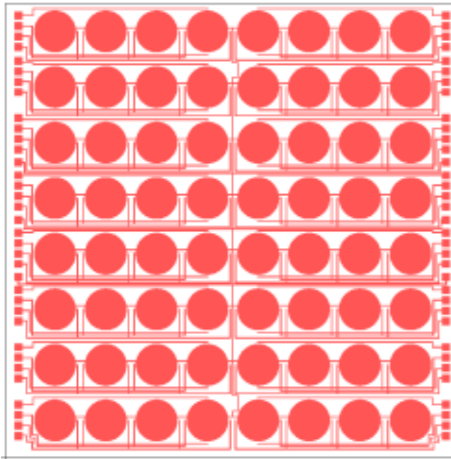
(a) POLY0 Mask



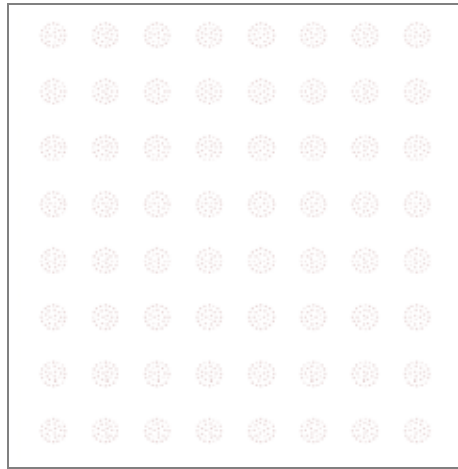
(b) DIMPLE Mask



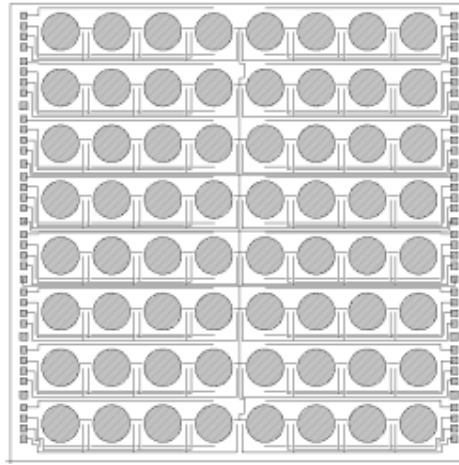
(c) ANCHOR1 Mask



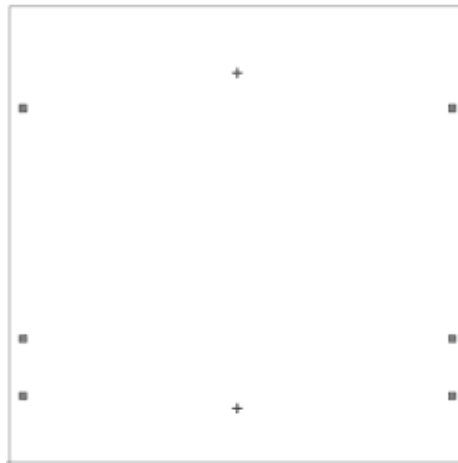
(d) POLY1 Mask



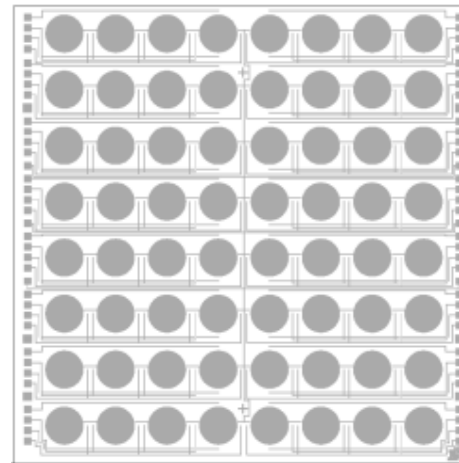
(e) HOLE1 Mask



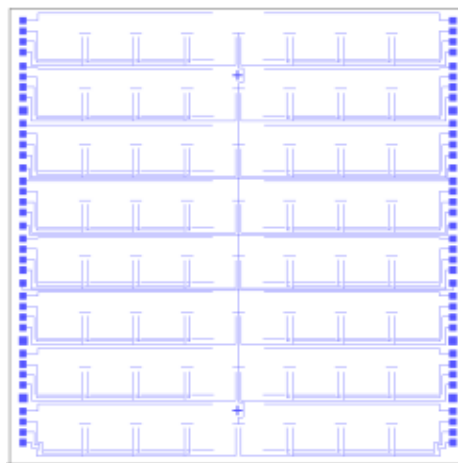
(f) POLY1\_POLY2\_VIA Mask



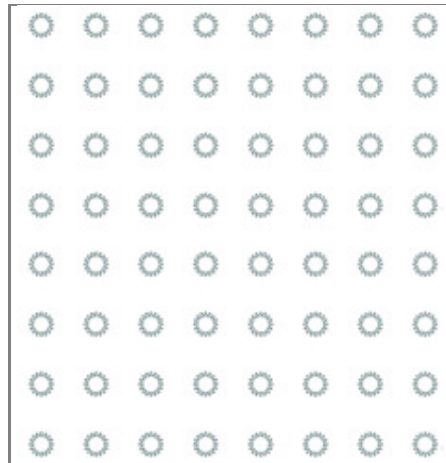
(g) ANCHOR2Mask



(h) POLY2 Mask

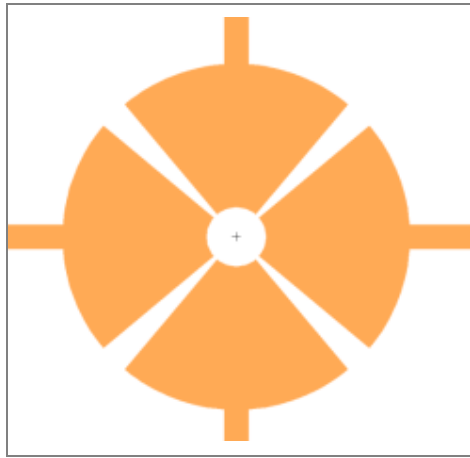


(i) METAL Mask

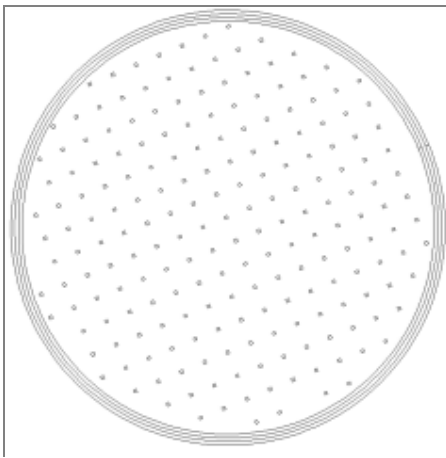


(j) HAIRPOST Mask

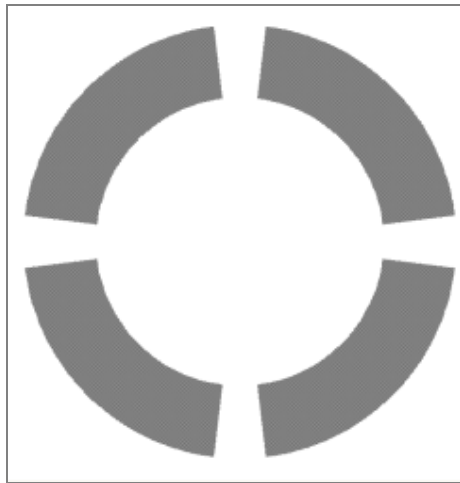
**Figure C.1 Hair-like shear sensors masks**



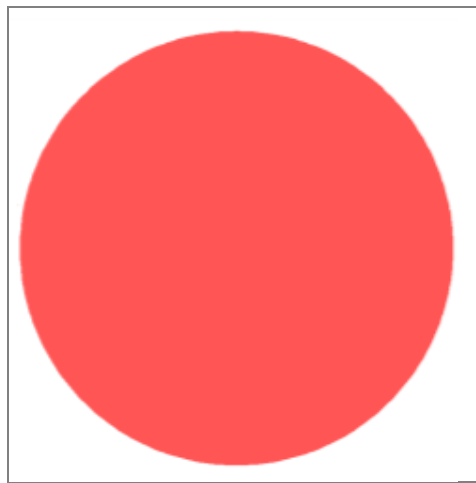
(a) POLY0 Mask



(b) DIMPLE Mask



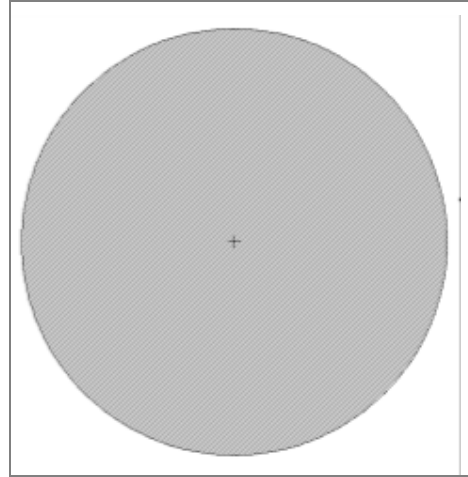
(c) ANCHOR1 Mask



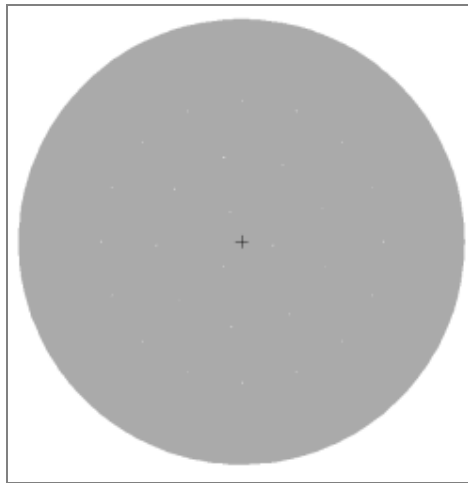
(d) POLY1 Mask



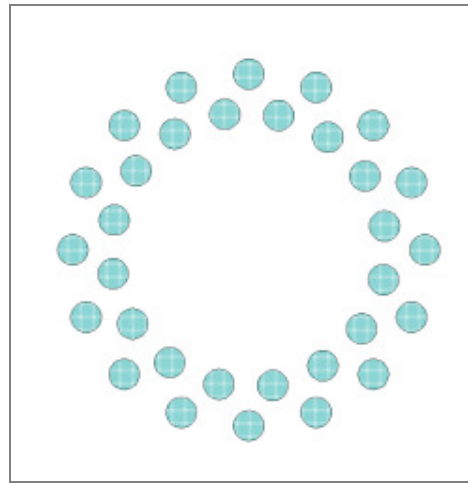
(e) HOLE1 Mask



(f) POLY1\_POLY2\_VIA Mask



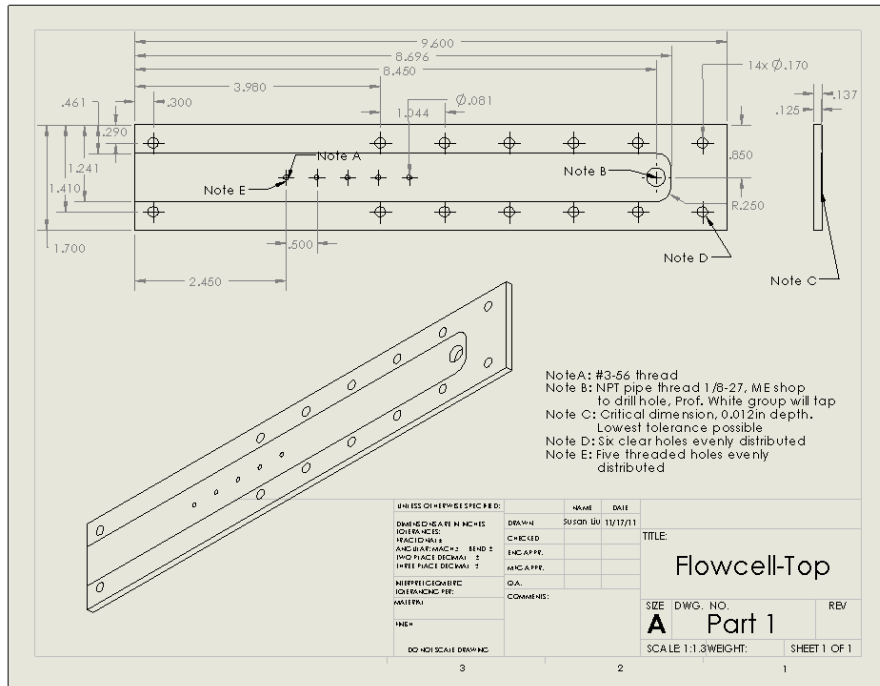
(g) POLY2 Mask



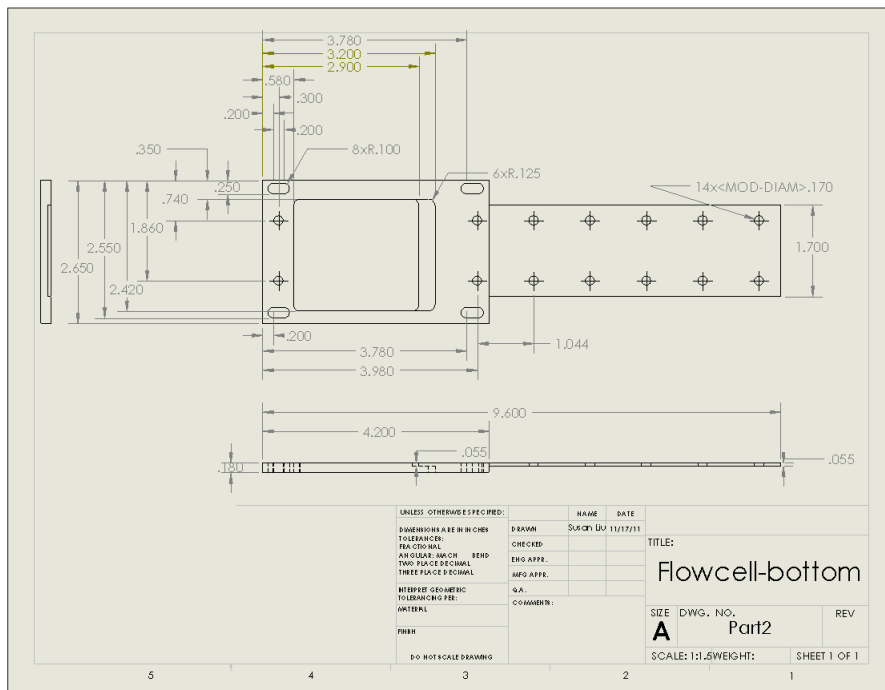
(h) HAIRPOST Mask

**Figure C.2 Individual sensor different layer layout**

# C2 Aluminum Flow Cell CAD Drawing



(a) Top plate



(b) Bottom plate

Figure C.3 CAD drawing of aluminum flow cell (Dimension in inch)

## APPENDIX D: SENSOR FABRICATION RUNSHEET

Step Name	Parameters	Comments
<b>1. Examine chip</b>	Microscope	Take out one polysilicon chip and examine under microscope to see if there is any defect
<b>2. Strip of photoresist</b>	Soak the chip in one beaker of acetone for 10min and transfer to another beaker of acetone for 10 min. The chip is then submerged in IPA for 2min and lastly rinsed in DI water for 2min. Take out the chip and let it dry in the hood.	Acetone dissolves photoresist on the chip that comes from PolyMUMPs™ product. IPA cleans and removes residual acetone and DI water removes IPA.
<b>3. Photoresist coating on wafer</b>	Load a 4" silicon wafer on a photoresist spinner. Spin Hexamethyldisilazane (HMDS) At 4000rpm for 30sec. Then spin SPR3.0 photoresist at 500rpm for 30sec.	HMDS improves adhesion between SPR photoresist and wafer. SPR will be used to bond chips and silicon wafer.
<b>4. Align chips</b>	Before photoresist dries, use tweezers to place the polysilicon sensor chip in the middle of the wafer; then place 8 same size dump chips around the polysilicon chip. Carefully move chips around to make sure there is no gap between chips. Bake the wafer on 115°C hotplate for 90sec. Use tweezers to check if the chips are secured on the wafer.	This process is to enable feature alignment for hair posts.

Step Name	Parameters	Comments
<b>5. Clean polysilicon chip</b>	Soak the wafer along with the chips on it in HF:HCl (4:1) solution for 30sec. Then rinse the wafer in two consecutive baths of DI water 2min each to remove residual solution. Quickly dry the wafer with air gun and load the wafer on the spinner. Minimize the chance of polysilicon chips being oxidized.	This step is to strip off the oxidized polysilicon on sensor chips, which is essential to improve the adhesion between sensor and hair posts.
<b>6. SU8 2025 coating and baking</b>	Pour SU8 2025 on the wafer, covering the polysilicon chip and dummy chips. Spread SU8 at 500rpm for 30sec. and spin at 1000rpm for 30sec. Spin the wafer at 300rpm, and use acetone swab carefully remove the edge of coated SU8 film. Soft bake SU8 at 65°C for 4min and then at 95°C for 10min.	The dummy chips move edge bead effect away from polysilicon chip. The thick edge of SU8 is removed using acetone swap, making the SU8 film uniform.
<b>7. Alignment and expose</b>	Place HAIRPOST mask on mask holder in OAI aligner. Place the wafer on wafer holder and align the features. Bring the wafer close to mask. Then place UV filter on top of mask. Expose SU8 for 16sec.	It is important to bring the mask and wafer close enough to ensure good exposed feature but it can not to be too close in case SU8 stuck on mask. UV filter eliminate T-topping effect and prevent SU8 absorb low wavelength light.
<b>8. Post exposure bake</b>	Bake the exposed wafer at 65°C for 2min and then at 95°C for 8min.	

<b>Step Name</b>	<b>Parameters</b>	<b>Comments</b>
<b>9. Develop</b>	Submerge the wafer in SU8 developer for 20min. Use tweezers to take out the wafer and spray IPA on the edge of wafer. If undeveloped SU-8 remains, it will turn the IPA milky. Then put the wafer back to developer for longer develop time until SU8 is fully developed.	Developing time for SU8 is not same for every experiment. IPA is a good indicator for fully developed SU8.
<b>10. Separate chip from wafer</b>	After SU8 is fully developed, examine the wafer under microscope. Then soak the wafer in acetone to dissolve the SPR photoresist so that the polysilicon chip can be separated from the wafer. Then rinse the chip in IPA for 2min and DI water for 2min. Let the chip dry in the hood.	Sometimes the chip is really hard to be separated from wafer. A sharp blade can be used to lift the chip from the wafer
<b>11. Examine the chip</b>	Examine the chip under microscope. Use Dektak <sup>®</sup> profilometer to measure the posts heights and use Qcapture <sup>®</sup> to measure post diameters.	

## Bibliography

1. Allen, J.B. and S.T. Neely, *Micromechanical Models of the Cochlea*.  
Physics Today, 1992. **45**(7): p. 40-47.
2. Davis, H., *An Active Process in Cochlear Mechanics*. Hearing  
Research, 1983. **9**(1): p. 79-90.
3. Duke, T. and F. Julicher, *Active traveling wave in the cochlea*.  
Physical Review Letters, 2003. **90**( 15): p. 158101 - 1.
4. Gold, T., *Hearing. II. The Physical Basis of the Action of the  
Cochlea*. Proceedings of the Royal Society of London. Series B,  
Biological Sciences, 1948. **135**(881): p. 492-498.
5. von Békésy, G., *Experiments in Hearing*. 1960, New York:  
McGraw-Hill.
6. Cooper, N.P., *Two-tone suppression in cochlear mechanics*.  
Journal of the Acoustical Society of America, 1996. **99**(5): p.  
3087-3098.
7. Naidu, R.C. and D.C. Mountain, *Measurements of the stiffness  
map challenge a basic tenet of cochlear theories*. Hearing Research,  
1998. **124**(1-2): p. 124-131.
8. Naidu, R.C. and D.C. Mountain, *Longitudinal coupling in the  
basilar membrane*. Jaro, 2001. **2**(3): p. 257-267.
9. Emadi, G., C.P. Richter, and P. Dallos, *Stiffness of the gerbil  
basilar membrane: Radial and longitudinal variations*. Journal of

- Neurophysiology, 2004. **91**(1): p. 474-488.
10. Dallos, P.F., Richard R., *The Cochlea*. Springer Handbook of Auditory Research. Vol. 8. 1996.
  11. Peter Dallos, A.N.P., Richard R. Fay, *The Cochlea*. Springer handbook of auditory research. Vol. 8. 1996.
  12. White, R.D., *Biomimetic Trapped Fluid Microsystems for Acoustic Sensing*, in *Mechanical Engineering*. 2005, University of Michigan,; Ann Arbor.
  13. Corey, D.P. and A.J. Hudspeth, *Ionic Basis of the Receptor Potential in a Vertebrate Hair Cell*. Nature, 1979. **281**(5733): p. 675-677.
  14. Brownell, W.E., et al., *Evoked Mechanical Responses of Isolated Cochlear Outer Hair-Cells*. Science, 1985. **227**(4683): p. 194-196.
  15. Fettiplace, R. and C.M. Hackney, *The sensory and motor roles of auditory hair cells*. Nature Reviews Neuroscience, 2006. **7**(1): p. 19-29.
  16. Ashmore, J., *Pushing the Envelope of Sound*. Neuron, 2011 **70**(6): p. 1021-1022.
  17. Iurato, S., *Functional Implications of the Nature and Submicroscopic Structure of the Tectorial and Basilar Membranes*. The Journal of the Acoustical Society of America, 1962. **34**(9B): p. 1386-1395.

18. Voldrich, L., *Mechanical-Properties of Basilar-Membrane*. Acta Oto-Laryngologica, 1978. **86**(5-6): p. 331-335.
19. Robles, L. and M.A. Ruggero, *Mechanics of the mammalian cochlea*. Physiological Reviews, 2001. **81**(3): p. 1305-1352.
20. Lynch, T.J., V. Nedzelnitsky, and W.T. Peake, *Input Impedance of the Cochlea in Cat*. Journal of the Acoustical Society of America, 1982. **72**(1): p. 108-130.
21. Neely, S.T. and D.O. Kim, *A Model for Active Elements in Cochlear Biomechanics*. Journal of the Acoustical Society of America, 1986. **79**(5): p. 1472-1480.
22. Ramamoorthy, S., N.V. Deo, and K. Grosh, *A mechano-electro-acoustical model for the cochlea: Response to acoustic stimuli*. Journal of the Acoustical Society of America, 2007. **121**(5): p. 2758-2773.
23. Allaire, P., S. Raynor, and M. Billone, *Cochlear Partition Stiffness - Composite Beam Model*. Journal of the Acoustical Society of America, 1974. **55**(6): p. 1252-1258.
24. Miller, C.E., *Structural Implications of Basilar-Membrane Compliance Measurements*. Journal of the Acoustical Society of America, 1985. **77**(4): p. 1465-1474.
25. Steele, C.R. and L.A. Taber, *Comparison of Wkb Calculations and Experimental Results for 3-Dimensional Cochlear Models*. Journal

- of the Acoustical Society of America, 1979. **65**(4): p. 1007-1018.
26. Naidu, R.C. and D.C. Mountain, *Basilar membrane tension calculations for the gerbil cochlea*. Journal of the Acoustical Society of America, 2007. **121**(2): p. 994-1002.
  27. Edge, R.M., et al., *Morphology of the unfixed cochlea*. Hearing Research, 1998. **124**(1-2): p. 1-16.
  28. Schweitzer, L., et al., *Anatomical correlates of the passive properties underlying the developmental shift in the frequency map of the mammalian cochlea*. Hearing Research, 1996. **97**(1-2): p. 84-94.
  29. Allaire, P., Raynor, S., Billone, M., *Cochlear partition stiffness---a composite beam model*. The Journal of the Acoustical Society of America, 1974. **55**(6): p. 1252-1258.
  30. Günter, E., *Stiffness gradient along the basilar membrane as a basis for spatial frequency analysis within the cochlea*. Vol. 64. 1978: ASA. 1723-1726.
  31. Gummer, A.W., B.M. Johnstone, and N.J. Armstrong, *Direct Measurement of Basilar-Membrane Stiffness in the Guinea-Pig*. Journal of the Acoustical Society of America, 1981. **70**(5): p. 1298-1309.
  32. Miller, C.E., *Structural implications of basilar membrane compliance measurements*. The Journal of the Acoustical Society

- of America, 1985. **77**(4): p. 1465-1474.
33. Olson, E.S. and D.C. Mountain, *In vivo measurement of basilar membrane stiffness*. The Journal of the Acoustical Society of America, 1991. **89**(3): p. 1262-1275.
  34. Ishii, T., M. Takayama, and Y. Takahashi, *Mechanical Properties of Human Round Window, Basilar and Reissner's Membranes*. Acta Oto-laryngologica, 1995. **115**(s519): p. 78-82.
  35. Fleischer, M., R. Schmidt, and A.W. Gummer, *Compliance profiles derived from a three-dimensional finite-element model of the basilar membrane*. Journal of the Acoustical Society of America. **127**(5): p. 2973-2991.
  36. Richter, C.P., et al., *Basilar membrane vibration in the gerbil hemicochlea*. Journal of Neurophysiology, 1998. **79**(5): p. 2255-2264.
  37. White, R.D. and K. Grosh, *Microengineered hydromechanical cochlear model*. Proceedings of the National Academy of Sciences of the United States of America, 2005. **102**(5): p. 1296-1301.
  38. Wittbrodt, M.J., C.R. Steele, and S. Puria, *Developing a life-sized physical model of the human cochlea*, in *Auditory Mechanisms: Processes and Models*. 2006. p. 512-513.
  39. Zhou, G., et al., *A Life-Sized Physical Model of the Human Cochlea with Optical Holographic Readout*. Journal of the Acoustical

- Society of America, 1993. **93**(3): p. 1516-1523.
40. Hemmert, W., et al., *A life-sized, hydrodynamical, micromechanical inner ear*, in *Biophysics of the Cochlea: from Molecules to Models*. 2003. p. 409-416.
  41. Liu, S. and R.D. White, *Orthotropic material properties of the gerbil basilar membrane*. Journal of the Acoustical Society of America, 2008. **123**( 4): p. 2160 - 2171.
  42. Budynas, R.G., *Advanced Strength and Applied Stress Analysis*. 2nd ed. 1999: McGraw-Hill.
  43. Dowling, N.E., *Mechanical Behavior of Materials*. 1999, New Jersey: Prentice Hall.
  44. Jurvelin, J.S., M.D. Buschmann, and E.B. Hunziker, *Optical and mechanical determination of Poisson's ratio of adult bovine humeral articular cartilage*. Journal of Biomechanics, 1997. **30**(3): p. 235-241.
  45. Lai-Fook, S.J., et al., *Elastic constants of inflated lobes of dog lungs*. J Appl Physiol, 1976. **40**(4): p. 508-513.
  46. Gueta, R., et al., *Measurement of the mechanical properties of isolated tectorial membrane using atomic force microscopy*. Proceedings of the National Academy of Sciences of the United States of America, 2006. **103**(40): p. 14790-14795.
  47. Skrodzka, E.B., *Mechanical passive and active models of the*

- human basilar membrane*. Applied Acoustics, 2005. **66**(12): p. 1321-1338.
48. Lim, K.M. and C.R. Steele, *A three-dimensional nonlinear active cochlear model analyzed by the WKB-numeric method*. Hearing Research, 2002. **170**(1-2): p. 190-205.
  49. Fernandez, C., *Dimensions of the Cochlea (Guinea Pig)*. Journal of the Acoustical Society of America, 1952. **24**(5): p. 519-523.
  50. Tonndorf, J., *Fluid motion in cochlear models*. Journal of the Acoustical Society of America, 1957. **29**(5): p. 558 - 568.
  51. Hemmert, W., H.-P. Zenner, and A.W. Gummer, *Characteristics of the travelling wave in the low-frequency region of a temporal-bone preparation of the guinea-pig cochlea*. Hearing Research, 2000/04/. **142**( 1-2): p. 184 - 202.
  52. Zerlin, S., *Traveling-wave velocity in the human cochlea*. Journal of the Acoustical Society of America, 1969. **46**( 4): p. 1011 - 15.
  53. Cannell, J.K., *Cochlear Models*. 1969, University of Warwick.
  54. Helle, R., *Increase in Selectivity in a Hydromechanical Cochlea Model with Basilar-Membrane and Tectorial Membrane*. Acustica, 1974. **30**(6): p. 301-312.
  55. Chadwick, R.S. and D. Adler, *Experimental Observations of a Mechanical Cochlea Model*. Journal of the Acoustical Society of America, 1975. **58**: p. 706-710.

56. Cancelli, C., et al., *Experimental Results in a Physical Model of the Cochlea*. Journal of Fluid Mechanics, 1985. **153**(APR): p. 361-388.
57. Lechner, T.P., *A Hydromechanical Model of the Cochlea with Nonlinear Feedback using  $\text{Spvf}_2$  bending transducers*. Hearing Research, 1993. **66**: p. 202-212.
58. Bonita Tam, A.F.a.R.W. *Coiled hydromechanical sacel model of the inner ear*. in *Mechanics of hearing*. 2011. Williamstown, MA.
59. Tam, B., A. Fakhraee, and R. White. *Coiled hydromechanical sacel model of the inner ear*. in *Mechanics of hearing*. 2011. Williamstown, MA.
60. Lumley, H.T.a.J., *A first course in turbulence*. 1972, Cambridge, MA: The MIT press. 300.
61. Corcos, G.M., *Resolution of Pressure in Turbulence*. Journal of the Acoustical Society of America, 1963. **35**(2): p. 192-&.
62. Willmarth, W.W. and C.E. Wooldridge, *Measurements of the Fluctuating Pressure at the Wall beneath a Thick Turbulent Boundary Layer*. Journal of Fluid Mechanics, 1962. **14**(2): p. 187-210.
63. Lofdahl, L. and M. Gad-el-Hak, *MEMS applications in turbulence and flow control*. Progress in Aerospace Sciences, 1999. **35**(2): p. 101-203.
64. Hyman, D., et al., *Microfabricated shear stress sensors, Part 2:*

- Testing and calibration.* AIAA JOURNAL, 1999. **37**(1): p. 73-78.
65. Pan, T., et al., *Microfabricated shear stress sensors, Part 1: Design and fabrication.* Aiaa Journal, 1999. **37**(1): p. 66-72.
66. Schmidt, M.A., et al., *Design and Calibration of a Microfabricated Floating-element Shear-stress Sensor.* IEEE Transactions on Electron Devices, 1988. **35**(6): p. 750-757.
67. Jiang, F.-K., et al. *A surface micromachined shear-stress imager.* in *IEEE Ninth Int. Workshop on Micro Electro Mechanical Systems.* 1996. Amsterdam.
68. Kalvesten, E., *Pressure and wall shear stress sensors for turbulence measurements.* 1996, Royal Institute of Technology: Stockholm.
69. Chen, Y.-R. and E. Reshotko. *Study of Flow Around a MEMS Shear-Stress Sensor Element.* in *54th Annual Meeting of the Division of Fluid Dynamics of the American Physical Society.* 2001. San Diego, CA.
70. Chen, J., et al., *Two-dimensional micromachined flow sensor array for fluid mechanics studies.* Journal of Aerospace Engineering, 2003. **16**: p. 85.
71. Engel, J.M., et al., *Polyurethane rubber all-polymer artificial hair cell sensor.* IEEE/ASME Journal of Microelectromechanical Systems, 2006. **15**(4): p. 729-736.
72. Grosse, S. and W. Schroder, *Mean wall-shear stress measurements*

- using the micro-pillar shear-stress sensor MPS3*. Measurement Science and Technology, 2008. **19**(1): p. 015403.
73. Grosse, S. and W. Schroder, *Wall-shear stress patterns of coherent structures in turbulent duct flow*. Journal of fluid mechanics, 2009. **633**: p. 147-158.
74. Grosse, S. and W. Schroder, *Two-Dimensional Visualization of Turbulent Wall Shear Stress Using Micropillars*. AIAA Journal, 2009. **47**(2): p. 314-321.
75. Naughton, J. and M. Sheplak, *Modern developments in shear-stress measurement*. PROGRESS IN AEROSPACE SCIENCES, 2002. **38**(6-7): p. 515-570.
76. Haritonidis, J.H. *Advances in Fluid Mechanics Measurements*. 1989.
77. Hanratty, T.J. and J.A. Campbell, *Fluid Mechanics Measurements*, ed. R.J. Goldstein. 1983: Hemisphere Publishing Corporation. 559-615.
78. Winter, K., *OUTLINE OF TECHNIQUES AVAILABLE FOR MEASUREMENT OF SKIN FRICTION IN TURBULENT BOUNDARY-LAYERS*. PROGRESS IN AEROSPACE SCIENCES, 1977. **18**(1): p. 1-57.
79. Stanton, T., D. Marshall, and C. Bryant, *On the conditions at the boundary of a fluid in turbulent motion*. PROCEEDINGS OF THE

ROYAL SOCIETY OF LONDON SERIES A-CONTAINING  
PAPERS OF A MATHEMATICAL AND PHYSICAL  
CHARACTER, 1920. **97**(687): p. 413-434.

80. Preston, J.H., *The determination of turbulent skin friction by means of Pitot tubes*. J. R. Aero. Soc., 1953. **58**: p. 109-121.
81. Konstantinov, N.I. and G.L. Dragnysh, *The measurements of friction stress on a surface*. Energomashinostroenie, 1955. **176**: p. 191-200.
82. Reiss, L. and T. Hanratty, *Measurement of instantaneous rates of mass transfer to a small sink on a wall*. AICHE Journal, 1962. **8**(2): p. 245-247.
83. Reiss, L. and T. Hanratty, *An experimental study of the unsteady nature of the viscous sublayer*. AICHE Journal, 1963. **9**(2): p. 154-160.
84. Lofdahl, L. and M. Gad-el-Hak, *MEMS-based pressure and shear stress sensors for turbulent flows*. MEASUREMENT SCIENCE & TECHNOLOGY, 1999. **10**(8): p. 665-686.
85. SCHMIDT, M., et al., *DESIGN AND CALIBRATION OF A MICROFABRICATED FLOATING-ELEMENT SHEAR-STRESS SENSOR*. IEEE TRANSACTIONS ON ELECTRON DEVICES, 1988. **35**(6): p. 750-757.
86. Zhe, J., V. Modi, and K. Farmer, *A microfabricated wall*

- shear-stress sensor with capacitive sensing.* JOURNAL OF MICROELECTROMECHANICAL SYSTEMS, 2005. **14**(1): p. 167-175.
87. Ng, K.-Y., J. Shajii, and M.A. Schmidt, *A liquid shear-stress sensor fabricated using wafer bonding technology.* Solid-State Sensors and Actuators, 1991. Digest of Technical Papers, Transducers '91., 1991 International Conference on, 1991: p. 931-934.
88. Barlian, A.A., Park, S.-J., Mukundan, V., Pruitt, B.L., *Design and characterization of microfabricated piezoresistive floating element-based shear stress sensors.* Sensors and Actuators, A: Physical, 2007. **134**(1): p. 77-87.
89. Li, Y., et al., *A laterally-implanted piezoresistive skin-friction sensor,* in *Solid-State Sensors, Actuators, and Microsystems Workshop.* 2008: Hilton Head, SC. p. 304-307.
90. Padmanabhan, A., et al., *A wafer-bonded floating-element shear stress microsensors with optical position sensing by photodiodes.* Journal of microelectromechanical systems, 1996. **5**(4): p. 307-315.
91. Padmanabhan, A., et al., *Micromachined sensors for static and dynamic shear-stress measurements in aerodynamic flows.* TRANSDUCERS 97 - 1997 INTERNATIONAL CONFERENCE ON SOLID-STATE SENSORS AND ACTUATORS, DIGEST OF

- TECHNICAL PAPERS, VOLS 1 AND 2, 1997: p. 137-140.
92. Tseng, F. and C. Lin, *Polymer MEMS-based Fabry-Perot shear stress sensor*. IEEE SENSORS JOURNAL, 2003. **3**(6): p. 812-817.
93. Chen, T., et al., 2010.
94. Ayaz, U., T. Ioppolo, and V. Otugen, *High resolution Micro-optical wall shear stress sensor*. 49th AIAA Aerospace Sciences Meeting Including the New Horizons Forum and Aerospace Exposition, 2011(January).
95. Huang, J., et al., *A micro-electro-mechanical-system-based thermal shear-stress sensor with self-frequency compensation*. Measurement science & technology, 1999. **10**(8): p. 687-696.
96. Jiang, F., et al., *A flexible MEMS technology and its first application to shear stress sensor skin*. MEMS 97, PROCEEDINGS - IEEE THE TENTH ANNUAL INTERNATIONAL WORKSHOP ON MICRO ELECTRO MECHANICAL SYSTEMS - AN INVESTIGATION OF MICRO STRUCTURES, SENSORS, ACTUATORS, MACHINES AND ROBOTS 1997: p. 465-470.
97. Liu, C.a.b., H. J.-B. e. f. Z. Z. g. J. F. h. T. S. T. Y.-C. H. C.-M., *A micromachined flow shear-stress sensor based on thermal transfer principles*. Journal of Microelectromechanical Systems, 1999. **8**(1): p. 90-98.

98. Jiang, F., et al., *A flexible micromachine-based shear-stress sensor array and its application to separation-point detection*. *Sensors and Actuators A: Physical*, 2000. **79**(3): p. 194 - 203.
99. Jiang, F., et al., *A flexible MEMS technology and its first application to shear stress sensor skin*. MEMS 97, proceedings - IEEE the tenth annual international workshop on micro electro mechanical systems - an investigation of micro structures, sensors, actuators, machines and robots, 1997: p. 465-470.
100. Kalvesten, E., et al., *An integrated pressure-flow sensor for correlation measurements in turbulent gas flows*. *Sensors and Actuators a-Physical*, 1996. **52**(1-3): p. 51-58.
101. Sheplak, M., et al., *Characterization of a silicon-micromachined thermal shear-stress sensor*. *AIAA JOURNAL*, 2002. **40**(6): p. 1099-1104.
102. Grosse, S. and W. Schroeder, *Dynamic wall-shear stress measurements in turbulent pipe flow using the micro-pillar sensor MPS3*. *International journal of heat and fluid flow*, 2008. **29**(3): p. 830-840.
103. Grosse, S., T. Soodt, and W. Schroeder, *Dynamic calibration technique for the micro-pillar shear-stress sensor MPS3*. *Measurement science & technology*, 2008. **19**(10).
104. Engel, J.M., et al., *Development and characterization of an*

- artificial hair cell based on polyurethane elastomer and force sensitive resistors*, in *2005 Ieee Sensors, Vols 1 and 2*. 2005. p. 1014-1017.
105. Engel, J.M., et al., *Polyurethane rubber all-polymer artificial hair cell sensor*. *Journal of Microelectromechanical Systems*, 2006. **15**(4): p. 729-736.
  106. Liu, C., *Micromachined biomimetic artificial haircell sensors*. *Bioinspiration & Biomimetics*, 2007. **2**: p. 162-169.
  107. Timoshenko, S., Woinowsky-Krieger, S., *Theory of Plates and Shells*. 1959, New York: McGraw-Hill.
  108. Krause, J.S., et al., *MEMS Pressure Sensor Array for Aeroacoustic Analysis of the Turbulent Boundary Layer*. *ASME Conference Proceedings*, 2008. **2008**(48746): p. 771-779.
  109. Fox, R.W., P.J. Pritchard, and A.T. McDonald, *Introduction to fluid mechanics*. seventh ed. 2009: John Wiley & sons, inc. 752.
  110. *MS3110 Universal Capacitive Readout<sup>TM</sup> IC*. 2000, Irvine sensors corporation.
  111. Allen Cowen, B.H., Ramaswamy Mahadevan, and Steve Wilcenski, *PolyMUMPs Design Handbook v13*. 2011.
  112. Miller, D.C., et al., *Mechanical Effects of Galvanic Corrosion on Structural Polysilicon*. *Microelectromechanical Systems, Journal of*, 2007. **16**(1): p. 87-101.